Doctoral Thesis

Transport phenomena and correlation effects in MgZnO/ZnO interface confined high mobility two-dimensional electron systems

(MgZnO/ZnO界面における高移動度
二次元電子の輸送現象と相関効果)

ジョセフ　リンジー　フォルソン

Contents

List of Figures

List of Tables

Abstract

This thesis presents an experimental study on the growth of $Mg_xZn_{1-x}O$/ZnO heterostructures and the physical phenomenon displayed by the two-dimensional electron system confined the heterointerface. Through the use of distilled ozone as a source material in molecular beam epitaxy the low temperature electron mobility of heterostructures was enhanced to a maximum value of over 900,000 $cm^2\ V^{-1}\ s^{-1}$. In such high mobility samples, the quantum scattering time was observed to reach values of τ_q = 20 ps. Both of these values suggest that the quality of the $Mg_xZn_{1-x}O$/ZnO 2DES is on par with the cleanest semiconductor materials in existence.

The quality of these heterostructures is supported by the observation of both the integer and fractional quantum Hall effects at low temperature. In characterising the parameter space realised in this 2DES, it is revealed through electrical measurements that the spin susceptibility of two dimensional electrons is highly dependent on the charge density of the system. Moreover, the raw magnitude of the spin susceptibility of electrons is large enough to enable access to controllability of the spin polarisation of electrons at the chemical potential through sample rotation experiments. Pursuing this experimental degree of freedom at ultra-low temperatures, a rich array of electron correlation mediated ground states which display intricate dependencies on both the spin and orbital character of electrons at the chemical potential are observed. Most notably, in addition to a vast number of odd-denominator fractional quantum Hall states, an anomalous series of states which take an even-denominator is realised. The observation of these elusive even-denominator fractional quantum Hall states outside of the AlGaAs/GaAs 2DES establishes a new regime for probing their proposed applicability to topological quantum computation.

This work firmly establishes the experimental techniques for ultra-high quality oxide molecular beam epitaxy growth while defining the MgZnO/ZnO two dimensional electron system as a unique platform among prevailing material systems.

本論文では$Mg_xZn_{1-x}O$/ZnO ヘテロ界面に形成される二次元電子系の作製と物性に関する実験結果 を報告する。オゾンを用いた分子線エピタキシー法の開発により、試料の品質を反映する電子の低温移動度が900,000$cm^2\ V^{-1}\ s^{-1}$ まで上昇した。また、量子散乱時間（τ_q）は20 psまで到達したことによって、最高品質の半導体と並ぶほどのクリーンな系を実現した。
二次元電子系の品質は、極低温における整数 ・分数量子ホール効果の観測によって示唆される。さらに、この系の物理パラメータを調べることによっ て、大きなスピン感受率を有することと、そのキャリア濃度依存性を明らかにした。 その大きなスピン感受率を利用して、試料回転という実験 的な自由度を用いることで、化学ポ テンシャルにおける電子スピンと軌道成分の制御により電子相関に由来 する基底状態の探求に挑んだ。特に通常観測される奇数分母の分数量子 ホール状態に加え、偶数分母状態の発見につながった。これらの状態は AlGaAs/GaAs 二次元電子系のみで観測されてきたが本研究によって新たな実験パラダイムが可能となり、理論的に予想されているトポロジカル量子計 算への応用が期待される。
本結果は酸 化物の成長技術 の向上による超高品質化を実現し、多く存在する二次元系材料のなかでMgZnO/ZnO 二次元電子系がユニークな舞台であることを示した。

Chapter 1

Introduction and overview

Exciting new frontiers continue to develop within the realm of condensed matter physics. At the heart of such developments lies the never ending pursuit of the discovery of new, and continued development of ever higher quality and more accessible experimental systems. While this is true for all areas of condensed matter material physics, this thesis is focuses on materials which are known to host, or inherently are, two-dimensional electron systems (2DES) (or two-dimensional hole systems (2DHS)). In this field of research, perhaps the most exemplary case of steady advances enabled through technological leaps is that of ultra-high mobility AlGaAs/GaAs heterostructures. Using a measure of 'quality' as the electron mobility (μ) (see section 2 for an introduction to this term in the picture of Drude conductivity), the AlGaAs/GaAs 2DES now displays values exceeding μ = 10^7 cm^2 V^{-1} s^{-1} . This results in mean free paths of electron motion (roughly speaking, the length scale between scattering events) reaching macroscopic scales. Indeed, the improvements demonstrated in the AlGaAs/GaAs system have induced a positive feedback spiral, where the thirst for new physics drives the pursuit of higher quality samples, which is enabled through growth technology advances which ultimately unveils the underlying physics which was previously masked by residual disorder. These advances are numerically shown in Fig. 1.1 in terms of mobility as a function of temperature. It can be seen that the mobility dramatically increases when approaching liquid Helium temperatures (4.2 K) as a result of the suppression of phonon scattering of electrons. Restricting the discussion to low temperature, which reflects the rate of scattering from imperfections within the sample structure, it becomes clear that over the past 30 years the mobility of the system has shown steady advances as a result of technological leaps [1]. The developments achieved over time undoubtedly have far reaching implications across many fields of science, beyond isolated applications to the AlGaAs/GaAs system. Most notably, these advances have shaped the molecular beam epitaxy (MBE) apparatus - the work-horse of high quality crystal growth and used in this work - to be what it is today.

The AlGaAs/GaAs platform exists as a heterostructure which is on the order of micrometers thick and grown on inch-sized wafers. The system of focus in this work, the 2DES confined at the heterointerface of MgZnO/ZnO heterostructures, as well as other interface confined 2DES, such as Si systems, share this form (see Fig. 1.2). This large size has enabled the development of a wide range of devices, from macroscopic to mesoscopic, enabling a vast array of experimental frontiers. More recently, an entirely new paradigm of sample preparation has emerged. At least in the world of low dimensional physics, the poster material for this class of materials is graphene[2]. Instead of pursuing complex (and expensive) fabrication technology such as MBE for making semiconductor heterostructures, materials

which are fundamentally 2D in nature can be made clean when exceptional care is paid during the device fabrication process. The technique used is entitled exfoliation and involves the isolation of thin layers (down to single atomic layers) of the material of interest being isolated from a larger bulk to then be measured independently. In the case of graphene - a single honeycomb layer of carbon atoms is isolated from bulk graphite through a repeated transfer process of increasingly thin specimens. This technique is enabled through the nature of graphene sheets having strong in-plane bonds, but weak out of plane interactions. The development of this technique has provided a completely new regime for sample fabrication and materials research, as now the role of sample "growth" is decentralised. The worlds of crystal growth and exfoliation are now colliding again with the current boom in the research of topological insulators, which combine the art of materials growth with the exotic physics possible in Dirac electrons, similar to those observed in graphene, and transition metal dichalogenides[3] which similarly are two-dimensional van der Waals materials but may be grown synthetically. It is clear however that across all of these systems, it is a prerequisite that the quality of samples be improved in order for the underlying fragile physical phenomena to be revealed.

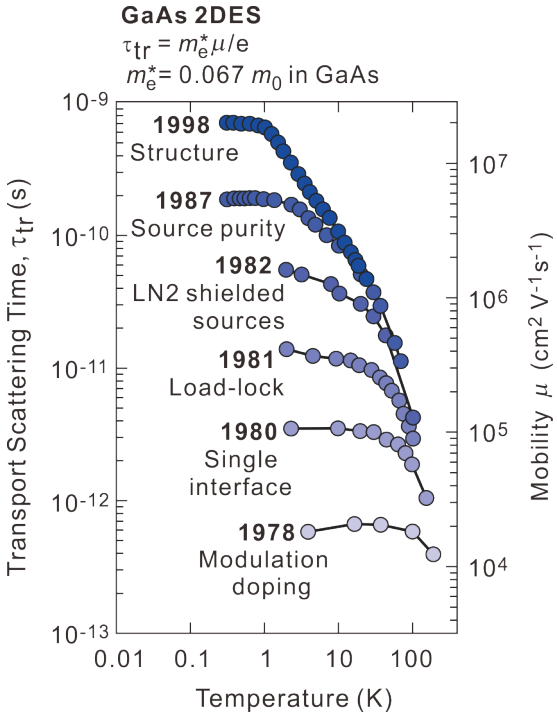

Figure 1.1: Transport scattering time and mobility of the AlGaAs/GaAs as a function of temperature through the years. Technological advances are noted next to each data set. Adapted from Ref. [1].

Amongst this momentum, this thesis reports on the growth, characterisation and exploration of electronic ground states observed in the 2DES confined at the heterointerface of $Mg_xZn_{1-x}O$ and ZnO. From a thin film growth point of view, this is an exciting frontier as these materials are outside the realm of traditional semiconductor materials. Indeed, they are oxides which, despite encompassing a large portion of the earth's crust, are still seen to be "dirty" compared to their semiconductor cousins due to their complex chemistry and range of crystal structures. This has limited their exploration in the realms of both fundamental research and the electronics industry. However, momentum has built in the past years as all aspects of the materials production process are improved [4], and niche applications are

realised, for example indium-gallium-zinc oxide (IGZO) displays. The process of making these materials "clean" begins from the ground up - purifying source materials and achieving high quality single crystal growth. In the case of thin film growth, substrates must then be manufactured. Owing to the large range of crystal structures and lattice parameters observed in the realm of oxides, the range of substrates available are accordingly extensive and ever expanding. Only once these basic requirements are fulfilled could one contemplate exploring the growth of thin films and heterostructures. However, if these challenges can indeed be tackled, a realm of inherently rich degrees of freedom awaits. Indeed, the wide range of elements possible to incorporate in oxide thin film growth with oxygen as the "glue" is astounding. This range of compositions combined with the modified parameter spaces induced by the ionicity of oxide crystals evidently induces numerous exotic physical phenomenon[4]. In this work we take this field into uncharted territories by pursuing truly "ultra-high" quality growth. The goal is simply to take oxides to a level of quality which matches and surpasses that of the best semiconductor materials. This should be stimulating from a technical, chemical and physical point of view.

This thesis aims to achieve this goal by pursuing ultra-high quality MgZnO/ZnO heterostructures. This encompasses technical improvements in the field of sample growth and design, while establishing the criteria for the efficient screening and assessment of samples grown. As an extension of this, it aims to present a new twist on quantifying "quality" of a 2D system by comparing the MgZnO/ZnO with other prevailing 2D materials both quantitatively in terms of scattering times and mechanisms, as well as qualitatively, through the comparison of electron ground states which are observed. By the former criteria it is made clear that the MgZnO/ZnO achieves a level of quality which is best compared with the highest quality AlGaAs/GaAs heterostructures. We aim in the process of this discussion to demonstrate that new physics is possible if a materials' unique parameter space is identified and then experimentally explored.

In beginning this thesis, some of the first questions that may be posed include *'in the context of a three-dimensional world, what are two-dimensional electrons?'*, *'How and in what materials are they realised?'* and *'What special physics may be observed?'*, and most importantly *'Why ZnO?'*. While the nuances of such answers hopefully become clear through the course of this thesis, the basic context is introduced below.

1.1 2D material systems

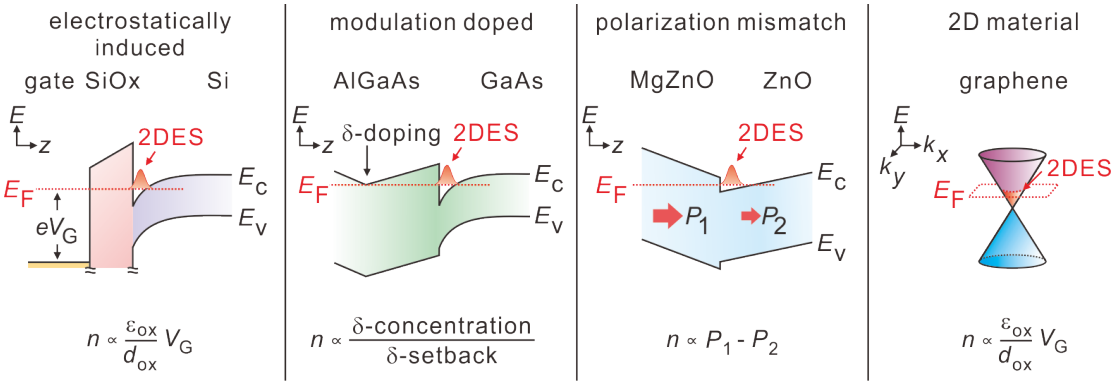

Figure 1.2: A schematic representation of four scenarios in which a two-dimensional conducting system is realised.

Amongst the first points to be clarified is the concept of two-dimensional charge carriers. Four different scenarios of systems which display such character are schematically presented in Fig. 1.2. Each of these systems represents a unique family of materials. For the first three scenarios, that is the SiOx/Si, $Al_xGa_{1-x}As$/GaAs and $Mg_xZn_{1-x}O$/ZnO , the common character is the formation of a quantum well (QW) at the heterointerface of two materials with differing band gaps (E_g). In the simplest picture, electrons form discrete energy levels ('subbands') as conduction band bending occurs at the heterointerface. An analogous event unfolds for holes if the material is p-type and the valence band contributes to conduction. The reduction of three dimensional electrons into planar electrons can be shown though a simple finite wall approximation where the band bending creates a potential well. Beginning with the wavefunction of electrons where the x, y motion is decoupled from the z-motion of electrons,

$$\Psi(x, y, z) = \Psi(x, y)\Psi(z) \tag{1.1}$$

The Schrödinger equation reads,

$$\frac{-\hbar^2}{2m^*}\frac{d^2\Psi(z)}{dz^2} + V(z) = E\Psi(z) \tag{1.2}$$

Where $\hbar$ is the reduced Planck constant and m^* is the effective mass of carriers. We place the electrons within a delta-function potential given as,

$$V(z) = V_0\delta(z) \tag{1.3}$$

and note the wavefunction in the z-direction decays at,

$$\Psi(z) = \Psi_0(z)e^{-\beta z} \tag{1.4}$$

Solving this gives the relationship,

$$\beta = \sqrt{\frac{(V(z) - E)2m^*}{\hbar^2}} \tag{1.5}$$

Therefore as $V(z) \to \infty$, $\beta \to \infty$ and therefore the wavefunction is pushed to the two dimensional limit. The remaining term $\Psi(x, y)$ finds wavevectors only in the (x, y) plane,

$$E = E_n + \frac{\hbar^2 k_F^2}{2m^*} = E_n + E_F \tag{1.6}$$

$$k_F = \sqrt{\frac{4\pi n}{g_s g_v}} \tag{1.7}$$

Here, E_n is the confinement energy from the notch of the QW to lowest energy subband E_0 level and k_F is the Fermi wavenumber. The final term gives the Fermi energy (E_F) of the system, and is related to the density of charges (n), and the degeneracies present in the system, for example spin (g_s) and valley (g_v). Such degeneracies are material dependent and greatly influence the variety of physical phenomenon encountered.

While the above energetics are common between the first three scenarios presented, the mechanism to form the QW in the first place differs. For SiOx/Si, the formation of a metal-oxide-semiconductor

field effect transistor (MOSFET) facilitates the tuning of E_F through the application of an external gate voltage, V_G. This results in band-banding and the formation of a triangular confinement potential at the heterointerface of SiOx and Si. The charge accumulated at the heterointerface is proportional to the electric field, which is dependent on the dielectric (ϵ) properties of the respective materials incorporated in the heterostructure. A similar principle is at the heart of silicon based circuitry used in the semiconductor industry, where conduction may be switched between an on-off state.

An alternative option is the placement of dopants within or close to the QW. It is the latter scenario, termed 'modulation doping' which is widely utilised in $Al_xGa_{1-x}As$/GaAs heterostructures. All heterostructures shown in Fig. 1.1 are modulation doped. In this system, the band offset at the heterointerface is determined by the alloyed content of aluminium (x) in the capping layer, and carriers are donated by intentionally doping impurities, typically silicon for electrons and carbon for holes, remotely from the heterointerface within the AlGaAs capping layer. In the simplest picture, the doping content and the setback distance between dopants and heterointerface determines the charge density, as shown in 1.2. The insight to place impurities far away from the conducting layer takes advantage of the fact that within the Thomas Fermi screening approach the external potential imposed by a scattering centre decays as $1/r^2$ in 2D. Placing dopants away from the 2DES therefore both preserves a high E_F (*i.e.* charge density) which can screen any impurities while simultaneously reducing the magnitude of the potential fluctuation induced. In addition, the near perfect crystal lattice matching of the AlGaAs and GaAs layers means that the heterointerface formed is sharp and without strain induced dislocations. These features, combined with purification of source materials and improvements in chamber design have resulted in the exceptional quality of the AlGaAs/GaAs 2DES. The majority of past research on the fragile ground states encountered in 2DES, as explored later in this thesis, has been performed on AlGaAs/GaAs heterostructures exactly for this reason.

A third option is the exploitation of internal polarisation (P) fields present in crystal structures which lack inversion symmetry. This is the case in $Mg_xZn_{1-x}O$/ZnO heterostructures, the focus of this thesis, and the mechanism of inducing a 2DES is explained in more detail in section 3.2. The alloying of Mg into ZnO has the effect of distorting the crystal structure, shrinking the c-axis and expanding the a-axis. This results in a quantitative modification in P. In the case of epitaxial growth of a heterostructure of $Mg_xZn_{1-x}O$ grown on top of ZnO, the a-axis of the $Mg_xZn_{1-x}O$ layer will be locked to the underlying ZnO layer (assuming the film does not relax, which is the case for all films discussed in this work), but the c-axis length will experience some finite distortion. As schematically displayed in Fig. 1.2, this leads to a mismatch in P at the heterointerface. The charge accumulated to screen this mismatch can be well approximated through the relationship $n \propto \frac{\Delta P}{e}$. Therefore, the concentration of the 2DES can be controlled through the alloy content x of the capping layer. The same mechanisms is at work in AlGaN/GaN heterostructures which share the same inversion asymmetric Wurtzite crystal structure as ZnO. The advantages of such a system is the simplicity of design and the lack of intentional doping of impurities anywhere in the sample which will be ionised (as is the case with silicon or carbon in AlGaAs/GaAs heterostructures) when donating carriers and hence modify the disorder landscape within the sample.

The fourth option pictured is different to those scenarios above. As mentioned above, a new generation of fundamentally 2D materials[5] has emerged in recent years. The most prominent example is graphene [2]; a single atom thick honeycomb lattice of carbon atoms which may be isolated from bulk graphite. This is made possible through the fact that the in-plane covalent bonds are strong, while the out-of-plane van der Waals force is weak. The momentum around this material, and in a more broad

view, the fabrication process it utilises, is immense. Instead of requiring multi-million dollar specialised vacuum equipment (i.e. a MBE) dedicated to growing a single material, the process of exfoliation has enabled the prospect of high quality 2D samples being realised in a much more economical and flexible manner. Such exfoliated flakes are placed on extremely flat substrates and contacted via electron beam lithography defined electrodes due to their small size scales (on the order of micrometres). The use of conducting substrates allows the application of an electric field to the device if a dielectric layer is present, which is usually the case as SiOx/Si is widely used. Through the years, more sophisticated devices have emerged. These include the incorporation of a buffer layer of exceptionally flat single layer dielectric materials such as boron nitride[6], or the physical suspension of the graphene flake away from the substrate [7]. These steady technological advances have had a dramatic positive impact on both sample quality and the degrees of freedom available in experiments. Moreover, the physics observed in graphene, which hosts massless Dirac Fermions, is in many ways unique to that observed in traditional semiconductor materials with massful electrons. The legacy of graphene technology is already evident. New frontiers of 2D materials continue to emerge including the family of transition metal chalcogenide materials[3] given by the formula MX_2 (M = Mo, W and X = Se, S), and the more exotic topological insulators, who similarly host 2D Dirac electron conductivity on the surface of an insulting bulk, which may be fabricated both through thin-film growth, or exfoliation of thin crystal samples.

1.2 Outline of thesis

Having canvassed the spectrum of material options available, the obvious question arises - "*Why ZnO?*". This is an especially poignant question considering the quality now offered by AlGaAs/GaAs heterostructures, and the accessibility and degrees of freedom achievable in the fabrication of graphene or other 2D materials[5]. This thesis aims to explore this question and to amass evidence that the MgZnO/ZnO 2DES offers a unique parameter space for the exploration of the fragile physical phenomenon observed in 2D conducting systems. In the context of this work, the first question is then "*How do you achieve high quality ZnO?*", for if high quality MgZnO/ZnO heterostructures were not available, all efforts would in turn be irrelevant. Throughout the course of this thesis, significant technological advances have been made to enable high quality growth of MgZnO/ZnO heterostructures via oxide-MBE (OMBE). This in turn has unveiled the parameter space achieved and the underlying rich physics which was not observed in previous generations of lower quality films. Indeed, it is shown that some of the ground states observed are unique from any other material system in current existence. It is therefore the combination of high quality with an understanding of the parameter space establishes the MgZnO/ZnO 2DES as a distinct platform among all 2D materials. The remainder of thesis conveys this information and is divided in the following ways:

The Second Chapter introduces the basic physical concepts explored throughout this thesis. By building on the basis of classical conduction and electron scattering, the concept of the formation of Landau levels (LL) in a 2DES exposed to a perpendicular magnetic field is introduced. A rich array of physics exists at high magnetic field within these discrete levels in high quality samples. These include the integer and fractional quantum Hall effects. Past research on AlGaAs/GaAs has shown that distinct regimes exist within these phenomenon depending on the orbital nature of the LL. We canvass this history and put it in perspective for later chapters of this work. While an attempt is made to touch on most theoretical aspects required for the understanding in this thesis, some components are introduced at later

stages in combination with experimental results.

The Third Chapter is dedicated to exploring the physical growth of $Mg_xZn_{1-x}O$/ZnO thin films and technical advances in growth technology. Beginning with an introduction to the material system, the details of the MgZnO/ZnO heterostructure are introduced from a materials point of view. A significant portion of this chapter is dedicated to exploring the technical advances in OMBE growth technology which have been made during the course of this thesis. This encompasses work dedicated to reducing the sources of impurities through improved apparatus design and material choices. In addition, the growth window and parameters along with heterostructure design of MgZnO/ZnO samples is introduced and improved on compared to previous works. The quality of samples is primarily gauged based on physical characterisation techniques such as surface roughness, as well as basic electrical measurements such as the zero field mobility (i.e. conductivity). The peak mobility achieved exceeds a value of 900,000 cm^2 V^{-1} s^{-1} which is nearly an order of magnitude higher than previous generations of growth.

The Fourth Chapter explores the physical parameter space that is realised in the MgZnO/ZnO 2DES. These parameters range from details of the confinement potential of the QW formed at the heterointerface to the spin susceptibility of electrons. A number of experimental techniques are introduced, including luminescence, resonance and transport techniques. The majority of work is performed at moderate temperatures of T = 500 mK with a number of results obtained through collaborations. Many of the parameters explored require the application of an external magnetic field, which induces LL quantisation. For example, through a careful analysis of the low field magnetotransport of heterostructures, the total scattering time (also known as the single particle relaxation time or quantum scattering time, τ_q) is measured and compared across a range of samples. When comparing this value with the transport scattering time (τ_{tr}), which is representative of the sample mobility, it becomes possible to infer specific scattering mechanisms prominent in the samples grown. Through this analysis we find the surface of heterostructures to impose significant disorder on the 2DES. We discuss the implications for heterostructure design. In a concluding spirit, an inter-material comparison of such numerics is performed. We reveal that in terms of both τ_{tr} and τ_q, the MgZnO/ZnO is essentially on-par with the extremely clean AlGaAs/GaAs 2DES.

The Fifth Chapter reports the experimental results obtained in high mobility samples at ultra-low temperatures ($T \approx$ 15 mK). It is seen that through proper cooling of high mobility samples, a rich array of ground states are observed. These include the integer and fractional quantum Hall effects. The requirement of such low temperatures is due to the observation that many states have small activation energies on the order of 100 mK. For the fractional quantum Hall effect, we observe robust states which take an even-denominator in their filling factor (ν). These states are exceptionally rare and fragile. We observe a well developed state at ν = 7/2 and discover it possible to induce a fully developed state at ν = 3/2 in tilted magnetic field experiments. This is the first observation of such behaviour in any 2D system. In addition, a rich interplay is observed between characteristics akin to charge-density-wave physics and the spin degree of freedom. These observations are difficult to reconcile within the current range of prevailing knowledge and experimental results in AlGaAs/GaAs 2DES. Key to understanding and exploring these ground states is the exploitation of the high magnitude of spin susceptibility of MgZnO/ZnO 2D electrons. We demonstrate that the stability of both odd and even denominator fractional states may be probed through rotation studies as a function of spin polarization and orbital character. This is an experimental technique not often used in AlGaAs/GaAs investigations due to the small $g_e^* m_e^*/m_0$ of

that system. The availability of this degree of freedom concomitantly to the high level of sample quality demonstrated establishes the MgZnO/ZnO as a unique entity among prevailing 2DES.

The Sixth Chapter introduces on-going projects and technical developments beyond the focus of the earlier parts of the thesis. These include gating of heterostructures via a novel structure termed an "air-gap" field effect transistor, and fine lithography processes to define mesoscopic devices. In the latter, the phenomenon probed are on the order of microns. Therefore, the ability to perform such experiments is a direct result of the increase in electron mobility which is extensively explored in earlier chapters of this thesis. These techniques are introduced within the context of delivering new experimental degrees of freedom in order to answer questions which inevitably remain from the previous chapters. Finally, the conclusions of this work as well as an outlook on new frontiers and challenges to be pursued in future work is presented.

Chapter 2

Fundamentals of 2D materials

As presented in the introduction, a range of material systems host or inherently are, two dimensional conductors. In general, the discussion presented in this section will be restricted to carriers with a parabolic dispersion (thus excluding systems with a linear dispersion such as graphene or surface states of topological insulators). In these materials, reduced dimensionality may be achieved through finite size effects in the formation of a QW, quantising the electron energy spectrum into discrete levels. While each material system is garnished with subtle differences, common aspects exist and the underlying physics is mostly shared. In this section we begin by describing the basics of classical conduction with the intent of linking this framework with the ability to screen samples which have been grown in section 3. In the later parts of this section, the application of a magnetic field perpendicular to the 2DES is seen to induce a highly discrete spectrum of quantised energy levels, entitled Landau levels (LL). The variety and nature of the exotic ground states observed within this framework is the focus of this thesis and is explored extensively in section 5. Much more extensive accounts of the introduced physics exist in the literature, for example [8–11].

2.1 Classical transport

Classical transport of electrons within an electric field is described by the Drude theory. The average drift velocy of electrons is given by,

$$v_d = \frac{-e\boldsymbol{E}\tau_{tr}}{m_e^*} \tag{2.1}$$

Here, $\boldsymbol{E}$ is the electric field, m_e^* is the electron effective mass, and τ_{tr} is the average time between scattering events. This last term is important and will be explored later in detail. It is also termed the transport scattering time. Following, the current density is given as,

$$j = -nev_d = \sigma_0\boldsymbol{E} \tag{2.2}$$

where $\sigma_0 = ne^2\tau_{tr}/m^*$ is the conductivity of the system in the absence of a magnetic field.

At this point we highlight,

$$\tau_{tr} = \frac{\mu m^*}{e} \tag{2.3}$$

This establishes the connection between mobility (μ) and the m_e^* of a charge system. This is an important relationship as it scales the mobility (which is simply related to the conductivity of the sample) by the effective mass of charge carriers. Therefore, when comparing different material systems with differing effective masses, the use of τ_{tr} more accurately reflects the underlying characteristics of electron conduction. At low temperature the electron gas is degenerate and only electrons at the E_F can scatter. We restrict the discussion from now on to such a scenario.

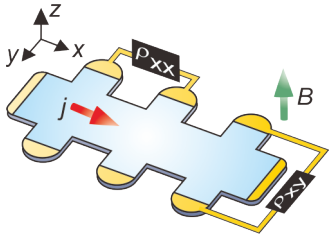

Figure 2.1: Schematic representation of a Hall bar with the a current j being passed along the x direction and a magnetic field B in the z-direction. The longitudinal (ρ_{xx}) and Hall (ρ_{xy}) resistance measurement configurations are shown.

We here highlight that the total relaxation rate in a 2DES is actually related to the sum of different scattering processes. Matthiessen's rule states,

$$\frac{1}{\tau_{tr}} = \frac{1}{\tau_{impurities}} + \frac{1}{\tau_{subband}} + \frac{1}{\tau_{roughness}} + \frac{1}{\tau_{remotedoping}} \dots \tag{2.4}$$

Here, the subscript signifies a scattering event originating from a certain type of scattering centre. For example, unintentional impurities in the vicinity of the 2DES, inter-subband, roughness of the interface or remote doping induced potential fluctuations. At higher temperatures there would be a phonon scattering mediated term in this equation, but, as stated, we assume the temperature is very low and phonon scattering does not contribute. All scattering events are therefore elastic.

We now identify that the transport scattering time has a large bias towards events which have a large angle change in the electron momentum vector. This is schematically shown in Fig. 2.2 and is numerically signified by the relationship,

$$\frac{1}{\tau_{tr}} = \frac{m^*}{\pi\hbar^3}\int_0^{\pi} d\theta |V(q)|^2 (1 - cos\theta) \tag{2.5}$$

where θ is the angle between incident momentum and final momentum vector and $V(q)$ is related to the potential deformation imposed from respective scattering mechanism [12]. Analytic expressions for each variety exist in the literature, which allows quantitative analysis of experimental results. The cosθ term therefore biases large angle events to influence τ_{tr}.

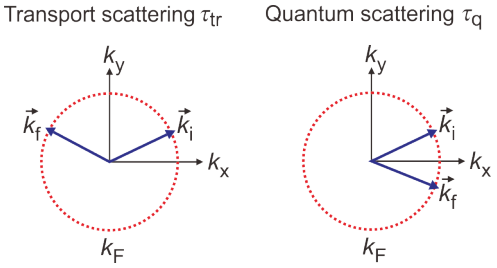

Figure 2.2: Elastic scattering processes where **a**, There is a large angle between initial (k_i) and final (k_f) wavevectors which has a strong effect on τ_{tr} and **b**, a small angle which affects τ_q.

In contrast, small angle scattering events contribute to another relaxation time coined the quantum scattering time (or alternatively single particle relaxation time). For this, the weighting term towards

large angle events is dropped, and therefore this includes all scattering events. Accordingly, this time is shorter when experimentally measured.

$$\frac{1}{\tau_q} = \frac{m^*}{\pi\hbar^3}\int_0^\pi d\theta |V(q)|^2 \tag{2.6}$$

However, this quantity is more difficult to measure as it is not reflected in the zero field resistivity of the sample. Instead, the quantum oscillations in resistance with applying a magnetic field must be analysed. It is thought that since this value should include all scattering events, it is a more accurate assessment of a samples "quality", as opposed to the transport scattering time. In section 4.3 this is experimentally explored.

With the application of a magnetic field B in the z direction, the conductivity and resistivity (ρ) become tensors,

$$\sigma = \begin{pmatrix} \sigma_{xx} & \sigma_{xy} \\ \sigma_{yx} & \sigma_{yy}, \end{pmatrix}, \quad \rho = \begin{pmatrix} \rho_{xx} & \rho_{xy} \\ \rho_{yx} & \rho_{yy}, \end{pmatrix} \tag{2.7}$$

A Lorentz force must also be added to the velocity equation,

$$v_d = -e(E + v_d \times B)\frac{\tau_{tr}}{m^*} \tag{2.8}$$

In the x, y plane,

$$\sigma_0 E_x = \omega_c \tau_{tr} j_y + j_x \quad \text{and} \quad \sigma_0 E_y = \omega_c \tau_{tr} j_x + j_y \tag{2.9}$$

where $\omega_c = \frac{eB}{m^*}$ is the cyclotron frequency. These lead to the relationship between resistivity and conductivity,

$$\sigma_{xx} = \frac{\rho_{xx}}{\rho_{xx}^2 + \rho_{xy}^2} \quad \text{and} \quad \sigma_{xy} = \frac{\rho_{xy}}{\rho_{xx}^2 + \rho_{xy}^2} \tag{2.10}$$

Using Ohms law, ***E*** = ρj (and noting that $j_y = 0$), it can be shown that,

$$\rho_{xx} = \frac{1}{ne\mu} \tag{2.11}$$

$$\rho_{xy} = \frac{B}{ne} \tag{2.12}$$

This is the foundation of a Hall measurement. The Hall term (ρ_{xy}) therefore is independent of the effective mass and scattering rate. It shows that transport measurements are a convenient means for determining the charge density of the system. We note that throughout this thesis we alternatively refer to ρ_{xx} and ρ_{xy} as the resistance R_{xx} and R_{xy}. While a 1:1 correlation may be made between these Hall terms, the relationship between the longitudinal terms requires scaling of the resistance according to the device proportions. This however does not affect the underlying physics. A Hall experiment is shown schematically in Fig. 2.1. An alternative experimental geometry is the van der Pauw geometry, there electrodes are placed at the edge of an ideally square sample. In this case, the zero field resistivity is given by,

$$\rho_{xx} = \frac{\pi R}{ln2} \tag{2.13}$$

where R is the average resistance measured in orthogonal directions.

We now address the raw magnitude of the Coulomb interaction felt by the confined electrons. To characterise the strength of electron-electron interaction in the absence of a magnetic field, the ratio of Coulomb to Fermi energy is taken. This is termed the Wigner Seitz radius, and is a dimensionless value,

$$r_s = \frac{E_c}{E_F} = \frac{e^2 m_e^*}{2\pi\epsilon\hbar^2\sqrt{\pi n}} \tag{2.14}$$

It can be seen therefore that reducing the charge density enhances this value, resulting in an expected increase in electron correlation strength when diluting the 2DES. Indeed, multiple theoretical works predict that the magnitude of r_s can have a dramatic impact on the ground state of the electron system even without applying a magnetic field [13, 14]. Some predictions include Wigner crystallisation when $r_s \geq 30$ with paramagnetic to ferromagnetic transitions. Experimental observations of such phases are however extremely difficult due to real world effects, such as disorder and finite temperature. As can be seen, increasing r_s inherently implies that the charge density be reduced or Coulomb interaction be strengthened. Usually it is a combination of both. Doing this however greatly reduces the ability of electrons to screen disorder as the Fermi energy is lowered, which, can ultimately send samples insulating before the onset of exotic physics. It is only in recent experiments in ultra-clean AlGaAs/GaAs 2DHS samples that evidence for a zero field Wigner crystal is amassing [15]. As will be compared in later sections (see table 4.1), the AlGaAs/GaAs 2DHS has a much larger effective mass ($\approx 0.5m_0$) than the AlGaAs/GaAs 2DES ($\approx 0.069m_0$) but should have a similar disorder landscape. This opens a unique experimental frontier when compared to the 2DES.

As can be seen from the Table 4.1, the MgZnO/ZnO finds itself in a similar parameter space to the AlGaAs/GaAs 2DHS due to its large effective mass, which is on the order of $\approx 0.4m_0$ in real 2DES samples. In later sections of this thesis we explore this parameter independently and quantitatively and reveal that distinct effects of the expectedly strong electron interaction are revealed in the enhancement of the mass. This in turn affects the spin susceptibility ($g_e^* m_e^*/m_0$)of electrons. This is shown in sections 4 and 5.

2.2 Landau levels

Moving from classical transport to the quantum mechanical result, it is possible to prove that the constant density of states of the 2DES develops into discrete Landau levels (LL) with the application of B (or strictly speaking a perpendicular magnetic field B_p). We again assume the temperature is low ($k_B T < \hbar\omega_c$) for all discussions below. The Hamiltonian is given by,

$$\mathcal{H} = \frac{\mathbf{P}^2}{2m^*} + V(r) \tag{2.15}$$

The first term is the kinetic term with $V(r)$ related to the Coulomb energy, as briefly introduced above. For the demonstration of LL we ignore this term, and also the spin degree of freedom, which we will add to the Hamiltonian at a later point.

The canonical momentum given is as ,

$$\mathbf{P} = \frac{\hbar}{i}\nabla - e\mathbf{A} \tag{2.16}$$

With **A** the electromagnetic field, which we set to zero. The energy of one electron is given by

$$E_k = \frac{\hbar^2 k^2}{2m^*} = \frac{\hbar^2}{2m^*}(k_x^2 + k_y^2) \tag{2.17}$$

With the wavenumber resistricted to,

$$k_x = \frac{2\pi}{L_x} n_x, \text{and} \quad k_y = \frac{2\pi}{L_y} n_y \tag{2.18}$$

with n_i integers 0, $\pm$ 1, $\pm$ 2, . . . , with the Pauli exclusion principle requiring that only one electron can occupy each state. The two-dimensional density of states, which is apparently constant, is given by,

$$g(E)_{2D} = \frac{m^*}{\pi\hbar^2} \tag{2.19}$$

Integrating this to E_F gives,

$$E_F = \frac{\hbar^2 k_F^2}{2m^*} \tag{2.20}$$

with $k_F = \sqrt{4\pi n}$ when ignoring any spin degeneracy. With the addition of spin degeneracy two electrons (up and down spin) may occupy each state and $k_F = \sqrt{2\pi n}$. The situation described here is shown in Fig. 2.3**a**.

We now add a magnetic field perpendicular to the 2DES plane and show that discrete energy levels form within the previously constant density of states. These are termed Landau levels. Within the Landau gauge, **A** $= B(-y, 0, 0)$ the Hamiltonian becomes,

$$\mathcal{H} = \frac{1}{2m^*}(p_x - eBy)^2 + \frac{p_y^2}{2m^*} = \frac{p_y^2}{2m^*} + \frac{1}{2}m^*\omega_c^2(y - y_0)^2, \tag{2.21}$$

with

$$y_0 = \frac{p_x}{\hbar} l_B^2 = k_x l_B^2 = \frac{2\pi l_B^2}{L_x} \tag{2.22}$$

Here we have introduced the magnetic length as the length scale of the problem,

$$l_B = \sqrt{\frac{\hbar}{eB}}, \tag{2.23}$$

p_x therefore defines the centre of a harmonic oscillator in y with a frequency given by,

$$E_N = (N_e + 1/2)\hbar\omega_c, \quad N_e = 1, 2, 3, \ldots \tag{2.24}$$

Here, N_e is the quantum number (an integer) of the Landau levels which develop. We often add the subscript N_e to emphasise these levels belong to the orbital motion of electrons. We next address the degeneracy of these levels as a function of B. In a rectangular geometry where $L_x = L_y$, y_0 is set by evenly spaced discrete values,

$$\Delta y_0 = \frac{h}{eB_p L_x} \tag{2.25}$$

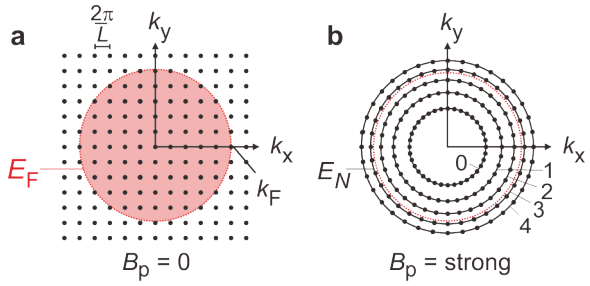

Figure 2.3: Two dimensional electrons in **a**, zero magnetic field where the electrons occupy energy states up to the E_F **b**, A strong magnetic field where the constant DOS is split into LL.

The degeneracy of a level is therefore given by,

$$N_L = \frac{L_y}{\Delta y_0} = \frac{L_y L_x e B_p}{h} = \frac{Area.B_p}{\phi_0} \tag{2.26}$$

where ϕ_0 = h/e is the flux quantum. Here, the numerator is equivalent to the total field piercing the sample. Therefore, the number of filled levels, the "filling factor" is given as the ratio of charge density to level degeneracy,

$$\nu = \frac{n}{N_L} = \frac{hn}{eB_p} \tag{2.27}$$

The representation of LL in k-space is shown in Fig. 2.3**b**. The radius of each circle is defined as $k_N^2 = \frac{1+2N_e}{l_b^2}$. With increasing the magnetic field these circles steadily spread to higher k vectors and are depopulated, as the above section details.

An alternative representation of the above scenario is given in Fig. 2.4. Starting from the constant density of states (panel **a**), the LL develop with increasing field (panel **b**). It is also timely to state that with the application of a magnetic field, the zero field E_F ceases to be a well defined value. Rather, the chemical potential (μ_c) is used. Finally, we note that the LL are in reality not infinitely sharp levels. Rather, disorder within the sample broadens these. The broadening can be estimated as,

$$\Gamma = \frac{\hbar}{\tau_q} \tag{2.28}$$

where τ_q is the quantum scattering time previously identified. The magnitude of disorder therefore has dramatic impacts on the range and stability of ground states which the LL can host, as will be explored later.

Finally, we note that different degeneracies of these LL can exist, including valley or spin. Spin is generally ubiquitous in semiconductor materials, and hence is the Zeeman coupling to the total field (B_t),

$$E_z = g_e^* \mu_B B_t \tag{2.29}$$

Here, g_e^* is the systems g-factor (a material dependent quantity) and μ_B is the Bohr magneton.

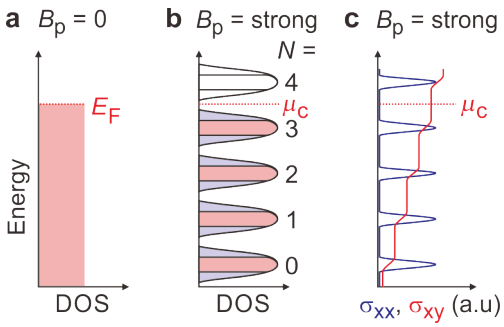

Figure 2.4: Two dimensional electrons in **a**, zero magnetic field where the electrons occupy energy states up to the E_F **b**, A strong magnetic field where the constant DOS is split into LL and **c** the longitudinal and Hall conductivity in arbitrary units. The chemical potential is shown by the dotted red line.

We therefore add this term to describe the fully ladder of spin split LL,

$$E_N = (N_e + 1/2)\hbar\omega_c \pm g_e^* \mu_B B/2 \tag{2.30}$$

where a + (-) signifies down (up) spin assuming g is positive.

The formation of LL is the underlying mechanism for the observation of the integer quantum Hall effect in transport. This result is schematically shown in Fig. 2.4**c**. The longitudinal (blue) and Hall (red) conductivity of the sample is shown as a function of chemical potential. With increasing B_p the levels are successfully depopulated and the chemical potential crosses the LL. Here, the effects of disorder and level broadening are crucially important. As a general rule, the resistivity is proportional to the DOS $\rho_{xx} \propto g(E)_{2D}$. This already provides a clue as to what occurs at integer fillings of LL, where, the DOS at μ_c oscillates and even becomes zero. Indeed, the longitudinal resistivity is seen to disappear under this condition. Simultaneously, the Hall resistance enters a plateau at values of,

$$\rho_{xy} = \frac{h}{\nu e^2}, \quad \nu = 1, 2, 3, \ldots \tag{2.31}$$

Here, we restrict the filling factor to be an integer number. This behaviour can be extended far beyond exact integer filling factors through high amounts of disorder. When electrons enter the DOS of localised states which are below the mobility edge (purple shaded regions in Fig. 2.4**b**), no contribution to transport occurs and the resistance remains in a plateau at the quantised values.

The origin for the quantisation of the Hall resistance lies in the conducitivity of a single LL and the development of edge states. When a LL is full, all electrons are undergoing cyclotron motion and localised in the bulk of the sample. The only remaining open orbits are found to bounce along the edge of the sample. These effectively carry the current. This is schematically shown in Fig. 2.5.

According to the formalism by Büttiker [16], the current fed into each edge state is given by

$$I = \frac{e}{h}\Delta\mu_{potential} \tag{2.32}$$

where $\mu_{potential}$ is the external potential applied to excited to 2DES. The total current is therefore given by summing over the total transmission of all edge channels (**T**),

$$I = \frac{e}{h}\sum_{i=1}^{i=N} \mathbf{T}_{ij}\Delta\mu_{potential} \tag{2.33}$$

Each fully transmitted channel contributes e/h current. The voltage drop is given by $\Delta\mu_{potential} = eV$, and therefore the resistance is,

$$\rho_{xx} = \frac{h}{\mathbf{T}e^2} \tag{2.34}$$

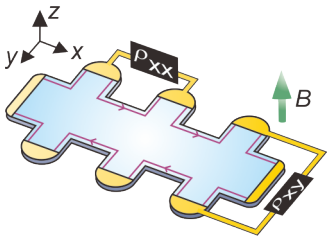

Figure 2.5: Schematic representation of a Hall bar with a magnetic field inducing edge channels to flow around the sample according to the Landau-Büttiker model [16].

The edge channels propagating around the sample enter and leave the contacts at the samples edge, as shown in Fig. 2.5. This intuitively explains the experimental observations schematically shown in 2.4. A measurement of ρ_{xx} will mean that the potential of the edge channels is the same between the contacts, therefore $\Delta\mu_{potential}$ = 0, and so the resistance is zero. A measurement of ρ_{xy} however incorporates edge channels which a finite $\delta\mu_{potential}$, as the two ends of the Hall bar correspond to the excited state and ground. A finite resistance will hence be measured, in units of h/e^2, as discussed above. This also explains the compatibility of the van der Pauw geometry with the measurement of the quantum Hall effect - since the currents flow along the edges no mixing can occur and the longitudinal and Hall resistivities are independently resolved. It is noted that this model describes the sample bulk being completely insulating and the current entirely carried by edge channels. Experiments point to this interpretation being oversimplified and reality being rich with details[17]. It does however act as a very useful way to visualise the effect.

2.2.1 Lowest Landau level

We now temporarily isolate the discussion to the lowest LL by going to very high field and setting $\nu < 1$. In this regime, all kinetic energy and spin degrees of freedom are quenched, and only the Coulomb term of the Hamiltonian remains.

$$\mathcal{H} = \sum_{j<k}\left(\frac{e^2}{r_j - r_k}\right) \tag{2.35}$$

Given this Hamiltonian, it is not immediately obvious that further ground states can be achieved. However, it is spectacularly obvious from experimental facts that new states are observed, and they are extremely numerous. Superficially identical behaviour to the integer quantum Hall effect occurs at fractional fillings factors in high mobility structures [18]. This effect is termed the fractional quantum Hall effect and is one of the main focuses of this thesis. The original observation was of a minimum in R_{xx} and developing plateau in R_{xy} of a high mobility (for the time) AlGaAs/GaAs heterostructure at filling $\nu = 1/3$. This was later explained to be due to the formation of a many-body ground state, where mutual repulsion between electrons causes gapped excitations leading to incompressibility and

hence dissipationless transport [9].

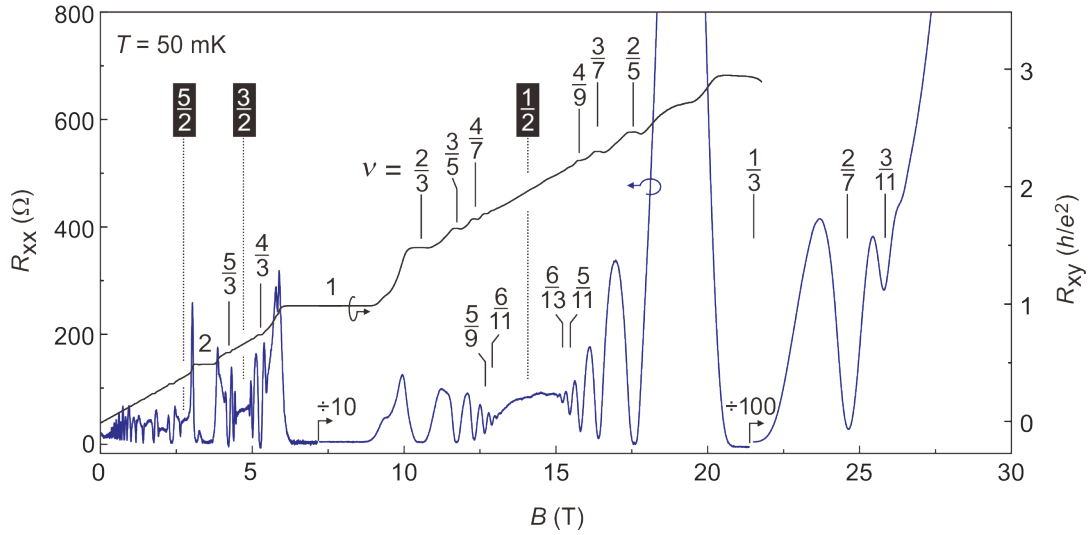

Figure 2.6: Low temperature T = 50 mK magnetotransport of a MgZnO/ZnO heterostructure when exposed to high magnetic fields. The filling factor (ν) is shown and a number of ground states are identified at integer and fractional fillings where the longitudinal resistance(R_{xx}) becomes zero and the Hall resistance (R_{xy}) quantised in units of $h/\nu e^2$.

In Fig. 2.6 we show magnetotransport of a high mobility MgZnO/ZnO heterostructure. This was measured at the High Magnetic Field Laboratory in Nijmegen, The Netherlands. These results will be published in detail in a dedicated manuscript [1]. Here, we highlight the exceptional array of ground states which can be achieved by accessing high magnetic fields and low temperatures. In addition to the integer quantum Hall effect which may be understood in the single particle framework introduced above, correlated electron ground states at ν = 1/3 along with more fractions at ν = 2/3, 3/5, 4/7, 5/9, 6/11, 6/13, 5/11, 4/9, 3/7 and 2/5 are observed around 1/2. In addition, states at 2/7 and 3/11 around ν = 1/4, and at 5/3, 8/5, 11/7, 10/7, 7/5, 4/3, 12/7, 9/7 and 6/5 around ν = 3/2 and 8/3 and 11/3 at even higher fillings are resolved. It is an exceptionally rich series of ground states which are difficult to intuitively understand. In the following paragraphs we canvass these regimes.

The many-body wavefunction of the ν = 1 ground state is given by 2.36

$$\Psi_{\nu=1} = \prod_{i<j}(z_i - z_j)e^{-\sum_i z_1^2/4} \tag{2.36}$$

Due to the Pauli exclusion principle, the wavefunction is a Slater determinant to achieve anti-symmetry. Following the discovery of a new ground state at μ = 1/3, Laughlin proposed the following many-body ground state,

$$\Psi_{1/m} = \prod_{i<j}(z_i - z_j)^m e^{-\sum_i z_1^2/4} \tag{2.37}$$

The wavefunction of 2.37 requires that m be odd to maintain anti-symmetry of the wavefunction. The integer form of the wavefunction provides an intuitive understanding. Increasing m to 3 effectively

[1] *in preparation*, D. Maryenko, J. Falson, Y. Kozuka, A. Tsukazaki, M. Kawasaki, A. McCollam, J. Bruin, U. Zeitler and J. K. Maan.

reproduces the lowest LL wavefunction with an additional two zeros in the wavefunction. The effect therefore manifests at $\nu = 1/m$. Numerical results show that this describes the opening of a gap at ν = 1/3 through electrons mutually avoiding each other. The same wavefunction is applicable to higher values of m, but the effect is weaker from an experimental point of view.

Before attempting to explain the full series of states observed in Fig. 2.6, we present a more general form of this wavefunction. As emphasised, the many body wavefunctions described above requires that due m be odd due to the Pauli exclusion principle. This is the reason for the effect most prominently manifesting at nu = 1/3. However, in systems where there is an additional internal degree of freedom, it is possible to construct a multicomponent wavefunction for the ground states by generalising Laughlin's wavefunction, as performed by Halperin [10],

$$\Psi_{m1,m2,n} = \prod_{k_1<l_1}^{N_\uparrow} (z_{k_1}^\uparrow - z_{l_1}^\uparrow)^{m_1} \prod_{k_2<l_2}^{N_\downarrow} (z_{k_2}^\downarrow - z_{l_2}^\downarrow)^{m_2} \prod_{k_1,k_2} (z_{k_1}^\uparrow - z_{k_2}^\downarrow)^n e^{-\sum(|z_{l_1}^\uparrow|^2/4+|z_{l_2}^\downarrow|^2/4)} \quad (2.38)$$

Ground states may therefore emerge at filling factors of,

$$\nu = \frac{m_1 + m_2 - 2n}{m_1 m_2 - n^2} \quad (2.39)$$

where m_1 and m_2 correspond to the interaction strength within a degree of freedom, and n between degrees of freedom. Here, the degree of freedom is signified by $(\uparrow, \downarrow)$ which according to the construction of the wavefunction, can be real spin or psuedospin. The idea of pseudospin may be realised in systems such as bilayer samples. In putting the values 3,3,1 in, an even denominator state becomes plausible at ν = 1/2. Indeed, such a state has been observed in GaAs bilayer 2DES[19], wide quantum wells of both GaAs 2DES [20] and 2DHS [21], and in other rare circumstances of an addition degree of freedom, such as the crossing of heavy and light bands in the GaAs 2DHS [22]. Other two component states have been observed at other odd denominator states[23] or even integer states at ν_{total} = 1.

We now return to the transport in Fig. 2.6 which is quick to show the limits of Laughlin's wavefunction. The construction of Laughlin's wavefunction in its simplest form imposes limitations on the range of ground states predicted - 1/3, 1/5, etc. While this can be expanded on with Halperin's generalisation, it is still not easy to understand the presence of higher order fractions such as ν = 2/3, 3/5, 4/7, . . . , and others that are observed in such high quality samples (even richer behaviour has been observed in AlGaAs/GaAs heterostructures [24]).

2.2.2 Composite Fermions

An extremely intuitive understanding of the fractional quantum Hall effect may be gained through the composite fermion model[11]. This is helpful for experimentalists for interpreting the rich series of states which are observed. The model involves the formation of quasiparticles which capture magnetic flux to cancel the external field being applied to the 2DES. The motivation for formulating this model comes from experimental observations. Still focusing on the fully spin polarised lowest LL $\nu < 1$ it can be observed that a strong qualitative link exists between the series of fractional quantum Hall states there and the behaviour of the integer quantum Hall effect at low field. The fractional series may be mapped by integer fillings p through the relationship,

$$\nu = \frac{p}{2mp \pm 1} \tag{2.40}$$

ν	$\Longleftrightarrow$	p
1/3	$\Longleftrightarrow$	1
2/5	$\Longleftrightarrow$	2
3/7	$\Longleftrightarrow$	3
1/2	$\Longleftrightarrow$	∞
3/5	$\Longleftrightarrow$	3
2/3	$\Longleftrightarrow$	2

Table 2.1: Conversion table between electron and composite fermion filling factors when m = 1.

This series intuitively suggests that through some mechanism, the integer quantum Hall effect is being reproduced at a magnetic field displaced from $B = 0$ T. In fact, the series present in experiments suggests that the fractional quantum Hall states are centred on ν = 1/2, where in a usual 2DES (without added degrees of freedom present in the Halperin wavefunction) a fractional quantum Hall state is not observed. The model effectively states that the fractional quantum Hall effect is instead the integer quantum Hall effect of a new type of quasiparticle which forms at ν = 1/2, and which moves in an effective magnetic field away from half filling,

$$B_{eff} = B - B_{\nu=1/2} = B - 2mn\phi \tag{2.41}$$

where , $2m$ is the number of vortices bound to the electron, n is the charge density and $\phi = h/e$ is the flux quantum piercing the sample

These quasiparticles have been entitled "composite fermions", and may be considered as electrons which have bound with an even number of flux quanta to form a new quasiparticle, as shown in Fig. 2.7**b**. Multiple experimental approaches have probed these quasiparticles beyond the qualitative resemblance of the integer and fractional quantum Hall effects. These include surface acoustic wave experiments [25], temperature scaling analyses [26], commensurability experiments [27–30] and cyclotron resonance experiments [31]. The series of fractional states expected from the composite fermion model is too is observable in the MgZnO/ZnO transport shown in Fig. 2.6, reproducing the series presented in table 2.1. These suggest that similar physics is taking place in MgZnO/ZnO with a Fermi sea being formed at half filling in the spin polarised lowest LL, and composite fermions act in a semi-classical manner in an effective magnetic field, supporting the above model.

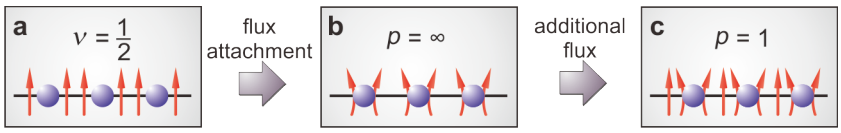

Figure 2.7: Formation of composite fermions. In panel **a** the filling factor is set to be 1/2 according to electrons. Panel **b** then attaches the magnetic flux to the electrons to make composite fermions. **c** the addition of extra flux then makes a ratio of 1:1, which indicates an integer filling of composite fermions, which is analogous to ν = 1/3 for electrons.

The model can be intuitively understood through the following construction. In the composite fermion picture the wavefunction describing the ground states is modified to read,

$$\Psi_\nu = \phi_{\nu^*} \prod_{i<j} (z_i - z_j)^{2m} \tag{2.42}$$

where ϕ_{ν^*} is an antisymmetric wavefunction for non interacting electrons at an effective filling factor. The second factor pins two vortices to the electrons by enhancing the ability of electrons to remain apart (as the probability of approaching each other now takes the form $r^{2(2p+1)}$). If the case is $\nu^* = 1$,

$i.e.p$ = 1, the wavefunction is transformed to read

$$\Psi_{\nu=1/2m+1} = \prod_{i<j}(z_i - z_j)^{2m}[\prod_{i<j}(z_i - z_j)e^{-\sum_i z_1^2/4}] \tag{2.43}$$

$$\Psi_{\nu=1/2m+1} = \prod_{i<j}(z_i - z_j)^{2m+1}e^{-\sum_i z_1^2/4} \tag{2.44}$$

which recovers Laughlin's wavefunction when m = 1. This therefore maps the problem onto p filled composite fermion levels. This scenario is showed schematically in Fig. 2.7**c** where an extra flux per composite fermion establishes the effective filling factor 1 as seen by the quasiparticles, or alternatively, ν = 1/3 as seen by the electrons.

Mapping these states into non-interacting particles at a defined magnetic field allows us to infer (roughly) the expected gap of the states,

$$\Delta = \hbar\omega_{CF} = \frac{\hbar e B_{eff}}{m^*_{CF}} \tag{2.45}$$

This relationship suggests that the gaps of fractional quantum Hall states rise linearly with increasing B_{eff} away from ν = 1/2, and have an effective mass of their own (m^*_{CF}). This is not related to the electron effective mass, which is not present in the Hamiltonian. While this linear increase is not exactly true (the mass indeed scales as $\sqrt{B}$ with the Coulomb interaction[32]), a qualitatively similar scenario is observed in experiment [33, 34], further supporting the model as a valuable tool for understanding the effect.

We now consider adding a spin degree of freedom. This is easiest to do by filling up the lowest spin branch of the lowest LL and placing the chemical potential at ν = 3/2. Since we maintain the orbital character of the electron LL, the construction of composite fermions and the underlying physics should be similar. We however modify the effective magnetic field felt to read,

$$B_{eff} = 3(B - B_{\nu=3/2}) \tag{2.46}$$

as only one third of the electrons in the system form composite fermions and participate in transport at the chemical potential. Previous works [35] in AlGaAs/GaAs have explored this degree of freedom and revealed a rich series of discrete spin transitions of the ground state when the physics is isolated within the lowest LL. In that work, the filling factor is also modified to read

$$\nu = 2 - \frac{p}{2mp \pm 1} \tag{2.47}$$

This is due to particle hole symmetry within the lowest LL. A similar scenario will be explored later in this thesis in section 5.3. The results we present shine a new light on composite fermions with a spin degree of freedom as we observe interaction between composite fermions formed in the lowest LL and the second LL. As detailed below, the second LL is host to drastically different physics due to the nodal structure of higher LL wavefunctions. This leads to a thus-far unobserved manifestation of composite fermions at ν = 3/2 in MgZnO/ZnO heterostructures.

2.2.3 Higher Landau levels

As discussed above, the odd-denominator fractional quantum Hall effect reigns supreme in the lowest LL due to hard-core repulsion of electrons and the formation of composite fermions. Only in exceptional circumstances may states outside of this series, such as an even-denominator state (thought to be described by the multi-component Halperin wavefunction [10]) be observed. At even higher fields crystalline states such as a Wigner crystal develop [36, 37], but, this is again due to the hard-core Coulomb repulsion of LL electrons. We now weaken the magnetic field and place the chemical potential within the second LL ($N_e = 1$, $4 > \nu > 2$, assuming a spin degree of freedom is present with no valley degeneracies). When moving to lower magnetic fields the Coulomb interaction weakens, and the orbital nature of the harmonic oscillator electron LL changes, developing nodes. From an experimental point of view, these electronic details have a surprisingly dramatic impact on the variety of ground states observed at low temperature.

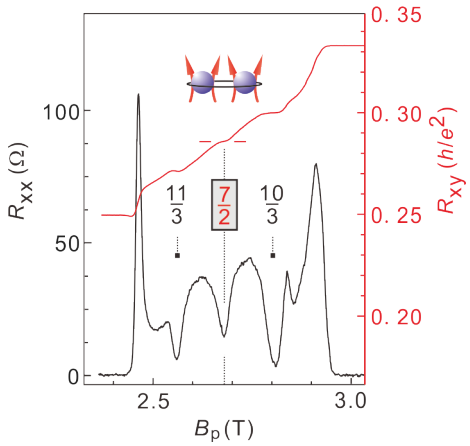

Figure 2.8: Data on a MgZnO/ZnO heterostructure (T < 20 mK) showing the development of an even-denominator fractional quantum Hall ground state at ν = 7/2. The observation of this ground state is associated with the pairing of composite fermions.

The dominance of the odd-denominator fractional quantum Hall effect is due to the effectively cancellation of the Coulomb interaction through the production of composite fermions and the mapping of these quasiparticles into non-interacting integer filling factors, as per Eq. 2.44. However, in the second and higher LL, the repulsive interaction is weakened due to the nodal structure of the electron wave function. This calls into question the applicability of the composite fermion model [38]. Specifically for the $N_e = 1$ LL, the flux attachment to form composite fermions overscreens the coulomb interaction at half filling, leading to spectacular experimental results. Clearly new physics emerges here as a quantised even denominator state at ν = 5/2 and 7/2 in sufficiently high AlGaAs/GaAs heterostructures [39–41]. Importantly, these ground states occur without the intentional incorporation of extra degrees of freedom required by the Halperin wavefunction given in Eq. 2.38. This is surprising considering the fundamental consideration that a Fermi sea should form at half filling according to the composite fermion model.

An attractive interaction sparks the idea of pairing of particles. Indeed, the observation of a fractional quantum Hall state at ν = 5/2 and 7/2 has lead to the idea of the pairing of composite fermions in a zero effective magnetic field being responsible for condensation into a gapped ground state[42].

Theoretical works have dealt with this, and yield a reasonable overlap the so called "Moore-Read" wavefunction[43],

$$\Psi_{MR} = Pf(\frac{1}{z_i - z_j}) \prod_{i>j} (z_i - z_j)^2 e^{-\sum_i z_1^2 i/4} \tag{2.48}$$

where,

$$Pf(\frac{1}{z_i - z_j}) = A(\frac{1}{z_1 - z_2}\frac{1}{z_3 - z_4} \dots) \tag{2.49}$$

This resembles the wavefunction for a BCS superconductor in real space. Another candidate is the Anti-Pfaffian wavefunction[44] which is the particle-hole conjugate in the absence of level mixing. Significant momentum has emerged around the investigation of these states due to this prediction of the ground state being an magnetic field equivalent to a $p_x + ip_y$ chiral superconductor. If this system is spinless[45], the excitations of the ground state may display non-Abelian statistics. Taming these excitations in an experimental environment has the potential to lead to their application in fault-tolerant topological quantum computation[46]. That said, experiments are still currently at the level of probing the character of the ground state. Two experimental fronts which have attracted interest is probing the spin polarisation[47, 48] and fractional charge[49, 50]. For the former, conflicting data from magnetotransport measurements had hampered efforts to reach conclusions for decades [51, 52], but consensus seems to have been reached with recent nuclear magnetic resonance measurements. With the latter experiments too, some conflicting results suggesting the Halperin-wavefunction described ground state still emerge in tunneling experiments [53]. Even more complex experiments in an actual interferometer-like device geometry remains an exceptionally difficult pursuit[54] as the ground states are fragile even in the best virgin samples with an activation energy on the order of 500 mK [55]. Modifying any samples into the complex geometries required to truly probe such statistics inevitably reduces the quality of the ground state, compounding an inherently difficult measurement with extremely strict device fabrication requirements[46].

The physics of the second and higher LL are however more rich than just pairing at half filling. In higher LL the effective Coulomb interaction is modified by the form factor of the LL character of electrons,

$$V_N^{eff}(q) = V(q) F_N^2(q) \tag{2.50}$$

where $V(q)$ is the standard Coulomb interaction term with the form factor as,

$$F_N(q) = L_N(\frac{l_B^2 q^2}{2}) e^{-l_B^2 q^2/4} \tag{2.51}$$

Here L_N is the Laguerre polynomial. Such form factors result in a softening of the hard-core repulsion present in the lowest LL where the Coulomb term decays monotonically with increasing distance. By placing electrons at (0,0) and (Δx,0), a single minimum in the potential is observed between such electrons, meaning mutual repulsion exists. In higher LL however ripples develop in this potential, meaning electrons may bunch together when the distance between them is comparable to the cyclotron radius[56]. This spectacularly manifests as "stripes" and "bubbles" [57] in $N_e \geq 2$ in high mobility AlGaAs/GaAs 2DES [58, 59]. The common observation is highly anisotropic transport at half fillings, which is associated with the formation of a unilaterally aligned rotationally variant stripe phase. This

is schematically shown in Fig. 2.9. Recent NMR measurements confirm the density modulation in such unilaterally aligned phases [60]. Other phases emerge at quarter fillings which are thought to resemble bubbles of electrons forming a super Wigner crystal. This is characterised by the reentrant integer quantum Hall effect, where the Hall resistance shows anomalous behaviour of oscillating between a quantised and non-quantised value. Finally, theory predicts and recent experiments confirm that at the edge of integer quantum Hall filling factors Wigner crystals can form[61], distinct from those realised at high magnetic fields and low filling factors. As with the ground states identified in the above sections who are part of the fractional quantum Hall effect, the charge density wave states too are extremely sensitive to thermal fluctuations, with temperatures $T \leq 100$ mK a basic requirement for their observation.

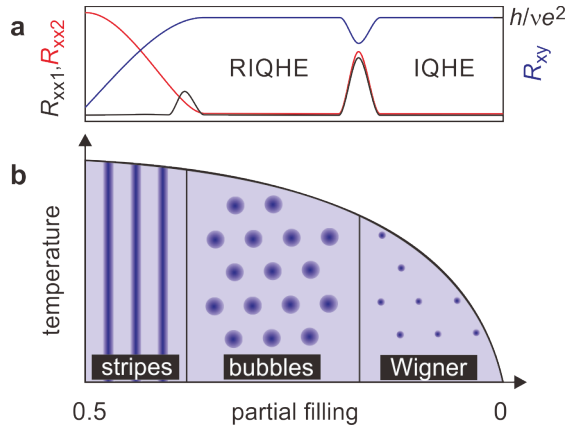

Figure 2.9: Cartoon representation of the ground states and their appearance in magnetotransport observed in higher LL ($N_e \geq 2$). **a** The resistance of the sample depending on the partial filling factor. Anisotropic behaviour is observed for half fillings. **b** predicted microscopic structure of the ground states. Higher density regions are shown as darker blue. A transition from stripe to bubble and eventually Wigner is shown.

The fascinating facet of such ground states in excited LL is the vague at best correlation between their stability and the zero-field mobility of the device under investigation[62, 63]. From a growth and materials point of view, this is exciting as device design and an analysis of scattering mechanisms becomes imperative. Moreover, states beyond the odd-denominator fractional quantum Hall effect only been reported in AlGaAs/GaAs **2DES** - they have not been observed in 2DHS despite the expectation of a similar disorder landscape between the two (although, a two-component even denominator ground state has been observed in the 2DHS [21, 22]). There is one report [64] in suspended bilayer graphene of an even denominator state at $\nu = 1/2$, with theoretical support to suggest that the ground state is described by the Moore-Read wavefunction [65]. These observations highlight that the realisation of similar physics in more material systems with unique degrees of freedoms will have significant impact on elucidating their true nature.

Chapter 3

Growth of MgZnO/ZnO heterostructures

It could be argued that for most semiconductor materials, and especially for III-V AlGaAs/GaAs growth, the combination of "oxygen" and "high quality" is a paradox. In such traditional material systems, the formation of stable oxides of both gallium and aluminium contributes to significant disorder and scattering centres in the crystal, hence lowering the final sample quality. This is an inconvenience while ever material growth takes place in an oxygen containing atmosphere, *i.e.* on earth. The ubiquitous presence of oxygen inevitably imposes strict requirements on the vacuum quality of the apparatus. Ultra-high vacuum (UHV) pressures on the order of 10^{-10} Pa are therefore a basic requirement in order to achieve high quality samples. This can only be achieved through the use of cryopumps, ion sublimation pumps, turbo molecular pumps or a combination of all. The procedure to mitigate oxygen contamination does not end there, however. All aspects of materials handing and system maintenance must take into account potential contamination in the event of materials coming in contact with air.

Many of these concerns are mitigated in the art of oxide thin film growth. This field has gained momentum in recent years due to the wide variety and rich chemistry of materials made possible by using oxygen as the "glue". The richness of physical phenomenon observed across the range of prevailing materials is truly remarkable [4]. Instead of oxygen being an unwanted impurity as it is in semiconductors, it transforms into a powerful tool for controlling the crystallography, oxidisation state, thermodynamics and kinetics during growth. As a result of technological advances, these materials are now being fabricated as increasingly complex and high quality structures, allowing access to unknown inter-material interactions. A number of growth techniques are now in wide use, including sputtering, chemical-vapour deposition, pulsed laser deposition and MBE, which is the focus of this thesis. While coherent thin films growth may indeed be achieved in all techniques, the "quality" of a sample is a relative concept rather than an absolute. Ultimately, it remains a fact that in the realm of oxide thin film growth, as with the field of semiconductor materials, MBE reigns supreme in terms of the technique for achieving the highest quality films possible. In the case of OMBE, molecular oxygen, oxygen radicals, or highly reactive ozone is injected into the growth chamber during growth. This results in a relaxation of the apparatus' vacuum requirements compared to traditional MBE systems. Indeed, usually a turbo molecular pump will (or must) suffice, as cryopumps have a limited capacity which will soon be reached if the gas flow is high. Similarly, equipment maintenance may generally be performed

under regular atmospheric conditions, provided the source material is not too reactive with oxygen (for example europium). What develops is experimental equipment in close analogy to that used in more traditional material systems, with modifications and specific requirements in order to cope with the persistent presence of oxygen. This, however, is a formidable pursuit in itself when high temperatures are introduced. Significant design modifications along with a careful selection of materials used in the chamber design is required.

In this chapter we report on the latest generation of OMBE growth of MgZnO/ZnO thin films. The defining feature of this work is the use of pure liquefied ozone as the oxidising agent. We demonstrate that this is a key component in achieving ultra-high quality samples. A significant portion of this work has also been spent modifying and refining the OMBE design. While it comes as no surprise that most metals are incompatible with high temperature and highly oxidising environments, we show that even with metals specifically designed for this purpose, certain limitations exist and not all metals are equal.

It is highlighted that a number of the results presented in this chapter are interlinked and must be digested in combination with each other to fully convey the end result. For example, the doping regimes introduced in the early sections are only useful if the technical concerns of later sections are dealt with. Specifically, these technical concerns attempt to mitigate sources of impurities originating from origins other than the source material. Therefore, this chapter is roughly divided into two sections; a discussion of the growth of heterostructures assuming "all is fine", following by a discussion of problems encountered.

3.1 ZnO material overview

The material of interest in this thesis is ZnO and its alloy, $Mg_xZn_{1-x}O$. While this thesis focuses on the character of 2D electrons that form at the heterointerface of these two materials, ZnO itself has a wide range of industrial applications including extensive use in the rubber and cosmetic industries. In addition it has unique characteristics of interest in the realm of both fundamental research and electronics industry. A review article has recently been published providing an overview of the history of single crystal ZnO based devices [66]. Table 3.1 summarizes some material parameters of ZnO.

Parameter	a (nm)	c (nm)	E_g (eV)	E_c (eV)	E_v (eV)	E_x (meV)	m_e^*/m_0	ϵ/ϵ_0
Value	0.3250	0.5204	3.37	4.1	7.5	60	0.29	8.3

Table 3.1: Summary of material parameters of ZnO[66]. a and c are the a-axis and c-axis lengths, E_g is the band-gap, E_c and E_v are the conduction and valence band edge energies, E_x is the exciton binding energy, m_e^* is the (electron) effective mass and ϵ is the dielectric constant.

As can be inferred from Table 3.1, the large band gap of 3.37 eV results in ZnO being transparent to visible light. Yet, despite this large band-gap, ZnO naturally shows n-type in conductivity at room temperatures with charge densities of the order $n \approx 10^{17}$ cm^{-3} and a mobility of 200 cm^2 V^{-1} s^{-1} [67]. The combination of these characteristics continues to motivate efforts to realising high mobility transparent transistor devices. It is again the large band-gap of the material, combined with the large exciton binding energy of 60 meV, which has instigated a front of experiments focused on the optical properties and applications of ZnO. Highly notable are the efforts to realise light-emitting diode (LED)

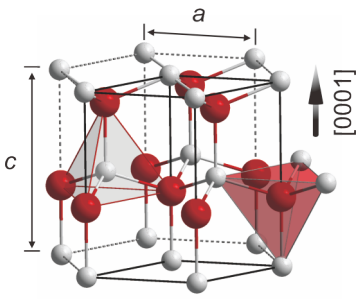

Figure 3.1: The ZnO crystal structure. The [0001] crystal direction is shown along with the c-axis and a axis lengths.

devices[68, 69], which entails the formation of a p-n junction. This however has been met with the great technical challenge of realizing p-type ZnO. In Ref. [69] a co-doping scheme of $Mg_xZn_{1-x}O$:N was utilised to achieve the p-doped layer. The alloying of relatively high contents of Mg has the desirable effect of reducing the residual charge density of the host crystal[70], enhancing the ability to realise p-type conduction. This pursuit sowed the seeds for the work outlined in this thesis, as the heterostructure design and fabrication apparatus, minus the incorporation of N-dopants, is common.

Throughout this thesis, single crystal ZnO substrates of Zn-polarity have been employed. Their size is 1 $\times$ 1 cm and thickness 350 μm. The single crystals are grown by hydrothermal method by Tokyo Denpa and the final product has a low resistivity of less than 10 Ωcm. As ZnO is naturally n-type due to charged defects in the form of Zn interstitials and/or oxygen vacancies (both of which are 2+ charged), a low resistivity in fact indicates a higher quality crystal. This is because a lower charge density (increasing resistivity) occurs through the compensation of charges, which is typically achieved by the unintentional doping of impurities such as lithium during the crystal growth process. Prior to usage, the substrates are etched in hydrochloric acid [71] to remove residual particles left over from the substrate polishing process. The acid treatment (HCl, pH $\approx$ 0) dissolves these and a finite thickness of ZnO. The thickness of ZnO dissolved is much more for the O-polar surface, which develops deep pits and does not etch uniformly. In contrast, the Zn-polar surface etches much more slowly and remains flat. Once the substrate is loaded into the chamber, high temperature annealing is performed under high vacuum. Experiments on this process are discussed in section 3.18.

3.2 MgZnO/ZnO heterostructures

The crystal structure of ZnO is shown in Fig.3.1. Under ambient conditions the structure takes the inversion asymmetric Wurtzite structure with neighbouring atoms tetrahedrally coordinated by sp^3 hybridised covalent bonds. In an ideal Wurtzite structure the ratio of $\frac{c}{a}$ is 1.633, but this is distorted in the case of ZnO to values of roughly 1.6 due to the electronegativity of oxygen distorting the bond angles within the tetrahedrons[72]. This deviation from a centrosymmetric structure results in formation of a spontaneous polarization field in the [0001] crystal direction.

The formation of this spontaneous polarisation is the essential character which is exploited in the case of $Mg_xZn_{1-x}O$/ZnO heterostructures. Indeed, it is the different magnitude of the polarisation field of the capping $Mg_xZn_{1-x}O$ and lower ZnO layer which induces a 2DES at their heterointerface. In analogy to the AlGaN/GaN, which too shares the Wurtzite crystal structure, the polarisation induced charge in 3D is given as,

$$p_{3D} = -\nabla \cdot P \tag{3.1}$$

The magnitudes of P are constant in the bulk of the two materials but discontinuous at their interface, equivalent to placing two vectors of different magnitude head-to-tail. The charge density at the interface is therefore the negative of the divergence of polarisation,

$$p_{3D} = -\lim_{\Delta x \to 0} \frac{\Delta P}{\Delta x} \rightarrow p_{3D}\Delta x = p_{2D} = \lim_{\Delta x \to 0} \Delta P \tag{3.2}$$

The spontaneous polarisation magnitude in ZnO has been estimated as -0.057 C/m^2 [73] and for in epitaxially locked Mg$_x$Zn$_{1-x}$O where x = 0.1 ΔP can be estimated as 0.0024 C/m^2, or alternatively, a charge density of $n \approx 1.5 \times 10^{12}$ cm^{-2} [66]. This distortion is a result of a shift in the tetrahedron centre of mass due to the incorporation of Mg, which prefers octahedral coordinate of oxygen as is the case in MgO. Therefore, to achieve low density samples of $n \approx 1 \times 10^{11}$ cm^{-2}, dilute doping regimes where x = 0.01 or so are likely required. This is explored later in section 3.5.1 and is met with its own set of technical challenges.

3.3 Sample evaluation and screening

One of the first outstanding questions is *"what is the yard-stick used to judge quality?"*. This is indeed a question applicable to all research efforts. For p-type doping of ZnO, the challenges include lowering the residual carrier density hence bringing the system closer to an intrinsic state, combined with the inclusion of active dopants to induce p-type conductivity. This was the case with the previous generation of growth [70] which aimed at industrial scale production of ZnO based light emitting diode devices. Refining the scope of discussion to the Mg$_x$Zn$_{1-x}$O/ZnO 2DES with the goal of exploring exotic electronic ground states formed at ultra-low temperatures, a new set of techniques, parameters and goals must be defined.

Firstly, it is obvious that electrical measurements will play a prominent role. In that sense, it may seem logical to explore each sample at ultra-low temperatures to gain a deep understanding. This in theory could be achieved by loading each sample in a dilution refrigerator and exploring the electrical characteristics at mK temperatures. However, this would involve at least a two-day turn-around between samples and require significant attention paid to the measurements. This is not-ideal for a grower who may produce on the order of 5 samples per week. A compromise must be found, where enough information may be gained through a reasonable investment of time, and in a quick and efficient time frame.

The approach taken throughout the course of this study is a combination of physical and electrical characterisation techniques aimed at gaining enough information to screen samples and to direct the grow regime in a direction which increases quality. Promising samples are then explored at much lower temperatures to investigate the nature of ground states. The first line of characterisation techniques employed on films grown include:

Physical characterisation

- Optical microscope
- α-step film thickness measurement
- Atomic-force microscopy
- X-ray diffraction and/or photoluminescence

Electrical characterisation

- ρ-T measurements
- Magnetotransport @ ^{3}He T
- Magnetotransport @ dilution T

The physical characterisation techniques are employed primarily to evaluate the bulk crystallinity of the grown structure. Minimal information about the quality of the underlying 2DES is obtained. In the case of X-ray diffraction or photoluminescence, the goal is to quantify the x content of films and this is explored in detail in section 3.5.1. This however, as can be seen later, is inherently linked to the charge density n of the resulting 2DES. It is therefore possible to infer this from electrical measurements. Moreover, the lower resolution limit of lab-based X-ray diffraction apparatus occurs at $x \approx 0.02$, which is on the high end of doping contents used to achieve high mobility samples [74]. These physical characterisation experiments are therefore not performed for every film grown. Much more relevant are electrical measurements. In turn, these form the main focus of this thesis. The two simplest measurements are the temperature dependence of resistance (ρ-T) and transport measurements with the application of an external B-field. It is the latter which yields both electron mobility (μ), density n and gives hints about the more abstract concept of "quality". A detailed discussion of transport phenomenon is deferred to the next chapter 4, with a section dedicated to evaluating the "quality" of the 2DES. Electrical measurements are performed in either Hall bar or van der Pauw geometry. In the latter years of this work, van der Pauw geometry was exclusively used in transport measurements, except for the mesoscopic results shown in section 6.2. Both techniques yield the same result - clearly defined R_{xx} and R_{xy} signals, as the current in the quantum Hall regime flows along the edges and mitigates the effect of mixing of these signals, as experienced in other conducting systems. In the case of Hall bar devices, a mesa is patterned by photolithography and etched using argon ion-milling in order to expose the 2DES at its edges. To this, electrodes of either Au/Ti (the Au is simply to mitigate oxidation of the Ti, which forms the actual ohmic contact) or indium are evaporated. In more complex devices, a field effect transistor may be formed[75]. In van der Pauw geometry, a chip measuring roughly 4 $\times$ 4 mm is cut from a raw wafer. To its edges, four or eight contacts are either hand soldered or evaporated. In this geometry, no surface gate is generally present. We have however developed a novel technique for gating these macroscopic samples in the form of an air-gap field effect transistor, as outlined in section 6.1. Indeed, the surface is never touched with any chemicals. This ensures pristine quality, and arguably has contributed significantly to the ability to observe the rich phenomenon capable of being hosted by the underlying 2DES.

3.4 Overview of the molecular beam epitaxy apparatus

It is difficult to overstate the role that MBE has played in the advances experienced in the realm of semiconductor research. As explained in the introduction of this thesis, the most striking theatre for such advances is without doubt AlGaAs/GaAs heterostructures[1] where in the space of roughly 30 years the electron mobility of the GaAs 2DES has increased from the order of 10^4 cm^2/Vs to beyond 10^7 cm^2/Vs, a roughly 1000-fold improvement (see. Fig. 1.1). Such advances have spurred a positive spiral

of technological development inducing further gains, which in turn enables further physics discoveries. A number of pieces of literature containing technical summaries of such advances have now become available recently [76, 77] and act as a nice guidebook for understanding the basics principles of the chemistry of growth, the design of MBE apparatus and an understanding of the fragile ground states achieved from a growth point of view.

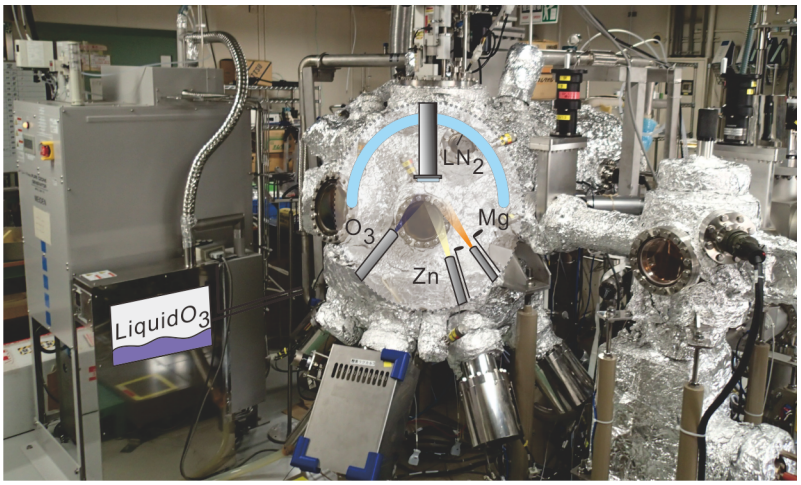

Figure 3.2: An overview of the ZnO MBE apparatus used throughout this thesis for sample growth. To the left hand side is the ozone generator which feeds ozone gas through piping connected to the rear of the MBE chamber. Within the chamber the ozone, Zn and Mg cells are visually represented.

An adapted form of such an apparatus is used throughout this thesis. The OMBE apparatus is specifically designed for ZnO growth, and has slowly evolved through time. Figure 3.2 displays a photograph of the OMBE apparatus used throughout this work with a cartoon representation of major components overlayed. It shares the same fundamental principles with traditional III-V, IV and other solid source MBE apparatus. It is comprised of a three-chamber chain with descending base pressure (higher vacuum). The first barrier is the load-lock chamber which is leaked on regular occasions with pure nitrogen ($\approx$30 ppm O_2 content). This chamber is evacuated by a rotary pump connected to a standard turbo molecular pump (TMP) of pumping rate 350 L/s. The chamber is equipped with a quartz backed tungsten heating coil which is used to heat the freshly inserted substrate to a temperature of 200°C in order to remove any residual moisture remaining from the wet etching procedure. This load-lock chamber has a base pressure of $\approx 1 \times 10^{-6}$ Pa and reaches pressures on the order of 1×10^{-5} Pa within 30 minute of being exposed to the atmosphere. The pre-heating of the substrate is performed once the chamber reaches this level of vacuum. The next in the chain is a buffer chamber of base pressure $\approx 1 \times 10^{-7}$ Pa, evacuated by an ion sublimation pump of pumping speed 150 L/s. No heating apparatus is equipped in this intermediate chamber. This chamber is however bakeable and the vacuum is rarely broken. The final component in the chain is the growth chamber which is evacuated by a dry-pump backed TMP of pumping rate 2000 L/s. The chamber is equipped with a liquid nitrogen shield which is filled only during growth. The flow of liquid nitrogen is therefore stopped after each growth which allows the chamber walls to heat up and regenerate after each growth. The background pressure of the cold chamber is $\approx 1 \times 10^{-8}$ Pa. At this pressure the mean free path of gas molecules will be of the order 10^6 m. This main chamber is equipped with 8 ICF152 ports around the circumference of the base of the chamber. The current arrangement of cells is shown in the photograph taken from the top of

Figure 3.3: Photograph of inside the MBE apparatus showing the base partitioned into 8 sections, corresponding to the 8 ICF152 ports which host the source materials and view ports. Individual components are labelled.

the open chamber in Fig. 3.3. Finally, the temperature of the substrate is read by two means. Behind the substrate at the centre of the heating coil a thermocouple is installed. In addition, a thermocamera sensitive to long wavelength (8 μm wavelength) emissions is placed outside the chamber and aimed at the centre of the substrate through a BaF_2 window. This is believed to represent the real substrate temperature, with the thermocouple indicative of the coil temperature.

As can be seen in Fig. 3.3, the basic arrangement is two Zn, two Mg, one ozone, one oxygen plasma and one BaF_2 (for thermography) viewport. This results in one empty port which has been previously equipped with either a Ga cell or a nitrogen gas source [69]. The two Zn cells and Mg cells are arranged within the chamber in opposing positions to reduce the real-space spread of impending flux on the substrate when only one cell is used. While both Zn cells are used for each growth, usually only one Mg cell is open as the flux required for inducing the 2DES is very low. Therefore, in order to avoid a composition spread, the substrate is rotated at a speed of roughly 6 rpm [78]. In this photograph, the two Zn cells have their shutters removed, which reveals the white pBN crucibles. The remaining ports visible around the cells are viewports which are all equipped with shutters, and correspond to the Mg cells.

As introduced in section 2.1, the conductivity of electrons may be understood quantitatively through the electron mobility, μ, or alternatively the transport scattering time, τ_{tr}. These values both take into account the rate of large angle scattering events an electron encounters. This value is ultimately limited by the presence of scattering centres which originate from a range of origins. Now it seems that at least in the AlGaAs/GaAs system where the heterointerface has near perfect crystal lattice matching, the most prominent mobility limiting factor in ultra-high mobility samples [63] is the finite concentration of back ground impurities unintentionally incorporated into the heterostructure[79]. One origin of such impurities is the quality of vacuum of the chamber, as any gas molecule which collides with the substrate during growth has the potential to be incorporated into the crystal. This is the motivation for increasing the size and number of pumps on the growth chamber and to cool the chamber walls. However, it is now generally thought that in the case of AlGaAs/GaAs heterostructures, the background pressure is not the origin of impurities which limit the mobility. The most obvious origin of impurities which inevitably find their way into the material grown is the source material which is evaporated. Both experiments [63] and theory[79] consider the background impurity content to be the primary mobility limiting mechanism, and if the concentration could be reduced by an order of magnitude to 10^{12} cm^{-3}, the mobility could increase beyond the psychological barrier of 100,000,000 cm^2 V^{-1} s^{-1} .

While in MgZnO/ZnO heterostructures the understanding of scattering mechanisms is not as advanced as AlGaAs/GaAs heterostructures, the same mobility limiting principles apply. The purity of

source materials may be labelled as XN purity. For example, 7N is equivalent to 99.99999% pure. This of course leaves a window for unwanted impurities to enter the source material. The source material used throughout this thesis is, to the best of our knowledge, the highest purity that is currently commercially available. Both Zn and Mg are provided by DOWA electronics (Japan). The Zn ingots used may tentatively be classified as 7N5 in purity, but are sold as 'super' zinc, as exact determination of the impurity content is not analytically possible. The impurity content breakdown as measured by glow discharge mass spectroscopy is below the following concentrations in ppm = parts per million (wt):

Element	ppm	Element	ppm	Element	ppm
Li	0.01	Al	0.01	K	0.01
B	0.01	Si	0.01	Ca	0.02
F	0.01	S	0.03	Cr	0.01
Na	0.01	Cl	0.01	Fe	0.01

Table 3.2: Elemental breakdown of impurity content of 'super' zinc ingots used in growth. Here, the concentration is reported in parts per million (wt).

Similarly, the Mg ingots used are of 6N purity. While ideally higher purity is desirably, this is not currently available. Both Zn and Mg source materials are loaded in conventional Knudsen cells (K-cell) with pyrolytic Boron Nitride crucibles. Each Zn ingot is 35mm $\times$ ϕ27mm, for a total of volume of 20 cc, and each Mg ingot is 25mm $\times$ ϕ20mm, giving a total volume of roughly 8 cc. As mentioned earlier, two cells of each element are installed in the chamber opposing each other, as shown in Fig 3.3. Both Zn and Mg have relatively high vapour pressures which results in a working K-cell temperature of $\approx$ 300°C for both elements with the effective pressure of flux read as 1×10^{-3} Pa for Zn and 1×10^{-5} Pa for Mg as per beam flux monitor. Despite the relatively large volume of Zn present, the high flux required to achieve high mobility samples results in the two ingots of Zn being consumed after roughly 40 growth cycles. This necessitates opening of the growth chamber every two months or so. From a positive viewpoint, the volume of Zn evaporated over the years has resulted in the entire inner surface of the chamber being coated in high purity Zn. This suppresses impurities which originate from the chamber itself. One Mg ingot on the other hand lasts roughly 200 growths under normal usage due to the significantly lower flux required. Both cells are proned to slight surface oxidation after opening the growth chamber to the atmosphere. This usually requires an extended period of time of above growth temperature cell heating to remove the oxidised surface layer. After this process, the cell flux returns to a stable, reproducible level. After opening the chamber a moderate bake period of 4 to 7 days is performed at a temperature of 150°C. After baking, only the H_2 peak remains in the residual gas analysis (RGA).

Unique to this study is the use of distilled ozone for providing the oxygen species during growth. This is in contrast to previous generations of ZnO growth[80, 81], and the vast majority of oxide MBE experiments around the world (irrespective of material), which use RF plasma sources to generate oxygen radicals for growth. The ozone generator produced by Meidensha (Model MPOG-104A1-TH) is shown on the left hand side in Fig 3.2. It is a self-contained, two-button operation, highly automated apparatus with much attention paid to the safe handling of the gas, even in the event of sudden black-outs or earthquakes. A volume of ozone gas is specified by the user (maximum 8000cc in the model used)

and is generated by coronal discharge using G1 oxygen as a source gas. The coronal discharge method alone yields only $\approx$ 15% O_3 and therefore distillation is required to increase this purity. To achieve this, the gas is passed through a cryochamber held at 90 K. This temperature is carefully selected and maintained via a PID controlled heater. At this temperature ozone has a very low vapour pressure and therefore the ozone gas that enters the chamber will condense as a liquid. Simultaneously, impurities such as N_2 or CO_2 either evaporate, or freeze as a solid. By cycling the chamber to 120 K post liquefaction of the required volume of O_3, oxygen may be expelled, resulting in a pool of high purity O_3. When ozone is required for growth, the pool of ozone is heated to $T \approx$ 130 K via PID, which gives a vapour pressure of roughly 4000 Pa within the ozone chamber. This gas phase is then fed one-way through gas lines in close proximity to the MBE chamber. To these lines a piezoelectric controlled leak valve (Oxford Applied Research PLV1000) is attached. On the other side of the valve is the MBE chamber. A high tension spring enables the valve to be compatible with ultra high vacuum. By applying a voltage to the piezo stack, the spring is compressed which opens the inside of the chamber to the gas lines. This leaks a proportion of the flowing gas within the external lines into the MBE. The pressure of ozone is read by both a capacitive baratron gauge in close proximity to the leak valve, and a naked ion-gauge present in the main chamber. At the baratron gauge this is usually on the order of 100 mTorr. This results in a main chamber pressure on the order of 1×10^{-5} Pa during growth as per the naked ion-gauge. This value however is very susceptible to fluctuations in chamber temperature and Zn flux, which acts like a getter material. Hence, the baratron reading is used as the measure of ozone flux. This baratron reading is independently read by an external program which uses this as an input to control the voltage applied to the piezo stack. This establishes a stable flow of ozone for each growth.

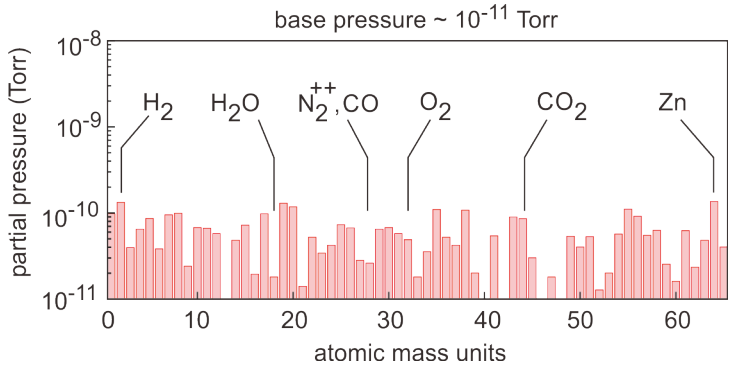

Figure 3.4: Residual gas analysis of the ZnO MBE chamber when cold and at base pressure. Atomic mass units of plausible gas impurities are shown.

The situation described in the paragraphs above looks detrimental to the quality of vacuum achievable in the system. Both Zn and Mg have very high vapour pressures, and for every growth cycle significant amounts of gas are injected into the chamber for long periods of time. Despite this, 12 hours after finishing a growth cycle, the cold chamber displays a RGA spectrum as shown in Fig. 3.4. This was taken using a Stanford Research Systems RGA 100 apparatus at the slowest sweep rate. All signals are at the noise level (which is rather high) of the apparatus. If any peaks were to appear we would expect those at 2, 16 or 32 amu, originating from H_2 or oxygen. Other plausible contaminants are labelled in the figure but are all seen to be at the noise level of the signal. Due to the high vapour pressure of Zn, a peak at 64 amu often appears, especially after baking the chamber.

3.5 Growth window and parameters

We now focus on the growth window and parameters which can be explored as experimental degrees of freedom in MgZnO/ZnO growth. We note that the results presented here do not touch on the technical challenges experience in other facets of growth, which are explored later in detail. It is therefore assumed that there are no uncontrolled contamination sources such as the manipulator or substrate holder present.

Work performed prior to the commencement of this thesis has established many of the fundamental parameters for ZnO MBE growth using single crystal ZnO substrates[71, 80]. The adaptation of ozone in the growth process has necessitated reassessment of the growth window and growth parameters. In previous generations of growth technology which utilised oxygen plasma as the oxygen source [82], high quality surfaces and crystal growth was observed for $T_G \geq 810^\circ$C. This temperature is that read by the thermocamera, which is thought to reflect the substrate surface temperature. The thermocouple present behind the substrate is usually on the order of 100°C higher. Below this bottom bound of $T_G \leq 810^\circ$C, the surface morphology was seen to degrade significantly. Indeed, all samples which showed a high mobility 2DES were fabricated at high temperatures of $\approx 920^\circ$C, in line with the best knowledge of the day. Figure 3.5 shows that by using ozone, a high quality surface may be preserved down to $T_G \approx 730^\circ$C. This is important as in the following sections it will be highlighted that the mobility of the 2DES is significantly lowered by contamination when high temperatures are used (see section 3.6.1). Above this lowest temperature of $T_G \approx 730^\circ$C, the samples surface morphology as shown in Fig. 3.5 according to AFM and optical microscope does not show dramatic improvements. Δz in AFM remains below 10 nm over a length scale of 10 μm. Under optical microscope some particles are visible on the surface. However, these are generally associated with the condition of the zinc source material, and not the growth temperature. For $T_G = 700^\circ$C coherent crystal growth is not achieved, and therefore we gauge the lower limit of growth temperature to be roughly $T_G = 730^\circ$C.

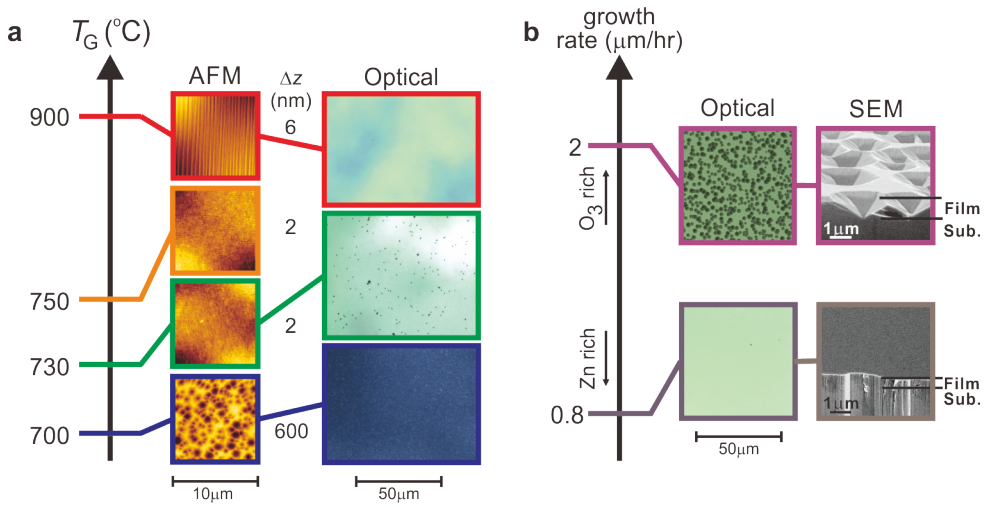

Figure 3.5: An overview of the growth window of ozone assisted OMBE growth of ZnO. **a** Growth temperature dependence of the surface morphology measured via AFM and optical microscope. **b** Growth rate dependence of surface morphology measured via optical microscope and SEM.

In the growth of GaAs based heterostructures it is well known that the growth rate of films may

be controlled by the ratio of Ga to As flux. Due to the very high vapour pressure of As, excess must be continually provided, of which the majority re evaporates and condenses on the chamber walls. In analogy, the growth rate of ZnO films may be controlled by the ozone flow rate. Zn too has a very high vapour pressure and will only react to form ZnO in the presence of oxidizing species. In Fig. **??b** the growth rate is varied by changing the ozone flux, while keeping the Zn flux at very high levels of 10^{-3} Pa as measured by beam flux monitor. Two contrasting scenarios are shown. At a modest growth rate of 800 nm/h the surface remains clean and smooth. However, by increasing ozone flux to enable a growth rate of 2 μm/h the surface quality on a macroscopic scale is significantly degraded. An understanding of this is gained through the SEM images presented. While locally the surface is seen to be smooth, deep pits appear in films grown under high ozone flux. Importantly, it appears that the pits originate from the substrate and increase in surface area as the film is grown thicker. It is indeed a universal observation that in all MgZnO/ZnO films grown throughout this work a certain density of pits are encountered. However, the density of such pits is usually much lower than that presented in the fast growing film of panel 3.5**b**. The origin is likely related to the polarity of the substrate and the excess flux species. In the case of Zn-polar substrates (as used in this work), the surface is covered by a single unoccupied chemical bond originating from the terminating Zn atoms which host hybridised sp^3 orbitals. An impending flux of excess oxygen species will occupy these sites and saturate the surface, resulting in three chemical bonds per oxygen available on the surface. Any Zn that then reaches the surface will be strongly bonded due to these, while providing only a single available bond at the apex of the sp^3 orbitals, which will soon be occupied by oxygen which limits the mobility of the Zn atom. The story then repeats, with the reduced mobility of Zn limiting its ability to form layer-by-layer or step-flow growth. It is therefore imperative to provide excess Zn flux in the case of Zn-polar substrates to make sure the macroscopic surface quality is maintained.

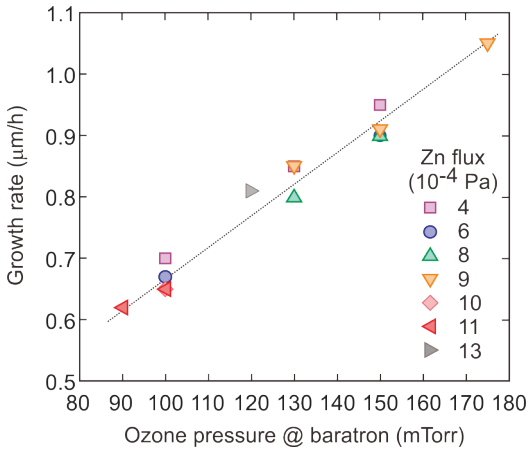

Figure 3.6: Relationship between the ozone flow and growth rate of films. A linear relationship is achieved across a wide range of flow rates despite the Zn flux (shown as colour shapes) having a large variation. This indicates the growth rate is limited by the ozone flow.

The relationship between growth rate and impinging flux is explored in more detail in Fig. 3.6. In this representation two variables are present - the combined Zn flux measured from two cells by beam flux monitor, and the ozone flow as measured the barometer pressure at the base of the ozone cell. The Zn flux varies between values of roughly $4 \sim 13 \times 10^{-4}$ Pa. Despite this large variation, the growth rate of films is shown to be entirely dependent on the flux rate of ozone. It increases roughly linearly

with increasing the flow. This indicates for the range of Zn fluxes presented here, the conditions are universally Zn rich. This in turn yields a smooth sample surface, as represented in Fig. 3.5. It is however noted that this growth rate can decrease through time as Zn metal finds its way onto the orifice of the ozone cell through which the pure gas passes on its way towards the substrate. This orifice is comprised of holes roughly 1mm in size and is designed to ensure uniform delivery of the gas across the substrate surface area. These holes get slowly clogged as Zn re evaporates through multiple growth cycles. This orifice (which may be detached easily) is therefore cleaned in nitric acid roughly once per year.

3.5.1 Mg doping calibration

As detailed in the above sections, the Mg content of the $Mg_xZn_{1-x}O$ film plays a crucial role in determining the charge density of the 2DES. However, as a result of the 2DES being induced via crystal distortion, it is to be expected that such distortion in turn will contribute to scattering of electrons. This is evidently acutely obvious in the MgZnO/ZnO 2DES. As detailed in [83], during the course of this thesis the effect of Mg content was evaluated across a wide range ($0.003 < x < 0.4$) through electrical measurements. It is highlighted that previous works have focused on relatively high Mg contents of $x \approx 0.05$ or higher[80, 84–86], resulting in moderately dense 2DES samples. As a result of the robust screening impurities, relatively high mobilities were obtained. However, in delving into the dilute Mg doping regime the mobility was seen to fall dramatically. In this context, the superiority of ozone for achieving high mobility samples well into the dilute Mg, and therefore dilute carrier regime, becomes apparent.

Before delving into electrical measurements, we firstly must establish the techniques for accurately determining the Mg content across a wide range of concentrations. These results have been published in Ref. [74]. In contrast to previous works which have endeavoured to perform similar tasks[87–89], this work uses single crystal ZnO substrates and the all the films are epitaxially locked to the substrate. They are also of much higher quality compared to all previous works.

There are a number of experimental techniques which can be utilised to determine the Mg content in $Mg_xZn_{1-x}O$ films. These include lab-based techniques such as photoluminescence and X-ray diffraction, as well as analytical techniques such as Rutherford backscattering spectrometry (RBS) and secondary ion mass spectroscopy (SIMS). Obviously, establishing efficient, easy access lab-based techniques is most important for growers. However, to reliably utilise the lab-based techniques it is important to first thoroughly calibrate them by analytical means. During the course of this endeavour a technical challenge arose - while Mg content can be quantified via analytical techniques, no single technique can analyse the full range of concentrations explored in this work ($0.003 < x < 0.4$). Inevitably, more than one analytical technique is required to cover the full range, which must be divided up. In the final result, we have utilised RBS for $x \geq 0.14$ and SIMS for $x \leq 0.015$. The Mg contents quantified analytically are then used to calibrate X-ray diffraction and photoluminescence spectrum. In the former this means calibrating either the angle of the (0002) or (0004) diffraction peak of the MgZnO layer, from which a c-axis length may be calculated as per Bragg's law, $n\lambda = 2dsin(\theta)$, where d is the spacing between atomic layers. In the latter, the localised exciton peak originating from the MgZnO capping layer is tracked as a function of x. Both techniques have been reported in previous works [87–89]. Such previous works however fail to cover the full range of x fabricated in this work, and/or report samples based on different growth regimes (for example growth on sapphire substrates which results in relaxed films).

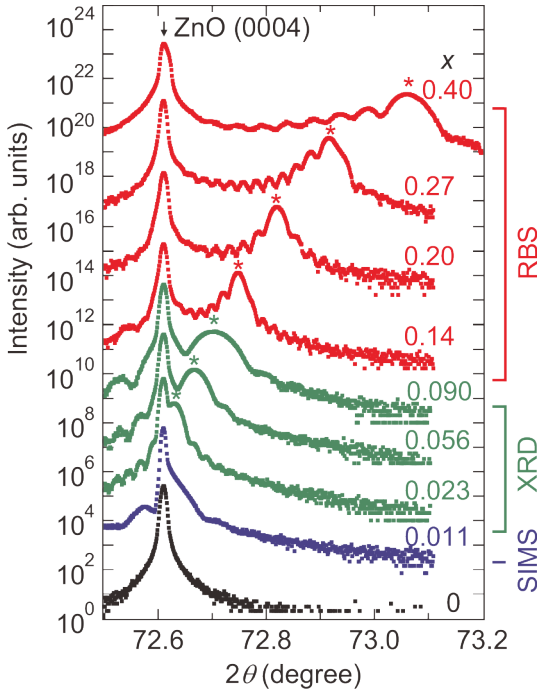

Figure 3.7: X-ray diffraction patterns of $Mg_xZn_{1-x}O$/ZnO heterostructures as a function of x. The three colour regimes correspond to the calibration technique used for determining x. Two peaks are observed, the (0004) ZnO peak which stays stationary at θ = 72.6° and the $Mg_xZn_{1-x}O$ peak which is marked by a star and shifts with changing x. Laue fringes are observed supporting the high quality of the films.

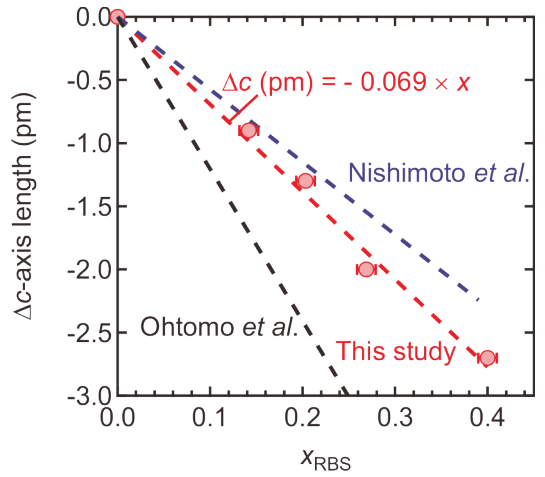

Figure 3.8: Difference in c-axis length between $Mg_xZn_{1-x}O$ and ZnO as a function of x as calibrated by RBS. Data from Ohtomo, *et al.* [87] and Nishimoto, *et al.* [88] is included for comparison.

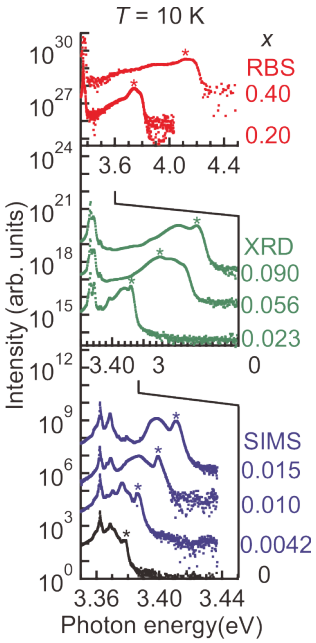

Figure 3.9: Photoluminescence spectra of $Mg_xZn_{1-x}O$/ZnO heterostructures for a range of x values. Note the horizontal axis ranges shift with each concentration as a result of the increasing band gap. The $Mg_xZn_{1-x}O$ localised exciton peak which is used to determine x is denoted by a star.

A series of X-ray diffraction patterns are shown in Fig. 3.7 with differing x contents from the high concentration limit to a pure ZnO substrate. The data was taken using a four-bounce Ge (220) monochrometer (X`Pert XRD, Panalytical Co. and SmartLab, Rigaku Co.). The spectrum coloured red have been gathered after x was determined from RBS. The difference between the bulk ZnO peak and the $Mg_xZn_{1-x}O$ peak (identified by a star) should be a linear function of x according to Vegard's law. Plotting Δc as the difference between the c-axis length of ZnO and $Mg_xZn_{1-x}O$ as a function of x_{RBS} gives the relationship shown in Fig. 3.8. This delivers a qualitative agreement with previous works with a slight quantitative difference compared to Nishimoto, *et al.* [88]. The large difference with Ohtomo, *et al.* is due to the different substrate used (sapphire (0001) single crystals) and hence vastly different strain placed on the grown $Mg_xZn_{1-x}O$ layer. Having established a dependency of Δc on x in the high concentration regime, we can extend the linear relationship to below the detection limit of RBS. Using this the Mg content of films with relatively low x can be determined from the trend identified in Fig. 3.8. These are shown as the green traces in Fig. 3.7. The $Mg_xZn_{1-x}O$ peak remains visible and shifts to lower angles with the lengthening of the c-axis with reducing x. It can be seen that the $Mg_xZn_{1-x}O$ peak is resolved in the diffraction pattern down to $x = 0.023$. For even more dilute films this peak merges into the bulk ZnO peak. This places a lower limitation on the Mg content that lab-based X-ray diffraction equipment can determine.

Having established the limitations of X-ray diffraction in the dilute regime, we now shift to SIMS as the analytical technique to determine the exact x content. We then use the analytically determined values of x to calibrate the low temperature photoluminescence spectrum of $Mg_xZn_{1-x}O$/ZnO films by tracking the energy of localised excitons originating from the $Mg_xZn_{1-x}O$ layer. In contrast to RBS, SIMS is very sensitive to trace amounts of specific atomic species and is therefore useful for this purpose. Using this technique for the quantification of x in $Mg_xZn_{1-x}O$, an upper limit of around $x \approx 0.015$ is encountered. For concentrations that are higher than this, it is not possible to accurately determine the content. For the luminescence experiments, the sample is cooled to T = 10 K or 100 K and illuminated with a He-Cd laser (325 nm wavelength) for $x \leq 0.1$ and Nd:YVO_4 (266 nm wavelength) for $x \geq 0.14$. A number of photoluminescence spectra taken at $T = 10$ K are shown in Fig. 3.9. The spectra at the top of

the figure correspond to higher x concentration films while the bottom of the figure shows dilute films. The feature labelled with a star is identified as the localised exciton luminescence of the $Mg_xZn_{1-x}O$ layer. With reducing x the band gap of $Mg_xZn_{1-x}O$ simultaneously decreases, which results in a shift of the exciton peak to lower energies. This is evident in the rescaling of the x-axis with increasing x content. Other recombination peaks originating from the pure ZnO are observed around 3.37 eV. Among these exists a free exciton peak.

The photoluminescence data is summarised in Fig. 3.10. Having measured SIMS for a number of samples, x is well known down to the dilute limit. In the figure we therefore plot the difference between the localised exciton peak energy of $Mg_xZn_{1-x}O$ and the free exciton of the ZnO bulk as a function x for the blue samples. As mentioned above, the x content of the green data sets are known by measuring X-ray diffraction and comparing the c-axis length with the interpolation presented in Fig. 3.8. To link the two sets of data we may then perform photoluminescence experiments on these films. The same applies for the high concentrations samples which have been directly quantified via RBS. Ultimately, the energy dependence of features identified in photoluminescence on x may be plotted for the entire range of doping levels presented. This yields the rather robust linear relationship $\Delta E = 2.2 \times x$..

Finally, we are left with two calibrated methods to determine x in $Mg_xZn_{1-x}O$ films grown epitaxially on ZnO substrates. These techniques both exploit finite physical or energetic differences between the $Mg_xZn_{1-x}O$ layer and ZnO layer, and are either X-ray diffraction by measuring the $Mg_xZn_{1-x}O$ peak position and comparing it to the bulk substrate's peak position, or by measuring the low temperature photoluminescence. The former has a definite lower limit of x = 0.023, while photoluminescence may be used up to high x. However, it can be seen at high concentrations that a deviation occurs from the linear trend identified. This is due to increased localisation strength with increasing x, effectively reducing the energy of such luminescence features. The technique is therefore more reliable in the dilute regime. The two techniques compliment one another and cover the full range of possible x contents.

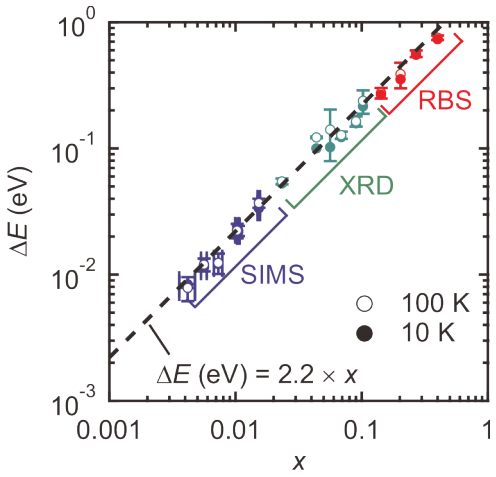

Figure 3.10: Energy difference (ΔE) between the localised exciton peak energy of $Mg_xZn_{1-x}O$ and the free exciton of the ZnO bulk as measured by photoluminescence as a function of the Mg content of films (x).

Using the photoluminescence technique described above, we have evaluated the in-plane doping distribution of Mg, which directly infers the homogeneity of the 2DES on a macroscopic scale. This

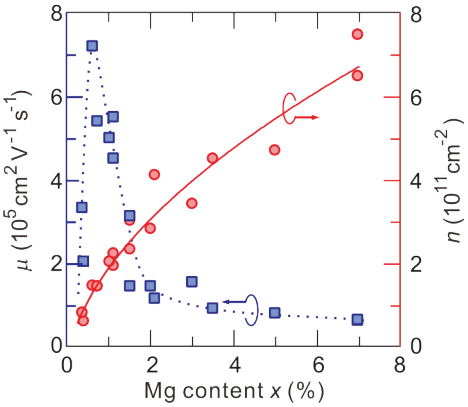

Figure 3.11: Mobility (blue) and charge density (red) of the $Mg_xZn_{1-x}O$/ZnO 2DES as a function of x down to the dilute limit for the first generation of ozone assisted growths. Data is published in Ref. [83]

was published in reference [78]. The result, shows that with rotation of the sample during growth the variation in Mg content may be suppressed to values of $\Delta x \approx 0.5$% across the centre of the sample. Such high uniformity over large areas therefore enables the measurement of electron characteristics in macroscopic sized van der Pauw geometries.

3.5.2 Mg doping dependence

As detailed in the above sections, the Mg content of the $Mg_xZn_{1-x}O$ film plays a crucial role in determining the charge density of the 2DES due to the distortion of the crystal structure. The next question is how this distortion can be explored experimentally and how it affects the quality and parameter space of grown samples. For example, it can be expected that alloying significant amounts of Mg into the capping layer will have a strong effect on enhancing the scattering of electrons at the heterointerface. Evidently, this effect is acutely obvious in the MgZnO/ZnO 2DES. We explore this in detail in this section. As detailed in [83], during the course of this thesis the effect of Mg content was evaluated across a wide range of contents. Leading up to the commencement of this thesis, previous works had focused on relatively high x contents, and accordingly relatively high charge density regimes [80, 84, 85]. The result was a maximum mobility on the order of 150,000 cm^2 V^{-1} s^{-1} for n = 3.5 $\times$ 10^{11} cm^{-2} , x = 0.05. In these previous works it was observed that by reducing x or alternatively density, the mobility would fall. This was associated with a relatively high impurity content, which acted to scatter electrons significantly in the presence of weak screening, greatly suppressing the mobility.

This work uses ozone which should have a much lower impurity content in comparison with oxygen plasma. As will be shown later, in Fig. 3.23 a SIMS measurement on a clean MgZnO/ZnO heterostructure is presented and shows that all impurities are below the detection limit of this analytical technique. That said, it ultimately is the electrons of the 2DES which will give the most accurate evaluation of sample quality. In the event of ozone really reducing the impurity content, a new regime of Mg doping contents should be accessible, with superior electron mobilities possible across the board. Figure 3.11 plots the dependence of mobility and charge density of $Mg_xZn_{1-x}O$/ZnO heterostructures over a range of 0.003 $< x <$ 0.07. This is already much lower than that of previous studies. Amazingly, the interface remains conducting down to extremely low Mg contents of much less then x = 0.01 when using ozone for growth. In the dilute limit it is striking to see that the mobility is maintained to be over μ = 2 $\times$ 10^5 cm^2 V^{-1} s^{-1}. This in itself is superior to the best results from oxygen plasma-assisted growth. Most remarkable however is the peak in μ observed when $x \approx$ 0.01. For such low Mg contents, the mobility shows a very strong dependence on x. The maximum mobility observed exceeds 7 $\times$ 10^5 cm^2 V^{-1} s^{-1} for n = 1.4 $\times$

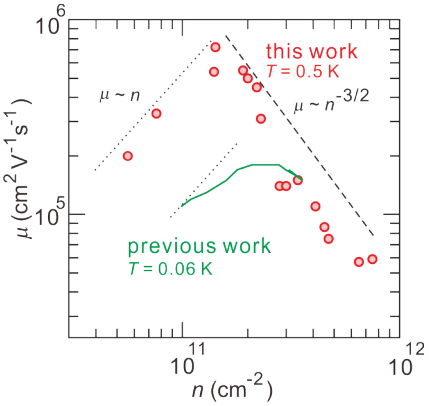

Figure 3.12: Mobility as a function of charge density for a ozone-assisted MBE generation samples (red) versus an oxygen plasma grown FET device (green) [85]. Data is published in Ref. [83].

10^{11} cm^{-2} at T = 0.5 K. Moving to higher Mg contents results in the suppression of mobility, ultimately dropping below μ = 1 $\times$ 10^5 cm^2 V^{-1} s^{-1} beyond $x \approx 0.04$. For the high density samples, the mobility is comparable to that of previous generations of growth (we note however that since publishing the data in Ref. [83] the mobility of the high density regime has similarly been enhanced beyond that of previous generations. See sections below.).

The dependency of the mobility on n described in Fig. 3.12 which allows us to infer the limiting scattering mechanisms present in the heterostructure. Beginning from the high density regime it is seen that there is not a huge difference between the samples grown using ozone or oxygen plasma, represented by the indicative set of data given as the green line [85]. Revisiting Matthiessen's rule in section 2.1 it can be seen that if one scattering mechanism is overwhelmingly present this will suppress the overall electron mobility preferentially. We interpret this high density regime to correspond to interface roughness and/or alloy scattering which is induced by increasing x of the capping layer. This suggest that the heterointerface itself is not making significantly sharper or cleaner simply by moving to ozone. The scaling given by $\mu \propto n^{-3/2}$ is also conducive with interface induced short range scattering. Below charge densities of $\approx 3 \times 10^{11}$ cm^{-2} , a discrepancy between the two data sets of ozone and plasma grown samples begins to emerge. While both series show rising mobility with reducing n from the high density regime, the peak mobility in oxygen plasma samples occurs at significantly higher n compared with those grown using ozone. While the overall trend presented (of increasing μ with decreasing n) is related to mitigating the effects of interface scattering caused by Mg doping, the peak is likely an interplay of impurity scattering and how effectively this can be screened.

The peak mobility obtained in ozone grown films at much lower n suggests that the overall disorder landscape is much improved, since even in the presence of fewer electrons the scattering rate is lower. Ultimately, the ozone films do show a reduction in mobility with reducing n. The slope of this reduction is $\mu \propto n^1$, which would suggest that screening with increasing n is improving the mobility and hence the primary scattering mechanisms is ionised impurities. Theoretical works however suggest that still interface roughness is the limiting mechanism of mobility[90]. These works also calculate that the residual impurity density of these heterostructures to be on the order of 10^{14} cm^{-2}. This is comparable to high quality AlGaAs/GaAs heterostructures [63].

In Fig. 3.13 the temperature dependence of a number of heterostructures with different n is displayed. In addition, a limitation set by acoustic phonon scattering of $\mu \propto T^{-1}$ is included as a simple guide line[91]. This figure highlights a number of characteristics. Firstly, the maximum of mobility as a function of temperature is shown to distinctly depend on charge density, with higher density samples

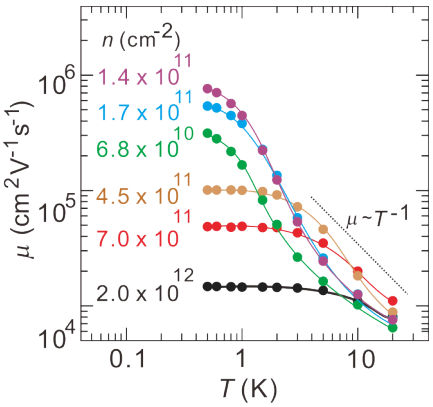

Figure 3.13: Temperature dependence of mobility for a range of charge densities. Data is published in Ref. [83]. A simple approximation of deformation potential phonon scattering limited mobility [91] is given $\mu \propto T^{-1}$ is given as the dashed line.

saturating at higher temperatures. This is due to the effects of interface roughness scattering, which, shows weak temperature dependence and is enhanced with increasing n (or alternatively, x). The other feature is the rate of μ increase as a function of T for low density samples. It can be seen the guideline present for phonon scattering only models the behaviour moderately well. Notably, for dilute samples a deviation occurs from this guideline, with a lower mobility being observed at higher T, with a rapid increase for $T \leq 2$ K.

The work presented in Ref. [90] has modelled this behaviour by considering a transition to the Bloch-Grüneisen (BG) regime under the condition $k_b T_{BG} = 2k_F \hbar u$, where k_B is the Boltzmann constant, T_{BG} is the BG temperature, $\hbar$ is the reduced Planck constant and u is the velocity of sound. In this regime, only acoustic phonons of wavevector $q < 2k_F$ contribute to scattering of electrons. In this regime, the $\mu \propto T^{-\alpha}$ relationship can take on powers which result in a dramatic increase in mobility at low T. For MgZnO/ZnO , $T_{BG} \approx 3$ K. This temperature coincides well with the dramatic behaviour which clearly deviates from the simple guidelines presented. From an experimental point of view it establishes the temperature ranges required for reasonable screening of sample quality (if mobility is the term under investigation). Clearly, the high mobility samples (corresponding to $n < 2 \times 10^{11}$ cm^{-2}) show a saturation in their mobility only below 1 K. This low temperature necessitates the use of a ^{3}He cryostat for standard sample evaluation. Fortuitously, such cryostats are not significantly more demanding to use than regular ^{4}He cryostats, meaning they may be used efficiently in the sample screening procedure. We also note that the data presented in Fig. 3.12 are measured at T = 500 mK. This means that the mobility of dilute samples has not yet fully saturated. This however does not prohibit us drawing the qualitative conclusions discussed above.

3.5.3 Capping layer thickness dependence

We now touch on the thickness dependence of the MgZnO capping layer required to accumulate the 2DES at the heterointerface. In the next chapter this is explored more extensively in the context of the quality of the 2DES. We note that previous studies [92] using oxygen radical as the oxidizing source and sapphire as substrates reports a saturation of the 2DES charge density when surpassing a MgZnO thickness of roughly 10 nm when x = 0.37 (resulting in $n \approx 5 \times 10^{12}$ cm^{-2}). This thesis focuses on the dilute regime of $n \approx 10^{11}$ cm^{-2} where the polarisation mismatch at the interface is weaker and the ability of electrons to screen disorder is reduced, due to the overall smaller E_F. Therefore, the goals of such thickness dependence experiments are not simply to probe the maximum density, but to gauge how the 2DES changes as a function of thickness.

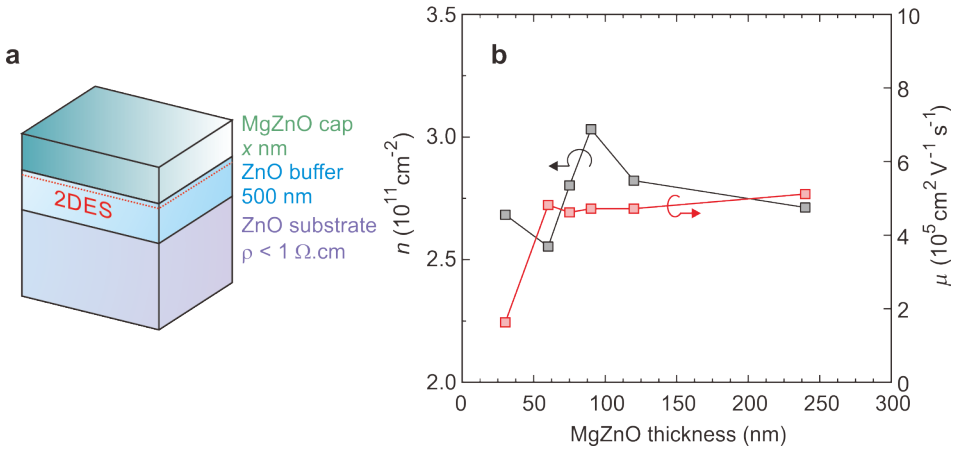

Figure 3.14: MgZnO thickness dependence of 2DES parameters. **a** Schematic of the heterostructure with the MgZnO capping layer thickness as the variable. **b** Charge density and mobility as a function of MgZnO thickness.

Figure 3.14 displays the capping layer thickness as the variable between a number of heterostructures grown in series. The Mg flux and ozone flow is constant between all samples, as is the 500 nm buffer layer thickness of ZnO. The charge density shows a peak when MgZnO achieves a thickness of 100 nm or so. It declines in both thinner and thicker samples. The thinnest sample, at 30 nm displays a charge density comparable to the thickest sample at 240 nm. In terms of charge density then, it appears that by 30 nm the 2DES is induced. This is in agreement with previous studies [92]. What is more important, however, is the behaviour of the mobility with reducing thickness. The mobility remains high (on the order of 500,000 cm^2 V^{-1} s^{-1}) down to a thickness of 60 nm. When making the capping layer thinner than this however, the mobility is reduced dramatically. Therefore, the thickness of the MgZnO capping layer has a more important role than to simply induce carriers at the interface. Clearly, a certain thickness is required to ensure scattering of electrons is suppressed and the mobility remains robust.

Changing view points on the above experiments entices questions whether or not the mobility maybe enhanced further by growing thicker films. We have found this quantitatively true for a range of samples grown with this question in mind. The trend is presented in Fig. 3.15 where films from Ref. [83] are plotted along with samples of t = 240 (purple), 500 (blue) and 1000 (red) nm thick MgZnO capping layers. The charge density (Mg content) is an additional variable in this plot, which should be interpreted taking into account the trend of samples across the entire range of densities probed. It rather conclusively shows that thicker films yield a higher mobility. We note that this mobility however has not saturated at T = 500 mK for films of low density (see Fig. 3.13), therefore, an even greater discrepancy may be ultimately observed when going to $T \leq$ 100 mK. Further improvements to the quality of the 2DES may be made by growing even thicker films. However the returns are likely to be less acute and may induce complications for probing of the 2DES, for example in optical or mesoscopic measurements.

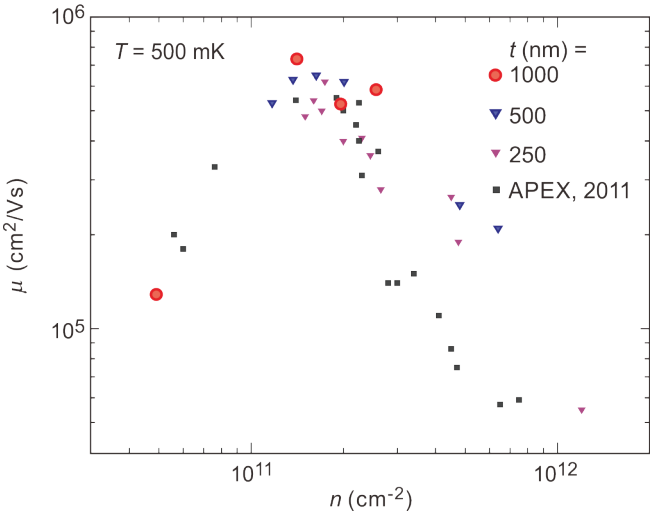

Figure 3.15: Mobility of a range of heterostructures with differing MgZnO thickness capping layers. Black dots are the data points presented in Ref. [83]. Purple data points correspond to t = 240 nm films with blue t = 500 nm and red t = 1000 nm.

3.6 Substrate heating configurations

The requirement of injecting large amounts of oxygen species into an MBE apparatus with internal components operating at high temperature creates a unique set of considerations and requirements for the materials to be utilised in the chamber components. In MBE apparatus which do not intentionally incorporate oxygen into the growth process, the choice of materials is fairly well established - high purity metals with low vapour pressures, such as tungsten (W), tantalum (Ta) and molybdenum (Mo), combined with ceramic materials such as pyrolytic Boron Nitride (pBN) and alumina (Al_2O_3) for electrical and thermal insulation. This is the case in high mobility GaAs systems, where the main substrate heating coil is Tungsten. Effusion cell crucibles are pBN or alumina, depending on the source material. However, while W, Ta and Mo have low vapour pressures as metals, this may not be the case as oxides. This limits the use of such refractory metals in OMBE. Instead, the use of "super-alloy" materials is wide-spread. These are alloys which continue to exhibit mechanical strength while being exposed to high temperature and corrosive environments. They are often used in furnaces, gas-turbines and even rockets, where parts are exposed to demanding environments for extended periods of time. Due to their wide use in industry, a large range of materials are available, each aimed at specific uses and environments. They are usually constituted by a base element of nickel, cobalt or iron and their common character is the development of a tightly adhering oxide scale, which acts as a robust barrier and protects the internal metal. Differences between material strains include their strength at high temperature, weldability and acid resistance, among other characteristics. A material widely used in this work is "MA-23" (57Ni-22Cr-14W-2Mo-0.5Mn-0.4Si-0.3Al-0.10C-0.02La-5Co-3Fe-0.015B by mass%). This is also sold as Haynes 230. This is an alloy designed for maintaining mechanical strength of underlying metal while developing a robust nickel-oxide based scale.

For obvious reasons, such materials find extensive use in oxide MBE. They are used throughout the chamber in components exposed to heat or ozone flow, including the substrate holder materials. Throughout the course of this work, significant effort has been given to optimising the extent and choice of materials used. The first suspect in the hunt for optimisation is the main heating apparatus

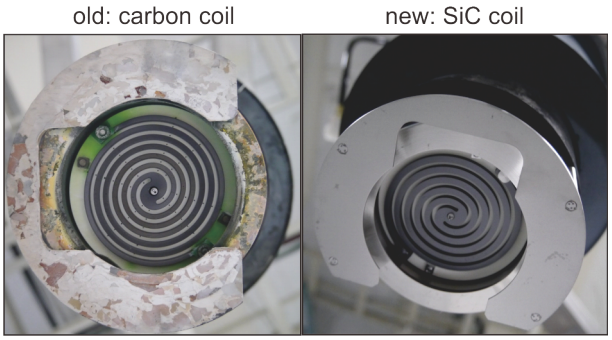

Figure 3.16: Photographs of pre-maintenance (left) and post-maintenance (right) manipulator units. The material of the heating coil is carbon on the left and SiC on the right.

of the MBE - the manipulator. Figure 3.16 shows a photograph of a manipulator unit used for ZnO MBE growth for more than 5 years. The centre of the photo displays a black coil - this is the heating element and is made from carbon and is roughly three inches in diameter. Backing this is a disc of pBN/Inconel601/pBN. Inconel601 is an alloy of composition (61Ni-Bal Fe -23 Cr - 1.4 Al - 0.1 C - 1 Mn - 0.015 S -0.5 Si). It can be clearly see that the pBN barrier has developed green areas. This is likely a nickel oxide, originating from the electrical feed-through bolts, too made from Inconel601, which secures the disc to the manipulator structure. Outer to this disc is a cover of Inconel601, which too has suffered significant oxidation through the course of usage. Finally, the most external piece of metal is used to hold the substrate close to the heating apparatus. This is most exposed to oxidising species and shows significant coverage of a white/brown film. This is likely highly disordered (Mg)ZnO, perhaps with components of the underlying metal structure integrated to form a tightly adhering film.

The power output required to achieve the T_G = 750° for the old manipulator apparatus had steadily increased through time from roughly 280 W dissipation in 2011 to 400 W at the end of 2013. Visually, it could be seen that significant heat was being lost around the edges of the sample as the warped metal shield began to reveal significant portions of the red-hot heating element. More importantly, it was becoming increasingly difficult to reproducibly produce high quality samples. To address this problem, a new manipulator unit was fabricated with modified components.

The new heating unit is shown on the right hand side in Fig. 3.16. This photo was taken immediately post assembly prior to any usage. The structure is similar but with slight modifications. Firstly, the heating element has been changed to high purity silicon carbide. While there was no overwhelming reason for changing from carbon to silicon carbide, the latter is arguably more prevalent in the world of OMBE. The size of the coil was reduced by some millimetres but may still accommodate substrates much larger than the 1 cm ZnO used in this work. Again, the use of tungsten or other refractory metals is not possible in oxide MBE heating coils due to the presence of oxygen. Other changes have been made in the choice of alloys used in the construction. The backing plate of the coil was modified to be a pBN/MA-23/pBN construction, which, evidently can cause problems (see section 3.6.1). The electrical feed through bolts were modified to MA-23. The reflector material closest to the coil was maintained to be Inconel601 due to its machinability. The outermost layer of the reflector which is shown in the old apparatus 3.16 to be significantly degraded through oxidation was thickened to 0.5mm thickness (previously design was 0.3mm). The platform where the substrate holder is placed (the outer most piece of material) was fabricated from MA-23 as this is the component most exposed to ozone flow. That said, the temperature of this component is significantly lower than the internal reflector components.

This maintenance resulted in significant improvements in the power dissipated during growth. While previously 400 W or so was required, the new manipulator unit may reach T_G with a dissipation on the order of 240 W, with visually much less wasted heat leaking around the unit.

3.6.1 High temperature contamination

Despite achieving much lower power dissipation by performing the above maintenance, other unanticipated problems instantly became apparent. After a thorough bake of the system followed by thermal cycling of the manipulator, it became obvious that a discrepancy existed between its performance and the previous (old) manipulator unit. While indeed new components likely are contaminated during their construction and installation, negligible improvement was observed through time. A useful tool for hunting down impurities is the RGA apparatus of the MBE. In Fig 3.17 we plot the residual gas analysis for 2, 28 and 32 amu as a function of time. These should correspond to hydrogen, nitrogen and/or carbon monoxide, and oxygen. At the top of the figure the growth cycle step by step is shown. Initially the chamber is cooled by liquid nitrogen (LN_2), after which the sample is transferred to the growth chamber where annealing, and later growth occurs. The annealing temperature is a variable in this plot. After annealing the substrate growth takes place following which the LN_2 flow is stopped, and the chamber is free to warm up over the hours following. In the figure, the partial pressures of the above gases are monitored. Three traces are presented - pre-maintenance carbon coil with an anneal temperature of T_{anneal} = 1050°C (as measured at the heater thermocouple) in red, post maintenance SiC coil T_{anneal} = 1050°C in blue and post maintenance SiC coil T_{anneal} = 900°C in orange. The substrate holder in use is common between all traces. The behaviour of 32 amu and 2 amu is similar between the three traces present; for 32 amu a strong peak emerges during the growth when ozone is injected into the chamber and for 2 amu a finite peak is observed for a similar time frame. Soon after the flow is stopped, the signal from both these masses quickly returns to the background level. After stopping the liquid nitrogen flow, a small amount of 32 amu is expelled from the cold chamber walls after roughly three hours. These traces however are distinct from 28 amu, which could correspond to either nitrogen or carbon monoxide. Most notably, a large difference is observed between the blue and orange traces for 28 amu when changing the anneal temperature between 900 and 1050°C. A notable degas of nitrogen is encountered when the temperature is raised. Indeed, during the pre-growth anneal a peak at 28 amu is resolved in the trace. This disappears when the temperature is reduced to the growth temperature of T = 900°C (measured at the manipulator thermocouple). However, even when reducing to T_{anneal} = 900°C, some degas is still evident post growth, as shown in the orange trace. This is still more than observed in the red trace from the original, well-used manipulator unit.

While it is difficult to pinpoint the origin of such degassing, we suspect that the backing plate of fresh pBN, or the thermal isolating components made from pBN are to blame. The substrate holder and other components are made from metals which we have significant experience with and have not observed such temperature dependent degassing. Being in closest proximity to the heating coil itself, the pBN in reality is exposed to the highest temperatures. Despite the thermocouple indicating $T =$ 1050°C, the real temperature is likely higher than this. This starts to enter the limits of the acceptable temperature range of pBN.

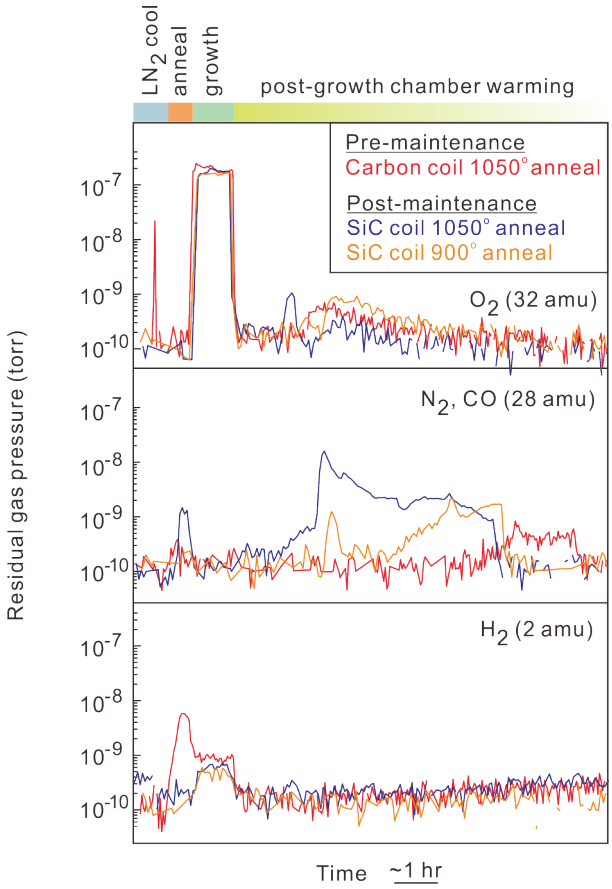

Figure 3.17: Residual gas analysis as a function of time and anneal temperature for 2, 28 and 32 amu. These should correspond to hydrogen, nitrogen or carbon monoxide and oxygen.

This contamination proves to be a serious problem for the quality of 2DES. This is conveyed in Fig. 3.18 where we plot the low temperature mobility and charge density of MgZnO/ZnO films as a function of anneal temperature. As defined in chapter 2, and utilised in the discussion above, we use the concept of the electron mobility to quantify the scattering rate and hence quality of samples. A very convincing trend develops in this figure. We stress that for all films grown in this figure the growth conditions are nominally identical including substrate resistivity and Zn:O ratio. Specifically the growth temperature is $T_G = 900^\circ$C as measured at the thermocouple or $T_G = 750^\circ$C as measured by thermocamera. The only difference is the anneal temperature. The reproducibility of the growth conditions is proven by the near constant charge density between samples (indicating both the Mg flux and growth rate are stable). The anneal time is held at 30 minutes once the anneal temperature is reached, which in itself takes roughly 30 minutes. By changing the temperature of anneal by only $\Delta T = 150^\circ$C the mobility of the samples is dramatically affected in a very systematic manner. The mobility of the lowest anneal temperature is more that twice that of the high anneal temperature sample. It is important to note that physical characterisation of the bulk crystallinity or surface morphology, for example AFM measurements, fail to reveal any notable difference between samples. This is shown on the left and right hand side panels of Fig. 3.18 for the highest and lowest mobility samples.

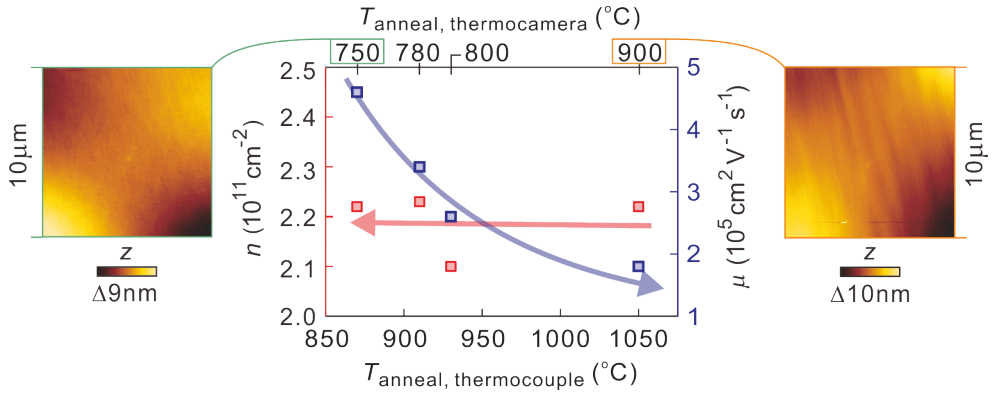

Figure 3.18: Mobility and charge density as a function of anneal temperature when using the post-maintenance apparatus (SiC coil). Both the temperature according to the thermocamera and thermocouple is indicated on the top and bottom axes. AFM images for samples exposed to low temperature (left hand side) and high temperature (right hand side) annealing pre-growth are shown.

We must conclude that this distinct dependence on the anneal temperature and hence the volume of degas is related to impurities expelled when parts of the manipulator are exposed to temperatures in excess of $T \approx 1000$°C. While we concede this temperature is at the lower end of the limitations of pBN, the observation of a peak at 28 amu in RGA suggests that it is to blame. If the metal components were to blame and it were CO being expelled, naively it would be expected that a steady decrease of the degas volume would occur with each growth cycle. This was not observed even after many growths - the degas volume stayed constant and only depended on the anneal temperature. Figure 3.18 shows that the problem may be largely mitigated by reducing the anneal temperature. However, even in the gas analysis corresponding to the lowest anneal temperature in Fig. 3.17, a finite peak corresponding to 28 amu is registered after growth. Further development of the manipulator unit is therefore required.

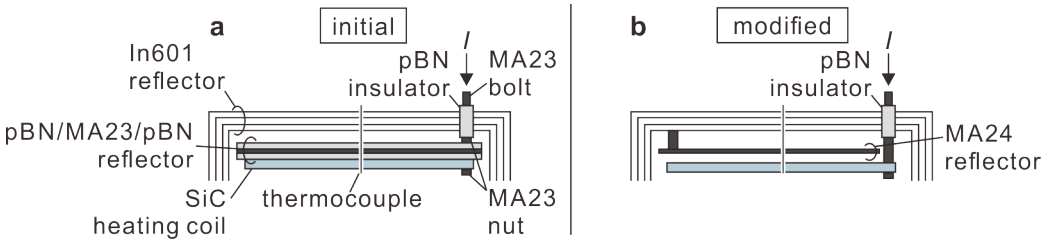

Figure 3.19: A comparison of the initial post maintenance manipulator design and the modified structure after noticing the high temperature contamination problems.

The first attempt at overcoming this problem through design improvements is shown schematically in Fig. 3.19. With the decomposition of pBN when its exposed to high temperatures as the prime suspect, the backing plate of the manipulator has been redesigned. In panel **a** the initial design following the initial maintenance to the SiC coil manipulator is shown. Here, the SiC heating coil was placed in direct contact with the pBN/MA-23/pBN backing plate. This was the same design used in the pre-maintenance old setup (see Fig. 3.16). However, after examining this well-used setup, a significant amount of pBN appears to have evaporated - the carbon coil is separated by some distance from the backing plate. In this initial construction the peak associated with 28 amu post growth was less obvious

(Fig. 3.17). In the hope of emulating this, we have modified the manipulator arrangement as per panel **b**. The pBN plates from the backing plate are eliminated. The MA-23 material has also been replaced by MA-24. MA-24 is another super alloy material of composition (75Ni-16Cr-4.5Al-3Fe-0.5Mn-0.2Si-0.1Zr-0.05C-0.01B-0.01Y by mass%) which should have superior oxidisation resistance compared to MA-23 when temperatures exceed $T \geq 955^{\circ}$C. This is due to a tightly adhering scale with contains a larger portion of aluminium compared to MA-23 (which is a mostly Ni or Cr based scale). The coil is also separated from the backing plate by 2 mm or so. This design reduces the use of pBN to a minimum. The only component remaining is the insulating material used on the electrical feed through bolts (top right hand side in the schematic). Further experiments are required to conclusively determine the improvements gained through this design. Anecdotal evidence however suggests this pursuit has been successful. Indeed, the power dissipation during the growth of films using this arrangement is low ($\approx$ 240 W). The magnetotransport show in section 4.16 is from samples grown after these changes have been implemented.

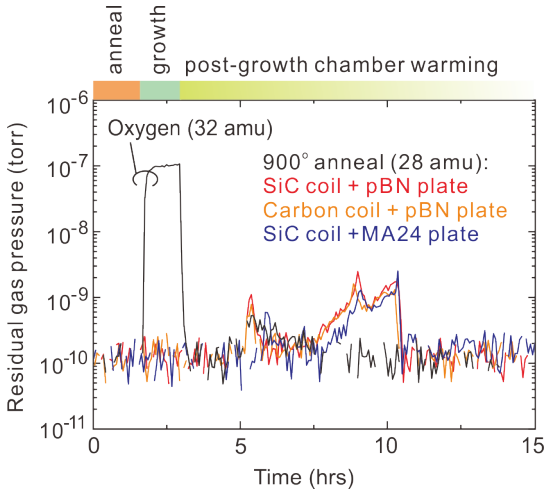

Figure 3.20: Residual gas analysis as a function of time for 28 for three different heating configurations and 32 amu.

In Fig. 3.20 a similar RGA trace is shown as a function of time for three different heating apparatus configurations. The red trace corresponds to the scenario introduced above (Fig. 3.19**a**); the initial post-maintenance setup where the SiC coil is in direct contact with a pBN backing plate. The orange trace corresponds to an intermediate step which was necessary for technical reason (but not discussed in detail), which entailed using a carbon coil separated from the pBN backing plate by carbon washers. Finally, the blue trace corresponds to the configuration in panel Fig. 3.19**b**. The black trace corresponds to 32 amu (oxygen), and serves as a guide to the eye for the growth period. A similar trend is encountered for all three heating arrangements; a degas of 28 amu is resolved some hours after the growth while the chamber warms up. However, quantitatively speaking, the blue trace (MA-24 backing plate) shows the smallest volume of degas. This representation clearly shows the problem is not completely resolved, but steps in the right direction have been made.

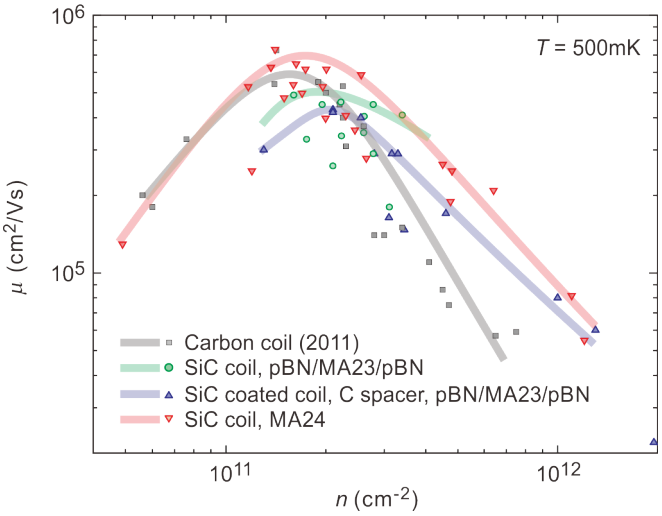

Figure 3.21: Low temperature mobility as a function of density for the four incarnations of the manipulator heating apparatus discussed above. The coloured lines act as a guide line to the 'maximum' value trend achieved. The data points corresponding the Carbon coil (2011) were published in Ref. [83].

The most concise means to evaluate the developments above is arguably the dependence of μ on n. Such a representation of the data is used throughout this thesis and was introduced above (see also Figs. 3.12 and 4.17). In the context of the discussion above, it is simply important to recognise that the mobility of samples grown using the SiC coil/MA24 backing plate (red triangles in Fig. 3.21), which corresponds to the scenario presented on the right hand side of Fig. 3.19 gives the highest mobility samples across a wide range of charge densities. We however highlight that this representation is somewhat misleading as in reality there are more variables than simply the manipulator construction (for example, finite variations in Zn flux, ozone purity, growth rate, film thickness, *etc*. exists within this figure). To dilute the effects of such variations, a large number of data points are included in order to unveil statistically the trend between arrangements. It convincingly shows that the final construction has overall resulted in the highest mobility samples to date.

3.7 Substrate holder materials

In a similar vein to the discussion above, the choice of materials required for substrate holders is too an integral component of high mobility growth. After the main manipulator heater, the substrate and substrate holder are the hottest parts of the MBE. Anything hot is a likely source of impurities, and must be addressed. As opposed to III-V systems where it may be tantalum or molybdenum which is used as substrate holder material, the choice of materials for ozone assisted MBE requires a more vigorous consideration. The environment experienced by the substrate holder is arguably the most extreme; in addition to temperatures on the order of 700°C, the underside of the substrate holder is exposed to the flux required for growth, which in this case, includes high purity O_3. This is in contrast to the internal components of the manipulator unit which are mostly shielded from direct ozone flow. When it comes to substrate materials the option of either ceramic materials, or again, super-alloys emerges. Previous research has shown that for MgZnO/ZnO growth, the use of Inconel can lead to the incorporation of Mn impurities which limited the mobility of heterostructures[80]. This lead to the use of quartz as the

substrate holder. During this work, the use of other super-alloys, beyond Inconel has been revisited.

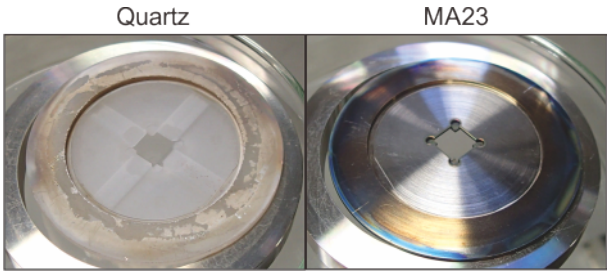

Figure 3.22: Substrate holders fabricated from quartz (left) and the super alloy "MA-23" (right), both after multiple growth cycles.

Figure 3.22 shows photographs of the a quartz and MA-23 substrate holder. Through multiple growth cycles the quartz holder develops a white scale of presumably highly disorder ZnO and MgO. In contrast, the super-alloy develops a green/blue scale. This scale, comprised mostly of Ni, Cr and Mo oxides, is the highly adhesive in the case of MA-23 and is key to the alloy retaining its strength even in high temperatures. However, for MBE growth, strength is less of a priority; even a small amount of the scale becoming mobile and entering the grown film will contribute to impurity scattering.

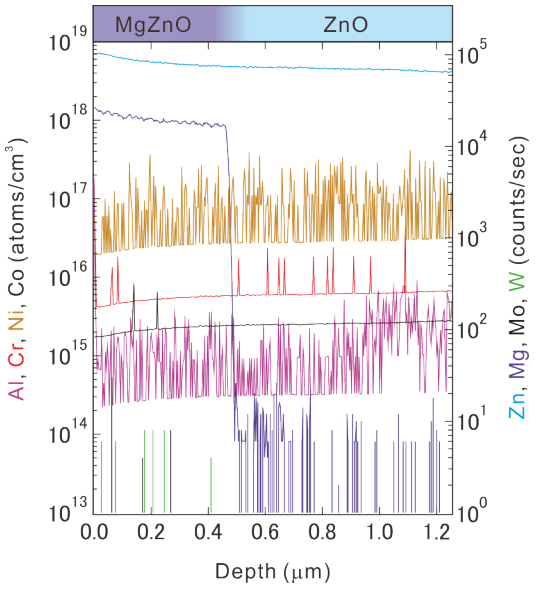

Figure 3.23: Secondary-ion mass spectroscopy analysis of a MgZnO/ZnO thin film grown with an MA-23 substrate holder.

Another consideration is the power dissipated during the use of these holders, as this heat will inevitably enter other components in the chamber, leading to other sources of impurities. In the case of a T = 900°C anneal and 750°C growth temperature (measured by thermocamera), the power dissipation of the heater at the power supply is 880/500 W for quartz and 400/240 W for MA-23 (when using the post-maintenance apparatus described in section 3.16). This is due to the transparency of quartz to the long wavelength radiation emitted from the heating coil. As a result, we had troubles with fabricating dilute Mg films using the quartz holder. In the case of the metal MA-23, however, this heat is more

effectively absorbed and contained.

Figure 3.23 shows the impurity content of films measured by SIMS. As introduced above, this physically destructive technique is very effective for detecting trace amounts of elements on the order of parts per million or lower concentration. It is therefore suited for hunting impurities. As can be seen, only Zn and Mg are detected, with the MgZnO heterointerface clearly observed. Below this interface the Mg content is very low, indicating no migration of the Mg content reverse to the growth direction. All other elements which form the MA-23 alloy are below the detection limit. This suggests the scale formed is robust with an undetectable level of impurities migrating into the grown crystal.

The importance of preserving the scale from developed from the virgin metal is shown in Fig. 3.24. Panel **a** shows the scale from the bottom side of the substrate holder. A robust green oxide layer is visible. Removal of this scale is possible with HNO_3 or HF, which unveils the underlying metal (not shown). However, this unexpectedly has a detrimental effect on the quality of films grown afterwards. While the first film grown is non-problematic (not shown), the second film grown after scale removal is of exceptionally poor quality, as can be seen in panel **b**. A distinct cloudiness is observed around the edge of the sample and appears the originate from the pins which support the substrate at its four corners. Taking a SIMS measurement of the crystal in this area (panel **c**) reveals that a large amount of Cr impurities are detected on the surface of the substrate. Also, the usually clear interface between MgZnO and ZnO is absent. It is suspected that during the first growth a scale develops which is evidently mobile, and this enters the second and subsequent film grown. This is not observed with virgin substrate holders, suggesting that a modification of the metal composition through use severely affects the ability to re-scale.

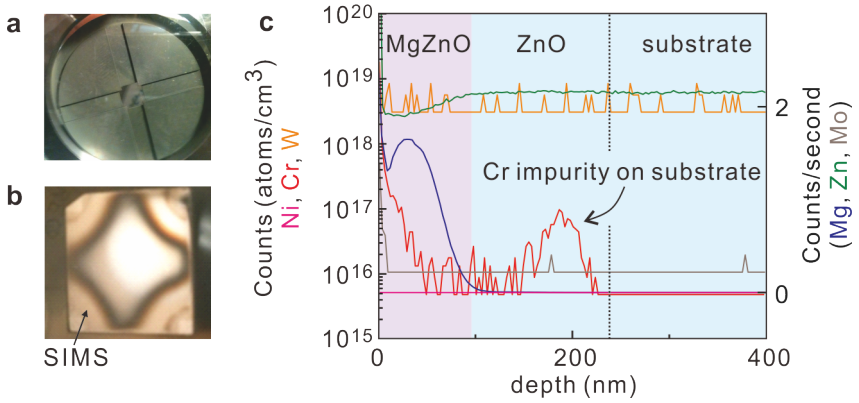

Figure 3.24: Contamination of grown films by poorly adhering oxide scale on an MA-23 substrate holder. **a** A photograph of the bottom of the substrate holder showing a well developed scale. **b** A photograph of a sample with significant contamination at the edges causing poor surface morphology. **c** SIMS profile of the edge of the sample shown in **b**, displaying significant Cr contamination on the substrate surface.

Ultimately, the use of MA-23 has proven to be very effective. Provided the scale is not removed, hundreds of high quality growths can be performed with one substrate holder. However, it remains unanswered whether or not a superior material exists to MA-23. As introduced above, MA-24 is another super alloy, which we have successfully employed in the manipulator heating apparatus. It is also widely used as a substrate holder material, for example in the growth of $SrTiO_3$, which requires very high temperature ($T_{growth} \approx 1200^{\circ}$C) for the highest quality films. However, we have found this material to be completely incompatible with the growth of ZnO films, which is performed at modest substrate

temperatures of $T \approx 750^{\circ}$.

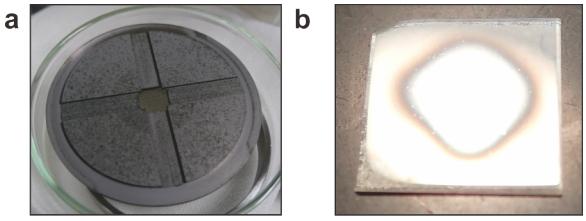

Figure 3.25: Growth with a substrate holder made from MA-24. **a** A photograph of the substrate holder after a number of growth cycles as well as baking in a muffle furnace at 1000°C. **b** Photograph of a sample grown with the MA-24 holder showing poor surface quality around the edges of the substrate.

This comparison is shown in Fig. 3.25, where a photograph of both the MA-24 holder (**a**) and a sample grown using this (**b**) is shown. The substrate holder develops a distinctly different coloured scale to MA-23. It has a white tinge, rather than being deep green. This is likely a result of the high aluminium content. This scale was achieved after baking the substrate holder in air at T = 1000°C for 24 hrs. This is because it is not possible to heat the substrate holder within the chamber to such high temperatures- which is required for this metal to form its ideal scale. However, the result is poor, as can be seen from panel **b**. Physically, the samples have cloudy edges, which is due to an overwhelmingly high density of pits. The centre of the sample, while clean physically, is essentially insulating. This result has important implications for the substrate heating apparatus. MA-24 is currently being employed as the backing plate. This appears to be successful at this moment in time, but it may be wise to review this in the near future.

Beyond nickel based super alloys, strains of iron or cobalt based superalloys exist and may be superior. This remains to be tests as literature searches (unsurprisingly) yield little information about the oxidisation mechanics under ultra-high vacuum and such materials usefulness in the growth of ultra-clean semiconductor materials.

Chapter 4

Parameters of the MgZnO/ZnO 2DES

Before delving into the complexities of the ground states observed in the MgZnO/ZnO 2DES at very low temperature, it is first appropriate to explore and quantify the physical parameter space achieved at the MgZnO/ZnO heterointerface. Such an exercise will prove extremely useful for understanding the results presented in later chapters. Throughout this chapter we explore experimentally a number of parameters, some of which are introduced in Table 4.1.

4.1 Optical probing of the confinement potential

Optical measurements provide a powerful means for quantitative probing of energy levels and recombination of non-equilibrium states in a material. In this section, we utilize low temperature (T = 0.5 K) photoluminescence to probe the recombination of 2D electrons confined at the heterointerface. The heterointerface is schematically shown in Fig. 4.1. A QW is seen to form at the interface with discrete energy levels forming due to finite size effects. The lowest energy subband is labelled E_0 and first excited subband E_1. In photoluminescence it is possible to observe the recombination of excited electrons of these energy levels with holes in the valence band. These measurements were performed in collaboration with V. V. Solovyev, A. B. Van'kov and I. V. Kukushkin of the Institute for Solid State Physics, Chernogolovka, Russia, and D. Zhang and J. H Smet of the Max Planck Institute for Solid State Research, Stuttgart, Germany. A full detailed discussion is presented in a dedicated publication [a]. The main results relevant to this thesis are presented here.

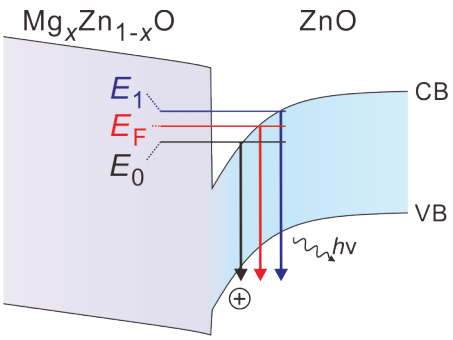

Figure 4.1: Schematic representation of the conduction band (CB), valence band (VB) and QW formed at the Mg$_x$Zn$_{1-x}$O/ZnO heterointerface. Three energy levels are indicated as the lowest subband minimum E_0, E_F and first excited subband E_1. Electrons from these energy levels will recombine with holes to emit radiation of energy hv.

[a] V. V. Solovyev, A. B. Van'kov, I. V. Kukushkin, J. Falson, D. Zhang, D. Maryenko, Y. Kozuka, A. Tsukazaki, J. H. Smet and M. Kawasaki. *Applied Physics Letters, Accepted*

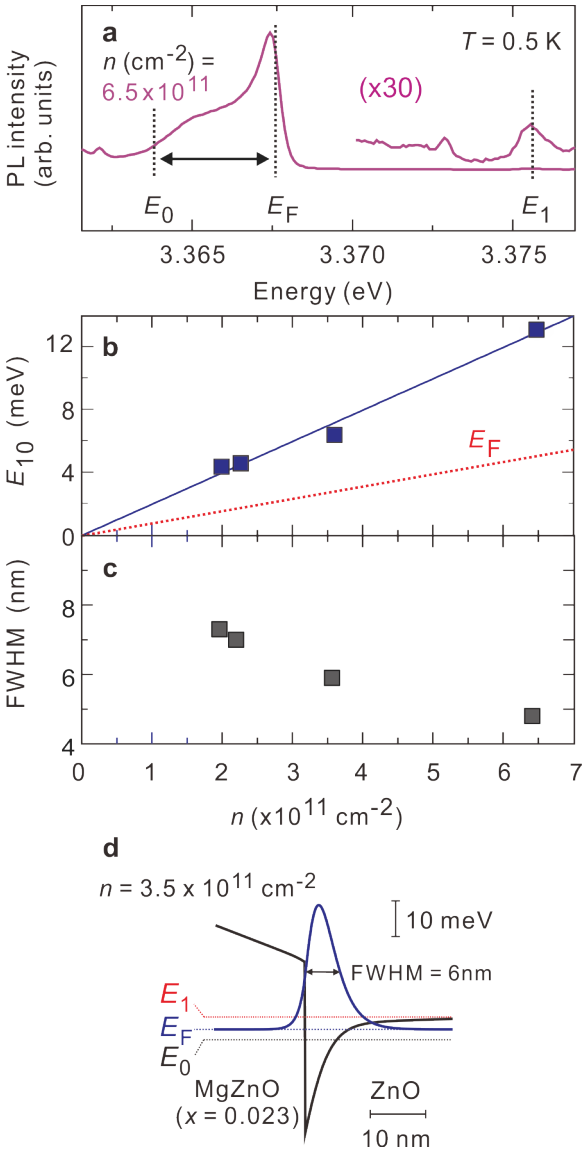

Figure 4.2: **a**, Low temperature photoluminescence spectrum of a MgZnO/ZnO heterostructure (n = 6.5 $\times$ 10^{11} cm^{-2}) with features E_0, E_F and E_1 identified (see text). **b**, Energy difference between the E_1 and E_0 luminescence features as a function of density. E_F is displayed as the dotted red line. **c**, Calculations of with FWHM of the electron wavefunction at the heterointerface. **d**, Visual representation of the confinement potential and electron wavefunction for n = 3.5 $\times$ 10^{11} cm^{-2} , x = 0.023.

Figure 4.2**a** displays a representative photoluminescence spectrum obtained at low temperature just above the fundamental band-gap of the ZnO bulk for a sample of n = 6.5 $\times$ 10^{11} cm^{-2} . A number of features are identified in this figure by the vertical dotted lines. A full analysis of their assignment and dynamics in a magnetic field will be presented elsewhere. Most importantly, all three features show a periodic modulation of either their intensity or peak energy when applying a magnetic field perpendicular to the 2DES. This strongly suggests that their origin is related to two-dimensional electrons at the interface[93]. In panel **a** the features are attributed to the bottom of the E_0 band, E_F and the first excited subband E_1. Similar measurements are performed in both photoluminescence and

reflectance for a range of densities down to n= 2.0 $\times$ 10^{11} cm^{-2} . The analysis allows us to plot the energy difference E_{10} as a function of n (panel **b**). The splitting may be well approximated by a linear interpolation with increasing n. This is due to narrowing of the QW with increasing the Mg content and hence ΔP at the interface. This is confirmed by the red-shift of the E_0 and E_F features with increasing n (not shown). In addition, E_F is plotted as calculated from the known charge density and band mass of electrons. The plot shows that for all n probed $E_{10} > E_F$, and that electrons only reside within the lowest subband of the QW.

Knowing the values of E_{10} and E_F provides a powerful tool to model the QW by calculations. Simple calculations [1] can be performed by taking x, which determines the band offset at the interface and is known from experiment and using the surface potentials of the flanking materials as variables so that E_F (and therefore n) and E_{10} reflect the measured values from photoluminescence. These calculations provide a visual representation of the wavefunction confined at the heterointerface. The full-width half-maximum of the calculated wavefunctions is shown in panel **c** for each charge density. It can be seen that calculations suggest the wavefunction is less than 10 nm wide. Panel **d** shows visually the conduction band (E_C) profile and wavefunction for a sample $n = 2.3 \times 10^{11}$ cm^{-2} and $x = 0.023$. As expected from a single heterointerface, a single maximum is observed in the wavefunction close to the interface. This result agrees well with previous experimental works [86], which measured a width of roughly 5 nm via capacitance measurements, and other theoretical reports [94].

This has important implications for the physics discussed in section 5. There are reports in AlGaAs/GaAs where the presence of electrons in an excited subband, or in quantum wells which host a wide wavefunction of electrons, the physics can be extremely rich. These states were introduced in early chapters in the context of the generalised wavefunction proposed by Halperin[10]. Establishing the details of the quantum well in MgZnO/ZnO heterostructures eliminates such degrees of freedom of excited electrons and greatly simplifies the analysis of ground states presented later.

4.2 Spin susceptibility and effective mass

A parameter central to the phenomena explored throughout the course of this thesis is the spin susceptibility of the 2D charge carriers. To begin with, describe the energy of the system to be,

$$E(k) = \frac{\hbar^2 k_F^2}{2m_e^*} - g_e^* \mu_B B_t \boldsymbol{S}/2 \tag{4.1}$$

where $\boldsymbol{S}$ denotes the spin orientation (= $\pm$ 1). This is the kinetic term plus the Zeeman coupling, analogous to the condition that was introduced in section 2. The bulk polarisation of the 2DES $\mathcal{P}$ = $(n^{\uparrow} - n^{\downarrow})/n$ is related to the spin susceptibility through the relationship,

$$\mathcal{P} = \frac{n^{\uparrow} - n^{\downarrow}}{n} = \frac{g_e^* \mu_B B_t g(E)_{2D}}{n} = \frac{g_e^* m_e^* e B_t}{2nh} \tag{4.2}$$

Here, $g(E)_{2D}$ is the 2D density of states. It is plain to see two material dependent parameters are involved in the polarisation of the 2DES. Moreover, these two parameters are present in the energy ladder scheme which develops in the 2DES with the application of B. The effective mass m_e^* is apparent in the cyclotron energy of the 2DES and the g-factor is at play in the Zeeman term. An overview of the magnitudes of these parameters for prevalent material systems is displayed in Table 4.1.

[1] "1D Poisson/Schrödinger" by Greg Snider, Department of Electrical Engineering, University of Notre Dame.

	GaAs 2DES	GaAs 2DHS	ZnO	AlAs 2DES	$LaAlO_3/SrTiO_3$	Si
m_e^* (m_0)	0.069	≈ 0.5	≈ 0.4	≈ 0.45	≈ 1	≈ 0.2
g-factor	-0.44	-0.44	≈ 4	≈ 2	2	≈ 2

Table 4.1: Summary of the effective mass m_e^* of charge carriers and the g-factor of prevalent 2D material systems. The capping layer material is sometimes omitted for brevity. References: AlGaAs/GaAs 2DES, AlGaAs/GaAs 2DHS [95], MgZnO/ZnO (this work), AlGaAs/AlAs [96], $LaAlO_3/SrTiO_3$ [97] and Si-MOSFET [98].

As can be seen from table 4.1 the well-studied AlGaAs/GaAs 2DES has a small effective mass and small g-factor. This leads to a ratio of $E_z/E_{cyc} \approx 1/70$. This has lead to the physics of each LL being largely isolated from that of neighbouring energy levels, due to their large energy separation. The constellation of such energetics is shown in Fig. 4.3**a**. The opposite is so for ZnO, as shown in **b**, where both m_e^* and g-factor are large and the energy levels from different LL are close. This character will be explored in more detail in Section 5 as a tool to unlock new ground states. However, in this section we explore the quantification of these parameters in the system, in order to better explain the results presented later.

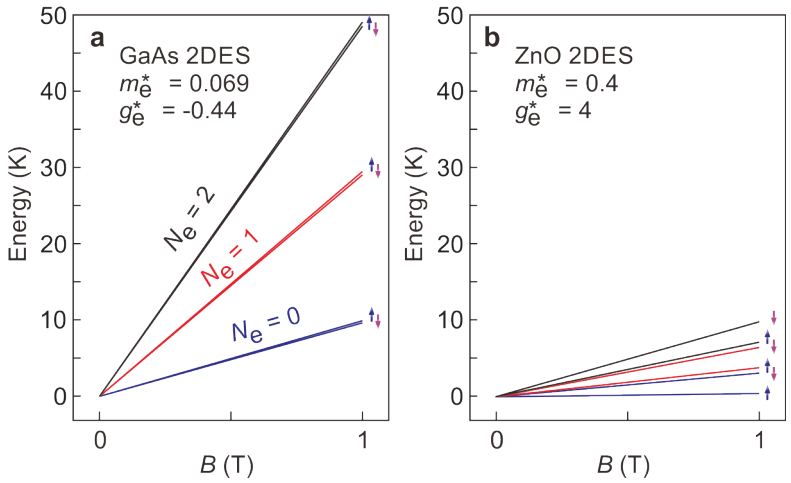

Figure 4.3: Spin split LL fans for **a** AlGaAs/GaAs 2DES versus **b** the MgZnO/ZnO 2DES using the values identified in Table 4.1. The orbital index is labelled with colours representing the scenario in MgZnO/ZnO .

In addition, it is apparent from the table that some values for certain systems are *approximate* values. This is due to this parameter showing some form of dependency on another, and hence its ability to fluctuate depending on sample characteristics, such as charge density or band structure of the material[95, 96, 98]. Quantifying these changes is therefore an important aspect of understanding a material. The MgZnO/ZnO 2DES is no different in this regard. As has been apparent from relatively early in the 2DES' development, the values of m_e^* and g_e^* are highly sensitive to n of the sample under investigation. This can phenomenologically be understood through Landau's theory of Fermi liquids and is briefly touched on here. More extensive explanations exist in the literature[99]. When a correlated electron is added to an excited state above the Fermi energy, the interaction effects will force the electron to relax into a many-body state. These excitations will modify the distribution function of the

liquid,

$$\delta n_D(k) = n_D(k) - n_D^0(k) \tag{4.3}$$

where $n_D(k)$ is the many-body quasiparticle distribution and $n_D^0(k)$ is the ground state distribution. This both leads to a modification of the density of states close to the Fermi energy,

$$g(E_F) \propto \sum_k \delta(E(k) - E_F) \tag{4.4}$$

which can have the effect of modifying the effective mass of electrons at $\approx k_F$. Finally, we define the Fermi liquid parameters,

$$F_l^s = g(E_F) f_l^s, \quad \text{and} \quad F_l^a = g(E_F) f_l^a \tag{4.5}$$

where f is representative of the angle between the correlated excitations in k-space, the superscript corresponds to the (s) symmetric and (a) anti-symmetric component of f and the subscript to the Legendre polynomial in the expansion. While not dwelling on the mathematical details it can be shown that the spin susceptibility of a Fermi liquid maybe modified through the relationship,

$$g_e^* = \frac{g}{1 + F_0^a} \tag{4.6}$$

This is intuitively due to the spin degree of freedom that interacting quasiparticles have and the tendency to align spins to reduce the repulsive energy.

From an experimental point of view such renomalisation effects are explored in this section. As an advancement from previous works [100, 101], the deployment of ozone and the associated improvement in the quality of samples expands the range of possible measurements, aiding our understanding of the parameters. The experimental approach to quantifying these values are numerous and have only been made possible through extensive collaborations. In the following sections we present results from electrical transport and spectroscopy methods to gain an overall view of the parameter space of the 2DES.

4.2.1 Transport measurements

We first focus on quantifying the spin susceptibility via transport measurements. As chapters 5 and 6 of this thesis are exclusively dedicated to transport measurements, understanding of the parameter space realised is essential to establish a framework for interpretation of results. In this section, the experiments are generally performed at a moderately low temperature of $T \leq 500$ mK. This temperature is convenient as it is generally low enough to clearly resolve the integer quantum Hall effect, but not low enough to fully resolve fractional quantum Hall states. As a result, slight modifications of the ground state (*i.e.* a spin transition in electron LL) should clearly be resolved in transport. As has been established in section 2, when talking in single particle terms, the LL of the 2DES rise in energy linearly with the perpendicular component of the magnetic field B_p, regardless of the N_e index or spin orientation, through the relationship $E_{cyc} = \hbar e B_p / m_e^*$ and $E_z = g_e^* \mu_B B_t$. Hence, with only increasing B_p, a crossing of these levels may never occur. In effect, this is shown in Fig. 4.3 for the case of AlGaAs/GaAs 2DES and the MgZnO/ZnO 2DES. This, however, may be circumvented by tilting the sample relatively

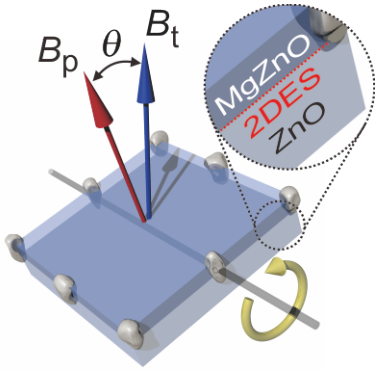

Figure 4.4: Schematic representation of a MgZnO/ZnO heterostructure tilted relative to B_t. θ defines the tilt angle, which decouples B_p.

to the magnetic field direction. This exploits the very simple fact that E_{cyc} is dependent exclusively on B_p while E_z energy is dependent on B_t. Tilting the sample unlocks this degree of freedom through the relationship $B_p = B_t\cos(\theta)$. A schematic of such an experimental arrangement is shown in Fig. 4.4, which shows the relationship between B_p and B_t. Pursuing such experiments results in the possibility of a crossing of these previously discrete levels occurring.

The expression which guides this analysis is given simply by the condition when these two energies are of the same, or multiples (given by the index j_e) of each other,

$$j_e E_{cyc} = E_z \tag{4.7}$$

$$j_e \frac{B_p}{B_t} = \frac{g_e^* m_e^*}{2m_0} \tag{4.8}$$

or alternatively,

$$j_e cos(\theta) = \frac{g_e^* m_e^*}{2m_0} \tag{4.9}$$

This scenario of level crossings is shown schematically in Fig. 4.5. In panel **a** a number of spin split LL are shown. The position of these levels relative to each other is not exact, but is indeed representative of the scenario achieved in MgZnO/ZnO heterostructures where E_{cyc} is comparable to E_z. With increasing tilt, E_z is enhanced and the levels cross. As described by the equation 4.8 the first level crossing ($j_e = 1$) occurs when $E_{cyc} = E_z$. Higher j_e index crossings may occur at higher tilts up until the 2DES becomes fully spin polarised. In the schematic, the chemical potential (μ_ν) is schematically shown for various filling factors, corresponding to ν = 5,4 and 3 (this condition can obviously not be achieved simultaneously). It can be seen that a crossing can occur exactly at μ_ν with increasing the tilt angle. In panel **b** we show experimental data that shows the moment the levels cross. This is a line trace following the minumum of the ν = 5 integer quantum Hall state as a function of tilt. This in effect is the same as what is schematically shown by $\mu_{\nu=5}$. When the chemical potential hits the crossing levels, a sudden increase in the DOS is realised and the ground state breaks down. Mapping out such transitions allows the quantification of $g_e^* m_e^*/m_0$ as per 4.9.

A more extensive rotation study is shown in Fig. 4.6 for a sample of n = 2.3 $\times$ 10^{11} cm^{-2} where the longitudinal resistance is mapped out as a function of tilt angle and perpendicular magnetic field in panel **a**. This plot reveals a number of features of MgZnO/ZnO transport. Firstly, multiple transitions are visually recognisable, corresponding to spin transitions and level crossings. In this plot, transitions up to $j_e = 5$ are unambiguously observed at the ν = 6 integer quantum Hall state at high tilt. For

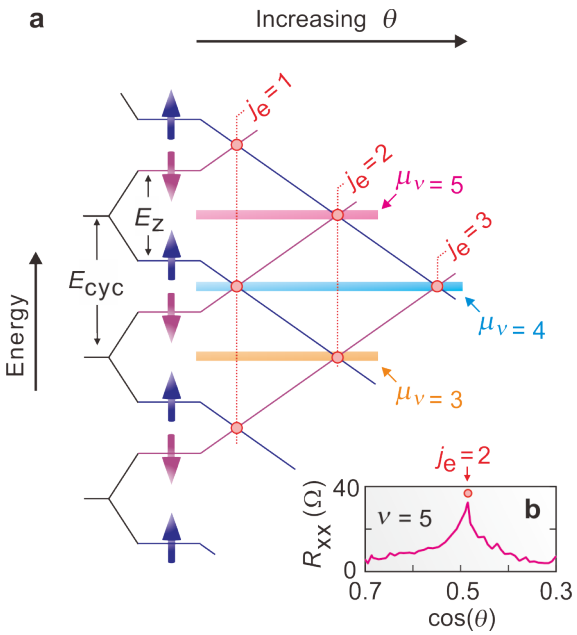

Figure 4.5: Schematic of the spin split LL achieved at high magnetic field in ZnO. **a** The levels are separated by their orbital energy E_{cyc} and spin splitting E_z. Increasing the rotation angle of the sample forces these levels to cross as E_z is enhanced. Their crossings are labelled with the index j_e. The chemical potential for ν = 5, 4 and 3 is shown, and passes through multiple crossings. **b** at such a crossing, the resistance shows a peak as the gap closes.

integer quantum Hall states which occur at lower magnetic field, a full breakdown may be observed. Moreover, plotting the transport in this representation allows the overlaying of the LL fan which was schematically shown in Fig. 4.5. This shows that depending on the tilt angle, the orbital and spin orientation of electrons at the chemical potential can change. As given by equation 4.8, $g_e^* m_e^*/m_0$ may be quantified by plotting the 1/cosθ vs j_e. This is performed in panel **b** and reveals that $g_e^* m_e^*/m_0$ for this heterostructure is approximately 1.9. Recent work on the MgZnO/ZnO 2DES shows that this value can be modified by a polarisation induced modification of $g_e^* m_e^*/m_0$ when moving to higher tilt, or alternatively, high j_e indexes[102]. However, this effect was seen to be rather weak and does not make the analysis restricted to low j_e indexes invalid. A magnitude $g_e^* m_e^*/m_0$ = 1.9 puts E_{cyc} slightly larger than E_z, but they are very close in magnitude, with j_e emerging by a modest tilt angle of $\theta \approx 20^\circ$. A discussion of the density dependence of $g_e^* m_e^*/m_0$ is presented later in this chapter.

The plot reveals another character of transport in MgZnO/ZnO . Plotted in panel **c** is the resistance of half fillings as a function of tilt. It can be seen in this plot, and also by simply observing panel **a** that the resistance oscillates when moving through the identified level crossings. The result is remarkably reproducible, both between the transitions shown in this heterostructure, and also in other heterostructures, for example that of Ref. [102]. Comparing the chequerboard-like pattern with the schematic given in Fig. 4.5, it is revealed that whenever the spin of electrons at the chemical potential takes on a majority spin orientation, the resistance is higher than that of when the chemical potential has minority spin. This behaviour supports the LL fan which is overlayed on the transport, along with the analysis presented above on the evaluation of $g_e^* m_e^*/m_0$ through the breakdown of the integer quantum Hall effect. The observation of a high resistance at majority spin and low resistance at minority spin seems to suggest that new physics involving spin-selective screening is at play. The story is most acute when

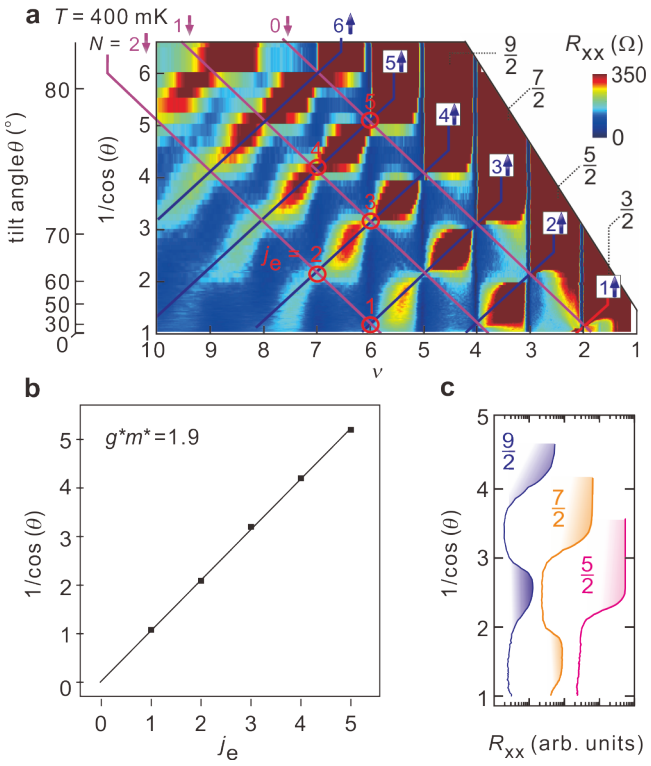

Figure 4.6: Tilt dependent magnetotransport and spin susceptibility of a sample with n = 2.3 $\times$ 10^{11} cm^{-2}. **a**, T = 400 mK magnetotranport mapping as a function of tilt angle and filling factor. The orbital index and spin orientation of LL are overlayed. **b**, Quantification of the spin susceptibility of the heterostructure **c**, Oscillatory resistance at various half-fillings as a function of tilt.

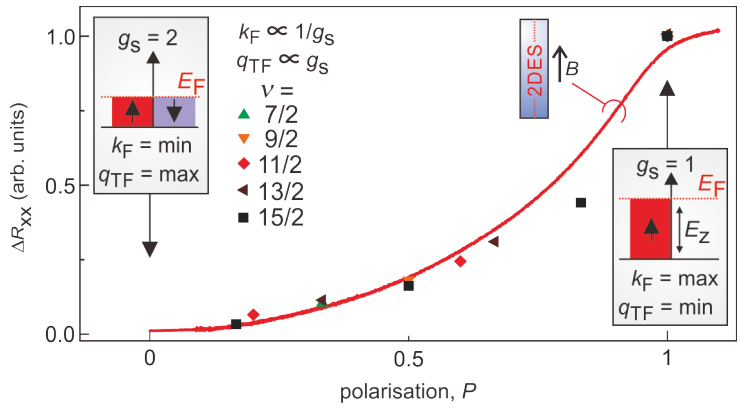

Figure 4.7: Experimental similarities between an in-plane field polarised MgZnO/ZnO 2DES and the oscillatory resistance presented in Fig. 4.6. For all data $T \approx 500$ mK. The red curve corresponds to the resistance change (ΔR_{xx}) from the zero field ($P = 0$) to the fully polarised ($P = 1$) condition. The DOS of states, k_F and q_{TF} for each condition are schematically shown in the insets. The coloured symbols correspond to the ΔR_{xx} at half fillings as the polarisation is increased (see text for details).

going to high tilt angles, which shows the resistance to increase dramatically, and take on a maximal value. In this regime the 2DES is fully spin polarised. This is hypothesis is supported by noting that the maximum number of transitions which can occur at half filling according to the schematic in Fig, 4.5 is i if the adjacent integer states are i and $i + 1$. We note that similar behaviour in the transport of AlGaAs/GaAs 2DHS [103] and AlGaAs/AlAs 2DES [104] have been reported. We note that a common characteristic of these systems is the heavy effective mass which affects screening within the 2DES. However, we are not aware of any rigorous theoretical works to quantitatively describe this matter.

Similarities between the result presented here and the response of a 2DES in a purely in-plane field may be drawn by comparing experimental results. In such in-plane experiments, the absence of a perpendicular component of the magnetic field means that no LL develop, and the magnetic field merely acts to polarise the 2DES. In doing so, if the sample under investigation is of the relationship $q_{TF} > 2k_F$ (where q_{TF} is the screening wavevector), an increase in resistance is observed[105–107]. Here, the effective mass enters the screening wave vector which plays a crucial role in explaining the observed behaviour. The MgZnO/ZnO is of the same parameter space with a heavy effective mass, and indeed shows analogous response to an in-plane field. The experimental result on the same heterostructure is shown in Fig. 4.6 (n = 2.3 $\times$ 10^{11} cm^{-2}) as the red line. It is noted that this is not a representation of the raw data. Rather, the zero field resistance is taken as zero, and the resistance at fully polarisation is taken as one, *i.e.* ΔR_{xx}. The horizontal axis is the polarisation of the 2DES, which again goes from 0 to 1, with 1 corresponding to the kink in ΔR_{xx} at high field. This is in-line with previous reports, which consider this to be a sign of full polarisation. It is speculated that the oscillatory behaviour presented in Fig. 4.6 probes similar physics. To convey this speculation, a simple analysis is performed. Again, the value of ΔR_{xx} is used to avoid quantitative complications. For each oscillation presented in Fig. 4.6**c**, ΔR_{xx} is taken between the condition where the chemical potential probes majority spin extended states (*i.e.* high resistance) and the adjacent minority spin extended states (*i.e.* low resistance). Using the relationship $P = (n^{\uparrow} - n^{\downarrow})/(n^{\uparrow} + n^{\downarrow}) = j_e/\nu$, the polarisation of the 2DES as a function of increasing tilt may be estimated. This increases in discrete steps. In Fig. 4.6 ΔR_{xx} for each oscillation maximum is plotted as a function of P. Finally, ΔR_{xx} is set to be 1 when P = 1. In plotting this data, a surprisingly good quantitative agreement with the in-plane field experiment is observed. Indeed the resistance of

the majority spin level appears to be related to the overall increase in polarisation of the 2DES. We highlight a number of issues with this model, which is entirely speculative at this moment. Firstly, screening deep within the quantum Hall effect is an extremely complex concept and no analytical model to explain the resistance exists. Second, all phenomenon observed in this figure show distinct temperature dependence. This is particularly true for the mapping transport, of which evolves into a complex array of correlated ground states at even lower temperatures. Also, the in-plane field experiments display a metal-insulator transition as a function of T. The temperature for the two data sets are not exactly the same (although both are around ^{3}He temperatures), and the measurements were performed between two different cool downs in two different cryostats. This temperature issue may lead to quantitative deviations, as is seen when approaching high P for ν = 15/2. To properly link these effects, a complete mapping of transport from the parallel condition to low tilt angles must be performed. Further support would be gained by performing temperature dependence of such mapping. A similar metal-insulator transition-like behaviour may emerge in the oscillatory resistance at half fillings, even in the presence of LL. Therefore, a complete unification of these results (or other another model, if the above is indeed incorrect) requires both further experimental and theoretical considerations.

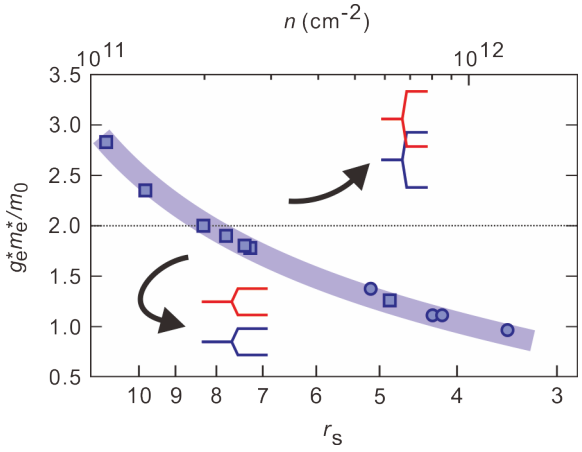

Figure 4.8: $g_e^* m_e^*/m_0$ as a function of n or alternatively r_s. Spin split LL are shown schematically for both sides of $g_e^* m_e^*/m_0$ = 2. Data points are a combination of those presented in [100] (circles) and samples investigated throughout the course of this thesis.

As shown in Fig 4.6**b**, $g_e^* m_e^*/m_0$ for a sample n = 2.3 $\times$ 10^{11} cm^{-2} was quantified to be 1.9. What proves to be even richer in the MgZnO/ZnO 2DES is the observation that $g_e^* m_e^*/m_0$ shows an acute dependence on n, or alternatively r_s. By repeating similar coincidence measurements for a number of heterostructures, $g_e^* m_e^*/m_0$ has been plotted as a function of n in Fig. 4.8. Some points have been published in [100, 101], with a number added from subsequent experiments. The data convincingly shows that with reducing n or enhancing r_s, $g_e^* m_e^*/m_0$ is significantly enhanced. Note here that r_s is calculated using the band mass value of $m_e^* = 0.29 m_0$. While this may technically be incorrect, it ensures consistency between the data presented in the following sections. Most surprisingly, the spin susceptibility passes through the value of 2 when $n \approx 2 \times 10^{11}$ cm^{-2} . This is a very important condition. As shown schematically in the figure, this means that in terms of single particle energetics, E_z becomes larger than E_{cyc}, and the arrangement of levels spontaneously swaps.

In coincidence measurements, it is ultimately the spin susceptibility which is measured. This includes contributions from both g_e^* and m_e^* as what is really measured is the condition of $E_{cyc} = E_z$,

with the former containing the mass and latter g_e^*. In an attempt to de-convolute this behaviour, separate measurements of the electron effective mass have been performed for a number of heterostructures. This experiment involves measuring the damping of Shubnikov - de Haas oscillations with increasing the temperature. Low field temperature dependent magnetotransport for a sample with n = 1.4 $\times$ 10^{11} cm^{-2} is shown in Fig. 4.9**a**. The formalism for the analysis is given by the following expression,

$$\frac{\Delta R_{xx}}{R_0} = 4\frac{\zeta}{sinh(\zeta)}exp(\frac{-\pi}{\omega_c\tau_q}) \tag{4.10}$$

where,

$$\zeta = \frac{2\pi^2 k_B T}{\hbar\omega_c} \tag{4.11}$$

We note that in the case of the MgZnO/ZnO 2DES which has a large $g_e^* m_e^*/m_0$, this analysis should be performed when the electron LL are brought into coincidence and before spin splitting in the oscillations occurs. Therefore, the sample must be tilted and then temperature dependence taken. When plotting $ln(\Delta R_{xx}/T)$ as a function of T, the slope reflects the effective mass of the carrier. A representative plot is shown in Fig. 4.9**b**. It can also be seen that within Eq. 4.10, the quantum scattering time enters. This can be estimated through analysing the amplification of the oscillations with increasing B. By plotting $ln[(\Delta R_{xx}/4R_0)sinh(\zeta)/\zeta)]$ as a function of 1/B, the slope is linear and reflects τ_q. This analysis is performed in panel **c**.

In this figure we have included an arrow for to represent the magnetic field at which the Shubnikov - de Haas oscillations become apparent. Observing the relationship of $\Gamma = \hbar/2\tau_q$, it comes apparent that this field can be used to calculate τ_q by considering that $\Gamma \approx \omega_0$, where ω_0 is the magnitude of cyclotron energy required to resolve the oscillations. From this magnetic field it is possible to determine τ_q through the relationship

$$\tau_q = \frac{1}{2\omega_0} \tag{4.12}$$

Through this type of analysis the sample presented in Fig. 4.9 displays a value of roughly 16 ps. This is in relatively good agreement with the value quantified through the Dingle analysis presented above which yields roughly 20 ps. A more extensive examination of the quantum scattering time will be performed later. We do note however that the values of 15 20 ps reported here are very large, and are comparable to the best AlGaAs/GaAs 2DES samples[63, 108]. This provides very strong support for the intrinsic quality of the MgZnO/ZnO , despite the modest mobility. The onset field of the oscillations is rather temperature dependent. By $T \approx$ 100 mK, the onset begins to shift to higher magnetic fields. This suggest that τ_q is very temperature dependent. We also note that the resistance at the onset of oscillations (signified by the arrow in Fig. 4.9) does not change with increasing temperature. This is the same for the mobility. These factors are very important for gaining a meaningful number from the fitting procedure described by Eqn. 4.10. Therefore, we isolate the analysis presented above to moderately low temperatures $T \leq$ 120 mK. These temperatures are however not extremely low, and indeed may be measured with fairly high accuracy from the calibrated thermometers equipped in the cryostat.

We now focus on the effective mass. A similar analysis of the mass has been performed for a number of heterostructures, as summarised in Fig. 4.10. Important to note is that the experiments have been performed in multiple cryostats. In all systems, there are calibrated thermometers and this is used to measure the sample. Some variation between data points occurs for the same charge density, however

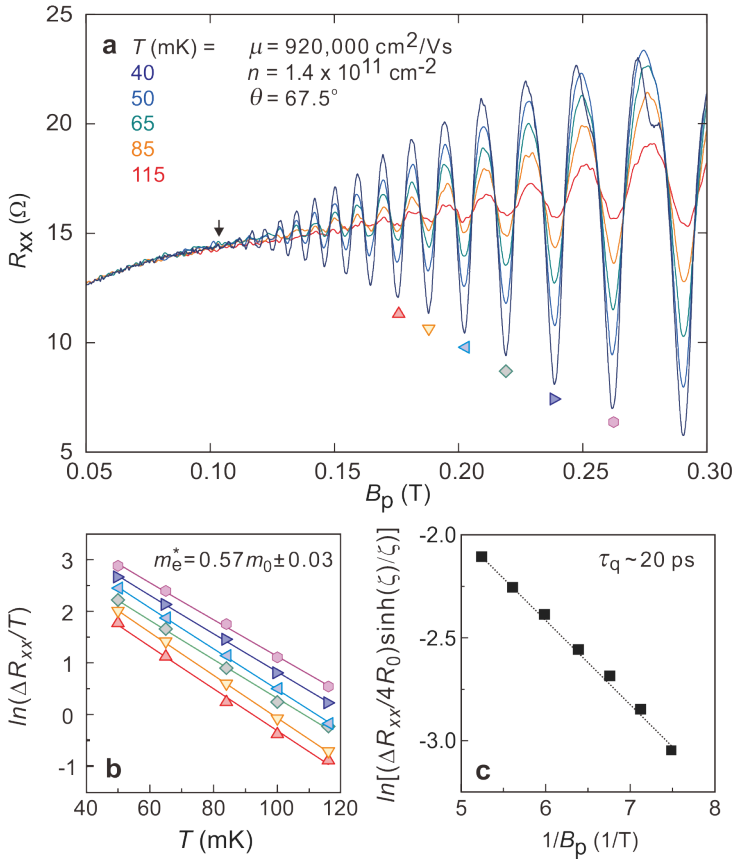

Figure 4.9: **a** Temperature dependent low field magnetotransport for a sample of n = 1.4 $\times$ 10^{11} cm^{-2} when the tilt angle is set at θ = 67.5°, corresponding to the coincidence position of this sample. Analysis of (**b**) the electron effective mass and (**c**) quantum scattering time as per the equation 4.10. The mass for this heterostructure is found to be m_e^* = 0.57$m_0 \pm 0.03$ and the quantum scattering time is estimated at τ_q = 20 ps at base temperate (T $approx$ 40 mK).

this is merely quantitative. This may be an artefact of the different experimental equipment used, and variations in the temperature read (or for example discrepancies between the mixing chamber temperature and the real sample temperature in dilution refrigerators). The result however is overall reproducible and the trend is remarkable. The mass is enhanced when moving to lower n and appears to exceed a value of $0.5m_0$ when n approaches 1×10^{11} cm^{-2} .

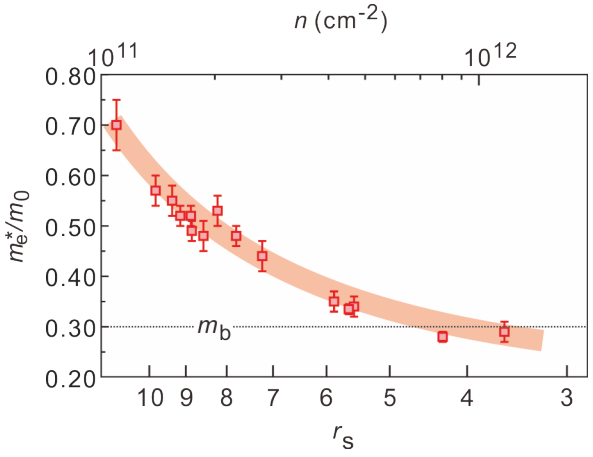

Figure 4.10: m_e^* as a function of n or alternatively r_s.

Having measured the mass independently, it is now possible to infer g_e^*. By interpolating the points measured in Fig. 4.10, the mass may be estimated for the entire charge density range. When comparing this to the measured spin susceptibility values of Fig. 4.8, g_e^* may be independently gauged. In Fig. 4.11, we plot g_e^*/g_b^* and m_e^*/m_b^*. This representation is not the raw values, rather it signifies the enhancement of each component when comparing it to the band values.

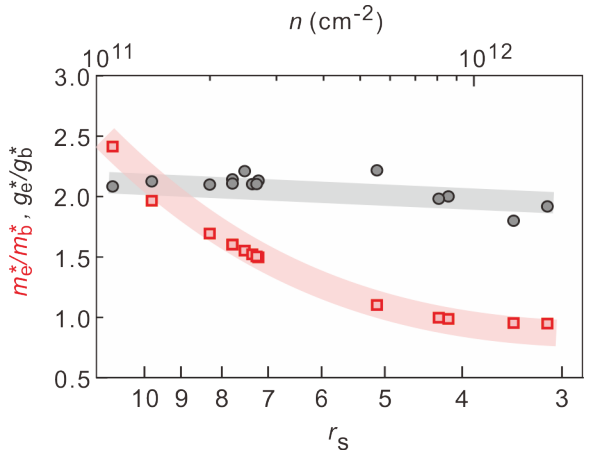

Figure 4.11: Ratio of enhancement of m_e^* (measured) and g_e^* (calculated) as a function of n or alternatively r_s.

While in Reference [101] we have reported that the mass appears to be only moderately enhanced while the g-factor is significantly enhanced when moving to lower n, the result presented here which contains more data points, suggests the otherwise. While indeed in Ref. [101] the value of $g_e^* m_e^*$ is consistent with the trend in identified in Fig. 4.8, the mass enhancement is not. With the addition

of numerous data points, each measured independently and with different equipment, the trend presented in this work appears to be reliable. This is in contrast to the reports on the AlAs 2DES, which is similar to the MgZnO/ZnO when only one valley is populated. In Ref. [96] it was seen that when only one valley is occupied in the AlAs 2DES while retaining the spin degeneracy, m_e^* was seen to show only a modest dependence on n, while g_e^* displayed an acute dependence. The reverse becomes true when the valley degeneracy changed to two. The latter effect was even more evident in Si-MOSFET devices. The change density and r_s ranges between previous works and this work are similar, but the results somewhat contradicting. While in this work not every device was tuned exactly to the point of coincidence for the measurements on the Shubnikov-de Haas oscillations (some finite error inevitably occurs), a large number of points where obtained in the region where n = 2 $\times$ 10^{11} cm^{-2} . As can be seen from Fig. 4.8, this corresponds to where $g_e^* m_e^*/m_0$ is approximately 2, and the levels are close to coincidence. Therefore the analysis should be valid. This story will be enriched by more quantitative experimental techniques which probe the correlation enhanced effective mass and/or g-factor.

4.2.2 Microwave measurements

In the spirit of further understanding the parameter space of the MgZnO/ZnO 2DES, spectroscopy measurements have been explored. These provide an alternative means of measuring 2DES parameters through observing the resonance of the energy scales present in the 2DES with that of externally introduced radiation. Such resonance is typically achieved with microwave radiation for the energy scales presented here. Of particular interest is the effective mass and *g*-factor of electrons. Two primary methods may be employed: cyclotron resonance (CR) (or more accurately, the plasmon resonance) and electron spin resonance (ESR). The advantage of such methods is that the parameters mentioned above may be measured independently and yield quantitatively precise results. The disadvantage is however that these techniques typically do not reflect the correlation enhanced values of the parameters under investigation. This is opposed to transport measurements (which probes electrons at the chemical potential, see section 4.2.1). There, it was the product, $g_e^* m_e^*/m_0$ which was revealed through the coincidence method rotation measurements. Such an analysis yielded a value significantly enhanced over that of the bulk, which is suspected to be as a result of electron correlation mediated renormalisation effects.

Both CR and ESR have been performed throughout the course of this thesis. The CR measurements were performed in collaboration with Y. Kasahara, Y.Oshima and Y. Iwasa and were published as Ref. [109]. In this work, CR was detected for a number of heterostructures and revealed that the effective mass of 2D electrons was roughly 0.3 m_0, in agreement with the value of bulk ZnO. A comparison with transport measurements on the same set of heterostructures yielded a clear discrepancy between the measured effective masses. This result provides evidence for the effects of coulomb interaction mediated renormalisation of the effective mass in ZnO heterostructures.

Since publishing this result, further collaborations with V. E. Kozlov, A. B. Van'kov, S. I. Gubarev, I. V. Kukushkin and V. V. Solovyev of the Institute for Solid State Physics, Chernogolovka, Russia, and J. H Smet of the Max Planck Institute for Solid State Research, Stuttgart, Germany, on lower temperature measurements with higher quality samples have been pursued. In this work, clear evidence of magnetoplasmon resonances were unveiled, which were absent in previous works. The analysis of this result, as outlined below, provides further insight to the surprisingly complex behaviour of the effective mass in the MgZnO/ZnO 2DES. These have recently been published in detail in Ref. [110, 111]. An outline of

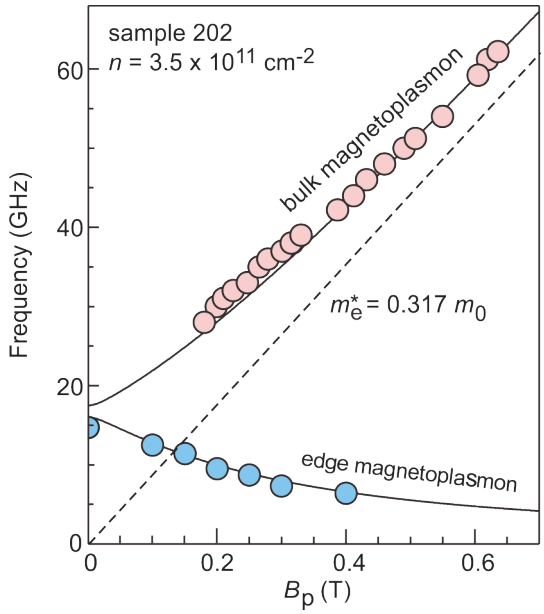

Figure 4.12: Frequencies of the magnetoplasma resonances versus perpendicular magnetic field for sample 202. Blue points correspond to the resonances from edge magnetoplasmons while pink points correspond to those of the bulk. The solid lines describe the theoretical dependencies given by Eq 4.15. The dashed line is the calculated cyclotron frequency using the measured electron effective mass.

these results is presented here in the context of determining the parameters of the MgZnO/ZnO 2DES and making a comparison with the results gained from transport measurements.

When a 2DES is exposed to microwave radiation in resonance with a plasma excitation of the sample, a redistribution of electrons across the energy spectrum occurs. In the experiments performed on the MgZnO/ZnO 2DES, this resonance has been detected by simultaneously performing luminescence measurements on the sample, and by comparing the spectrum when exposed and when not-exposed to radiation. By using the magnetic field and frequency of incident radiation as degrees of freedom a quantitative understanding of plasmon resonances may be gained as a function of the two energy scales. The technique is described a collaborative manuscript published on MgZnO/ZnO heterostructures [110].

In the absence of a magnetic field, the resonance frequency of plasmon resonances propagating in the x or y direction is given by,

$$\omega_x^2 = \frac{n_s e^2}{2m_e^* \overline{\varepsilon}} q_x, \tag{4.13}$$

$$\omega_y^2 = \frac{n_s e^2}{2m_e^* \overline{\varepsilon}} q_y. \tag{4.14}$$

where, n is the electron density, $\overline{\varepsilon}$=$(8.5 + 1)/2\varepsilon_0$=$4.75\varepsilon_0$ is the half space dielectric constant, and $q_x = \pi/a$ and $q_y = \pi/b$ are the wave vector components for the fundamental plasmon modes with a and b the sample size. The sample shown in Fig. 4.12 has size a = 1.1 mm and b = 0.9 mm. Following the formula in Ref. [112], the plasmon dispersions can be calculated as,

$$\omega_\pm^2 = (\omega_x^2 + \omega_y^2 + \omega_c^2)/2 \pm \{(\omega_x^2 + \omega_y^2 + \omega_c^2)^2/4 - \omega_x^2\omega_y^2\}^{1/2}. \tag{4.15}$$

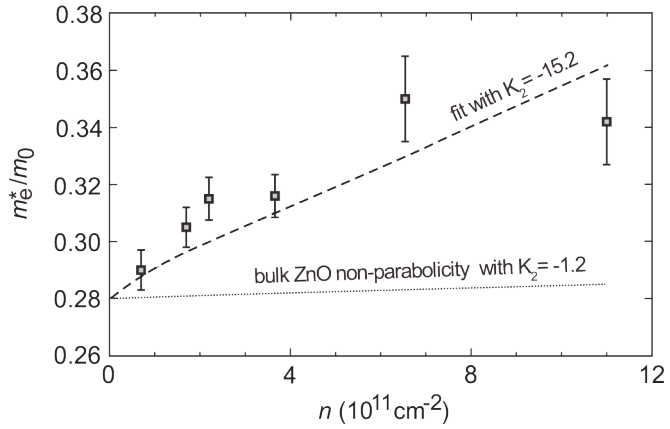

Figure 4.13: The electron effective mass m_e^* as a function of n for the six MgZnO/ZnO samples as extracted from the fitting parameters of the magnetoplasmon excitations. The dashed line is a fit to the data. Adapted from Ref. [111].

Here the cyclotron frequency enters as ω_c, which obviously contains the effective mass. At high frequencies the upper plasmon mode approaches the cyclotron energy. Fitting of these dispersions allows estimation of the m_e^*. In Fig. 4.12 the cyclotron energy calculated from the fitted effective mass = 0.317m_0 is shown as the dotted line in the figure. When approaching higher field, it can be seen that the upper plasmon branch approaches this condition.

We highlight that this mass is higher than the values of previous work [109], even when taking into account the error in the data and fitting procedure. In performing similar experiments on a number of samples, a convincing trend supporting this enhancement develops. This is shown in Fig. 4.13. The mass enhancement is reproduced in multiple samples when moving to higher charge densities. An almost linear relationship can be forged between m_e^* and n in low density regime where $n < 6 \times 10^{11}$ cm^{-2} . Beyond this, the value of m_e^* appears to saturate but remains well enhanced over the band value. These results are surprising, as the effective mass of charge carriers showing a distinct dependence on n was concluded to be as a result of correlation mediated renormalisation. Indeed, it is not expected according to Kohn's theorem, which states that excitations under uniform radiation are insensitive to interaction effects[113], to pick up such effects in CR. A possible explanation is non-parabolicity of the conduction band. However, the non-parabolicity in Wurtzite ZnO is predicted to be smaller than zinc-blende structures such as AlGaAs/GaAs [114] where effect of mass enhancement with increasing n is much less pronounced[115]. Hence, it is considered that this alone can not account for the large change in m_e^*.

While a full understanding of this behaviour remains an endeavour for future work, we note that it has been theoretically considered that the effects of strong electron interactions may be unveiled in the presence of non-parabolicity of the band structure[116]. As introduced earlier, the correlation effects are expected to be significantly stronger in MgZnO/ZnO than that of AlGaAs/GaAs 2DES due to the smaller dielectric constant and larger effective mass. We therefore speculate that in the presence of weak non-parabolicity some effects of coulomb interaction are indeed picked up in the plasma resonance data. This speculation is quantitatively supported by the following framework:

In previous work on AlGaAs/GaAs heterostructures, the finite increase in effective mass as measured by CR was attributed to the non-parabolicity of the conduction band[115] using a **k**·**p** model including three bands. As per the model presented in that work, the dispersion of the conduction band

may be written as,

$$E(k) = \frac{\hbar^2 k^2}{2m_e^*} + \frac{K_2}{E_g}\left(\frac{\hbar^2 k^2}{2m_e^*}\right)^2 \tag{4.16}$$

The parameter, K_2 is a coefficient controlling the size of the energy dependent non-parabolicity and E_g is the band gap The behaviour of m_e^* with energy is therefore given by

$$\frac{1}{m_e^*(E)} = \frac{1}{m_0^*}\left(1 + \frac{2K_2}{E_g}E\right) \tag{4.17}$$

In this expression, E is the energy of the electrons. It was established that for GaAs the value of K_2 was roughly -1.4. We note that the effects of polaron coupling (which also affects the non-parabolicity) are expected to be weaker in MgZnO/ZnO compared to AlGaAs/GaAs as the LO-phonon energy is larger than GaAs, and the cyclotron energy is substantially reduced due to the heavy effective mass. Moreover, the experimental results probe very low magnetic fields where the cyclotron energy remains small.

For a 2DES formed at a heterointerface, the energy E of electrons at E_F at low temperature is composed of two contributions: the kinetic energy, E_F, and the confinement energy, E_z, due to the finite extent of the wave function in the z-direction. Both of these energies are dependent on the charge density. Using the Fang Howard[117] variational wave function $\phi(z)$ approach, it is possible to estimate E_z for the first subband:

$$\phi(z) = \left(\frac{b^3}{2}\right)^{1/2} z\, e^{-bz/2}. \tag{4.18}$$

Here, $b = \left(12 m_z e^2 (n_{dep} + 11/32 n_s)/\varepsilon_{ZnO}\hbar^2\right)^{1/3}$. We use the following material parameters: $\varepsilon_{ZnO} = 8.5\varepsilon_0$, $m_z = 0.3 m_0$, $n_{dep} = 0$. This leads to

$$E_z = \frac{\hbar^2 b^2}{8 m_z}. \tag{4.19}$$

From the above parameters one may simulate the effective mass dependence on the carrier density via calculation of the total energy of electrons. The carrier density dependencies of both energy terms are given by $< E_z >= n^{2/3} \cdot 3.37$ meV and $E_F = n \cdot 0.795$ meV, where n is taken in units 10^{11} cm^{-2}. Returning to the experimental data given in Fig. 4.13, the best fit to the experimental data is achieved with a value of $K_2 = -15.2$ and the lower estimate is no less than $K_2 = -12$, as shown as the dashed line in the figure. For reference we include the trend predicted by $K_2^{bulk} \sim -1.2$, which is an experimental reported value of the non-parabolicity in bulk ZnO[114]. It is clear that the estimated K_2 values fro the experimental data obtained in this work are an order of magnitude larger than in GaAs.

The above considerations suggest that indeed non-parabolicity effects alone may not account for the observed magnitude of the enhancement of the effective mass. Further advances in spectroscopy methods on the MgZnO/ZnO system, specifically designed to incorporate interaction effects, are required to conclusively deconvolute the behaviour presented above.

Another resonance technique targets the spin degree of freedom of charge carriers - electron spin resonance (ESR). During this thesis, we have performed ESR measurements on the MgZnO/ZnO 2DES in collaboration with S. Teraoka, A. Oiwa and S. Tarucha of the University of Tokyo. The results have been published in a dedicated work as Ref. [118]. The main outcomes of this work are presented below. The

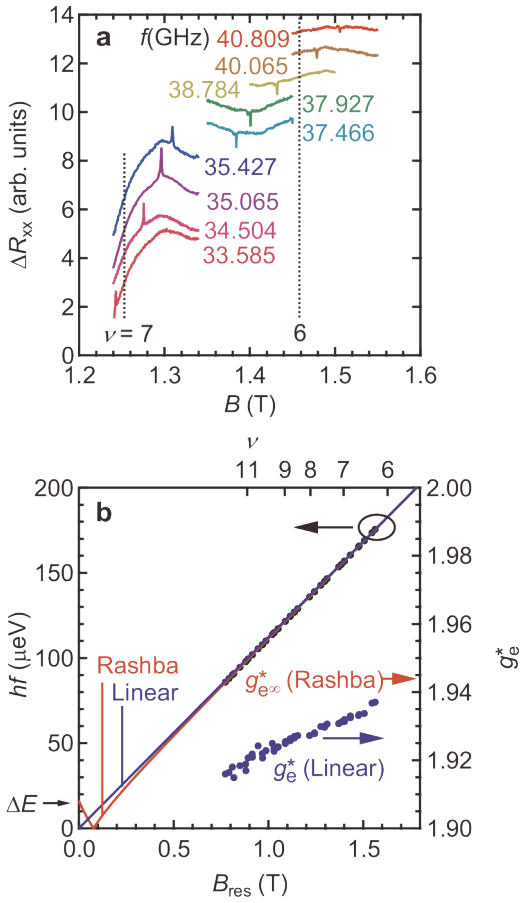

Figure 4.14: Resistively detected electron spin resonance in a MgZnO/ZnO heterostructure. **a** R_{xx} as a function of B for a range of microwave frequencies. Resonance appears as a sharp peak or dip. **b** plotting of the resonance frequencies as a function of B_{res}. The values of g_e^* as deduced from the resonance energies is shown on the right axis, and a linear interpolation of resonance data points is shown (blue). Including a finite zero-field spin splitting due to Rashba spin-orbit interaction yields the red curve, with g_e^* = 1.94. Adapted from Ref. [118].

technique utilised is termed resistively detected ESR. To detect ESR, the double lock-in technique is used which involves exciting the 2DES with a low frequency current, while simultaneously modulating the incoming rf-radiation at a second, different frequency. The first lock-in is tuned to the frequency of the alternating current while the second is tuned to the modulation of the rf-radiation. The 2DES is exposed to microwave radiation ($f \approx 30$ GHz) at low temperature and the longitudinal resistance of the sample is measured both with and without radiation. At resonance, heating of the 2DES occurs which leads to a change in resistance. This may be picked up as ΔR_{xx} in the lock-in measurements[119]. With applying a magnetic field the Zeeman coupling is enhanced as LL develop. When this energy equals that of the impending radiation resonance under the condition

$$hf = g_e^* \mu_B B \tag{4.20}$$

where f is the frequency of the rf-radiation, a spin flip excitation of electrons occurs between spin split LL. The resonance condition is signified by a spike or dip in ΔR_{xx}, and its width has a dependence on the transverse spin relaxation time (T_2). Some exemplary traces are shown in Fig. 4.14**a**.

Figure 4.14**b** plots the resonance conditions as a function of frequency and B_{res}. Calculating g_e^* as per Eq. 4.20 using the f and B_{res} of the data gives the values plotted on the right hand axis in blue. It clearly establishes that the *g*-factor is on the order of 2, which is very close to the bulk value of ZnO. However, it can be seen that g_e^* systematically trends to lower values when going to lower B_{res}. This signifies that E_z varies non-linearly with B. As interaction terms such as exchange are not considered to be probed in ESR measurements [120], another origin for a non-linear Zeeman coupling likely exists. One possibility is spin-orbit interaction within the 2DES. While in dilute MgZnO/ZnO heterostructures the tell-tale signs of strong spin-obit interaction, weak anti-localisation and beating in Shubnikov-de Haas oscillations, are not clearly observed nor have been reported, a finite magnitude of such interactions can not be completely neglected. An alternative fitting procedure incorporating a finite Rashba splitting at zero field ($2\alpha k_F = 16$ μeV, ΔE in the figure) gives a better fit to the data. We refer to the dedicated publication for more details on this result [118], including the fitting procedure and possible spin-orbit interaction mechanisms. The analysis performed ultimately shows that the spin-orbit interaction is very weak in the heterostructure under investigation. It also confirms the bulk g-factor of the electrons is applicable for the case of 2D electrons. For the remainder of this thesis, spin orbit interaction is ignored. Exploring this however as a function of charge density, into the higher x context regime where the electric fields within the heterostructure are enhanced and hence potentially spin orbit coupling strength, is an exciting experiment for future work.

We finally note that this result unveils some intriguing aspects of ESR in MgZnO/ZnO heterostructures. Firstly, in AlGaAs/GaAs heterostructure ESR measurements, the resonance was only achieved when the chemical potential is in between spin split LL[120]. Here however, resonance is observed both in the vicinity of odd and even filling factors. This observation therefore suggests that some underlying spin polarisation of the 2DES exists, the origin of which is not currently understood. We note that the low temperature of these measurements should exclude thermally excited carriers polarising the 2DES. Secondly, the direction of R_Δ is different for the resonances near odd (which shows a peak) and even (which shows a minimum) fillings. While a peak is typically observed and is related to heating of the 2DES, a minimum is more obscure. It appears to suggest the 2DES is cooled at the resonance position. These facets will be explored in detail in a future publication (A. V. Shchepetilnikov, Yu. A. Nefyodov, I. V. Kukushkin, J. Falson, Y. Kozuka, D. Maryenko, A. Tsukazaki, M. Kawasaki, and J. H. Smet, *in preparation*).

4.3 Quantifying quality

In Chapter 3, the focus was on rather superficial means of determining sample quality; surface roughness or surface defect density, combined with simple electrical measurements such as the zero field electron mobility (or alternatively, $\tau_{tr} = \mu m_e^*/e$). It is easy to understand however that physical characterisation such as AFM or optical microscopy gives limited information about the quality of the underling 2DES. Indeed, the surface morphology as measured via AFM shows little deviation between samples even when the film thickness, stoichiometry or growth rate is modified. This was also evident in the results discussed in section 3.18 where the anneal temperature of films was modified, which had a drastic impact on mobility but negligible effect on the surface morphology. In this section we explore more deeply the concept of 2DES quality through transport and scattering times analysis beyond τ_{tr}.

As mentioned, transport measurements at ^{3}He temperatures are performed for each sample grown as a means for directly screening and probing the quality of the 2DES. Beyond measuring the zero field

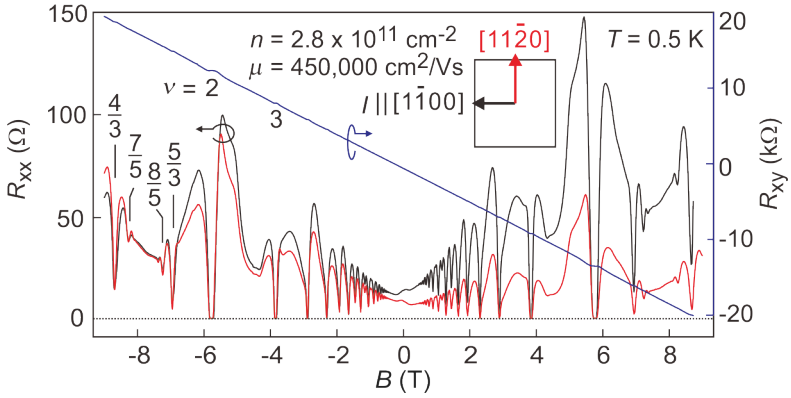

Figure 4.15: Magnetotransport of a MgZnO/ZnO heterostructure as measured at ^{3}He temperatures for characterisation purposes.

resistance, significant information about the quantised LL spectrum may be gained with the application of a magnetic field. As introduced in chapter 2, the integer and fractional quantum Hall effects should emerge in sufficiently high quality samples at sufficiently low temperatures. A typical trace performed in van der Pauw geometry is shown in Fig. 4.15. This is raw data (non-symmetrised resistance - not resistivity) measured from a sample which is contacted at its four corners with Indium solder. No annealing of the contacts is required for an ohmic contact. This was measured using a 1 μA DC current via resistance bridge. As can be seen, the transport is highly symmetric in both polarities of the magnetic field and similar between the two crystal directions (red and black traces) measured. The Hall resistance is quantised at the correct values. This is unsurprisingly considering the Landau Büttiker model[16] of the quantum Hall effect where edge channels dominate. This should prohibit mixing of R_{xx} and R_{xy}. A finite difference in resistance occurs between the two longitudinal crystal directions. This is occurs sample-to-sample in a random manner, and therefore is likely not due to anisotropy in mobility or quality, but rather due to the dimensions of the sample which are often not ideal squares.

The transport is rather rich considering the relatively high temperature (T = 500 mK). Shubnikov - de Haas oscillations may be resolved from $B \approx 0.4$ T. In addition to the emergence of the integer quantum Hall effect from $B \approx 1$ T, robust fractional states of ν = 5/3 and 4/3 are observed flanking ν = 3/2, and while still not zero resistance, their presence at temperatures as high as 500 mK suggests they have an activation energy on the order of 1 K. Higher order fractional states at ν = 8/5 and 7/5 are seen to be developing. The appearance of such states, as well as the width of integer quantum Hall states is used in a complimentary form to the measured mobility to determine the quality of sample. A slight complication occurs with changing the charge density between samples. As explored later in Chapter 5, the stability of the fractional quantum Hall states centred on $\nu = 3/2$ (which, given the maximum magnetic field of B = 9 T of the cryostat used for characterisation, are typically the only fractional states which are revealed) show a strong dependence on the ratio of E_z/E_{cyc}. This ratio changes dramatically in the MgZnO/ZnO system due to interaction effects renormalising the spin susceptibility of the 2DES (as explored in section 4.2.1). Therefore, using the absolute activation energy of these states as a measure of quality is a not a wise idea.

A parameter which is indeed seen to have an impact on the quality of 2DES is the thickness of the MgZnO capping layer. This degree of freedom was explored from a growth point of view in section 3.14, where it was seen that the mobility of samples with $t \geq 60$ nm appeared to only show modest gains

with increasing the thickness up to t = 240 nm. In Fig. 4.16 we explore this further by lowering the temperature and the charge density. As established earlier, low charge density samples are particular sensitive to the effects of impurity scattering due to the reduced ability of the 2DES to screen disorder. The same may be expected from surface defects which impose a long-range disorder of the 2DES. In this section a range of MgZnO thickness films were grown and their transport evaluated at low T. The Mg flux is again kept constant and the films were grown on consecutive days, under identical Zn/O_3 ratios. The ZnO buffer layer thickness is identical, and the resistivity of the substrates for each film is extremely close to one another. The growths are nominally identical, barring the MgZnO thickness. These differences are analysed through a number of means. Firstly, in Fig. 4.16**a** the discrete points as a function of t contain the information of charge density (left axis) and both transport and quantum scattering times. In agreement with Fig. 3.14, despite the growth conditions being nominally identical, with increasing t, the charge density that accumulates at the heterointerface steadily decreases. In the range of thickness probed in this figure a peak in n was not observed. However, the highest density was indeed the thinnest sample grown at t = 120 nm, which is in fairly good agreement with the results from the previous section. The reproducibility of this result suggests that similarities exist between the origin of charge carriers in the MgZnO/ZnO 2DES and remote modulation doped AlGaAs/GaAs heterostructures. There, the number of charges at the heterointerface is dependent on the distance and density of dopants[76]. Here, a similar dependence occurs by placing the surface further away from the heterointerface. If the mobile charges are originating from the surface, it may be anticipated that the charged defects left over have an impact on the scattering of confined electrons in the 2DES. It is therefore appropriate to explore τ_{tr} and τ_q as a function of t. We note that both of these are evaluated at $T \leq$ 100 mK following an evaluation of the effective mass of each heterostructure. The result supports the above hypothesis. Firstly, when reducing t to 60 nm, both the transport scattering time and quantum scattering time suffer dramatically. This is likely as a result of the lower n of these samples, compared to those in Fig. 3.14. Increasing t from there steadily increases these scattering time, with ultimately a τ_{tr} of 200 ps being achieved and τ_q exceeding 15 ps for the thickest film in this series. For the case ofτ_{tr} = 200 ps, the corresponding mobility in AlGaAs/GaAs heterostructures would be roughly 5×10^6 cm^2 V^{-1} s^{-1} . What is interesting though is this ratio which is seen to get smaller when lowering t of the capping layer. It is widely observed in AlGaAs/GaAs heterostructures that the ratio of τ_{tr}/τ_q is over 10 [108]. This is considered a consequence of the set back of the remote doping relative to the quantum well. As explained earlier in this thesis 2.2, the angle of scattering events determines their relative weighting in the scattering times. Remote doping does not inflict a large change in angle of the electron wavevector, and hence is mostly reflected in τ_q, which leads to a large ratio. The reduction of this ratio, however, indicates that the scattering centres are being brought closer to the 2DES and affect τ_{tr} more equally. This was similarly explored in Ref. [121] in a gated AlGaAs/GaAs heterostructure, where indeed surface charges were seen to significantly affect the scattering times in the 2DES. This therefore fits the hypothesis that charged defects exist on the surface of MgZnO/ZnO heterostructures and that they have a detrimental effect on scattering rates.

We now turn to the magnetotransport presented in Fig. 4.16**b**. This transport was taken when the sample is perpendicular to the magnetic field (θ = 0°). The transport around ν = 3/2 for the four films with different t MgZnO at $T \approx$ 40 mK as a function of filling factor. The transport is seen to vary dramatically between the films. A good qualitatively agreement with the trends identified in panel **a** is observed. For the film with t = 60 nm, even the most fundamental fractional quantum Hall states of ν = 5/3 and 4/3 are absent. The integer quantum Hall minimum are also much wider, indicating

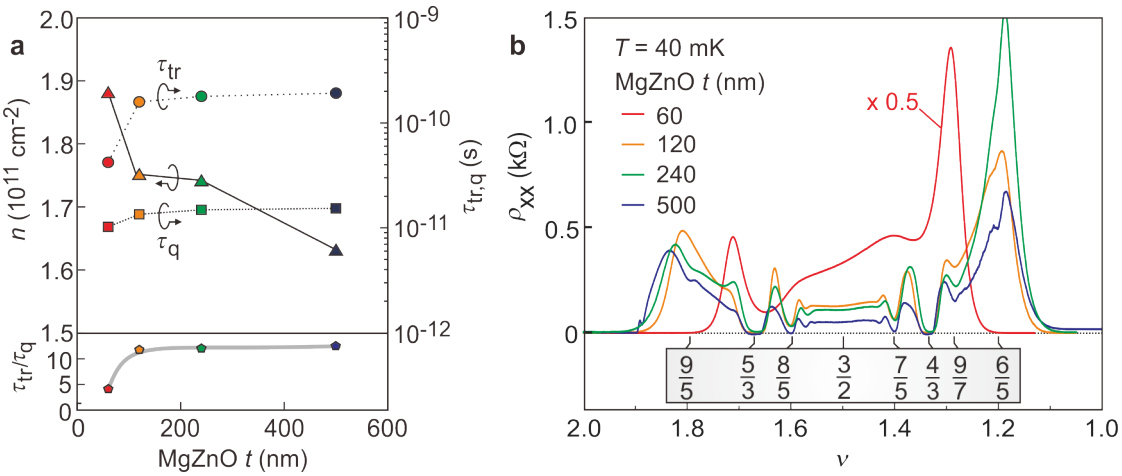

Figure 4.16: **a** Charge density, transport scattering time and quantum scattering time of four films as a function of MgZnO thickness. **b** Resistivity of four MgZnO/ZnO films with different MgZnO thickness as a function of filling factor around ν = 3/2. Prominent fractional quantum Hall states are noted.

more localised states in the DOS. For the films $t \geq 120$ nm, fractional quantum Hall states are suddenly evident and strong. The most fundamental fractions at ν = 5/3 and 4/3 are seen to be zero resistance for all films. Differences between these films becomes evident only in the higher order fractions. For example, the states of ν = 8/5 and 7/5 show much lower resistance minima in the t = 500 nm sample compared to the 120 nm film. While not so relevant, we note that the activation energy of these states is Δ = 270 and 160 mK in the 500 nm film and 160 and 85 mK in the 120 nm film. The 240 nm film shows similar activation energies as the 120 nm film. In addition, the thickest sample begins to display fractional states at ν = 9/7, 6/5 and 9/5. The next thickest film, t = 240 nm is arguably the next best sample due to the minimum associated with the ν = 9/7 state being resolvable, although its difference with the t = 120 nm film is not so acute. This is an important observation both in terms of advancing transport quality and structure design. In future work, when it is possible to utilise a deep 2DES (for example regular transport measurements), these should be pursued. However, this puts limitations on the ability to gate structures (as the electric field is weakened through increasing the distance) and the ability to create mesoscopic devices which require local density modulations by through fine lithographically defined structures.

An overview of scattering times measured for MgZnO/ZnO as a function of charge density is shown in Fig. 4.17. The transport scattering time for the data marked as this thesis is calculated from the mobility at low temperature after measuring the effective mass. The quantum scattering time is quantified from analysing the Shubnikov - de Haas oscillations at $T < 100$ mK, as per the analysis presented above in Fig. 4.9. Data points taken from Ref. [83] are included and plotted twice, once with the transport scattering time calculated from the band mass, and again using the tendency of mass enhancement as identified in Fig. 4.10. This only affects the data points quantitatively and not qualitatively. Some more recent samples where the quantum scattering time has also been measured are included. The peak in transport scattering time occurs for $n \approx 1.5 \times 10^{11}$ cm^{-2} , exceeding values of 300 ps. The quantum scattering time is also seen to increase with reducing n at a relatively reduced rate. This value however approaches 20 ps for the highest mobility samples presented in the plot.

In panel **b** we show the ratio of scattering times (τ_{tr}/τ_q) as a function of n for the available data points and highlights the trend of the superior enhancement of τ_{tr} with reducing n. The increase in

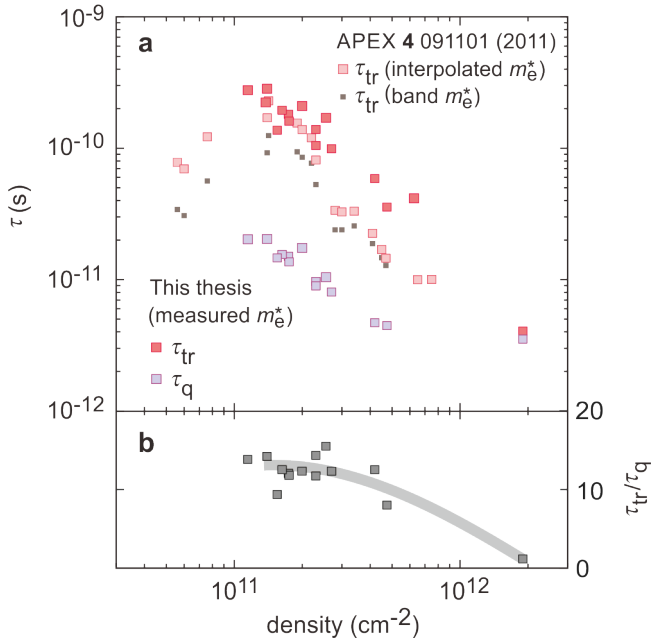

Figure 4.17: **a** Transport and quantum scattering times as a function of charge density for MgZnO/ZnO heterostructures. MgZnO/ZnO data points are a combination of those published in [83] and points newly presented in this work. For the former, the transport scattering time based on both the measured effective mass and band effective mass is shown. **b** The ratio of τ_{tr}/τ_q as a function of density.

τ_{tr} and τ_q signifies that the overall scattering rate including all mechanisms is falling. This is not surprising as the Mg content simultaneously falls, which in turn reduces interface roughness and/or alloy scattering. The drastic reduction of such short range scattering events explains the superior increase in τ_{tr} with reducing n. The presence of strong short range scattering is supported by the small ratio of roughly 1 at high n. This ratio however dramatically increases when moving to lower charge density with τ_q remaining relatively suppressed when entering the dilute charge density regime. The ultimate limitation on this value may be related to defects on the surface of MgZnO, which was implied by the experiments presented in Fig. 4.16. Therefore, further improvements may be achieved by mitigating such effects.

4.4 Material comparison

We conclude this section of this thesis with an inter-material comparison of scattering times. This aims to put the results of this thesis into perspective by a providing a comprehensive overview. The full data set is displayed in Fig. 4.18. Both τ_{tr} and τ_q are plotted as a function of charge density for various two-dimensional systems, including the AlGaAs/GaAs 2DES [63, 108, 122], AlGaAs/GaAs 2DHS [95, 123], AlGaAs/AlAs 2DES [124], AlGaN/GaN 2DES [125–127] and the $LaAlO_3/SrTiO_3$ [97]. Graphene is excluded due to the difficulty in determining a mobility as a result of the Dirac nature of electrons and the small size of samples (where the transport becomes ballistic in high mobility devices). We do note however that high quality suspended graphene devices[128] are considered to have a mobility on the order of 10^6 cm^2 V^{-1} s^{-1} and graphene on boron nitride on the order of 10^5 cm^2 V^{-1} s^{-1} [129], putting these amongst the highest quality platforms available. At the point of writing this thesis the mobility

of topological insulators remains relatively low, with reports of 30,000 cm^2 V^{-1} s^{-1} in HgTe quantum wells [130] (with conference presentations reporting higher, H. Buhmann, *et al.*, *High Magnetic Fields in Semiconductor Research*, Panama City beach, August 2014) and about 3,000 cm^2 V^{-1} s^{-1} in $BiSbTeSe_2$ [131]. The MgZnO/ZnO samples grown throughout this thesis are shown as red or pink squares. The red squares were as a result of the first generation of ozone-grown samples and were published in Ref. [83]. The bold red squares are recent developments. Though somewhat incremental, they lie above the pink data points delving into the higher charge density regime. This suggests the quality of the heterointerface is increased.

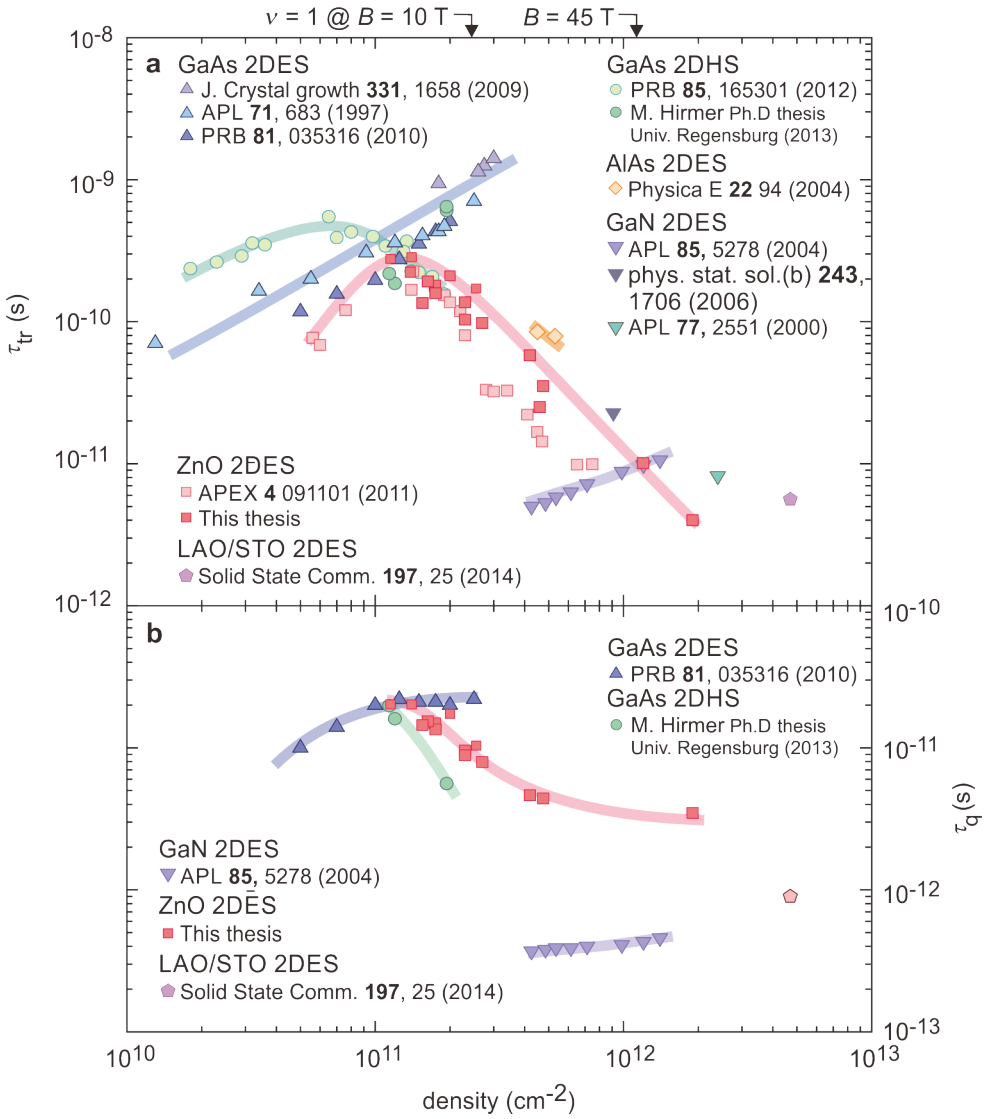

Figure 4.18: Inter-material comparison of transport and quantum scattering times as a function of charge density for prevailing heterostructure confined 2D systems. MgZnO/ZnO data points are a combination of those published in [83] and points newly presented in this work. The remaining references are: AlGaAs/GaAs 2DES [63, 108, 122], AlGaAs/GaAs 2DHS [95, 123], AlGaAs/AlAs 2DES [124], AlGaN/GaN 2DES [125–127] $LaAlO_3/SrTiO_3$ [97]. On the upper axis the charge density corresponding to achieving $\nu = 1$ at $B = 10$ T and 45 T are shown. Coloured lines are intended as visual guide lines to group data sets.

As introduced in section 2, the use of τ_{tr} involves scaling μ by m^* of the charge carriers. This can be a complex task for systems such as AlGaAs/GaAs based 2DHS or AlGaAs/AlAs 2DES, where effective mass can show a strong dependency on n, or other parameters (such as valley degeneracy of quantum well width). While we have strived to incorporate each individual sample's effective mass in the calculations, slight quantitative errors may occur exist. However, in the spirit of comparison, the plot is a valid representation.

We have endeavoured to include reports of state-of-the-art quality samples in the plot. Firstly, it comes as no surprise that the AlGaAs/GaAs 2DES reigns supreme in both τ_{tr} and τ_q criteria. The maximum mobility of the AlGaAs/GaAs 2DES now reaches above 36 $\times$ 10^6 cm^2 V^{-1} s^{-1} , and the quantum scattering time beyond 20 ps. Explicit reports of τ_q are relatively scarce, therefore we use Ref. [108] which shows a strong ν = 5/2 state (with activation energy Δ = 310 mK) suggesting quite high sample quality. The values of τ_q presented in that work also match that of Ref. [63]. Of recent years, the AlGaAs/GaAs 2DHS has too displayed significant improvements due to advances in low-power consumption carbon filament technology [132]. This system now shows similar scattering times to the AlGaAs/GaAs 2DES as a result. That said, the transport arguably remains relatively poor in comparison with the AlGaAs/GaAs 2DES [103]. Significant efforts have been paid to finding a link between the scattering times presented and the quality of transport realised in many pieces of work. For example, in this plot data points from ultra-high mobility AlGaAs/GaAs heterostructures are included from Ref. [63]. Within that work however, it is highlighted that the transport scattering time is not a good predictor of the quality of fractional quantum Hall features. In later sections of this thesis we attempt to contribute to this discussion (see section 5). Similarly, it has been shown that even in low mobility samples a fully developed ν = 5/2 fractional quantum Hall ground state may develop if the modulation doping scheme is tailored [62]. It is noted that despite the MgZnO/ZnO 2DES displaying a peak τ_{tr} that is one order of magnitude lower than the AlGaAs/GaAs 2DES, τ_q is seen to be comparable. We also note that the rich array of ground states identified in the next chapter rivals that of AlGaAs/GaAs 2DES. We therefore speculate the rich transport and high τ_q is a result of a lack of (intentional) modulation doping in MgZnO/ZnO heterostructures combined with the ability to mitigate the effects of surface potential fluctuations through heterostructure design.

We conclude the MgZnO/ZnO 2DES displays characteristics of strong electron correlation effects while existing in a niche parameter space where the spin susceptibility is both large and a tunable degree of freedom. Moreover, this is character is achieved concomitantly to sample quality comparable to the cleanest semiconductor materials in existence.

Chapter 5

Correlated electron ground states in MgZnO/ZnO heterostructures

This chapter focuses on the ground states which are realised in MgZnO/ZnO heterostructures. Until now, we have mostly been focusing on the physical characteristics of heterostructures at temperatures of T = 500 mK. This has been accessed through the use of ^{3}He cryostats, which rely on the evaporation of ^{3}He atoms from a liquefied phase. Key to revealing the ground states of the 2DES is to achieve even lower temperatures, as the effects encountered are activated at temperature scales of $\approx$ 100 mK. Therefore to clearly resolve the details, temperatures much lower than this are required. To access such temperatures, a dilution refrigerator is used [133]. The process involves dissolving a "concentrated" liquid phase of ^{3}He isotopes into a "dilute" phase of $\approx$6% ^{3}He in ^{4}He liquid through the closed circuit circulation of ^{3}He species. Both of these phases act as Fermi liquids at low temperature due to the presence of the Fermion ^{3}He atoms. However, the superfluidity of the ^{4}He atoms modifies the interaction between ^{3}He atoms in the dilute phase, and hence effective mass. This results different Fermi temperatures of the concentrated and dilute phase. In equilibrium their chemical potentials must be equal, and hence a finite solubility of the dilute phase occurs. The equilibrium may be disturbed through the external pumping of the system and evaporating ^{3}He species from the dilute phase. In doing this, an osmotic pressure develops, and ^{3}He atoms are forced from the concentrated phase to the dilute, traversing the phase boundary to replace those lost. This process of adding atoms to the dilute phase increases the entropy of the system, which must be compensated by the absorption of heat from the environment. This is where we place the sample, at the coldest part of the apparatus. Two varieties of dilution refrigerator were used throughout the course of this thesis. The most extensively utilised apparatus was an Oxford Instruments top-loading into the mixture cryostat at the Max Planck Institute in Stuttgart, Germany. The system has numerous advantages. Firstly, it has a low base temperature of $T \approx$ 15 mK with the sample located within the mixing chamber. It is therefore exposed to the liquid mixture during measurements. This, in combination with effective heating sinking of the measurement wires (which too pass through the mixture) ensures excellent thermalisation of the sample. Secondly, this apparatus is equipped with an exceptionally efficient rotation stage. The quasi-frictionless string controlled stage allows rotation of the sample over roughly 90° with minimal heating of the sample or mixture. This is in vast contrast to geared Swedish rotator systems where even a small rotation of a couple of degrees will increase the temperature of the mixture significantly. This increases the time

needed for measurements, as a wait time is required for the mixture and sample to cool. As introduced in section 4.2, the large spin susceptibility is a defining character of the MgZnO/ZnO 2DES. Therefore, in the absence of a vector magnet, rotation of the sample in the magnetic field as shown in Fig. 4.4 is essential for the selective enhancement of E_z.

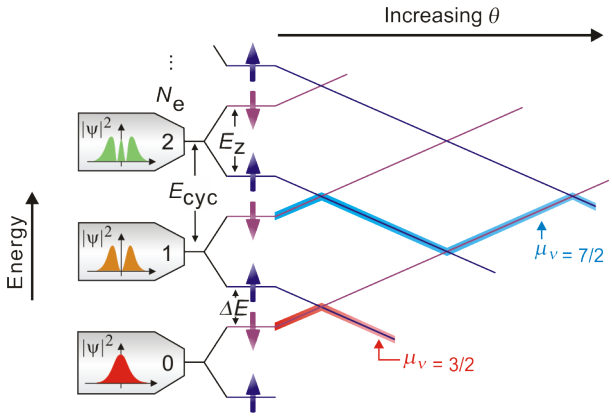

Figure 5.1: A schematic of the energy level arrangement achieved in MgZnO/ZnO heterostructures at high magnetic field. With increasing tilt the levels are seen to cross, and the chemical potential (shown schematically for ν = 7/2 and 3/2) is seen to transition between levels of different spin orientation and orbital character.

A concept explored throughout this section is schematically shown in Fig. 5.1. The selective enhancement of E_z through tilting the sample will induce a level crossing at a certain angle. This is analogous to the schematic presented in 4.5. However, instead of putting the chemical potential at an integer number of filled levels and use this breakdown of the integer quantum Hall effect of measure $g_e^* m_e^*/m_0$, we can put it at partial filling within the extended states of a LL and observe the behaviour the ground states with rotation at low temperature. This means that the electrons at the chemical potential will experience a change in orbital character and spin orientation with rotation. The high $g_e^* m_e^*/m_0$ in MgZnO/ZnO combined with sample rotation should establish a powerful platform for exploring the anticipated dramatic effects on the nature of ground states observed. In this section such phenomenon are explored through transport measurements.

5.1 Magnetotransport of MgZnO/ZnO heterostructures

In this section we explore the base temperature magnetotransport of high quality heterostructures in van der Pauw geometry. Most of the results come from a single state-of-the-art heterostructure (sample 229) and have been accepted for publication (J. Falson, D. Maryenko, B. Friess, D. Zhang, Y. Kozuka, A. Tsukazaki, J. H. Smet and M. Kawasaki, Even-denominator fractional quantum Hall physics in ZnO, *Nature physics, in press*.) The sample is excited by a 10 nA current and has charge density n = 2.3 $\times$ 10^{11} cm^{-2} , mobility μ = 530,000 cm^2/Vs and $g_e^* m_e^*/m_0$ = 1.9. This puts the first coincidence position $j_e = 1$ at very modest tilt angles of $\approx 20^\circ$, and is close to the scenario schematically presented in Fig. 5.1. τ_q is estimated to be roughly 10 ps.The measurements were performed at the Max Planck Institute in Stuttgart in an Oxford top-loading system. The sample is placed within the mixing chamber at a temperature of $T \approx$ 15 mK. In the first sets of figures, the magnetic field is applied perpendicular

to the 2DES, i.e. the sample is not rotated. As shown in Fig. 5.2, Shubnikov - de Haas oscillations begin from B_p = 0.15 T and the integer quantum Hall effect is visible from $B_p \approx$ 0.5 T. The low field transport also shows that beating is absent and only two peaks are visible in the fast Fourier transform presented in panel **b**. These two peaks correspond to the spin split and non-spin split components of the Shubnikov - de Haas oscillations. This result suggests that indeed electrons reside only in the lowest subband and that the spin orbit interaction is weak, in agreement with the results presented in section 4.

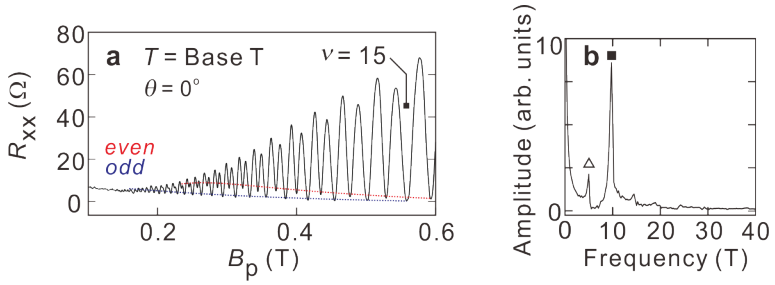

Figure 5.2: **a** Examination of low field magneotransport in a high mobility MgZnO/ZnO 2DES. Minimum corresponding to odd fillings are seen to be resolved before even fillings. A clear beating is absent visually and is supported by the fast Fourier transform of the oscillations in panel **b**. Two peaks are observed, corresponding to spin split (solid square) and non-spin split (open triangle) oscillation frequencies.

We now expand the range of magnetic field and show the full transport down to $\nu = 1$ in Fig. 5.3. This reveals ground states associated with the integer and fractional quantum Hall effects. Focussing first on $4 > \nu > 2$, which traditionally should correspond to transport in N_e = 1, an intriguing pattern begins to develop. Firstly, a number of fractional quantum Hall states are observed, despite the relatively low magnetic field. Most exciting however is the observation of a quantised state at half filling for ν = 7/2, but not for 5/2. Moreover, weak minimum are seen at and around ν = 9/2. This series can not be explained through existing experience and reports in AlGaAs/GaAs nor with the simple schematic presented in 5.1. Throughout the discussion below we endeavour to account for this discrepancy.

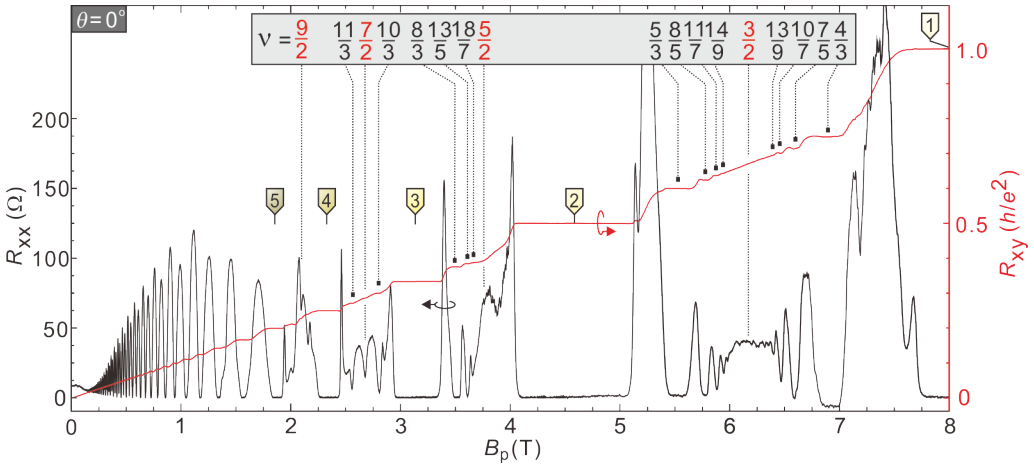

Figure 5.3: Base temperature ($T \approx$ 15 mK) magnetotransport for sample 229. A rich series of integer and fractional quantum Hall states are observed.

Moving to higher field between $2 > \nu > 1$, a rich series of odd-denominator fractional quantum Hall states are observed. This is shown again in 5.4**a**. The half-filling is also compressible. Well defined minimum corresponding to fractions as high order as 14/9 and 13/9 are observed - a testament to the quality of the sample. This transport is associated with the lowest LL, accounting for the appearance of robust odd-denominator states, a compressible half filling, suggesting the behaviour may be well modelled by the composite fermion approach to the fractional quantum Hall effect.

We now rotate the sample to moderate tilt angles of $\theta \approx 40^\circ$ in panel **b**. A dramatic change across the entire partial filling occurs. Most amazingly, the half filling transforms from a compressible sea to a fully developed even-denominator fractional quantum Hall state. Odd denominator states simultaneously weaken significantly. In this trace, all that remains are states at ν = 5/3, 10/7 and 4/3.

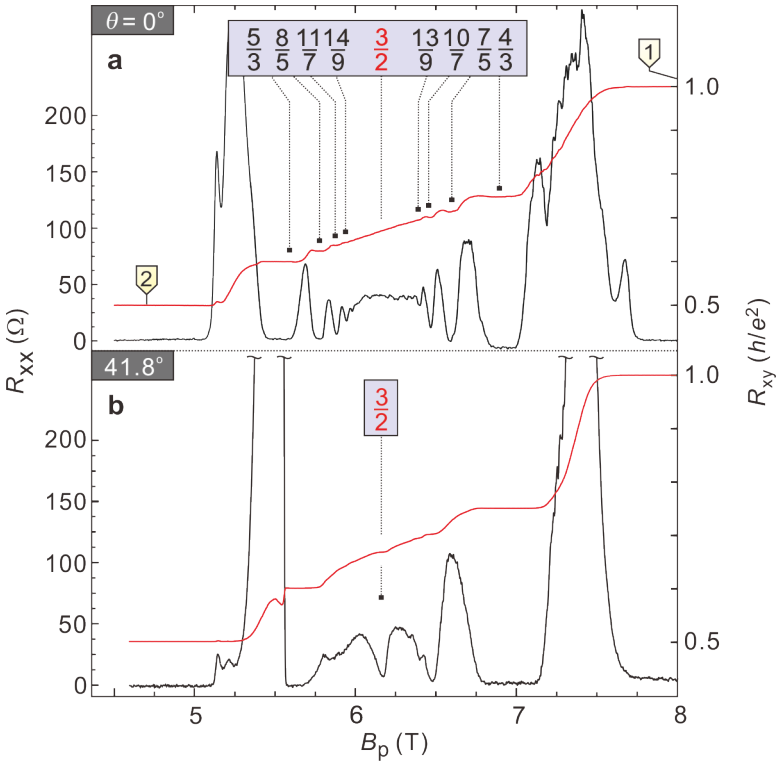

Figure 5.4: Base temperature magnetotransport around ν = 3/2 for sample 229 for **a**, θ = 0° and **b**, rotated to θ = 41.8°. Under tilt, a fully developed even denominator state at ν = 3/2 emerges.

5.2 Odd even-denominator fractional quantum Hall series

The magnetotransport in Fig. 5.3 and 5.4 clearly shows that the ground states observed in the MgZnO/ZnO 2DES are not merely an analogue of a modest quality AlGaAs/GaAs 2DES [39, 62]. The presence of a quantised ν = 7/2 state in the absence of a quantised 5/2 state is particularly poignant [41]. The reverse may be plausible due to the 5/2 state being more robust than the 7/2 state[52]. Such an observation suggests another degree of freedom is in play and affects the series of ground states observed. Hints are instantly available from the behaviour at ν = 3/2 where the half filling may be pushed between a non-quantised to quantised state under rotation. This suggests that the Zeeman energy, which we suspect may influence the orbital nature of electrons, plays a role. This suspicion is

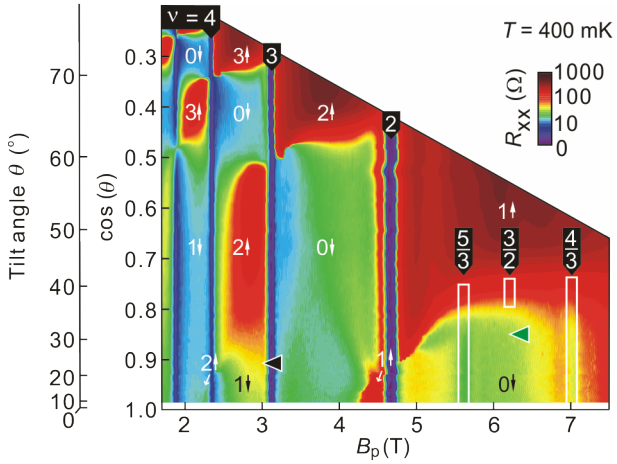

Figure 5.5: Mapping of magnetotransport as a function of tilt up to large tilt angles of $\theta > 70°$. The resistance is seen to oscillate between high (red) and low (blue/green). Each region may be labelled with an orbital number and spin orientation.

further supported by looking at the transport at ν = 9/2. Instead of robust charge-density-wave physics which imparts anisotropy on the magnetotransport as is observed in high mobility AlGaAs/GaAs [58, 59], minimum are observed at filling factors very close to those expected for fractional quantum Hall states.

To orient the discussion of what occurs at low T, it is convenient to raise the temperature and reveal the high/low resistance character of majority/minority spin electrons at the chemical potential. This has the convenient effect of destabilising the fractional quantum Hall ground states, and, as discussed in section 4.6, allows us to label each filling factor a spin orientation and orbital number as a function of tilt, by counting the number of transitions which are observed and comparing that with the ideal single particle scenario. The same transport is shown in Fig. 5.5, but now with the vertical axis as cos(θ), as we want to have greater resolution of the behaviour at low tilt angles. We will continually refer to this transport to guide the discussion in this section.

Initially focussing the transport at ν = 3/2, we can see that one transition is observed from low to high resistance. Returning to the schematic in Fig. 5.1, it can be seen by plotting the chemical potential of ν = 3/2, only a single transition is predicted and this corresponds to a change from $N_e = (0, \downarrow)$ to $(1, \uparrow)$. We now lower the temperature back to base T and fully map the transition in Fig. 5.6 focusing on the transport around $\nu = 3/2$. In this counter plot, fractional quantum Hall states run vertically up the page as the horizontal axis contains only the perpendicular component of the magnetic field. Across this range of tilt angles, the transport displays multiple dramatic changes. Firstly, from low tilt up until $\theta \approx 33°$ (as shown by the green triangle on the vertical axis), the transport shows robust odd-denominator fractional quantum Hall physics centred around ν = 3/2. Features in the resistance of these minimum are observed and will be analysed later in section 5.3. Focusing on half filling it can be seen that the resistance remains largely unchanged up to this same angle. Beyond this angle however, the transport gradually develops into a new regime.

The resistance of half filling $\nu = 3/2$ is shown in Fig. 5.7**b**. This will be contrasted later in the discussion with the behaviour of ν = 7/2 which is shown in panel **a**. As discussed above, the transport remains mostly unchanged up until $\theta \approx 33°$ and this too is reflected in the plots of the resistance at half filling as shown in the figure shown as the blue (baseT) and red (400 mK) lines. Beyond this

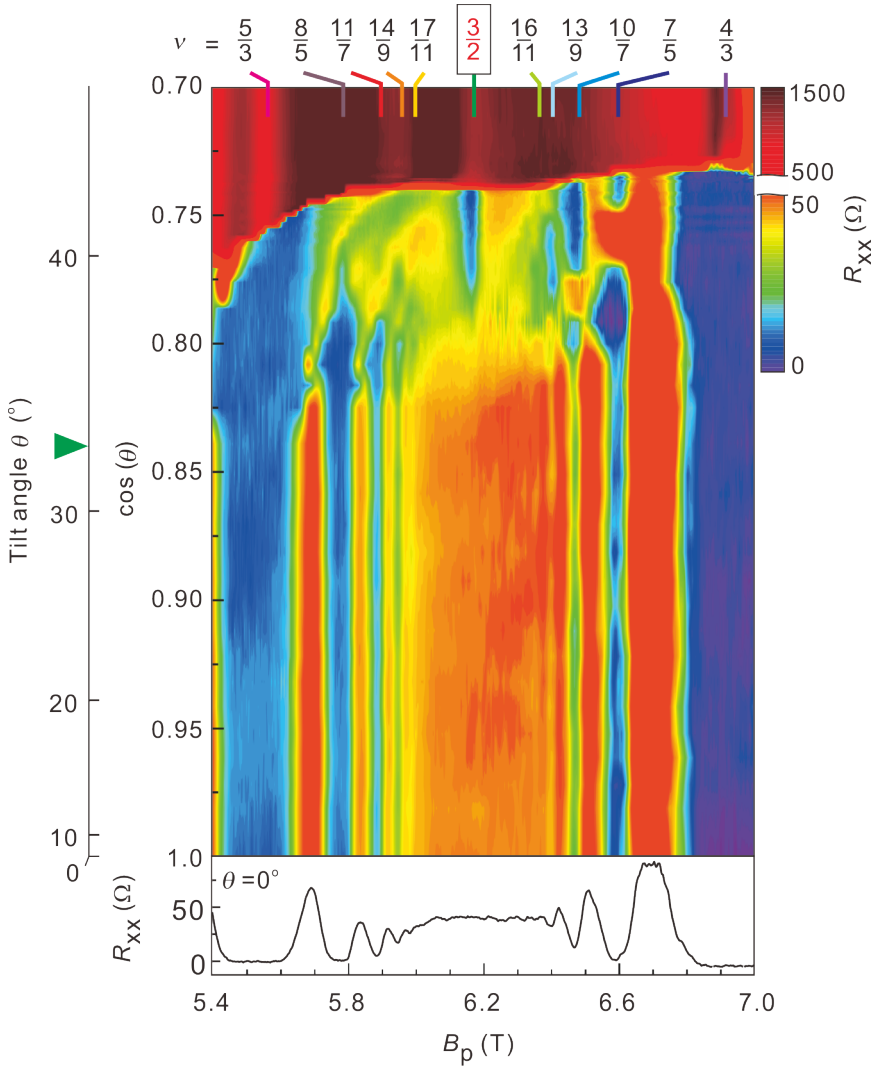

Figure 5.6: Mapping of magnetotransport around $\nu = 3/2$ as a function of tilt up to $\theta = 45°$. The bottom panel shows a line trace of the transport for $\theta = 0°$. Beyond $\theta \approx 33°$ (green arrow) the resistance at half filling begins to fall and the even denominator ground state emerges. Oscillatory behaviour is observed for odd denominator states and is explored in section 5.3.

angle however the behaviour of the resistance at $T = 400$ mK and base temperature begins to deviate. When plotting the resistance for T = 400 mK, the resistance begins to rise from $\theta > 33^\circ$ but for the base temperature cut, it begins to fall. Windows of transport around half filling at base temperature are also shown in the insets of this figure. It can be seen that at high tilt the fall in resistance at base temperature is associated with the minimum of the quantised fractional quantum Hall state emerging. Returning to the orbital assignments of transport regimes identified in Fig. 5.5, the high tilt transport should correspond to ($N_e = 1, \uparrow$). This assignment may account for the contrasting behaviour observed, for at high T it is empirically shown that the resistance is higher when the partially filled level has majority spin, and for base T, an $N_e = 1$ orbital assignment may, within the realm of prevailing knowledge, accommodate an even-denominator ground state.

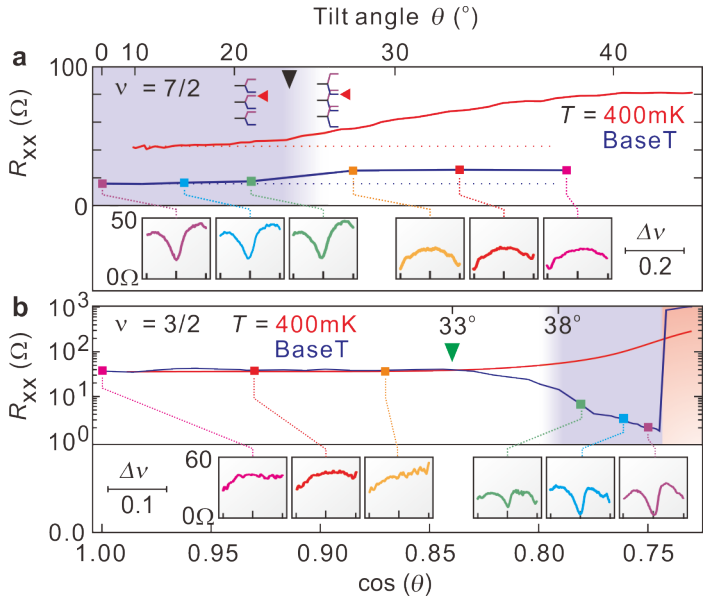

Figure 5.7: Comparison of the behaviour around half filling for **a** 7/2 and **b** 3/2 for both T = base T and 400 mK as a function of tilt. The purple shaded regions correspond to the range of tilt angles where the half filling is quantised. Small panels show the transport around half filling as a function of filling factor.

At even higher tilt ($\theta \approx 42^\circ$) the transport displays a second transition. Suddenly the resistance rises and the quality of fractional quantum Hall states suffers. Indeed, the unambiguous identification of quantised states in this regime is not possible, although weak minimum remain at prominent fractional fillings. A new phase apparently appears as a result of the loss of spin degeneracy (at high tilt the 2DES is fully spin polarised). While at this point in time this transition is not fully understood, it will be discussed later in section within the current limits of understanding (see section 5.4).

We next discuss the observed ν = 7/2 state. This transport appears rather conventional - a quantised half filling flanked by weak odd-denominator states. We highlight however, that despite the observation of a quantised ν = 7/2 state in AlGaAs/GaAs 2DES [41], concomitant observation of the 10/3 and 11/3 states has until now remained elusive. Just recently has the 10/3 state been unambiguously observed [134]. The series presented here is therefore reminiscent of the 8/3, 5/2, 7/3 series often seen in the lower spin branch of the second LL in AlGaAs/GaAs 2DES. Returning to the single particle energetics schematic of 5.1, it too suggests that ν = 7/2 has $N_e = 1, \downarrow$ character at zero tilt. This is confirmed in the high temperature transport in Fig. 5.5. The ν = 7/2 state is therefore highly likely to be mediated by

$N_e = 1$ orbital character and an analogue of that seen in AlGaAs/GaAs 2DES. Comparing its behaviour to the $\nu = 3/2$ state in Fig. 5.7 supports the prevailing hypothesis of the importance of the $N_e = 1$ orbital character of electrons at the chemical potential. In panel **a** the behaviour at ν = 7/2 is shown as a function of tilt for T = 400 mK and base T. Up until moderate tilt angles of $\theta \approx 23^\circ$ (black triangle in figures) the ground state is properly quantised with a deep minimum. Beyond this, the transport makes a sudden transition to being compressible. Simultaneously, the resistance at $T = 400$ mK too increases, suggesting a change in spin orientation. As discussed above, the exact opposite is observed for ν = 3/2. Indeed, the tilt angles for where these states are quantised never overlaps, suggesting that levels must cross and the orbital character be exchanged for the states to emerge. The swapping of levels and the change of orbital character of electrons at the chemical potential therefore explains this behaviour concisely.

While the single particle energetics picture invoked thus far provides an intuitive and coherent explanation for the stability of the even denominator states at ν = 3/2 and 7/2, it can not explain the lack of ν = 5/2 and apparent observation of a state at ν = 9/2 as seen in the transport. While it is clear that the observation of an even denominator state is inherently linked with the incorporation of $N_e = 1$ character of electrons at the chemical potential, this hypothesis requires more careful scrutiny for the remaining partial fillings. For example, the schematic in Fig. 5.1 suggests 5/2 should be quantised at zero tilt, and 9/2 not so. Here, again it is the high temperature data in Fig. 5.5 which aids the analysis significantly.

Focussing first on ν = 5/2 and on the high/low resistance pattern it can be seen clearly that the resistance at low tilt is "low", corresponding to a down spin orientation of electrons at the chemical potential. The single particle energy schematic of 5.1 however suggests that at zero tilt, the chemical potential for 5/2-filled levels should be majority, and hence the resistance high. Rotating the sample further reveals that while the schematic predicts two transitions, only one is observed at $\theta \approx 60^\circ$. This is from a low to high resistance state, and it is the last transition observed, even when moving to higher tilt angles. From this transition, the partial filling becomes fully spin polarised. It is apparent the first transition is missing for half-filling. A pocket of high resistance on the low field side of ν = 2 is observed and we tentatively attribute this to ($N_e \uparrow$) electrons. If indeed the first transition has occurred for half filling, the character of electrons at zero tilt would correspond to that of $N_e = 0, \downarrow$. Looking at the base T data, this hypothesis seems to fit. Firstly and most obviously, the half filling is not quantised. This is expected of $N_e = 0$ character electrons. Moreover, the odd-denominator states observed at 8/3, 13/5 and 18/7 are unusually robust, when compared to the second LL behaviour in AlGaAs/GaAs 2DES [55]. The latter two fractions are indeed never seen concomitantly to a quantised state at ν = 5/2 in AlGaAs/GaAs . However, the lowest LL accommodates such odd-denominator states happily through the formation of composite fermions. This supports the hypothesis that despite the single particle energy scenario suggesting otherwise, through some mechanisms the orbital character of ν = 5/2 in this heterostructure is anomalously $N_e = 0, \downarrow$. In Fig. 5.8, the base temperature magnetotransport for $6 \leq \nu \leq 2$ is shown. In agreement with the above hypothesis, a quantised state at ν = 5/2 never develops.

Finally, we address the behaviour at ν = 9/2. As the minimum here is weak and shows rather anomalous temperature dependence (see Fig. 5.14 in the next section), a conclusive assignment and account of this behaviour is not possible based on this heterostructure alone. While indeed there is a plateau in R_{xy}, the value of quantisation is not that which is expected ($2h/9e^2$). The high temperature data in Fig. 5.1 gives hints again that a deviation from the behaviour expected from single particle energetics

occurs. Similar to the behaviour at ν = 5/2, it is not possible to conclusively say that for ν = 9/2 the resistance is "high" for low tilt angles. While it may be that a small upturn in resistance occurs, it is somewhat weak and unconvincing. Assuming that the first transition has occurred makes accounting for the ν = 9/2 state plausible. The single particle schematic in Fig. 5.1 gives an orbital character of $N_e = 1, \downarrow$ for electrons if the first transition has indeed occurred. This would be closely related to the constellation of the quantised nu = 7/2 observed and discussed above. However, as can be seen in the base temperature rotation data of 5.8, the minimum at ν = 9/2 is seen to collapse rapidly with rotating the sample. It has mostly disappeared by modest tilt angles of $\theta \approx 11^\circ$. The hypothesis formed above however would suggest that the partial filling has $N_e = 1, \updownarrow$ until tilt angles of $\theta \approx 60^\circ$. The minimum should therefore be robust up until this tilt angle. This is evidently not the case. The minimum is extremely weak to begin with (see. Fig. 5.14) and appears sensitive to an in-plane field. Therefore, in the absence of a clearer observation, we conclude that the emergence of the ν = 9/2 minimum is likely related to a spontaneous swapping of levels and the resulting modified orbital character, but it is easily destabilised by the presence of an in-plane field.

The failure of the single particle energy diagram forces the inevitable conclusion that there are energy terms such as exchange interaction which modify the ideal arrangement described in Fig. 5.1. It seems that the levels spontaneously swap whenever majority spin oriented electrons begin filling a LL. There are pieces of experimental evidence which support such a hypothesis and these will be shown later in section 5.4 and 6.

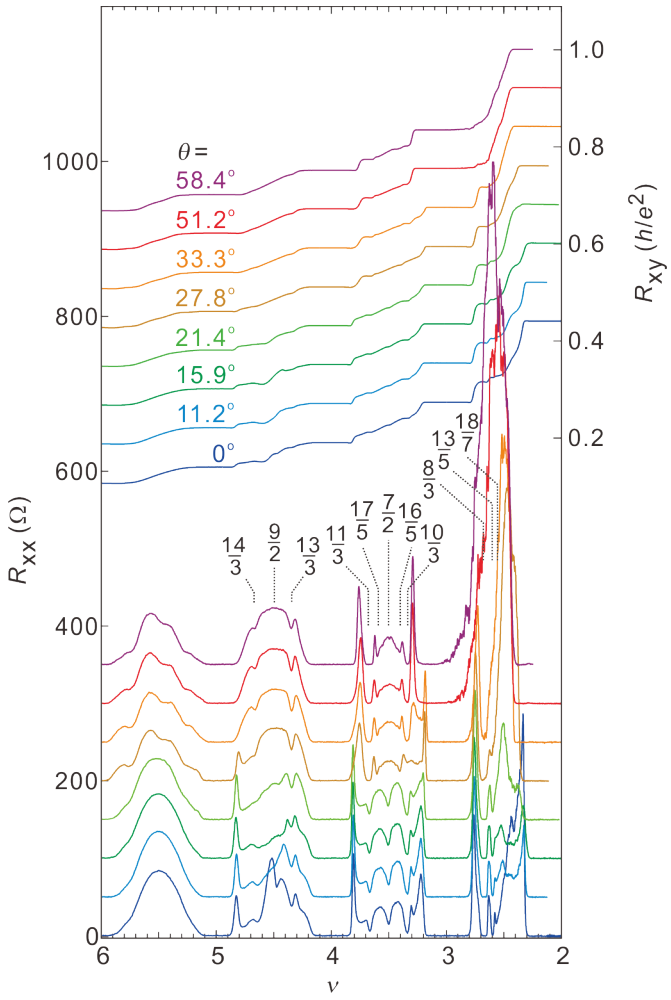

Figure 5.8: Base temperature magnetotransport presented as line traces for $6 > \nu > 2$ for a number of discrete tilt angles. Both the Hall and longitudinal resistances are shown, with primary fractional filling factors noted.

The results of this section put the MgZnO/ZnO in an elite club of materials to have reports of fractional quantum Hall states with an even denominator. The observation of a ν = 7/2 while the electrons at the chemical potential have $N_e = 1$ character strongly suggests that the orbital character of the second LL facilitates pairing of composite fermions[42]. This would make the ground state a genuine single component state and would suggest that it is described by the Pfaffian [43] or anti-Pfaffian[44] wave function. Aside from the AlGaAs/GaAs 2DES, the only other observation of such even denominator states has been in AlGaAs/GaAs 2DHS (see comments below), and suspended bilayer graphene where a unique constellation of LL exists. In that system, the N_e = 0 and 1 LL are inherently degenerate. However, an even denominator state has been observed at ν = -1/2 [64]. Theoretical works have subsequently suggested that this state originates from the N_e = 1 orbital character and is likely described by the Moore-Read wavefunction [135], rather than a two component state originating from the two orbitals acting as the degrees of freedom. This observation in graphene therefore has implications for the ν = 3/2 state observed here. For the state we present here, two scenarios a plausible. The above analysis unquestionably shows that with rotation the character of electrons at this partial filling makes a transition from $N_e = 0, \downarrow$ to $N_e = 1, \uparrow$ character. It does not prove however that it is the character of the first LL electrons which induces the ground state. The rotation of the sample forces the two levels closer to each other and they cross at one point. In a simple picture, this provides a new degree of freedom for electron to occupy. Indeed, the original wavefunction proposed by Halperin was proposed with a spin degree of freedom in mind. A similar scenario has recently been reported in AlGaAs/GaAs 2DHS, where an even-denominator ground state was observed at ν = 1/2 at high field when the energy bands corresponding to light and heavy holes crossed [22]. The authors tentatively attribute the state to be a two-component state as a result. The scenario there differs in the fact that both levels in play are of the same orbital character, and therefore are similar to the observation in wide quantum wells or bilayer systems where the layer degree of freedom acts as a pseudospin. We therefore consider the graphene scenario to be more analogous to the result in MgZnO/ZnO . The exclusion of a two-component state in bilayer graphene therefore suggests that the same story maybe unfolding at ν = 3/2 - $i.e.$, the ground state is described by a single-component wavefunction. This scenario will be discussed again later in section 5.3.

5.2.1 Temperature dependent magnetotransport

Temperature dependent magnetotransport can be used to provide a semi-quantitative understanding of the ground state which is formed. By measuring the resistance of the state while increasing the temperature, an Arrhenius plot may be formulated with the gap (Δ) of states quantified through the following relationship,

$$R_{xx} \propto e^{\frac{-\Delta}{2k_B T}} \tag{5.1}$$

In the measurement apparatus used, the temperature is related to the resistance of a calibrated ruthenium oxide thermometer whose output is read and recorded simultaneously during measurement. The motivation behind such measurements is the fact that the energy gaps of fractional quantum Hall states have the potential to reflect the nature of the ground state. For example, the gap of the ν = 1/3 fractional quantum Hall state is well established in numerical studies [136]. A comparison with experimental results therefore gives an idea of what other "real-world" factors, such as sample disorder, finite thickness, LL mixing, etc, exist in a certain sample or material system. The measurements also

may provide a glimpse into the stability of the observed states relative to each other. For example, the $x/3$ states in the lowest LL are according to theory, much more robust that those in the first excited LL ($N_e = 1$). This is established from both theory [137] and experiment [55].

In this spirit, we initially focus on the behaviour at and around ν = 3/2. The temperature dependent magnetotransport when the sample is not rotated in the magnetic field is shown in Fig. 5.9. With raising the temperature, it can be seen that the resistance at half filling remains mostly unchanged, as can be inferred from Fig. 5.7 but the minimum of fractional quantum Hall states is seen to rise. This is conducive with the activation of carriers above the energy gap of the ground state. This allows the quantification of the gaps of odd denominator states either side of half filling in panel **b**. Now, we introduce the rotation degree of freedom to explore the physics further. This induces the dramatic changes in magnetotransport as discussed above, and is shown in Fig. 5.4.

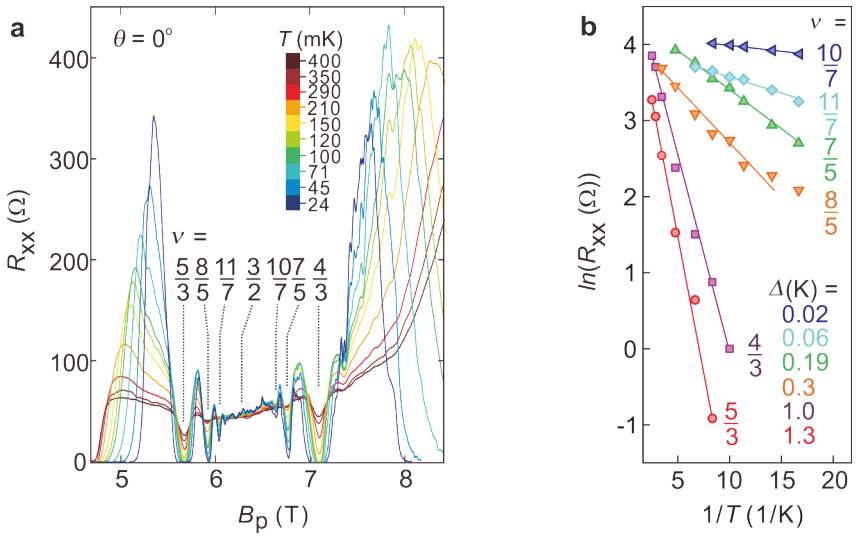

Figure 5.9: **a**, Temperature dependent magnetotransport around ν = 3/2 when the sample is perpendicular to the external magnetic field. **b**, Arrhenius plot representation of the temperature dependence of fractional quantum Hall states.

Figure 5.10**a** shows the transport around ν = 3/2 for the condition where the sample is rotated to θ = 42°. A quantification of the energy gaps is performed in **b**. Most notably, the compressible Fermi sea of composite fermions at half filling under zero tilt transforms into a fully developed, properly quantised even-denominator fractional quantum Hall ground state. This ground state emerges once the temperature falls below roughly 45 mK. The gap of this even-denominator ground state is $\Delta \approx 90$ mK. The activated behaviour of the entire region also differs from the zero tilt scenario. It can be seen that across the entire partial filling factor region, raising the temperature causes the background resistance to rise. This is conducive with a majority spin orientation of electrons at the chemical potential, as is evident in Fig. 5.5.

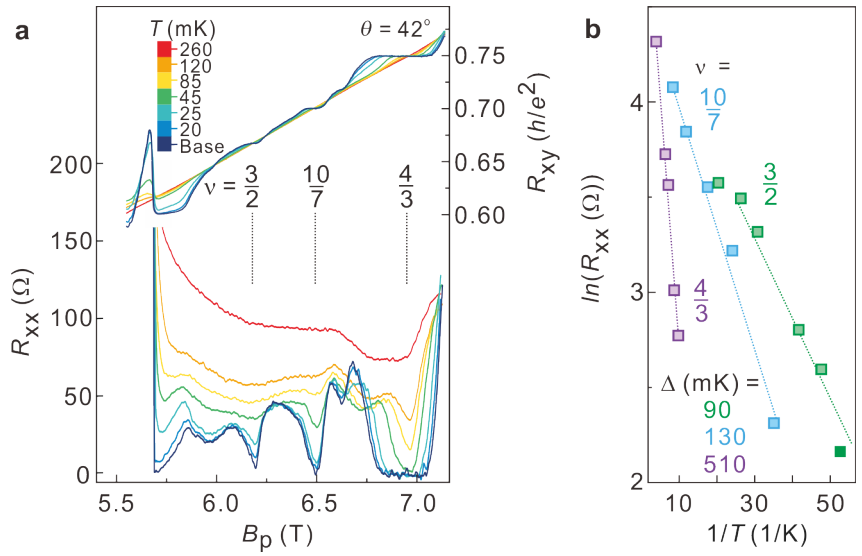

Figure 5.10: **a**, Temperature dependent magnetotransport around ν = 3/2 at a tilt angle of θ = 42°. **b**, Arrhenius plot representation of the temperature dependence of fractional quantum Hall states.

Figures 5.9 and 5.10 also highlight that the activation energy of the ν = 4/3 state is significantly reduced when delving into the high tilt region. As hinted at earlier, this is an expected outcome of shifting the orbital character of electrons from $N_e = 0$ to 1 [55, 137] as the repulsive coulomb interaction which stabilises the odd denominator states weakens when adding nodes to the electron wavefunction in the second LL. This should also be a generic outcome for all odd-denominator states. In Fig. 5.11 we explore this hypothesis further, by plotting the gaps of he ν = 5/3, 4/3, 8/5, 7/5 and 3/2 states as a function of tilt. For each tilt angle, the activation energy was quantified by sweeping the magnetic field back and forth while slowly cooling the sample from high $T \approx$ 400 mK to 20 mK. The process is about 8 hours per tilt angle and roughly 10 points are present in each Arrhenius plot. The temperature as measured by the ruthenium oxide thermometer is read continuously and output with each data point. It is therefore known precisely throughout the measurement. It is important to do this process slowly to ensure thermalisation of the sample and electrons as the mixture cools.

The trend revealed in Fig. 5.11 supports the working hypothesis of the appearance of the ν = 3/2 state being linked with population of the N_e = 1 LL. With rotation, all odd denominator fractional quantum Hall states are seen to weaken dramatically, or completely disappear. Rather sudden transitions may be identified for all states, all of which occur somewhat beyond $\theta = 30°$. This matches closely with the transition angle we identified in Fig. 5.6 for the visually recognisable transition in transport. The accurate quantification of these gaps is important. For example, it can be seen that for the ν = 4/3 state, the minimum of the state remains robust through all tilt angles, and actually gets wider at higher tilt. This would typically suggest that the state increased in stability with increasing tilt. A proper analysis reveals that this however is not the case and the state indeed weakens at higher tilt. It is only after all the odd-denominator states weaken that the ν = 3/2 state emerges. Its activation energy appears to saturate when exceeding angles $\theta = 40°$, just prior to the onset of the high resistance behaviour at even higher tilts. It shows a peak activation energy of Δ = 90 mK, which is comparable to the single component $5/2$ state in modest mobility AlGaAs/GaAs heterostructures [62]. We also note that this activation energy appears to be much lower than some reported values of two-component even-

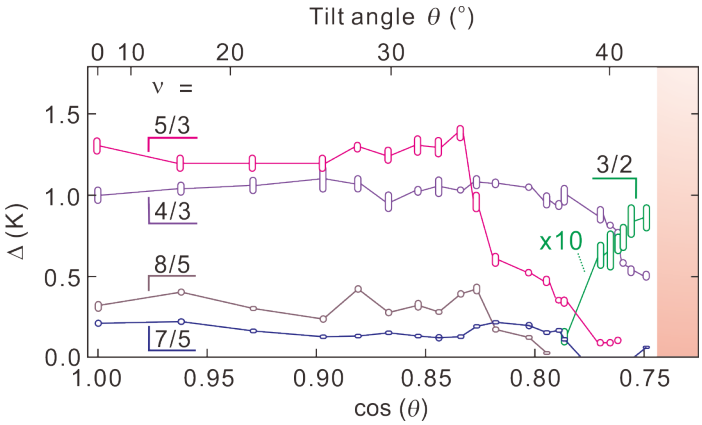

Figure 5.11: Activation energy of the ν = 5/3, 4/3, 8/5, 7/5 and 3/2 fractional quantum Hall states as a function of tilt angle.

denominator states observed in AlGaAs/GaAs heterostructures, where Δ can be on the order of 1 K [138]. Activation energy alone however can not conclusively differentiate between these two possible origins - it may only provide hints.

Here we highlight that in this figure the activation energy of the ν = 7/5 state completely disappears at a certain angle band then recovers at higher tilts. This behaviour is not exclusively observed at this filling factor. As can be seen from the mapped transport in Fig. 5.6, some states including 10/7 and 13/9 show similar behaviour and completely break down when approaching tilt angles of $\theta \approx 40°$ but recover again at higher tilt. These transitions are associated with spin transitions in the ground state described by the composite fermion model. With increasing the tilt angle a complex series of level crossings occurs within this model. The effect is reminiscent of the breakdown of the integer quantum Hall effect when there is a sudden increase of density of states at the chemical potential. In the section 5.3, we explore this extensively.

We now move to other filling factors. The temperature dependence of magnetotransport around ν = 5/2 is shown in Fig. 5.12. It is instantly apparent that the transport is very asymmetric around half filling. On the low field side high order fractional states at ν = 13/5 and 18/7 are identified. These states are never observed in AlGaAs/GaAs heterostructures when a quantized ν = 5/2 state is present. However, the series is not reproduced on the high field side of half filling. Instead, there is a total lack of fractional quantum Hall physics, including the ν = 7/3 state which would be expected in the presence of a 8/3 state [52]. Instead, the high field side reveals that a lone, robust reentrant integer quantum Hall state develops at intermediate temperatures. The defining feature of this phenomenon is the behaviour of the Hall resistance. When the temperature is raised to T = 47 mK (red traces) it can be seen that the Hall resistance reaches a quantised value for B_p = 4.1 T, but then falls back to smaller values for B_p = 4.3 T, only to return to the quantised value of $h/2e^e$ at higher field again. This is the reason for the title of the "reentrant" integer quantum Hall effect. This behaviour was schematically shown in Fig. 2.9 of the introduction. This is extremely surprising, for in AlGaAs/GaAs heterostructures such charge density wave states usually appear in twos or fours [139] and are typically enhanced when going to lower temperature, not higher. In the MgZnO/ZnO heterostructure presented here it seems that the reentrant integer quantum Hall state is "invisible" at base T, with electrons completely localised for 2.25 $> \nu >$ 2. A phase boundary with the ν = 2 integer quantum Hall ground state is thus revealed through raising the temperature. This state is explored in more detail in section 5.4 and 6.

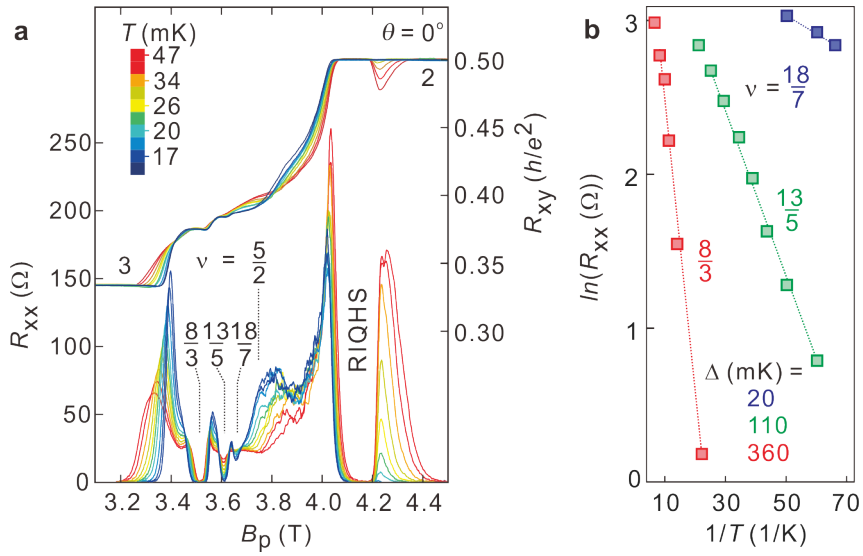

Figure 5.12: **a**, Temperature dependent magnetotransport around ν = 5/2. Prominent fractional quantum Hall states are labelled, along with the development of a re-entrant integer quantum Hall state. **b**, Arrhenius plot representation of the temperature dependence of fractional quantum Hall states.

The story returns to being a more conventional display of the physics expected of N_e = 1 electrons at and around $\nu = 7/2$, as shown in Fig. 5.13. The even denominator state at half filling has a modest activation energy of 50 mK, and still shows finite resistance even at base temperature of the apparatus. The series of fractional quantum Hall states expected in the presence of a quantised even denominator state is reproduced. For AlGaAs/GaAs , this is ν = 5/2, 7/3 and 8/3 for the lower spin branch. The upper spin branch of these states is evidently observed in MgZnO/ZnO , with strong minimum at ν = 7/2, 10/3 and 11/3 clearly observed with correct quantisation of the Hall resistance. The stability of the ν = 7/2 state is similar to that of the 3/2 state and again is of the same order of the single component ν = 5/2 state observed in modest mobility AlGaAs/GaAs 2DES [62]. The stability of the 10/3 state is higher than that of the 11/3 state, which is reproduced in AlGaAs/GaAs , where the 7/3 state is typically more robust than the 8/3 state [55]. As mentioned above, it is interesting to note that while the ν = 7/2 state is indeeed observed in AlGaAs/GaAs 2DES, the observation of the 10/3 and 11/3 state remains elusive. Just recently has the 10/3 state been confirmed in the AlGaAs/GaAs 2DES[134]. This result is surprising, as the quality of the MgZnO/ZnO heterostructure investigated here is still lower than that of the best AlGaAs/GaAs heterostructures current available. In such AlGaAs/GaAs there is a strong tendency for the development of charge-density-wave like ground states to emerge in higher LL. However, in the presence of the 7/2 state in the MgZnO/ZnO we observe no indications of the formation of such ground states down to the base temperature of the measurement apparatus. A more extensive discussion on other features in transport outside of this filling factor range which may be associated with the formation of such charge density wave-like ground states is presented in section 5.4. In the AlGaAs/GaAs 2DES these effects manifest both in the form of the reentrant integer quantum Hall effect and stripe-like phases. If these phases are energetically more favourable than fractional quantum Hall physics, the latter will not occur[56, 57]. The intrinsic mechanism for the discrepancy between these two systems will be an important character to investigate in future studies.

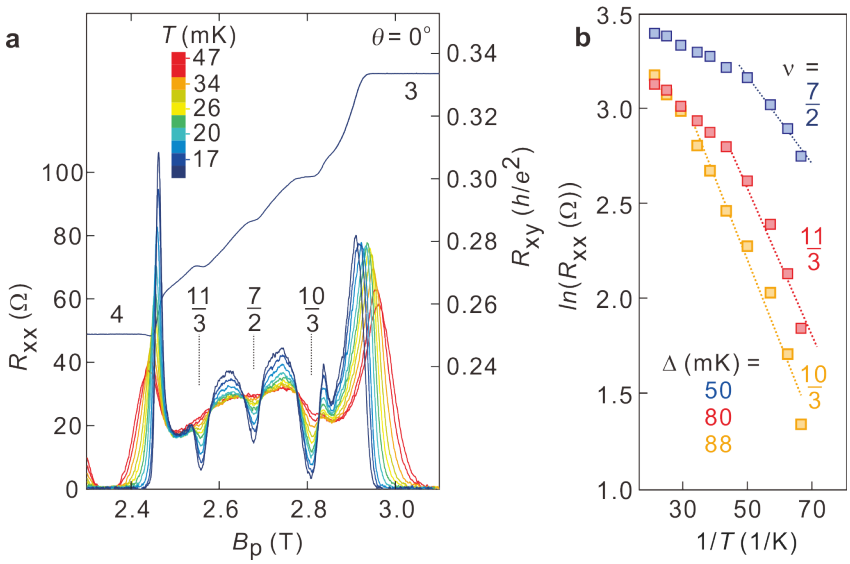

Figure 5.13: **a**, Temperature dependent magnetotransport around ν = 7/2. Prominent fractional quantum Hall states are labelled. **b**, Arrhenius plot representation of the temperature dependence of fractional quantum Hall states.

Finally, the behaviour at ν = 9/2 when raising the temperature is shown in Fig. 5.14. We recall that the working hypothesis is that the incipient features are resolved as a result of the electrons at the chemical potential obtaining $N_e = 1$ character even at zero tilt. To support this idea we recall that the fractional quantum Hall effect is not expected to be observable in higher LL ($N_e \geq 2$)[56, 57] as explored in Fig. 2.9. Instead, charge density wave like ground states appear energetically more favourable, as confirmed in both theory [56] and experiment on high mobility AlGaAs/GaAs heterostructures[58, 59]. Returning to the results on MgZnO/ZnO , as discussed in the previous sections the minimum at ν = 9/2 and flanking odd denominator fillings are extremely weak. A number of issues exist in the experimental data. With lowering the temperature it can be seen that the resistance of the partial filling factor unexpectedly increases. This too includes the resistance of the minimum associated with fractional fillings. This immediately prohibits the analysis of any activation energy via an Arrhenius plot. Moreover, the Hall resistance, while showing rather rich behaviour, shows significant temperature dependence. While at the half filling there is undoubtedly a plateau, the value of this plateau shifts with lowering the temperature. The same is true for the odd denominator fillings of ν = 13/3 and 14/3, which show a minimum but no exactly at the magnetic field expected. Given this quality of transport, it is not possible to conclude on the presence or absence of a state at ν = 9/2. We do note however that this is not so dissimilar to the first observation of the ν = 5/2 state in AlGaAs/GaAs heterostructures [39]. There, it took more than 10 years to confirm the quantisation of the ground state [40]. The rising resistance in the MgZnO/ZnO transport with reducing the temperature may indicate a competition between fractional quantum Hall physics and charge-density-wave physics, but, as will be shown later, no remnants of anisotropy are observed (see Fig. 5.22).

We close this section by noting that the appearance of the ν = 3/2 state is reproducible and for the currently available data sets, always occurs under finite tilt. Four magnetotransport traces are shown in Fig. 5.15, for when the sample is tilted to an angle which is just prior to the sudden increase in resistance encountered at high tilt. This tilt angle is related to the magnitude of $g_e^* m_e^*/m_0$, which is a function of

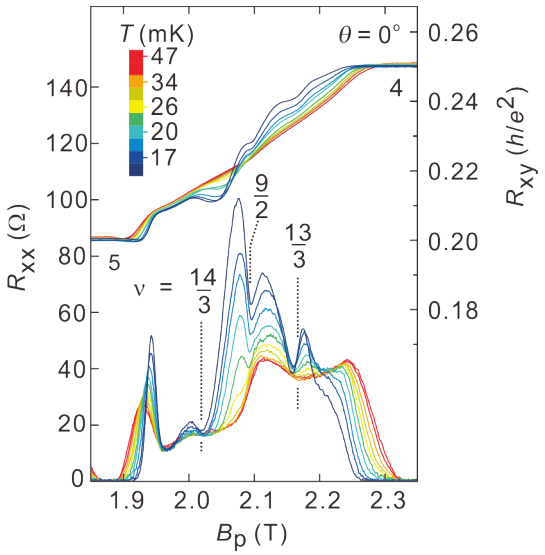

Figure 5.14: Temperature dependent magnetotransport around ν = 9/2. The filling factors of fractional quantum Hall states are indicated by vertical lines and are seen to closely correspond to the minima observed in the longitudinal resistance.

n. The exact range of tilt angles will be explored systematically in future studies. The most robust state observed thus far is that which has been described in this section at an activation energy of Δ 90 mK. In lowing the mobility to μ = 300,000 cm^2/Vs while retaining the same density a minimum is present and a quasi-gap of 10 mK may be estimated. However when reducing the charge density to 1.5 $\times$ 10^{11} cm^{-2} in a modest mobility sample, features of the ground state can not be observed. We do speculate that if the quality of the 2DES may be maintained in dilute samples (as is the case in state-of-the-art samples), it may be possible to observe the ν = 3/2 ground state in an un-tilted geometry. The estimated $g^*_e m^*_e/m_0$ to achieve this is on the order of 2.8, which, may be achieved at a density of roughly 1 $\times$ 10^{11} cm^{-2} . All the samples presented in Fig. 5.15 display similar physics at other partial filling factors of ν = 5/2 and 7/2, but have failed to clarify the conclusions drawn about the incipient ν = 9/2 state observed in the highest quality sample. Finally, we recall that in AlGaAs/GaAs heterostructures there has been significant efforts of recent years to understand the apparently poor correlation between the stability of the even denominator state at ν = 5/2 and the sample mobility [62, 63, 140]. While indeed there exists a certain threshold in mobility (thought to be on the order of 5,000,000 cm^2 V^{-1} s^{-1}) required to resolve the ground state, evidence has been amassed to suggest the disorder landscape imposed by remote dopants greatly affects the stability of such states but only has a modest effect on the mobility. The transport scattering time in the MgZnO/ZnO heterostructure presented here would be achieved in a AlGaAs/GaAs 2DES with a mobility of roughly 4,000,000 cm^2 V^{-1} s^{-1} . The robustness of states observed in MgZnO/ZnO is therefore rather surprising. Again, we spectulate that since in MgZnO/ZnO there are no intentional dopants incorporated in the heterostructure, the stability of these states may be superior. While this work has unveiled evidence that suggests the surface potential of the sample can have a dramatic effect on the quality of the 2DES (see section 4.16), its correlation with the stability of ground states remains in future work. From growth point of view, exploring the stability of the ground states identified in this work in heterostructures void of intentional impurity doping will be an important frontier for both the understanding of this system and more general considerations of correlated ground states achieved in 2DES.

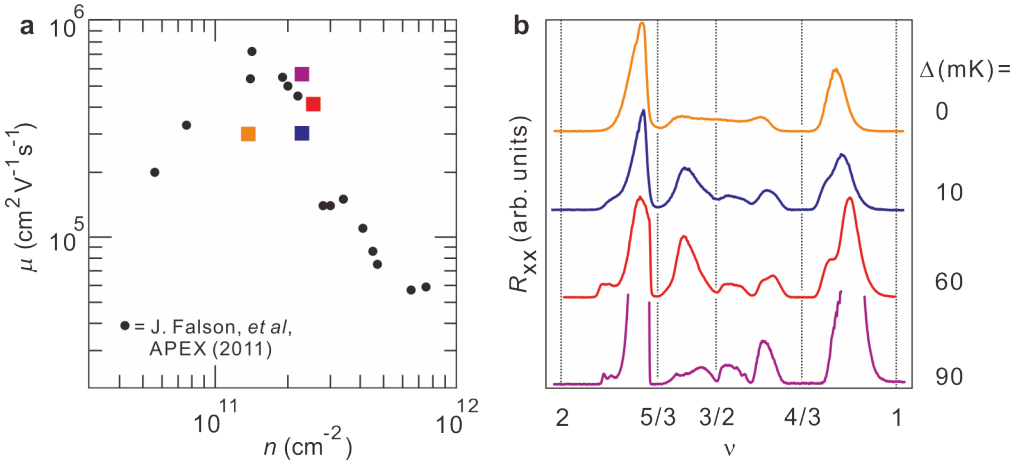

Figure 5.15: **a**, Mobility and charge density of samples presented in panel **b**, Base temperature (T = 15 mK) magnetotransport as a function of ν under tilt just prior to the high resistance regime. Activation energy of the state in each sample is shown on the right hand side. In panel **a** the black data points are taken from Ref. [83].

5.3 Composite fermions at ν = 3/2

As introduced in section 2.2.2, the transport of the lowest LL and sequence of fractional quantum Hall states can be nicely modelled using the composite fermion approach [11]. In this regime, the fractional quantum Hall effect of electrons is mapped into the integer quantum Hall effect of composite fermions through the relationship $\nu = \frac{p}{2mp\pm1}$ for the case of fractional states centred on ν = 1/2. This can be understood by considering that a Fermi sea of quasiparticles at half filling with a new series of discrete energy levels developing in an effective magnetic field B_{eff} when moving away from exactly half filling. These composite fermion levels are separated by a quasi-cyclotron gap, given by $\hbar\omega_{CF} = \frac{\hbar eB_{eff}}{m^*_{CF}}$. The model predicts accurately the appearance of the strongest states at ν = 1/3 and 2/3, as their p index corresponds to 1 and 2, respectively, and these are the most fundamental integer states which occur at the highest B_eff. This model has been very successfully deployed on the lowest spin branch of the lowest LL. However, the story becomes even richer when incorporating a spin degree of freedom to composite fermions. This spin degree of freedom has up until now been an essential and exciting aspect of MgZnO/ZnO transport, and here we show that this extends deep into the spin texture of the series of fractional quantum Hall states observed around ν = 3/2.

While spin transitions may be observed in the lowest spin branch, this degree of freedom can be explored more easily by shifting the filling factor to be ν = 3/2. Figure 5.16 schematically represents the level arrangements of electron LL and CF levels in this scenario using the energetics present in the MgZnO/ZnO 2DES. Firstly, it is important to identify that the spin degree of freedom imposed on composite fermions is inherently that of the electron LL. Therefore, we draw the composite fermion level fan originating from the spin split electron LL. In MgZnO/ZnO since E_z is large, the spin levels of different LL become close in energy. It is therefore convenient to define a new energy term, ΔE, which is the difference between E_{cyc} and E_z. In Fig. 5.16, two scenarios of ΔE being both negative and positive are shown in the upper and lower sets of panels. This difference will be discussed later.

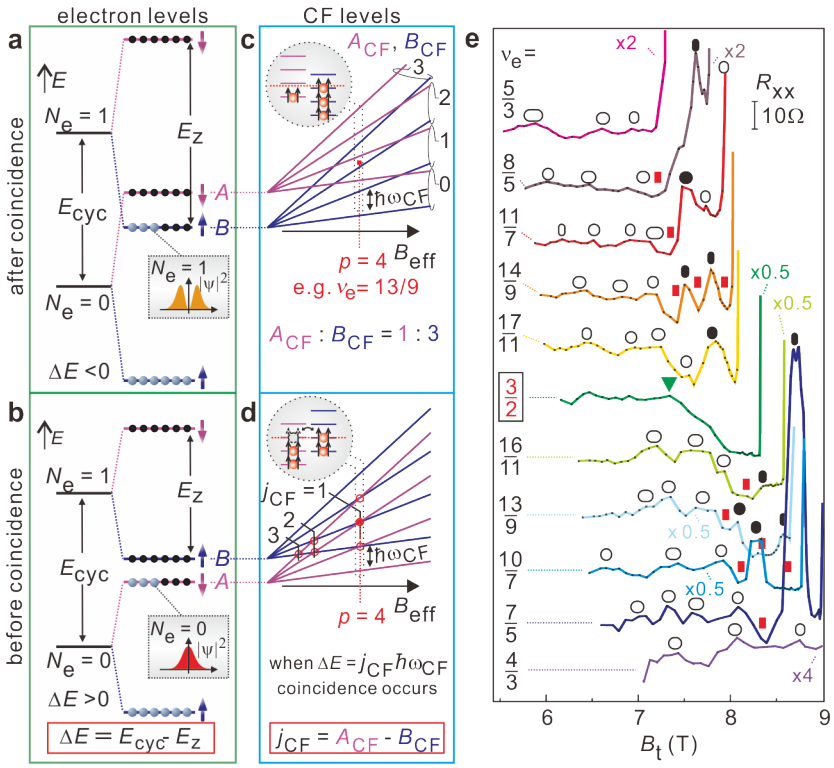

Figure 5.16: **a**, **b**, Schematic of electron LL (green panels) sequence after and before coincidence. The insets schematically show the differing wave function between N_e = 0 and 1. **c**, **d**, Intersecting CF level fans (blue panels) of the corresponding electron LLs A and B. When p (set to be 4 here for illustrative purposes) composite fermion LLs are completely filled the fractional quantum Hall effect arises. **e**, Tracking of the minima of FQH states centered on ν = 3/2 for base temperature. Local maxima are indicated by white or black bars with strong minima noted by red boxes (see text). Scaling factor of each resistance trace is indicated by coloured tags

Before probing any spin degree of freedom, we investigate the mass of composite fermions through the analysis of the temperature dependent transport reported in the previous section. This helps to set up our understanding of the physics in a semi-quantitative manner. Two techniques are available for determining the mass - through analysing the fractional quantum Hall minimum in analogy to Shubnikov - de Haas oscillations of electrons using the same Dingle formalism (as presented in section 4.10), and through measuring the gap and its enhancement in B_{eff}. We highlight here that at ν = 3/2 the effective magnetic field felt by composite fermions is $B_{eff} = 3(B_p - B_{p,\nu=3/2})$, as only 1/3 of electrons are taking part in transport at the chemical potential. The activation energy of fractional states should increase roughly linearly increasing B_{eff} through a linear increase in the cyclotron gap, given by $\frac{\hbar e B_{eff}}{m^*_{CF}}$. The slope of the gaps in B_{eff} is reflective of m^*_{CF}. Similar analyses have been performed in AlGaAs/GaAs 2DES, generally focusing on the behaviour around ν = 1/2 [33, 34], and in previous work in the MgZnO/ZnO at ν = 1/2 [141]. The results of the analysis from these two techniques is shown in Fig. 5.17. Both methods yield results which are in reasonable numerical agreement with each other and seem reasonable based on previous works. This value is not extremely useful for the remainder of the discussion but it at least provides a guideline value for comparing other numerical results.

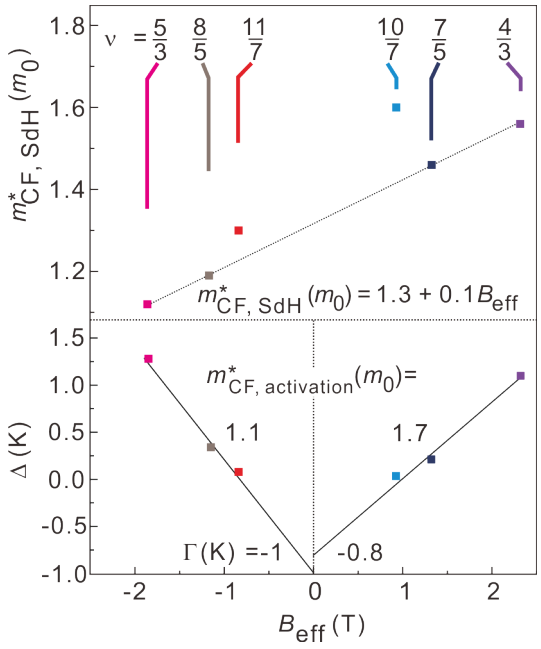

Figure 5.17: Analysis of the effective mass of composite fermions. **a** According to the temperature induced dampening of the oscillations centred on ν = 3/2 in analogy to Shubnikov-de Haas oscillations and **b** based on the linear growth of the fractional quantum Hall states gaps as a function of B_{eff}.

We now add the spin degree of freedom and analyse the behaviour of composite fermions with rotation. Returning briefly to the mapping data shown in Fig. 5.6, it can be seen in the experimental data that the minimum of odd denominator fractional quantum Hall states shows oscillatory behaviour when increasing tilt. This is highlighted in Fig. 5.16**e** where the resistance of the minimum of each state is plotted as a function of total magnetic field. It can be seen that a number of states display strong oscillations where the ground state may be completely destabilised. This was also seen in the earlier sections where the activation energy was plotted as a function of tilt (Fig. 5.11). Moreover, the minimum and maximum of each state appear to occur at different B_t, signifying that state specific transitions are occurring. This behaviour can be associated with the crossing of CF levels when E_z is enhanced with rotation. Analogous to what occurs at integer filling factors for electrons (see Fig. 4.6), a maximum in resistance of fractional quantum Hall states is associated with the intersection of two composite fermion levels. As introduced above, the composite fermion picture says that discrete energy levels (panels **c**, **d**) emanate from electron LL (panels **a**, **b**) when moving away from exactly ν = 3/2. The work presented in Ref. [35] describes an experimental result gained on the AlGaAs/GaAs 2DES and maps out the transitions until each is fully spin polarised. A recent work provides a similar understanding based on spin transitions between different subbands within a wide AlGaAs/GaAs QW [142]. In Ref. [35] it was found that an interpolation of all coincidence conditions yielded an origin of B_t = 0 for when the spin splitting energy on composite fermions is zero. This is what is expected from a simple model where the spin splitting is determined by E_z alone. In MgZnO/ZnO however, $E_{cyc} \propto E_z$ and therefore the two electron LL in focus are (N_e = 0 $\downarrow$) and (N_e = 1 $\uparrow$). These are labelled levels A and B in Fig. 5.16 for the sake of brevity. This is in contrast to AlGaAs/GaAs , where the small Zeeman energy means that the ($N_e = 0 \downarrow$) and ($N_e = 0 \uparrow$) show crossing events[35]. The energy separation between the electron LL in MgZnO/ZnO is $E_{cyc} - E_z = \Delta E$. Panel **c** depicts the scenario when ΔE is

negative and **d** when positive. The orbital quantization energy of the composite fermion levels is given by:

$$(N_{CF} + \frac{1}{2})\hbar\omega_{CF,X} \tag{5.2}$$

where

$$\hbar\omega_{CF,X} = \frac{\hbar e B_{eff}}{m^*_{CF,X}} \tag{5.3}$$

Each of these levels has an associated quantum number running 0,1,2 . . . . The spin degree of freedom is imposed from the host electron LL. Strictly speaking, the mass of composite fermions originating from the A and B levels may be different, as signified by the X subscript, due to the different orbital character of the host electron LL. In Fig. 5.17 it is considered that the mass of composite fermions emanating from level A was probed as ΔE is positive and large in the perpendicular field arrangement. This gives us a 'guideline' value for the analysis. Levels will exchange position when the effective spin split energy ΔE equals the difference between the orbital energy of composite fermion levels:

$$\Delta E = A.\hbar\omega_{CF,A} - B.\hbar\omega_{CF,B} \tag{5.4}$$

However, including independent effective masses depending on the orbital nature of composite fermions significantly complicates the fitting procedure. Therefore in the analysis below any difference of effective masses is ignored. This still allows extensive modelling of the situation and a generally good qualitative understanding of the underlying physics. As is evident in equation 5.4, and assuming that $\hbar\omega_{CF,A} = \hbar\omega_{CF,B}$, the coincidence positions (j_{CF}) of levels will occur when

$$\Delta E = j_{CF}.\hbar\omega_{CF} \tag{5.5}$$

The difference of the level index is signified by $j_{CF} = (A_{CF} - B_{CF})$, as shown in panels **c** and **d**. Analysing these transitions, they should all fall on a straight line when plotting their constellation in the (B_p, B_t)-plane as the former term depends on B_t and the latter on B_p. The features in transport should therefore reveal details of the full series of j_{CF} transitions which occur. Importantly, each j_{CF} line should pass through a common point when B_{eff} = 0 and therefore $\hbar\omega_{CF,B}$ = 0. This is important, as it is the condition which signifies ΔE = 0 and hence when the electron LL cross.

We now determine the filling factor of composite fermions by mapping the electrons into composite fermions with a spin degree of freedom. The number of levels filled is given by p, and is related to the electron filling factor by $\nu = 1 + \frac{p}{2p\pm1}$. Figure 5.16 shows the scenario when p = 4, which would indicate ν = 13/9 or 11/7. However, even when setting p to be constant, the ratio of $A_{CF} : B_{CF}$ can be different depending on the tilt angle. This is at the heart of this analysis - by shifting this ratio the stability and hence underlying nature of the states will be modified. In MgZnO/ZnO , this happens to be a modification of both spin and orbital character.

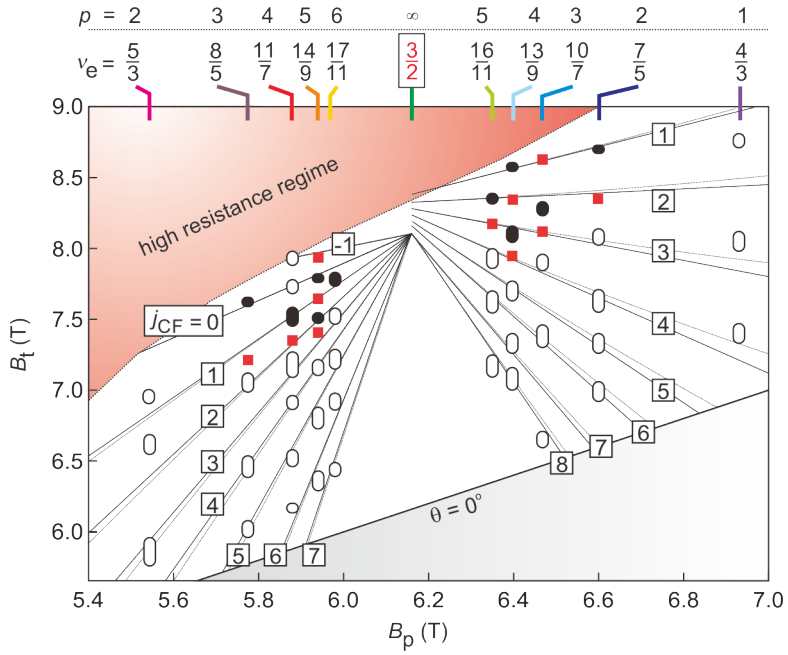

Figure 5.18: Mapping of the local maxima in the (B_p, B_t)-plane for prominent FQH states. j_{CF} index lines are overlaid. Black data points correspond to strong features in the longitudinal resistance. Red points signify deep minimum in the longitudinal resistance. White data points correspond weak features in the longitudinal resistance.

Figure 5.18 models the constellation of transitions which were identified in Fig. 5.16**e** when plotted in the (B_p, B_t)-plane. The following assumptions were used:

- The fractional quantum Hall states are described by the relationship $\nu = 1 + \frac{p}{2p\pm1}$. This is in contrast to previous works [35], which has used $\nu = 2 - \frac{p}{2p\pm1}$. The use of this series give a much better agreement with the strength of transitions at the chemical potential. This is because of the large Zeeman energy in the MgZnO/ZnO 2DES which separates the lowest LL spin up branch from the levels taking place in transport at ν = 3/2. A similar series has recently been observed in a wide AlGaAs/GaAs QW which utilises exploits the presence of a second subband [142]. This supports our assignment.

- For a constant j_{CF} index, the resistance must oscillate between high and low resistance, signifying a change between the chemical potential being at a crossing and in a gap. To aid fitting, the strong minima observed in transport are added to Fig. 5.16 and 5.18.

- Strong features where the ground state breaks down must be associated with a crossing of levels at the chemical potential. We note that "strong" features in addition to the broad peaks signifying the break down of the ground state, as is the case in positive B_{eff}, may appear as sharp resistance spikes, as shown in Fig. 5.19**b**.

- The spin susceptibility of composite fermions, $g^*_{CF}m^*_{CF}/m_0$ is constant for a certain j_{CF} index line, but it allowed to fluctuate between different index lines. Fits using a constant $g^*_{CF}m^*_{CF}/m_0$ are shown as solid lines in the figure. A quantitative analysis of each j_{CF} is performed later. Differences in slope are anticipated as the orbital nature of composite fermions too changes with rotation. Other fits incorporating a $m^*_{CF} \propto \sqrt{B_P}$ dependence are shown as dotted lines[32]. The text below discusses this fitting procedure, which qualitatively gives the same result as assuming a constant $g^*_{CF}m^*_{CF}/m_0$.

- The origin where B_{eff} = 0 is allowed to fluctuate between j_{CF} lines.

We highlight that the final two assumptions are not taken into account by the simple model presented in Fig. 5.16. However, evidently, relaxing these aspects allows a much better fitting of the experimental data. The fan plotted in Fig. 5.18 is also overlayed on the magnetotransport in Fig. 5.19, where the vertical axis is now cos(θ). Overlaying this constellation on the real magnetotransport makes it plain to the eye that when tracing a certain j_{CF} line the resistance oscillates between high and low and this hence enables the assignment of a j_{CF} index to all transitions. Under the condition $p > j_{CF} >$ 0, the maximum correspond to transitions where levels overlap with two different scenarios: If p is odd (even), the Fermi level will be in a gap for coincidences with j_{CF} odd (even) and a deep minimum in the longitudinal resistance is expected. In contrast, if j_{CF} is even (odd), the Fermi level will be located at the coincidence instead resulting in a breakdown of the quantum Hall effect and a maximum in R_{xx} can be expected. With increasing tilt, the states become increasingly polarised in the ($N_e = 1 \uparrow$) level. This is in distinct contrast to the work presented in Ref. [35] which explored the crossing of composite fermion levels originating from the same electron LL (since $E_z/E_{cyc} \approx$ 1/70 is small in AlGaAs/GaAs). The transitions there were hence exclusively changes in spin character. At lower tilt when ΔE is large and positive, the features identified in transport are all weak. It can be seen that according to the model, all these transitions correspond to $j_{CF} \geq p$ and hence are associated with the crossing of levels

above the chemical potential. In line with expectations, the state does not fully break down and only weak features in transport are identified.

We note that in the composite fermion model the effective mass should depend on the strength of Coulomb interaction, which has a $\sqrt{B}$ dependence[32]. For completeness we have estimated the effect of such dependence of the constellation fitted in Fig. 5.18 and 5.19. In both of these figures, dotted lines have been included for each j_{CF} line, which corresponds to $m^*_{CF} \propto \sqrt{B}$. Strictly speaking, these lines describe the condition

$$g^*_{CF} m^*_{CF}/m_0 \propto \frac{\sqrt{B_p}}{\sqrt{B_{p,3/2}}} \tag{5.6}$$

This in effect scales the behaviour analysed through assuming $g^*_{CF} m^*_{CF}/m_0$ is constant (solid lines in Figs. 5.18,5.19) by a $\sqrt{B}$ dependence relative to half filling. It is important however to note that the overall result is hardly affected in adding this facet to the fitting procedure. This is easy to understand since the absolute magnitude of Coulomb interaction strength will only change by $\approx$ 10% over the magnetic fields probled in this analysis (5.5 T $< B_p <$ 6.9 T). Adding this therefore does not overcome the requirement of relaxing the origin of j_{CF} lines, as discussed above.

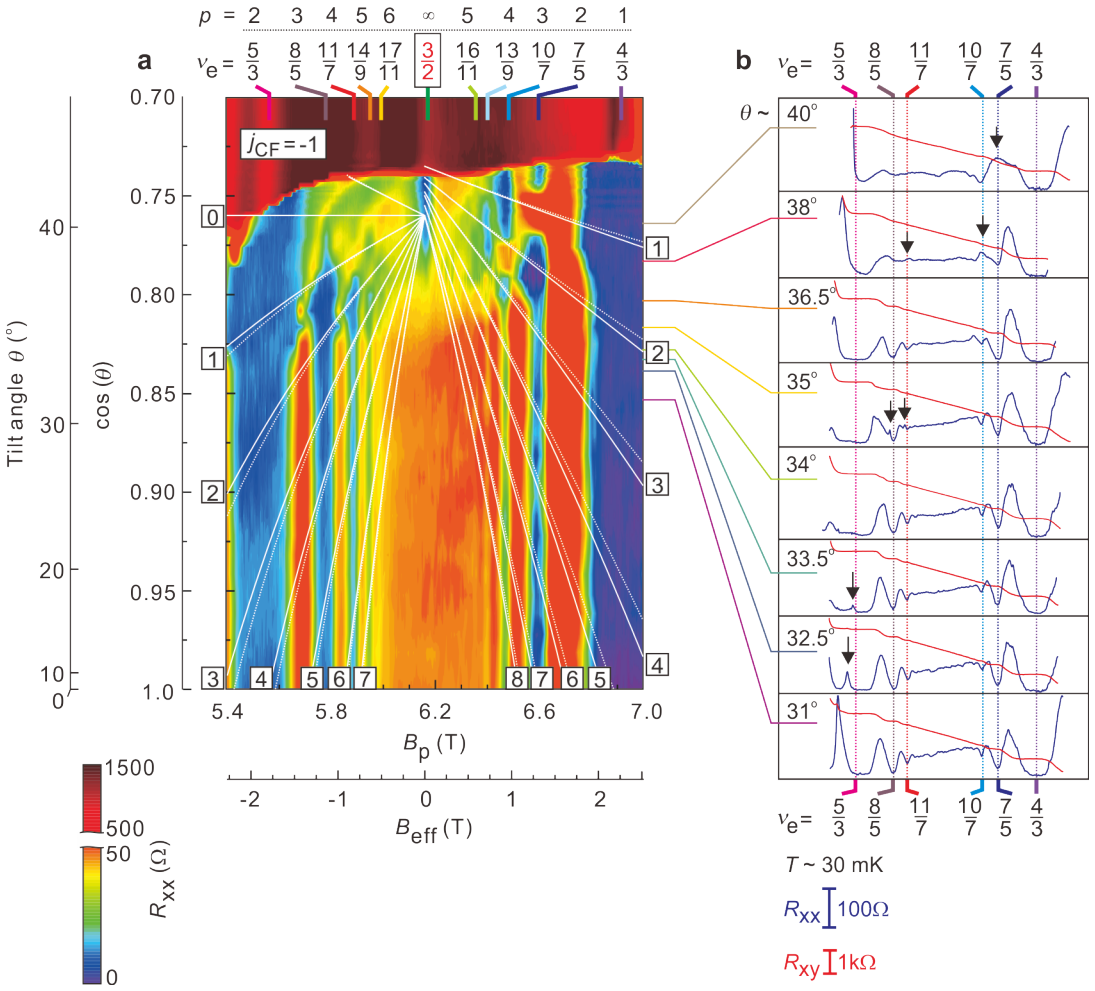

Figure 5.19: **a** Magnetotransport mapping around ν = 3/2 with the j_{CF} index transitions lines overlaid. The solid lines correspond to fits where the mass is independent of B where the dashed lines correspond to a $m^*_{CF} \propto \sqrt{B}$ dependence. **b** Line traces at intermediate temperatures $T \approx 30$ mK at discrete angles where spin transitions in fractional quantum Hall minimum are shown as black arrows. These features are enforced to correspond to CF LL crossings at the chemical potential.

In Fig. 5.20 we present the full array of transitions expected from the above model. Here, circles correspond to transitions expected at the chemical potential which should be strong and crosses correspond to transitions away from the chemical potential. The black line marks the condition where composite fermions become fully polarised in N_e = 0 (below line) and mixed in N_e = 0 and 1 (above line). Turning to the experimental results, shaded boxes correspond to strong features observed in transport, and (s) corresponds to spike features which show up in transport at intermediate temperatures. Both of these must be associated with a transition at the chemical potential. Evidently, a good agreement is achieved. The bottom set of bubbles schematically visualise the development of the ν = 13/9 state as a function of tilt with shifting spin and orbital polarisation.

ν =	5/3	8/5	11/7	14/9	17/11	16/11	13/9	10/7	7/5	4/3
p =	2	3	4	5	6	5	4	3	2	1
j_{CF}= -1	○	X	○	X	○	X	○	X	○	X
0	X	○	X	○	X	○	X	○	X	○
1	○ (s)	X	○	X	○	X	○	X	○	X
2	X	○ (s)	X	○	X	○	X	○	X	X
3	X	X	○ (s)	X	○	X	○	X	X	X
4	X	X	X	○	X	○	X	X	X	X
5	X	X	X	X	○	X	X	X	X	X
6	X	X	X	X	X	X	X	X	X	X
7	X	X	X	X	X	X	X	X	X	X
8	X	X	X	X	X	X	X	X	X	X

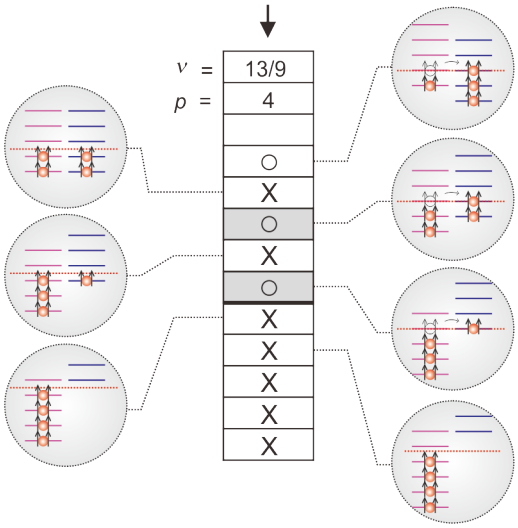

Figure 5.20: Composite fermion spin transitions predicted by the model discussed in the text for filling factors as a function of j_{CF}.Circles correspond to transitions expected at the chemical potential which should be strong. Crosses correspond to transitions away from the chemical potential. The black line marks the condition where composite fermions become fully polarised in N_e = 0 (below line) and mixed in N_e = 0 and 1 (above line). Shaded boxes correspond to strong features observed in transport, and (s) corresponds to spike features. The bottom set of bubbles schematically show the development of the ν = 13/9 state as a function of tilt and shifting spin polarisation.

j_{CF}	$\nu > 3/2$	$\nu < 3/2$
-1	8.6	-
0	-	-
1	8	10
2	8.2	10
3	8.2	9.4
4	8.2	9
5	7.4	9
6	6	9
7	5.6	8.6
8	-	8.4

Table 5.1: Summary of values of $g^*_{CF}m^*_{CF}/m_0$ used as slopes for the j_{CF} lines shown in Fig. 5.18 and 5.19.

The next step of this analysis is more quantitative and will investigate the spin susceptibility of composite fermions. In order to plot the constellation the j_{CF} lines, the condition of $\Delta E = \hbar\omega_{CF}$ must be met, which contains both a mass term and g-factor term. The slope of lines therefore reflects the spin susceptibility of composite fermions, $g^*_{CF}m^*_{CF}/m_0$. This is a free parameter in the fitting, along with the origin. The g-factor should be closely related to that of electrons for the spin degree of freedom is originating from the Zeeman split levels. The mass too should be similar (but not necessarily the same) to what was measured earlier in this section in Fig. 5.17. The values of $g^*_{CF}m^*_{CF}/m_0$ used in the fitting procedure are shown in Table. 5.1. As can be seen, the constellation is not achieved through using a constant $g^*_{CF}m^*_{CF}/m_0$ value. Instead, the spin susceptibility of composite fermions appears to be enhanced when moving to smaller j_{CF} index transitions. This is consistent with transport increasingly occuring in $N_e = 1$, as the mass of composite fermions (and hence $g^*_{CF}m^*_{CF}/m_0$) should be enhanced in excited LL.

Finally, having identified j_{CF} for all transitions using a rough estimation of $g^*_{CF}m^*_{CF}$, it is possible to quantify this value more accurately as a function of tilt for each state. This analysis is shown in Fig. 5.21. The expression below allows the extraction of $g^*_{CF}m^*_{CF}/m_0$ for each p filling by plotting the values of B_t/B_p as a function of j_{CF}:

$$-g^*_{CF}m^*_{CF} = j_{CF}.6m_0(B_p - B_{p,3/2}) - \frac{2m^*_{CF}m_0}{m^*_e}.B_p \tag{5.7}$$

According to the fitting procedure and the identified j_{CF} index for each index, it is possible to determine when the transport of fractional states is occurring in $N_e = 0$ exclusively, or mixing in $N_e = 1$ and 0. The condition for the latter would be $j_{CF} < p$. We signify this boundary in Fig. 5.21 by small vertical lines in panel **a**. Importantly, it can be seen that an inflection point in the interpolation between coincidence positions may be identified around this index. For transitions corresponding to $j_{CF} < p$, $g^*_{CF}m^*_{CF}/m_0$ is larger, revealing a consistent picture.

The model presented here reveals a new facets of the understanding of the nature and stability of composite fermions. It is the first time that such crossings have been observed between composite fermions originating from different electron LL. Most notably, the inclusion of N_e = 1 into the scenario has a dramatic impact: as discussed above at Fig. 5.11, all of the odd-denominator states are seen to be significantly weaker when going to higher tilt. Specifically, the complete breakdown followed by reemergence of states in this figure, such as the ν = 7/5 state is understood by attributing this transition

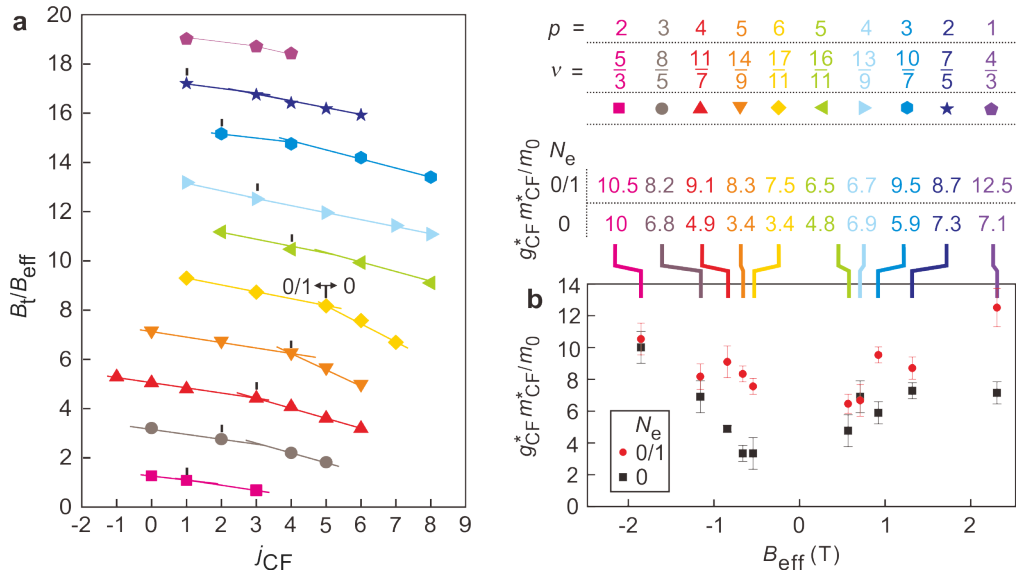

Figure 5.21: Detailed analysis of the spin susceptibility of composite fermions as a function of tilt. **a** B_t/B_p for transitions identified as a function of j_{CF}. The slope of interpolated points reflects the spin susceptibility of composite fermions. The small vertical tags indicate transition fully polarised in $N_e = 0$ or mixed in $N_e = 0$ and 1. **b** Summary of the spin susceptibility for each orbital regime as a function of filling factor or alternatively B_{eff}.

to a crossing of composite fermion levels at the chemical potential, with the ground state undergoing a discrete shift in orbital and spin polarisation.

Finally, we address the origin of the j_{CF} lines portrayed in Fig. 5.18 and 5.19. As stated above, no common origin can be identified in the fitting procedure, and therefore we relax this as a requirement, despite the fact that the numerics presented suggest otherwise. This suggests that a parameter is changing, whether it be m^*_e, m^*_{CF} or g^*_e, with rotating the sample and changing the magnetic field. As a result, this analysis does not allow us to pin point an exact angle at which the electron LL swap positions. However, it does appear that the origin lies within close proximity to where the ν = 3/2 state is quantised. This means that the two spin levels are close in energy, and arguably increases the likelihood that the state is stabilised by the presence of the extra degree of freedom. This would suggest a two component ground state [10]. However, transport can only give us hints about such details - more direct and specific measurements such as the spin polarisation of half filling will be required in the future to conclude on the origin of the state.

5.4 Beyond fractional quantum Hall states

Until now the ground states in focus have been those of the fractional quantum Hall effect. However, it has been mentioned multiple times that a different strain of ground state, in the form of charge density waves, may be observed in high mobility 2DES. This was canvassed over in chapter 2 and schematically presented in Fig. 2.9. Past experiments on AlGaAs/GaAs systems has shown that there is a spectacular collision of ground states in the second LL ($N_e = 1$) and an entirely new regime in $N_e \geq 2$. While for the lowest LL, the fractional quantum Hall effect dominates, it is widely reported that strongly anisotropic transport develops at $T < 100$ mK in higher LL ($N_e \geq 2$, $\nu > 4$) [58, 59].

In higher LL the relevance of the composite fermion model begins to be questioned as the fractional quantum Hall effect is dispelled. Indeed, there are no entirely convincing reports of this effect in $N_e \geq 2$. A significant number of theoretical works [56, 57] consider the nature of higher LL ground states to be correlated phases where a modulation of electron density forms in an easy crystal axis. This is termed the 'stripe phase' and it typically occurs at half-filling. Experimentally, this phase manifests as highly anisotropic resistance within the sample depending on whether current is passed long or across the stripe structure. The exact mechanism however for the determination of an easy/hard axis remains under debate. The situation is made richer by the application of an in-plane magnetic field ($i.e.$ rotation of the sample). Strikingly, the orientation of the stripes phases may re-orient depending on the relative direction of current and in-plane field[143, 144]. Moreover, filling factors which previously showed the fractional quantum Hall effect, for example ν = 5/2, develop to show robust anisotropy, indicative of a transition to a stripe-like ground state. Recent NMR measurements have probed this phase experimentally and have revealed a large modulation of the 2DES density on the order of 20 % of the total[60]. Given the apparent 'quality' of MgZnO/ZnO , the presence of these phases in the system should therefore be examined.

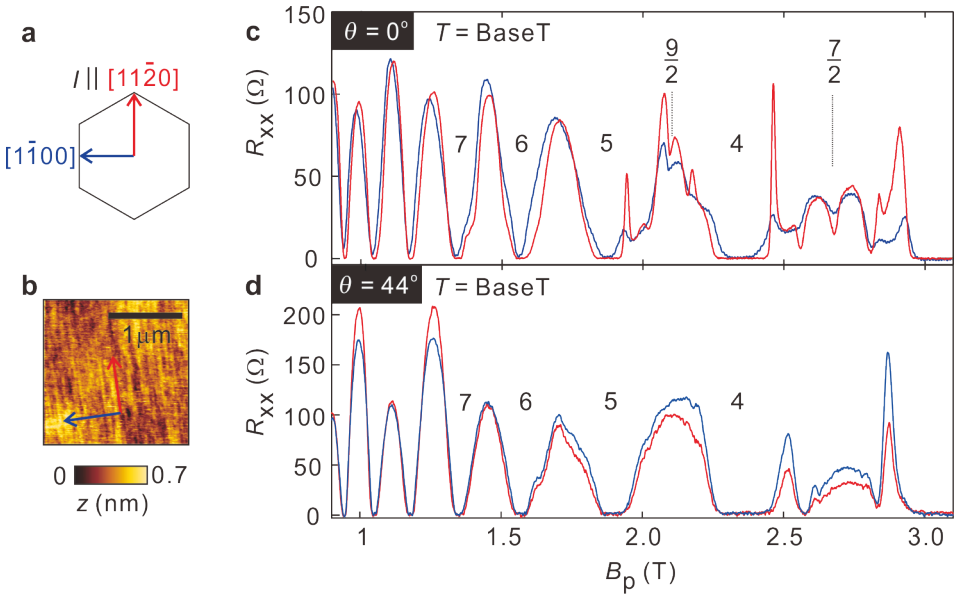

Figure 5.22: Isotropy of higher LL magnetotransport. **a** Crystal directions indicated on the hexagonal lattice structure and **b** their relationship to the surface morphology. **c** Magnetotransport of higher LL in the two crystal directions when the sample is not rotated and **d** when the sample is rotated to $\theta = 44°$.

The easiest detection method for exploring any anisotropy in transport is to measure the sample's longitudinal transport along different crystal directions. For such measurements, the use of van der Pauw geometry (as used in this work) is advantageous, as the current direction can be easily rotated by simply rearranging the measurement wires at room temperature, leaving the aspect ratio of the device under measurement unaffected. Figure 5.22 shows the transport in higher LL of sample 229 measured in orthogonal crystal directions. The current is fed in two directions relative to the hexagonal crystal structure of ZnO (panel **a**) which simultaneously results in the current being fed either along or across crystal steps which exist as a result of the substrate preparation. Evidently, the transport is isotropic - the resistance of transport in both crystal directions (see panels **a** and **b**) resembles each other in both

magnitude and appearance. This is true for both when the sample is not tilted (panel **c**) and when it is tilted to $\theta = 44°$, which corresponds to beyond the first coincidence position (this explains the lack of a quantised ν = 7/2 state in panel **d**). The lack of anisotropy even under tilt is surprising, as it is clearly shown in AlGaAs/GaAs structures that an in-plane field can induce a stripe phase [143, 144].

Another possible realm for anisotropy is the transport around ν = 5/2. In the previous section we identified in Fig. 5.12 that when increasing T a lone reentrant integer quantum Hall state emerges. This is a localisation phenomenon, typically associated with 'bubble' phases of electrons[56, 57]. In AlGaAs/GaAs systems these bubbles appear at ultra low temperatures [139] usually as pairs or as fours, and are isotopic in transport. Their appearance is often concomitant to the presence of highly anisotropic higher LL transport, associated with stripes at half filling. Despite this past knowledge, only one reentrant state is observed in the transport in MgZnO/ZnO . Therefore it is difficult to speculate from transport alone whether the microscopic nature of the state is similar to the phases seen in AlGaAs/GaAs Again, more direct measurements, rather than simple transport measurements, will be required to decipher this aspect. What is evident though, is that the transport is isotropic, as shown in Fig. 5.23. This is expected from the bubble like nature of the reentrant state in AlGaAs/GaAs which should in theory not show an easy/hard axis. What is unexpected is its behaviour in a tilted magnetic field. This will be shown in Figs. 5.26 and 5.27.

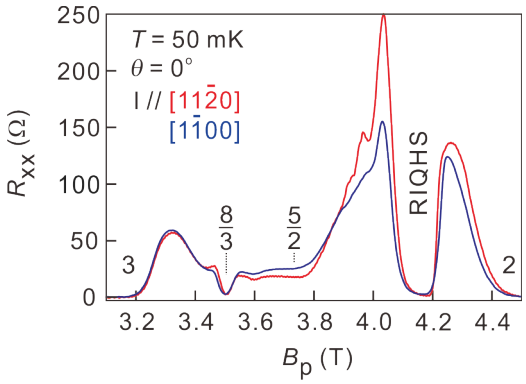

Figure 5.23: Crystal direction dependent magnetotransport around ν = 5/2.

The third plausible regime for anisotropy is the high tilt regime around ν = 3/2. As can be seen from Fig. 5.6, the resistance of this region increases dramatically when rotating the sample beyond $\theta \approx 42°$. This simultaneously leads to significant degradation of the fractional quantum Hall features. This is reminiscent of the tilt induced anisotropic phase observed in AlGaAs/GaAs either in higher LL or at ν = 5/2. [143, 144]. The current direction dependent magnetotransport is shown in Fig. 5.24. Though slight quantitative deviations indeed occur between the orthogonal directions, the transport is evidently isotropic. The temperature dependence behaviour too confirms this, with both crystal directions showing similar behaviour when decreasing T. This high resistance regime however is intriguing in many ways. The temperature dependence of this region is shown in Fig. 5.25.

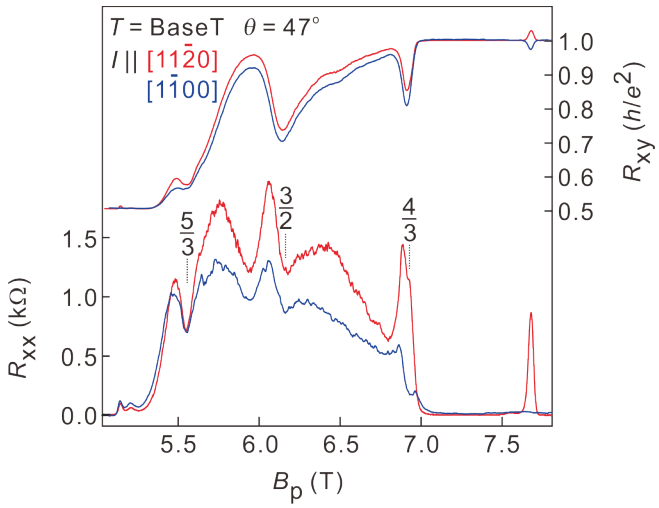

Figure 5.24: Crystal direction dependent magnetotransport around ν = 3/2 when the sample is rotated to an angle of θ = 47°.

We stress here that despite the absence of any obvious anisotropy, the Hall resistance in this regime shows extremely anomalous behaviour. While it is important to realise that the fractional quantum Hall states in this regime can not be conclusively identified as being quantised in the Hall resistance, minimum in the longitudinal resistance still do exist. However, outside the rational fractional fillings of ν = 3/2, 4/3 and 5/3, the Hall resistance tends towards either h/e^2 or $h/2e^2$ - reminiscent of the behaviour displayed by the reentrant integer quantum Hall effect. However, the direction of such deviation is not consistent with previous reports in the literature. For example, on the low field side of ν = 3/2, the Hall resistance tends towards h/e^2, whereas this would be expected to tend towards $h/2e^2$ based on previous work in AlGaAs/GaAs 2DES[41]. Moreover, the behaviour is very broad across a wide range of fillings. This is somewhat reminiscent of the Hall resistance in 2DES with intentionally incorporated alloy scattering within the vicinity of the 2DES [140]. We are not aware of a mechanism to explain such behaviour but highlight that in the case of MgZnO/ZnO where x = 0.01, it is difficult to define a clean heterointerface and the electrons must penetrate some depth into the MgZnO layer. This may lead to similar alloy scattering and thus be related to the result reported in Ref. [140]. Despite this, the onset of the high resistance regime itself remains enigmatic. While undoubtedly the behaviour only exists when the system is fully spin polarised, the sudden onset remains troubling. For example, a clear correlation with the analysis in 5.18 can not be established. If the onset was related with a certain spin polarisation of a fractional state, the borderline between low and high resistance would be gradual or even zig-zag like. Moreover, the onset can not be correlated conclusively with the origin (B_{eff} = 0 T) of the j_{CF} fit lines. For the states at lower magnetic fields than ν = 3/2 it seems that the j_{CF} = 0 coincidence is realised, suggesting the electron LL have crossed, all while the resistance stays low. This is however not the case on the high field side, where j_{CF} = 0 can not be identified. This suggests that there are other energetic terms, which are yet unknown, which exist and affect the onset of this behaviour. Its sharpness is also astounding. While in AlGaAs/GaAs 2DES a high resistance, anisotropic state has been reported under a tilted field (as discussed above) [143, 144], the transition to such behaviour is much softer than the data presented here. Given the current depth of knowledge, we are relinquished to speculating that the high resistance regime observed at high tilt signifies to a charge density wave like ground state which is induced by the loss of spin degeneracy. The lack of anisotropy may be simply due

to the six-fold geometry of the host crystal, which, may result in no easy/hard axis developing.

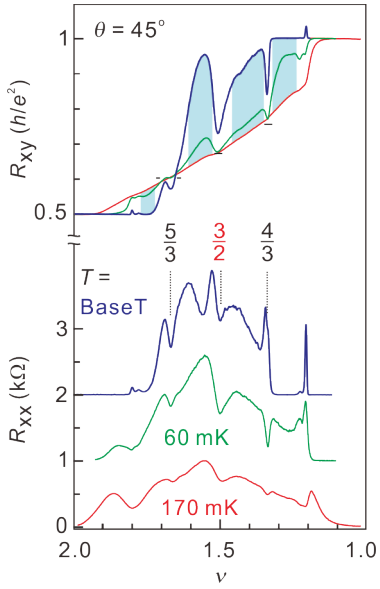

Figure 5.25: Temperature dependent magnetotransport around ν = 3/2 at a tilt angle of θ = 45°. Developing reentrant integer quantum Hall states in R_{xy} are shaded light blue

We speculate that the lack of anisotropy even in tilted fields may also be related to the relatively narrow wavefunction of the 2DES in MgZnO/ZnO heterostructures. We have quantified this is section 4.1 to be less than 10 nm. This is much more narrow than the quantum wells usually found in high mobility AlGaAs/GaAs samples. As a rule of thumb, when the magnetic length of the in-plane magnetic field component becomes comparable to the wavefunction width significant effects can be expected. This needs to be roughly 10 Tesla in the case of ZnO. In contrast, a 40 nm QW in a AlGaAs/GaAs structure will but much more susceptible. Higher in-plane magnetic field studies may therefore be a useful tool for investigating the wavefunction width via other experimental means. A

We now leave discussions of anisotropy and return to the reentrant integer quantum Hall state observed on the high field side of ν = 5/2 (see Fig. 5.12and 5.23). In tilting the heterostructure we discover a spectacular character of this state. While remaining isotropic, the reentrant state in MgZnO/ZnO moves dramatically in B_p when rotating the sample and enhancing B_t. This behaviour is shown in Fig. 5.26 as two indicative transport traces and Fig. 5.27 when fully mapped out. Throughout the process of rotating, the Hall resistance always tends towards $h/2e^2$, even after the state as traversed the ν = 2 integer state. This is in stark contrast to the results observed in AlGaAs/GaAs 2DES [145]. In that system, even modest tilt angles of $\theta \approx 10^\circ$ have a significant effect on the stability of the reentrant states, who are considered to "melt" as a result of the in-plane field. Instead, the anisotropic phase discussed above emerges. Prior to their melting, however, the reentrant states clearly do not move in B_p ($i.e.$ filling factor). The result in MgZnO/ZnO is therefore puzzling, and it strongly suggests that the states observed are unique.

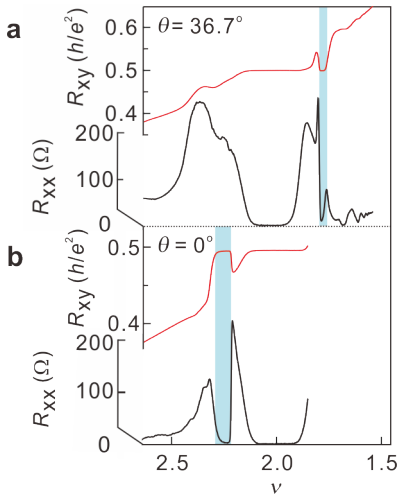

Figure 5.26: Magnetotransport trace of the reentrant integer quantum Hall state when the sample is **a** tilted to $\theta = 36.7°$ and **b** 0°. For both traces T = 60 mK.

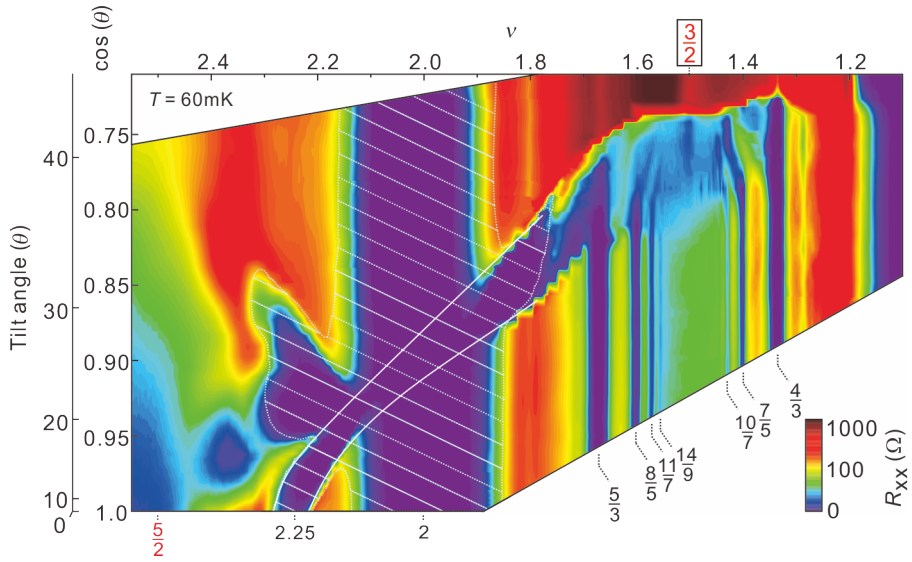

Figure 5.27: Mapping of magnetotransport at T = 60 mK with rotation. Areas corresponding to a quantised Hall resistance of $h/2e^2$ are hatched. The primary trajectory of the reentrant integer quantum Hall state is indicated by bold white guide-to-eye lines.

To understand this lone reentrant integer quantum Hall state further temperature dependent measurements are presented in Fig. 5.28. When the sample is not rotated the activation energy of the state is on the order of 1 K. Again, this highlights a discrepancy with the reports in AlGaAs/GaAs 2DES. The activation energy is an order of magnitude higher inMgZnO/ZnO [139]. The activation energy is slightly modified when the sample is rotated and the state is forced to traverse ν = 2, falling somewhat but still remains many hundreds of millikelvin. Observing the transport closely reveals a link with a previously identified feature in the transport. The temperature dependence shows that the transport at the filling factor corresponding to the reentrant integer quantum Hall state begins relatively low in resistance when the sample is warm, but then shoots up at intermediate temperatures. It is only a low temperatures ($T \leq$ 50 mK) that non-dissipative transport is achieved. Returning to the 400 mK mapping of magnetotransport presented earlier in this thesis in Fig. 5.5, it is revealed that the small portion of high resistance on the low field side of the ν = 2 integer quantum Hall state (which is tentatively associated with $N_e = 1, \uparrow$ electrons) is actually precursors of the reentrant integer quantum Hall effect presented here.

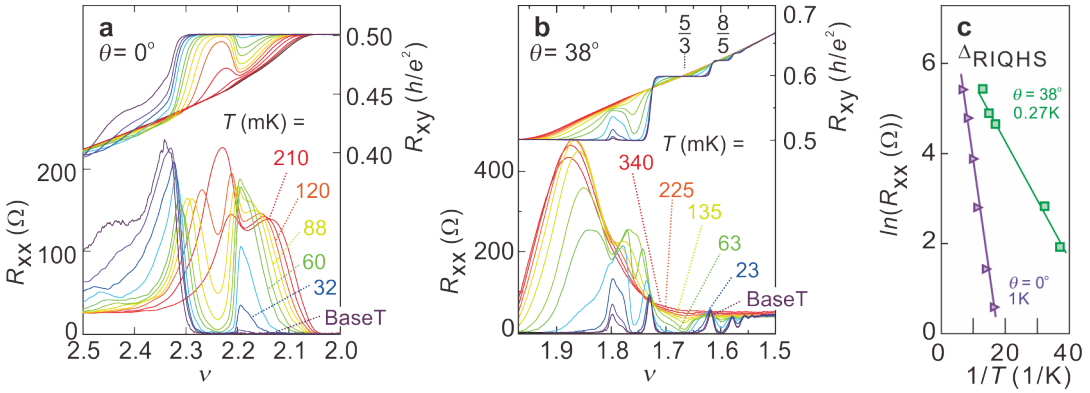

Figure 5.28: Temperature dependence of the reentrant integer quantum Hall state when **a**, the sample is not rotated and the state is observed at ν = 2.25 and **b** when the sample is rotated to an angle of $\theta = 38°$ and the state is observed at ν = 1.75. **c** Arrhenius plots of the longitudinal resistance quantifying the activation energy of both traces.

The location and trajectory of the reentrant state also coincides with regions of transport where we observe hysteretic behaviour depending on the direction of the magnetic field sweeps. This is shown in Fig. 5.29 where the sample is tilted to moderate tilt angles and the temperature is high. Such hysteresis has been observed in other 2D systems such as the AlGaAs/AlAs 2DES when levels are brought close to coincidence and then suddenly swap[146]. The behaviour has been attributed to a ferromagnetic domain structure developing resulting in the scattering of electrons along domain boundaries. Pulling all the pieces of evidence presented together, we consider the lone reentrant integer quantum Hall state observed in MgZnO/ZnO to be a manifestation of a unique interplay of spin physics with the nodal wavefunction structure of the second LL. Arguably precursor features have been observed in the AlGaAs/AlAs 2DES, but failed to develop into the rich display observed in MgZnO/ZnO . We must conclude that this is a result of the high quality of the MgZnO/ZnO 2DES.

similar physics, just in a much cleaner system, and therefore unrecognisable manner. This is seen in the zero tilt data where the state is completely localised and hence is not picked up in transport as a finite resistance.

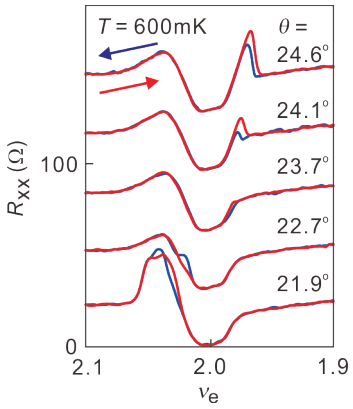

Figure 5.29: Hysteretic magnetotransport at elevated temperatures (T = 600 mK) around $\nu = 2$ when tilting the sample to moderate tilt angles.

This is perhaps not surprising, as the same effect is observed only in higher LL in AlGaAs/GaAs as well when a node is present in the electron wavefunction. Its sudden melting in our case when moving towards ν = 5/2 from high field is therefore associated with a spontaneous level crossing to $N_e = 0$ character. This would explain its movement with enhancing E_z, as the partial filling corresponding to $N_e = 1$, or alternatively, the switch to $N_e = 0$ is shifting.

Chapter 6

Summary and new frontiers

In this final section we aim to summarise the results and impact of this thesis while highlighting a number of open questions and frontiers. Arguably some of these are relatively straight forward, for example, the reproducibility of the ground states observed in this work and their stability as a function of 2DES parameters. This is particularly interesting in regards to the even-denominator fractional quantum Hall states, whose stability are only now being understood in heterostructures containing remote-dopants. However some questions require a much more technical experimental approach to be answered. Again, for the even-denominator states this would incite visions about determining the wavefunction which describes the ground state[10, 43, 44]. The following frontier would be to probe the statistics of the ground state's excitations. In this quest, transport measurements begin to fail and can lead to conflicting interpretations. An example is the surprisingly elusive question of "what is the spin polarisation of the 5/2 state?" (in AlGaAs/GaAs heterostructures). For decades, this remained murky through the analysis of transport measurements in isolation [147]. Ultimately, it was direct measurements of the spin-polarisation through nuclear magnetic resonance techniques which solved the puzzle[47, 48], and suggested the ground state is fully spin polarised. A similar quest has unfolded around the probing of the fractional charge of this state's quasiparticles, which were revealed to be e/4 through mesoscopic measurement techniques [49, 50, 53]. While it is not the goal in the MgZnO/ZnO 2DES to reproduce such experiments, it is certainly a priority to establish such experimental techniques enjoyed in other material systems, so that new facets of the physics maybe unleashed. In the remainder of this thesis we introduce two techniques which are sure to contribute significantly in future works in answering open questions which remain.

6.1 Gating of heterostructures

As evident in many portions of this thesis, the charge density of the 2DES itself is shown to impart significant parameter renormalisation in MgZnO/ZnO heterostructures. The is most obvious in the effect it has on the spin susceptibility, which we show can pass through a value of 2 (when $n \approx 2.0 \times 10^{11}$ cm^{-2}). In terms of single particle energetics, this condition indicates that the Zeeman energy becomes the same size as the cyclotron energy, and hence spin split LL spontaneously swap. From an experimental point of view, access to the charge density degree of freedom through electrostatic gating would therefore greatly enhance the range of experiments possible for probing such phase transitions. A noble frontier is obviously an investigation of the ν = 3/2 state, both in terms of its stability as a function of

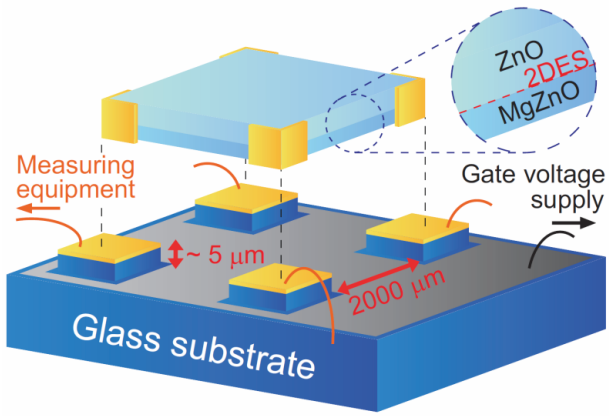

Figure 6.1: Cartoon representation of the air-gap FET device structure. The MgZnO/ZnO heterostructure is placed on top of four pillars which act as the bonding pads to contact the 2DES. These simultaneously separate the sample surface from the gate electrode, which is again bonded independently. The device is measured in van der Pauw geometry.

density while maintaining a common disorder landscape, and the pursuit of a better understanding of the emergence of this state with the low-field spin susceptibility. Indeed, it may be possible to induce this state in an un-rotated position if the density of the 2DES may be reduced and $g_e^* m_e^*/m_0$ enhanced. This would therefore eliminate complications arising from of an in-plane magnetic field, both in terms of experimental technicalities and physical interpretation. However, for all devices reported in this thesis, none have access to the charge density degree of freedom. That said, the technology to tune the Fermi energy of MgZnO/ZnO heterostructures exists and has been reported in the literature. Previous generations of gated devices have utilised two techniques. Through the deposition of a layer of insulating aluminium oxide it is possible to form a conventional metal-oxide-semiconductor field effect transistor device [75, 85, 148]. In such devices, however, the extensive series of fractional quantum Hall states that have been reported in this work (see Fig. 2.6 for an overview trace of an un-gated sample) have not be been reproduced. For example, in Ref. [148] the most fundamental fractional state at ν = 1/3 is unambiguously identified, but the observation of higher order fractional states beyond, such as 2/5, 3/7, etc. was not achieved. We consider this to be a result of significant disorder induced during the lithograph preparation of a Hall bar device and/or the deposition of the alumina insulating layer. Another gating technique involves the formation of a Schottky contact on the surface of the sample through the spin-coating deposition of the polymer PEDOT:PSS [86]. This polymer however has acidic character, and likely undergoes some chemical interaction with the crystal surface (which is known to dissolve in acid). This technique was developed when the heterostructure quality was significantly poorer and only the integer quantum Hall effect was observed. Its applicability to state-of-the-art structures therefore remains to be verified.

The above technical aspects are emphasised because the author considers that key to the unveiling of many of the fragile ground states identified in this work has been the exceptionally simple device fabrication procedure. For the vast majority of experiments raw chips of a heterostructure in van der Pauw geometry were used. These devices are fabricated in the following way: a chip is cleaved (or rather cracked, as ZnO will not cleave) from a freshly grown wafer and then contacted at the edges with indium solder. The only thing to ever touch the surface is soft wipes, when the sample is turned

over to be cracked. No chemicals or etchants touch the surface. No annealing is undertaken to achieve an ohmic contact. The process is fast and removes unknowns which can affect sample quality to the ultimate limit. While the ideal solution would be to gate these devices, the macroscopic size of the chips makes this difficult due to short circuiting problems between the contact and gate or 2DES and gate, for example in the case of depositing metal on the sample surface. To circumvent these problems, and those of the MOSFET or organic Schottky gates identified above, we have developed a gating unit which is entirely independent from the heterostructure under investigation. We have coined this the "air-gap FET".

The device is designed with influences from reports in the fields of organic FET research[149] and more close to home, suspended graphene[7]. Particularly for the latter, in separating the graphene flake from the substrate (typically SiO_2) a dramatic increase in sample quality was achieved [7]. This has revealed the underlying physics of the system which was previously masked by disorder [150]. The fundamental goal of the design is to keep the surface clean and untouched, while retaining the ability to apply an electric field. We have developed the air-gap FET technology to be used on macroscopic size MgZnO/ZnO heterostructures and the results are reported in detail in reference [151]. A device is schematically shown in Fig. 6.1. It consists of two components: the sample to be measured, which is a macroscopic chip cleaved from a grown wafer, and the gating unit. The gating unit consists of a glass substrate on which four pads are defined by photolithography. By exposing the glass substrate to high concentration HF acid, the remaining surface area is etched away to yield pillars of roughly 5 μm height. Alternatively, pillars may be defined by photoresist. The orifice surface area is then covered by a metal electrode through evaporation. This defines the gate. To the tops of the pillars metal is again deposited, but this is isolated from the orifice metal. For the sample, ohmic contacts are evaporated at the edges, which yields a device measurable in van der Pauw geometry. No lithography is performed on the sample. It is then placed on top of the pillars and makes contact with the metal surface present. The chip is then securely fastened by a BeCu flat spring which is screwed to the sample holder. Once the sample is fastened, it can remain in place and survive multiple cooling cycles. Finally, the tops of the pillars are contacted through wire bonding, as well as the orifice which acts as the gate. This completes the device. Ultimately, the surface remains separated from the gate, and therefore clean. We have found however that a short treatment of the surface with oxygen plasma is required to achieve satisfactory modulation ratio dn/dV_G.

While organic material and graphene devices usually have an air-gap distance on the order of 100 nm, the macroscopic size of the van der Pauw chip under investigation in our design imparts the requirement of a larger air-gap. Currently this gap is on the order of 5 μm. This reduces the risk of leaks between the sample and the gate electrode but simultaneously results in a significantly higher voltage being required to modulate the 2DES density. As can be seen in Fig. 6.2, the charge density maybe tuned from complete depletion to saturation (corresponding to the density of a virgin sample) between -100 to 200 V. Once this loop is established there is no hysteresis. The mobility simultaneously shows a dependence on the gate voltage, increasing with higher density as a result of more effective screening of disorder. We emphasise that the device under investigation in Fig. 6.2 comes from a wafer which displayed modest mobility to begin with. The ability to reproduce the virgin characteristics is the important aspect of the device which is conveyed in the data.

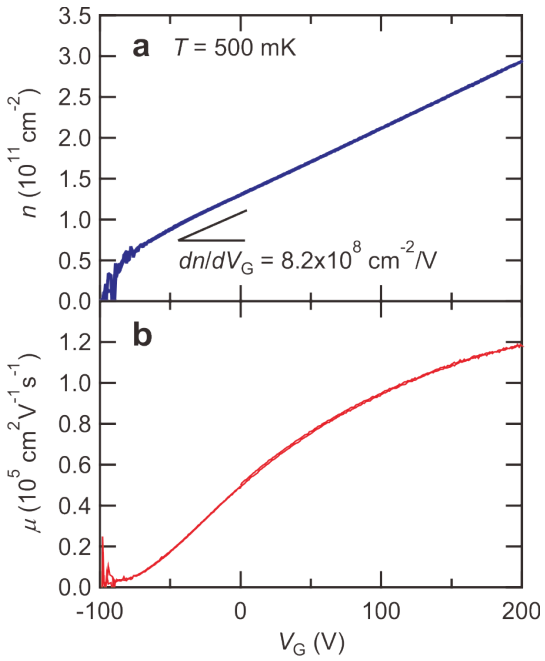

Figure 6.2: **a** Charge density and **b** mobility as a function of gate voltage for a MgZnO/ZnO air-gap field effect transistor device at low temperature (T = 500 mK).

The quality of magnetotransport of devices in this arrangement in ultra-low environments will be examined soon. Before this however we investigate the interplay of a gate-tuned density and the renormalisation of $g_e^* m_e^*/m_0$ on a different sample to that shown in Fig. 6.2. For the remainder of the discussion we assess a second sample which is of higher quality (the raw wafer has characteristics of n = 2.3 $\times$ 10^{11} cm^{-2} and μ = 400,000 cm^2 V^{-1} s^{-1}). In this measurement apparatus the voltage range was limited to $\pm$ 40 V due to the presence of capacitors in the line filters. This limits the range of densities accessible. These values drop when exposing the sample surface to oxygen plasma, as evidenced by the maximum n accessible in the experiment $\approx$ 2.1 $\times$ 10^{11} cm^{-2} but evidently the transport is still clean. Usually the carrier density depletion may be compensated through applying an external gate voltage, but this was not possible in the experiment presented due to technical reasons. In Fig. 6.3 data presenting discrete values of $g_e^* m_e^*/m_0$ quantified at different gate voltages under finite tilt are displayed. These values were measured by rotating the sample to finite angles ($\theta \approx 30^\circ$) and sweeping the gate voltage. As identified in Fig. 4.6, depending on the spin orientation of electrons at the chemical potential the resistance is high or low. We use a similar technique here to determine $g_e^* m_e^*/m_0$ for a range of gate voltages. It can be seen that a very good quantitative agreement is achieved between the gate-tuned values and those of individual samples. We note that the real range of $g_e^* m_e^*/m_0$ achievable is slightly wider than the data presented here. It therefore seems that the renormalisation of this parameter is an intrinsic effect purely related to the strength of Coulomb interactions, which is dependent on the charge density. We can therefore approach transport measurements with the goal of specifically probing features which are sensitive to the spin degree of freedom.

We now move to the transport, which is shown in Fig. 6.4. This was taken at T = 50 mK in a dilution refrigerator where the sample is in vacuum at the end of a cold-finger. In panel **a** we show a magnetic field sweep of the transport where the charge density is maximally accumulated. Fractional states up to ν = 8/3 are observed, including robust states around ν = 3/2, at 5/3, 8/5, 7/5 and 4/3, and 2/3 below ν = 1. In **b** we map the full magnetic field range across the accessible voltages and show that both the integer and fractional quantum Hall effect is observed even under external voltage. The slope of each fraction represents the filling factor. It can be seen that when reducing the charge density the series of fractional quantum Hall states originating from the lower spin branch of the lowest LL emerges, along with a compressible sea at ν = 1/2. All conducting electrons contribute to transport and no parallel conduction occurs - for all (robust) quantum Hall states the longitudinal resistance is zero and slopes remain linear in n. The quality of transport may be further advanced through both using higher quality samples to begin with and by refining the oxygen plasma treatment technique. It is unfortunate that this treatment step is required, but by shortening the length and/or strength of the treatment, damage may be further mitigated. Initially this treatment step was carried out for a duration of 30 seconds. However, we have now determined that only 3 seconds exposure yields a sufficient modulation ratio. With such short treatment the charge density of the 2DES is barely affected.

Finally the concept of exploring features of transport which display a distinct dependence on the spin degree of freedom is reintroduced. Such features include the reentrant integer quantum Hall state which is identified on the low field side of ν = 2 in panel **a**. With lowering the density and increasing $g_e^* m_e^*/m_0$, this feature appears to cross ν = 2. This agrees completely with the results presented in Fig. 5.27, but importantly, there is no in-plane magnetic field applied in this figure. Therefore, the reentrant state identified and its behaviour with enhancing E_z is purely related to the spin degree of freedom, rather than modified interaction effects when applying an in-plane field. Access to this degree of freedom therefore greatly compliments the ability to enhance E_z through rotating the sample.

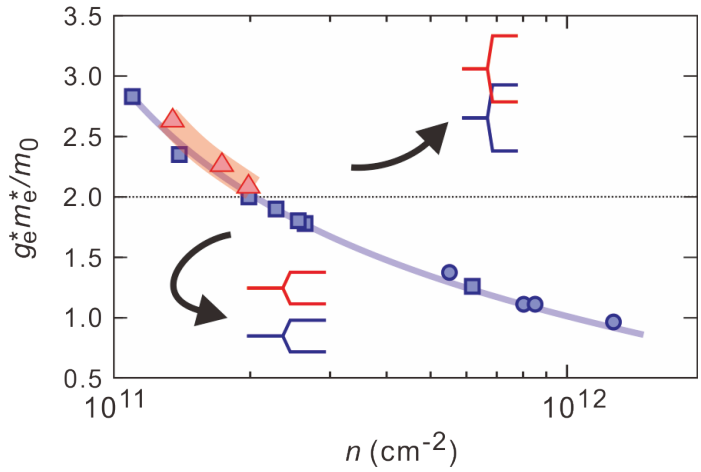

Figure 6.3: $g_e^* m_e^*/m_0$ of the MgZnO/ZnO 2DES as a function of charge density for single samples (blue squares from data of this thesis and circles from Ref. [100]) and for the air-gap FET device discussed in the text.

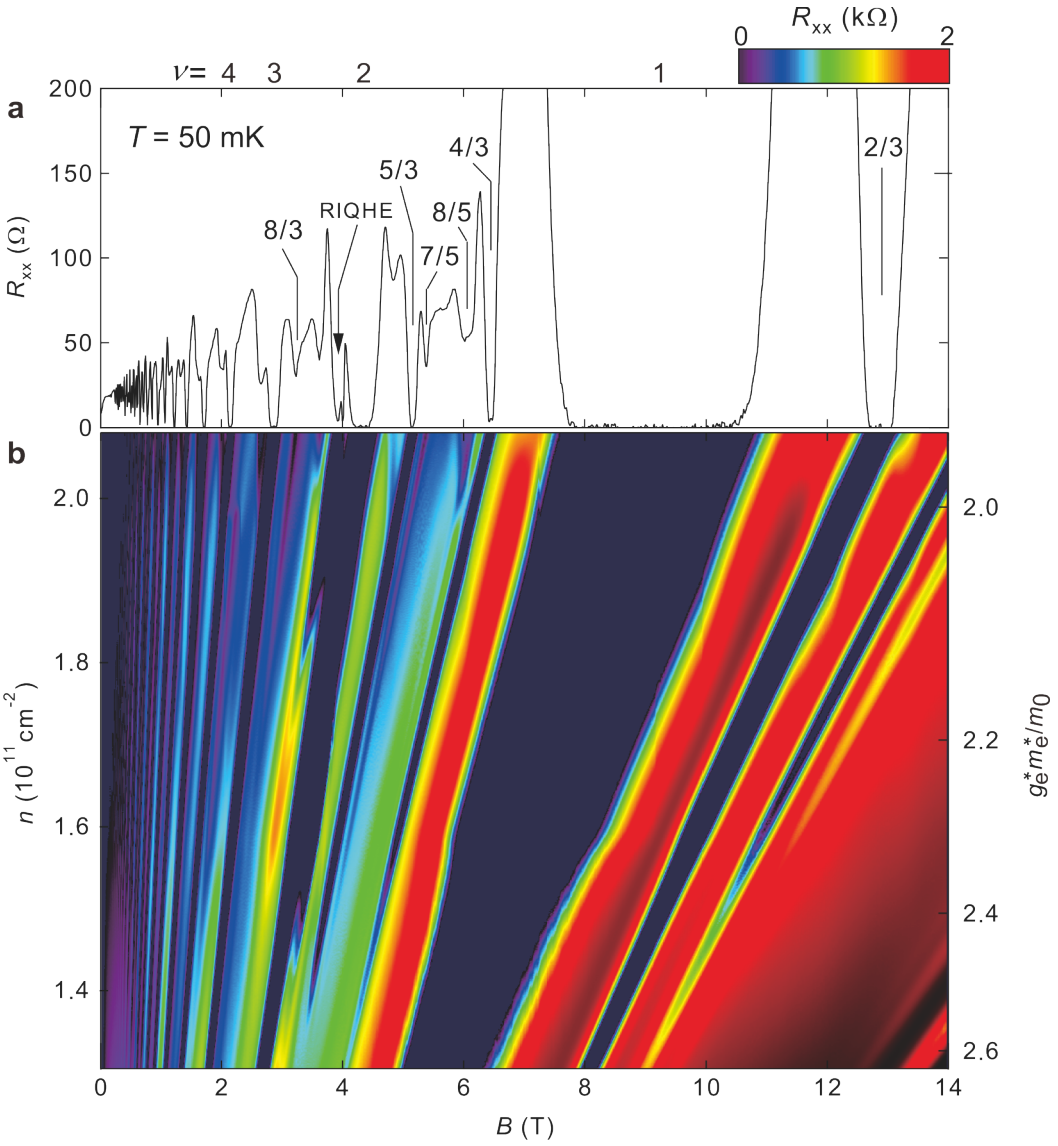

Figure 6.4: Mapping of magnetotransport of an air-gap field effect transistor device. Panel **a** shows a line trace for the maximum density n = 2.1 $\times$ 10^{11} cm^{-2} , showing robust integer and fractional quantum Hall features. **b** Mapping of the magnetotransport as a function of density and magnetic field. On the right panel, $g_e^* m_e^*/m_0$ is noted.

This added degree of freedom also emerges as a powerful tool for observing the hysteretic transport which is known to emerge near level crossings in the MgZnO/ZnO 2DES. Specifically, we focus around ν = 2, as shown in Fig. 6.5. As shown at the end of chapter 5, magnetic field sweep direction dependent hysteretic behaviour was observed around ν = 2 at high temperatures. This was considered to be a signature of spontaneous level swapping in the context of quantum Hall ferromagnetism [146]. In Fig. 6.5 we present a number of discrete traces which show either hysteresis in B or V_G. Panel **a** displays traces with V_G constant, with the magnetic field swept. Very distinct hysteretic behaviour is observed on the low field side of ν = 2, which corresponds to the realm of the reentrant integer quantum Hall effect identified. Panel **b** on the other hand plots interpolated traces which form the transport presented in Fig. 6.4, which was formulated by holding the magnetic field constant and sweeping V_G. While it is not presented in Fig. 6.4, both directions of the V_G sweep are recorded in formulating the data set and hence can enable an analysis of voltage sweep direction dependent hysteretic features. In panel **b** a number of cuts of Fig. 6.4 are presented for the same densities as shown in panel **a**. A pattern of hysteresis distinct to that of the magnetic field traces develops. In contrast to the B-field sweep data, no hysteresis is shown on the low field side of ν = 2. Rather on the high field side at dilute densities, a reproducible series of hysteretic traces are observed both in the vicinity of integer and fractional quantum Hall states. It is important to note that the temperature in these traces is thought to be constant as the magnetic field is stationary. Therefore, the contrasting hysteresis pattern gives clues about the location of level swapping in the vicinity of ν = 2, which in turn may help to elucidate the orbital character of the ν = 3/2 ground state. This work remains ongoing, and will be analysed in detail in a future dedicated publication.

We note that the report presented here and in Ref. [151] is specific to the MgZnO/ZnO 2DES. However, this technique in theory is applicable to a wide range of heterostructures and even 2D materials. For other heterostructures the procedure would be an analogue of that presented here. However for 2D materials it could be imagined that the gating unit could be clamped onto a substrate which has the exfoliated 2D materials already deposited and contacted. While in recent years the advent of boron nitride as a gate dielectric has preserved the high quality of transport in top and bottom gated graphene devices [129], it would become redundant in the event of using a top gate which is spatially separated from the sample surface. Ultimately, it may prove that the air-gap FET results in less disorder further enriching the physics.

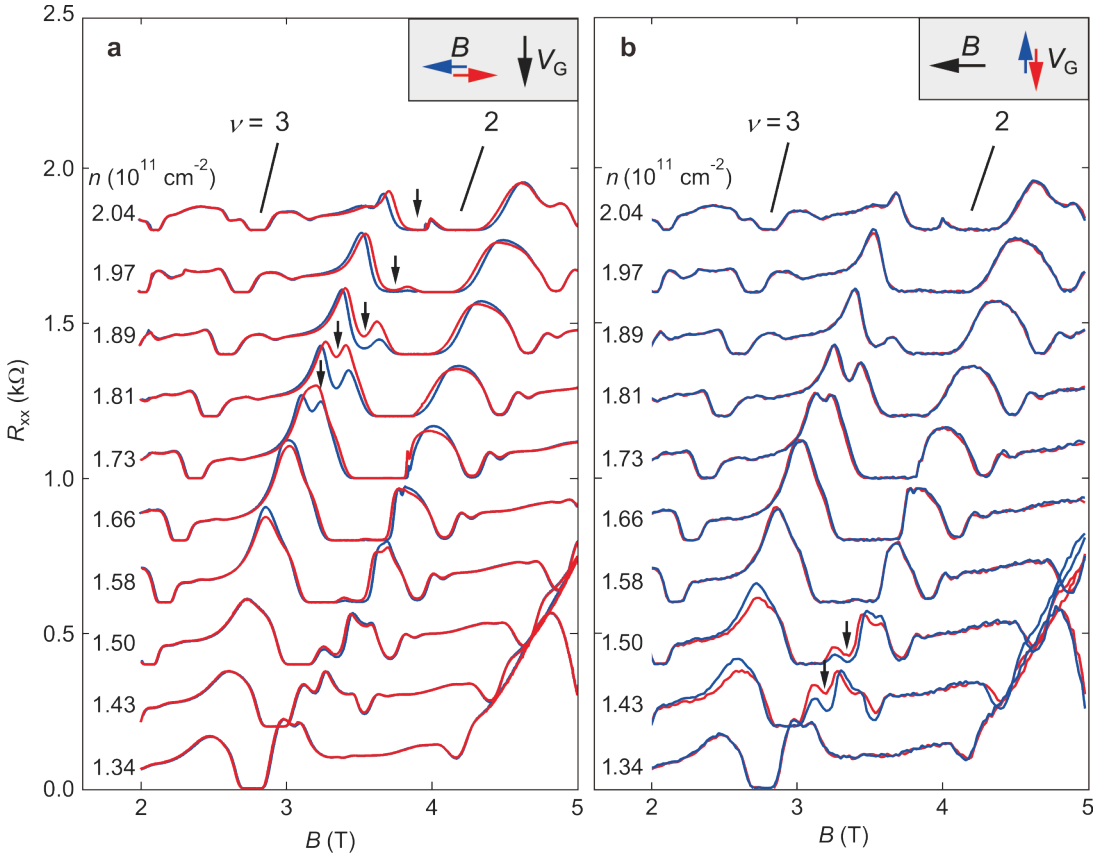

Figure 6.5: Discrete magnetotransport traces as a function of B. Panel **a** displays traces where the field is swept with constant V_g. Panel **b** displays discrete traces which are cut from the transport used to formulate Fig. 6.4. Arrows in both sets of data indicate regions of transport which display rich hysteretic behaviour.

6.2 Mesoscopic transport

In ultra-clean 2DES the mean free path of charge carriers can reach macroscopic scales. This is defined as,

$$l_{mfp} = \frac{\mu k_F \hbar}{e} \tag{6.1}$$

and defines statistically the length an electron travels on average before a scattering event. In ultra-high mobility AlGaAs/GaAs this can reach values of 300 μm. Using electron-beam lithography techniques, it is possible to define structures much smaller than such length scales. In doing this, transport is said to make a transition to the ballistic regime, where electrons can pass the entire length of the device without scattering. A number of interesting effects are observed in such a regime, including quantised conductance in 1D constrictions [152] and oscillations in the sample resistance when the electron motion in a magnetic field is commensurate with an externally applied periodic modulation [153, 154]. Such a modulation can be achieved through a number of methods. Most commonly, it is achieved by either putting dots on the surface which modulate the density directly below, or by drawing stripes perpendicular to the current direction across the length of the Hall bar. Such commensurability effects have been explored in MgZnO/ZnO heterostructures and are briefly introduced here.

A main result of this thesis is the reproducible production of samples with electron mobilities in excess of 500,000 cm^2 V^{-1} s^{-1} . In such heterostructures, the mean free path approaches 5 μm. While this still pales in comparing to AlGaAs/GaAs heterostructures (as the mean free path is not scaled by the effective mass), it does allow access to mesoscopic experiments which occur on relatively small length scales. For the commensurability effects we define patterns which apply a density modulation on the 2DES on scales of roughly 200 nm. The density modulation is imposed by first defining anti-dots by electron beam lithograph on top of the Hall bar and then by etching away the a finite thickness of the capping MgZnO layer. This leads to damage on the surface, which affects the density of the underlying 2DES. Alternatively, with the use of negative e-beam resist, dots may be defined on the surface and left as resist. This will affect both the surface potential of the sample and apply a tension on the underlying crystal surface during cooling of the sample. These lead to a periodic modulation without the need to etch (and hence damage) the Hall bar.

In the case of anti-dots on the surface, the condition for observing commensurability oscillations is given by,

$$\frac{2R_c}{a} = i \tag{6.2}$$

where

$$R_c = \frac{\hbar k_F}{eB} \tag{6.3}$$

Here, k_F is dependent on the degeneracies in the system, and i is an integer signifying the number of dots encircled. a is the period of the modulation imposed. With a tuning of a to be moderately long, the oscillations may emerge at low magnetic field before the development of Shubnikov - de Haas oscillations and the quantum Hall effect. When the condition described is achieved a peak in resistance occurs as shown in Fig. 6.6**a** and **b**, which shows low field magnetotransport of a MgZnO/ZnO heterostructure. The resistance increase may be accounted for either by the pinning of cyclotron like orbits which do not contribute to conduction, or an increase in scattering due to 'run-away' orbitals of electron motion. In the experiment, the red traces correspond to portions of the Hall bar which have a

periodic modulation imposed and the black trace to a neighbouring section of the Hall bar without the modulation. It is clear that the modulation causes significant changes to transport at low field, but the effects wear off as the field is increased. In panel **a** the modulation is in the form of a triangular lattice while in **b** it is a square lattice. Qualitatively the result is similar. Orbitals containing up to roughly 7 dots may be identified in the triangular lattice arrangement. The circumference of such an orbital approaches the mean free path of electrons and sets the limit on the number of observable peaks.

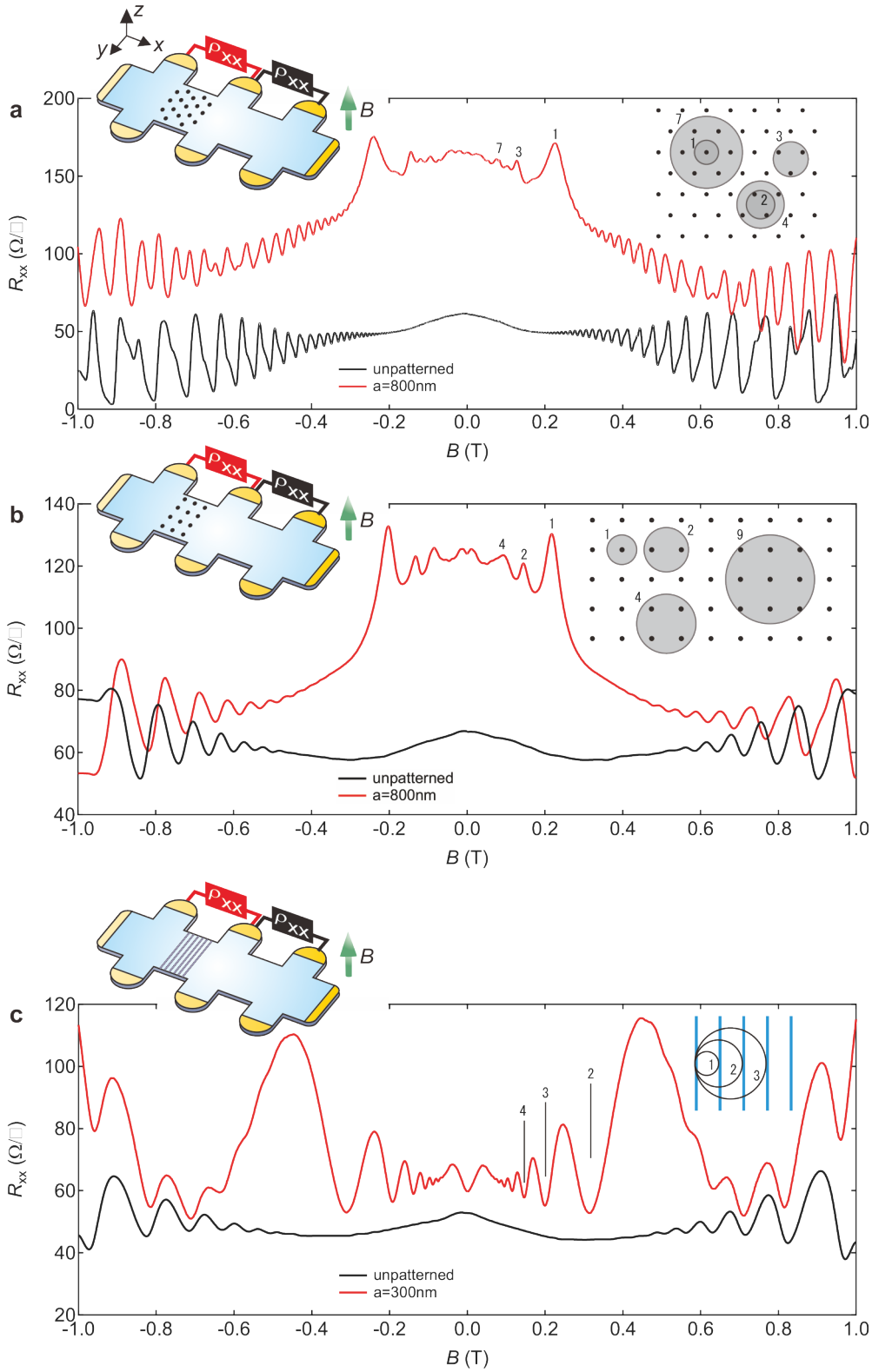

Figure 6.6: Magnetotransport of MgZnO/ZnO which are subject to a periodic density modulation in the form of a **a** a triangular anti-dot array, **b** a square antidot array and **c** unilateral stripes of photoresist defined on the sample surface. The insets of each figure show the commensurability orbitals. The temperature is T = 50 mK in panel **a** and 500 mK in **b** and **c**.

The effect has also been seen in samples where unilateral stripes are placed on the surface. This is shown in panel **c**. The effect occurs under a slightly different condition,

$$\frac{2R_c}{a} = i - 1/4 \tag{6.4}$$

This last factor is as a result of an oscillating y component of the group velocity which modifies the conductivity parallel to the stripe direction. Theory has shown the minimum in longitudinal resistance to occur under the condition introduced above. In this experiment the stripes are defined by leaving the resist on the surface of the Hall bar and can be made extremely thin (20 nm) through careful control of the development time. The exciting aspect of such experiments is its application to investigating the Fermi contour of composite fermions at high fields in ultra-clean samples (see Refs. [27–29], among others in the literature). The observation of such peaks centred on half fillings (the effect manifests most prominently at ν = 1/2 and more weakly at 3/2) provides support for the idea that composite fermions act as non-interacting particles in an effective magnetic field either side of half filling in the lowest LL. This technique is powerful as it can be used for determining both the spin polarisation of composite fermions as it is inherently linked to k_F, which is dependent on the degeneracies present in the system, and any anisotropy in the Fermi contour. In MgZnO/ZnO , we have identified in section 5.3 that the behaviour of composite fermions both at odd and even p filling factors for $2 > \nu > 1$ is particular rich. The model invoked in Fig. 5.18 however utilises the coincidence of odd-denominator states to infer the behaviour of composite fermions in zero B_{eff} at half filling. A number of limitations were previously identified in this model. Therefore, probing the commensurability oscillations of composite fermions directly is an interesting theme. In the following figures we present preliminary results on this topic.

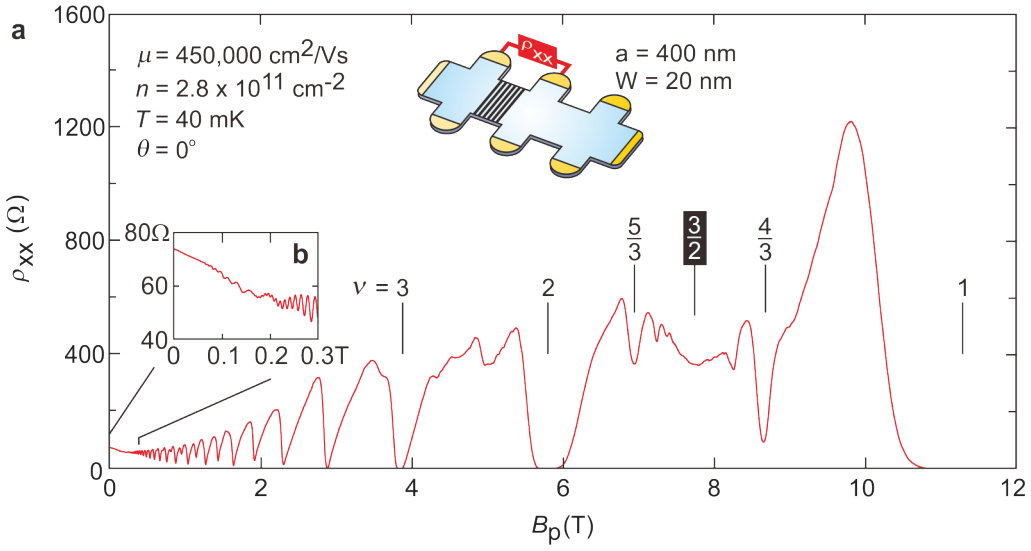

Figure 6.7: Magnetotransport of a MgZnO/ZnO Hall bar with a stripe pattern modulation (T = 40 mK). **a** Overview transport showing clear integer and fractional quantum Hall states. **b** a close up of the low field transport showing in addition to Shubnikov - de Haas oscillations an additional oscillation attributed to the commensurability condition of electrons.

Prior to any discussion of composite fermion commensurability measurements, it is essential to ensure that the quality of transport is extremely high. At least it would be expected that the fractional quantum Hall states around ν = 3/2 are robust, even in the presence of the periodic modulation. In Fig.

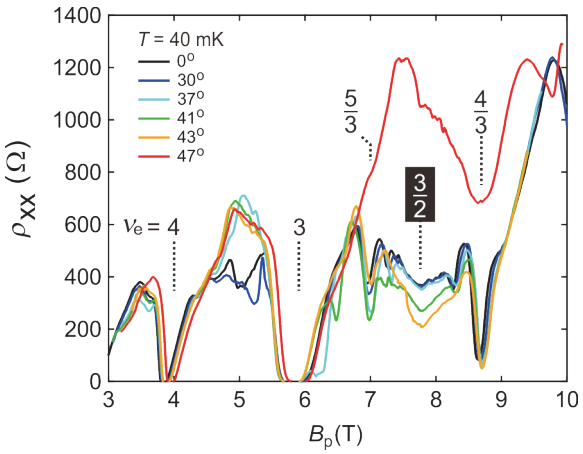

Figure 6.8: Magnetotransport of the stripe-modulated Hall bar with rotation. The tilt angles are noted in the top left of the figure. Prominent filling factors are noted.

6.7 we present transport on a portion of a Hall bar which has an e-beam resist defined stripe pattern on the surface of dimensions a = 400 nm and W = 20 nm. Pursuing extremely narrow stripes has enabled the high quality transport shown. As can be seen, fractional states around ν = 3/2 are indeed visible. Zooming in on the low field transport in panel **b**, it is clear that a modulation of the 2DES density is present, as weak oscillations in the resistance are resolved prior to the Shubnikov - de Haas oscillations. In terms of absolute resistance, the oscillations are smaller than shown in Fig. 6.6, likely as a result of the weaker modulation from the narrow stripes. It is also noted that at ν = 3/2 a weak dip is observed, similar to previous experiments [29] and the observations of electrons at low field.

Having established the quality of the heterostructure, we now add the degree of freedom of rotation. The goal, as stated above, is to observe oscillations centred on ν = 3/2 to identify if they (a), may be associated with the commensurability oscillations of composite fermions, and (b) if they provide any information about the spin polarisation. The raw rotation data is shown in Fig. 6.8 for a number of discrete tilt angles. It is important to note that the temperature is significantly higher than that of the traces presented in section 5. It can be seen that at intermediate tilt angles of $\theta \approx 41^\circ$ (green and yellow traces) the resistance at half filling is seen to fall. Beyond, this, the resistance rises (red trace). This is highly reminiscent of the behaviour in chapter 5. This will be touched on again later.

We now focus on the behaviour around ν = 3/2. The transport and analysis of this region is displayed in Fig. 6.9. Recalling that as per Eqn. 6.3, $k_{F,CF}$ should enter into the cyclotron radius of composite fermions, we can speculate that positions of commensurability features in B_{eff} contains information of the quasiparticles spin polarisation. This would take the form

$$k_{F,CF} = \sqrt{4f\pi n_{CF}} \tag{6.5}$$

where f would take the form

$$\begin{cases} f = 1 & polarised \\ 0.5 < f < 1 & partially \quad polarised \\ f = 0.5 & unpolarised \end{cases}$$

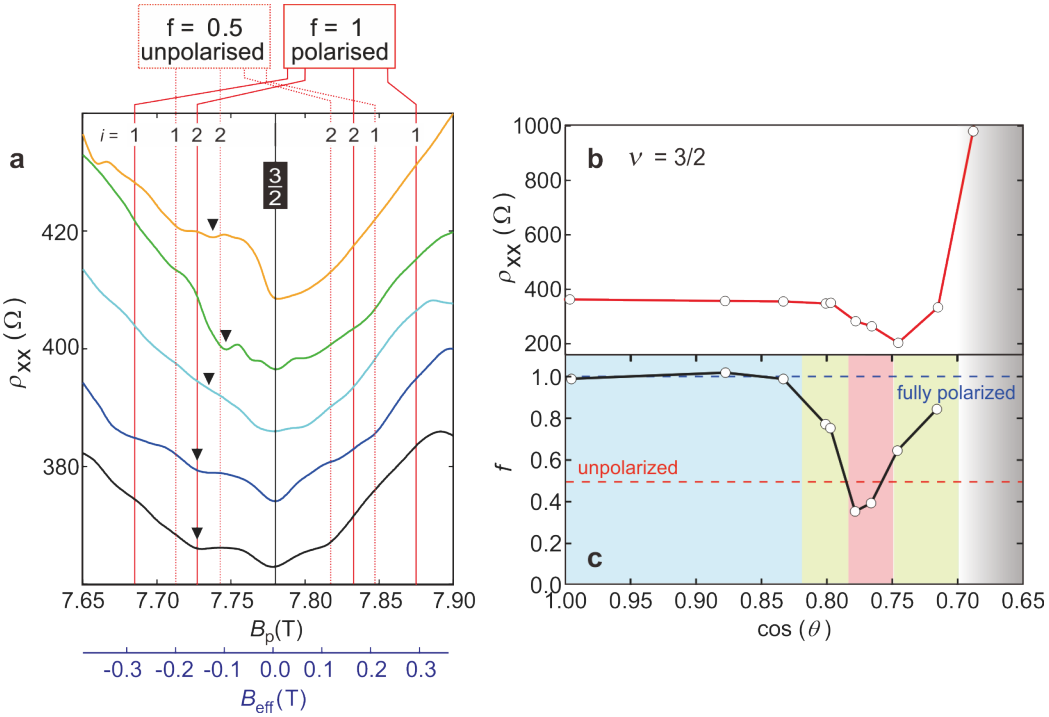

Figure 6.9: Composite fermion commensurability oscillations centred on ν = 3/2. **a** a close up of the transport in the vicinity of half filling. Coloured traces correspond to the tilt angles noted in Fig. 6.8. The horizontal axis plots both B_p and B_{eff}. **b** R_{xx} at ν = 3/2 as a function of tilt. **c** Calculated f value from the location of minima identified in panel **a**. The conditions for fully spin polarised (f = 1) and unpolarised (f = 0.5) are indicated.

Here, n_{CF} is the population of composite fermions at filling 3/2 = n/3, and B_{eff} is the effective magnetic field. This yields the cyclotron radius of

$$R_{c,CF} = \frac{\hbar k_{F,CF}}{eB_{eff}} \tag{6.6}$$

Anticipating this relationship, it is possible to identify the B_{eff} associated with oscillations corresponding to fully spin polarised composite fermions (solid red line) and spin unpolarised composite fermions (dotted red line) in advance, as shown in Fig. 6.9**a**. We then place the magnetotransport around ν = 3/2 on the same plot and compare oscillations in the resistance. A number of relatively weak features are observed in the longitudinal resistance around the i = 1 and 2 conditions for composite fermions commensurability. We tentatively associate these as commensurability oscillations of composite fermions and trace these features as a function of tilt. For negative B_{eff} an arrow is included on the magnetotransport to indicate this condition. At zero tilt, it appears that the minimum in the longitudinal resistance are achieved for the condition associated with f = 1, corresponding to a fully spin polarised composite fermion sea. This is in agreement with the result presented in chapter 5, which suggested the crossing of electron LL occurs at much higher tilt angles $\theta \approx 35^{\circ}$. Following the picture presented there, the composite fermion sea at zero tilt is therefore fully spin polarised in the N = 0 LL. Following the arrows in Fig. 6.9**a** shows that at higher tilt angles this feature moves to lower B_{eff}, only to move to higher fields at even higher tilt angles. We analyse this result in panel **c** of the figure in combination with the resistance at ν = 3/2, as per panel **b**. Panel **c** plots the value of f calculated from the magnetic field position of the oscillation minimum identified in panel **a**. As can be inferred from raw data, this value fluctuates with increasing tilt. It comes close to f = 0.5, indicated an unpolarised composite fermion sea at tilt angles of $cos(\theta) \approx 0.77$ ($\theta \approx 40^{\circ}$). Beyond, f rapidly increases indicating a shift to a fully polarised sea. Comparing with the resistance at ν = 3/2, we can get hints about the spin polarisation of the ground state. Firstly, according to this analysis, the crossing of electron LL occurs when the resistance at ν = 3/2 begins to rapidly fall. Beyond this, as the polarisation increases, the resistance at half filling increases and finally enters the "high resistance regime", as discussed extensively in the previous chapter 5. However, the previous chapter has clearly demonstrated that the ν = 3/2 ground state is indeed most robust just prior to the resistance shooting up at high tilt. Moreover, the ground state only appears significantly after the downturn in resistance at half filling is encountered. We therefore speculate on the current set of data that the crossing of electron LL, which would indicate a spinful composite fermion sea, occurs at tilt angles prior to those at which the 3/2 state is stabilised. This would suggest indeed the 3/2 state is resolved as a result of the spin polarised electrons of N = 1 origin.

The analysis presented is however by no means complete and requires advances in both sample fabrication techniques and measurement fidelity. First of all, the oscillations associated with the composite fermion commensurability are rather weak and asymmetric. Indeed, it could be argued that for positive effective fields the oscillations would suggest an unpolarised sea at zero tilt. Secondly, it is generally observed that the condition corresponding to the i = 2 orbital yields a more robust feature in the resistance. From simple "free mean path" considerations, this is counter intuitive, as indeed the i = 1 condition should be most robust. Third, a quantised ν = 3/2 state must be observed concomitantly to the oscillations associated with composite fermions in order to conclusively determine the tilt angles at which the ground state is stable. Only from such a direct comparison can the spin polarisation be analysed. This problem is compounded by recalling that $g_e^* m_e^*/m_0$ shows a strong dependency on n

in MgZnO/ZnO heterostructures. Therefore, it is not possible to define a universal range of tilt angles where ν = 3/2 is stable. Assessing the "ideal" charge density for such measurements combined with higher mobility samples and lower temperatures should resolve a number of these issues and lead to a very exciting experimental regime which is difficult to probe in other material systems.

6.3 Conclusions

In this section we conclude this thesis by canvassing and summarising its main experimental findings. Finally, comments on future prospects are given.

The growth of MgZnO/ZnO heterostructures by ozone-assisted molecular beam epitaxy has been explored extensively. This work is the first generation of samples to be grown using ozone as the oxidising agent [83]. Within a short amount of time it was realised that this technique yields vastly superior samples in comparison to previous generations of growth which utilised oxygen radical cells[80]. The switch to ozone, however, induces a unique set of technological challenges to ensure that the concentration of impurities originating from sources other than the ozone cell do not increase. Considerable experience has now been gained regarding the compatibility of ozone with various MBE components, namely the superalloys used throughout the chamber construction and for substrate holders. As a result of refining the choice of materials and their operational temperature, the concentration of impurities ultimately incorporated within samples has been reduced dramatically, and now is below the detection limit of analysis techniques such as secondary ion mass spectroscopy. Theory estimates this impurity to be on the order of 10^{14} cm^{-3} [90]. This is comparable to other clean traditional semiconductor systems, such as GaAs[79]. A systematic study of the growth window of samples including the exploration of the effects of magnesium doping down to the dilute doping limit ($0.1 > x > 0.003$) now enables the reproducible production of high mobility structures across a wide range of charge densities. As shown in Fig. 6.10, the peak mobility of the MgZnO/ZnO is now beyond 900,000 cm^2 V^{-1} s^{-1} . This occurs at a low Mg concentrations (≈ 0.01) where the effects of interface scattering are mitigated and is only made possible by ensuring the impurity content of films is suppressed. This value represents a raw mobility enhancement of roughly 5 times higher compared to previous generations of growth [80, 85], while accessing the dilute charge density regime. This is again an improvement of over 100 times the mobility of even older generations of samples grown by pulsed laser deposition [84].

The parameter space of the MgZnO/ZnO 2DES is explored through a number of experimental means, including luminescence, resonance and transport techniques. As a result of the unlocking the ability to produce high quality samples across a wide range of charge densities, the range of depth of possible characterisation experiments was greatly enhanced. Through photoluminescence measurements the energy levels of the quantum well formed at the heterointerface was probed and modelled through calculations. This reveals the 2DES at the interface occupies a single subband across a wide range of x contents, and has a wave function width on the order of 5 nm. The parameters which contribute to the spin susceptibility, $g_e^* m_e^*/m_0$, were explored quantitatively through cyclotron resonance, electron spin resonance and transport techniques. The two former techniques reveal values close to the band values but the latter reveals the renormalised values due to interaction effects. By reducing the charge density and increasing the strength of correlation effects $g_e^* m_e^*/m_0$ shows a strong enhancement and exceeds the value of 2 for $n \approx 2 \times 10^{11}$ cm^{-2} . This density fortuitously coincidences with a Mg

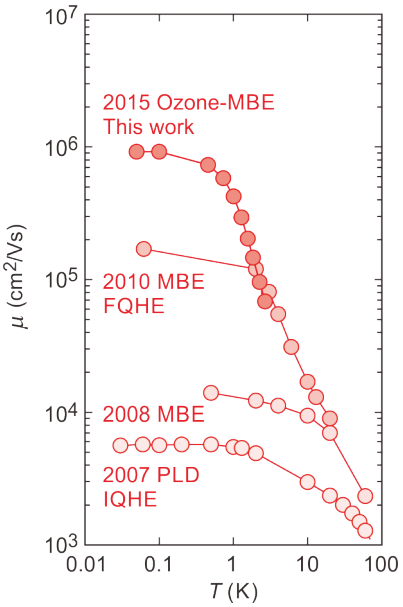

Figure 6.10: Summary of the mobility of the MgZnO/ZnO 2DES as a function of temperature for generations of growth up to and including this work.

doping regime which permits high electron mobility. To further understand the underlying quality of heterostructures, the transport and quantum scattering times were measured and compared across a wide range of densities. The ratio of these two values is roughly 10, indicating that the majority of scattering centres are remote to the 2DES. Through changing the thickness of the MgZnO capping layer we are able to infer that significant disorder is imposed by the sample surface. By making the 2DES much deeper, the quality of heterostructures is greatly improved. Finally, the peak in quantum scattering is observed to be roughly 20 ps. This value is comparable to the highest quality AlGaAs/GaAs heterostructures, suggesting the quality of MgZnO/ZnO samples is indeed among the highest crystal structures in existence.

The ground states observed in these high quality heterostructures have been revealed by cooling the samples down to temperatures on the order of 15 mK. In addition to robust integer quantum Hall physics, the fractional quantum Hall effect is observed over a large range of filling factors. In the lowest LL 2.6, higher order fractional states are observed up to index ν = 6/13, along with the most fundamental fractional state of ν = 1/3. At higher filling factors, a rich series of states is observed around ν = 3/2, 5/2, 7/2 and incipient features around 9/2. Moreover, an even denominator state is observed at ν = 7/2, which is the first observation of this state outside of the AlGaAs/GaAs system, all while the 5/2 state is conspicuously absent. Utilising the large spin susceptibility of the 2DES combined with sample rotation, we discover that forced level crossings have a dramatic impact on the strength and variety of ground states observed. This effect manifests most strikingly at ν = 3/2, which transforms from a compressible composite fermion sea at zero tilt to a fully developed even denominator fractional quantum Hall state at $\theta \approx 40^\circ$. This behaviour has not been observed in other 2D systems. We associate this transition with a change of orbital character of electrons at the chemical potential from $N_e = 0$ to 1. The latter orbital character is known to be able to accommodate an even-denominator ground state through the pairing of composite fermions into a superconductor-like ground state. We demonstrate

that there is a unique tendency for localisation effects in higher LL, evidenced by robust reentrant integer quantum Hall effect behaviour which shifts in B_p with rotation, and highly resistive R_{xx} transport inducing anomalous behaviour in R_{xy} at high tilts. We speculate that the latter behaviour is related to a yet unobserved charge density wave like ground state which is induced by the loss of spin degeneracy, which evidently greatly affects screening within the 2DES. Despite such charge-density-wave like transport features, all regimes in the transport are seen to be void of crystal-direction dependent anisotropy. This suggests the prevailing model of a stripe-like phase with an easy/hard axis is not directly applicable.

Many questions and future directions remain regarding the content presented in this thesis. From a growth point of view, it must be asked how further advances can be made. It is clear from this work that in the dilute carrier density regimes explored, there is a fine line between high mobility and modest mobility. This was made clear by the impact annealing has on the sample - when the temperature is above 750°C on the substrate the mobility falls dramatically. We consider this to be as a result of impurities emitted from hot parts which make their way into the grown crystal. It is reasonable to expect that other components are having a similar effect on sample quality, but are going unnoticed. The author still considers the heating unit to be the area of the MBE which can be improved most. Moving to a smaller coil or doing away with a heating coil all together and moving to a laser heating system may alleviate many problems. Other challenges remain with the choice of super-alloys used in the construction of parts and of the substrate holder. While MA-23 has enabled record mobilities, the oxide scale it forms is obviously fragile. A vast array of other super allows exist, yet remain to be tested. It can be said however that MA-24 was found to be inferior to MA-23 in the case of ZnO growth, regardless of its superior specifications. Other ideas include increased capacity Zn cells, potentially in the form of a valved cracker-like cells, which would greatly extend the number of growths that could be done per maintenance cycle.

Beyond mobility, a detailed investigation of the disorder present in heterostructures and the influence it has on the stability of fractional quantum Hall states remains high priority. It is surprising to see that in the work presented in section 5.6, such rich behaviour can be resolved from a heterostructure with a modest mobility of 530,000 cm^2 V^{-1} s^{-1} . An activation energy on the order of $\Delta_{3/2}$ = 90 mK and $\Delta_{7/2}$ = 50 mK is surprising. Moreover, some states reported, such as the ν = 11/3 state, remain to be resolved in AlGaAs/GaAs heterostructures[134], even when the mobility is beyond 20,000,000 cm^2 V^{-1} s^{-1} . Why this is so is likely related to the disorder landscape and inherent material parameters. With further improvements in sample quality and heterostructure design there is a real possibility that the stability of these states in ZnO could rival or surpass that of ν = 5/2 in AlGaAs/GaAs .

As mentioned throughout the work, the observation of even-denominator fractional quantum Hall states outside the realm of AlGaAs/GaAs 2DES, concomitantly to the ability to tune the orbital character of electron at the chemical potential establishes a beautiful new playground for exploring their nature. Moreover, the gears are in motion for more complex experiments. The mesoscopic transport presented in 6.2 alone provide a novel mean for probing the nature of composite fermions at ν = 3/2. The crossover of this partial filling when modifying the orbital character to $N = 1$ is of high interest. Moreover, this technology direct connects to more complex experiments of quantised conduction through 1D constrictions, shot noise measurements and ultimately interferometry devices. It is highly likely however that in order to pursue these experiments, significant efforts in sample growth will be required. While the growth of thick films may enhance mobility, it is highly undesirable for the mesoscopic experiments mentioned. We have also identified a number of insulating phases which are

difficult to explain based on available reports in the literature. These appear intimately connected with the spin degree of freedom which is difficult to probe in other material systems. The interplay of spin and screening on the stability of ground states is therefore a rather fundamental question.

Though beyond the scope of both growth and physics in this work, ZnO exists as a convenient platform in terms of nuclear spin. When it comes to natural abundance only 4% of Zn atoms have a nuclear spin (^{67}Zn, spin 5/2). MgZnO/ZnO heterostructures therefore are potentially a system where the effects of nuclear spin may be selectively investigated, both for enriched and purified regimes. This is not possible in the case of AlGaAs/GaAs 2DES, as all isotopes have a nuclear spin. Enrichment may open the pathway to nuclear magnetic resonance experiments which are extremely useful in the fractional quantum Hall and charge density wave regime, but purification to even lower isotope concentrations may establish ZnO as an extremely attractive platform for spintronic devices. That said, technical (and financial) challenges to produce at least 7N purity ingots of such source materials remain.

We finally return to the fact that ZnO is an oxide, and in theory it should have a chemical compatibility with a wide range of oxide materials. An interesting frontier is other alloys of ZnO, for it is not an foregone conclusion that Mg is indeed the ideal dopant for inducing a 2DES. Other directions include the combination of the MgZnO/ZnO 2DES with exotic materials, such as superconducting or ferromagnetic materials. These may be metals or other oxides. In order to pursue such experiments a significant expansion of the current growth apparatus will be required, as it would be unwise to add such elements to the main growth chamber currently in use. While this may not be plausible in the short term, the author hopes ambitious plans may eventuate in the not too distant future.

References

[1]L. N. Pfeiffer and K. W. West, ``The role of MBE in recent quantum Hall effect physics discoveries'', Physica E: Low-dimensional Systems and Nanostructures **20**, Proceedings of the International Symposium "Quantum Hall Effect: Past, Present and Future", 57–64 (2003).

[2]K. S. Novoselov, A. K. Geim, S. V. Morozov, D. Jiang, Y. Zhang, S. V. Dubonos, I. V. Grigorieva, and A. A. Firsov, ``Electric field effect in atomically thin carbon films'', Science **306**, 666–669 (2004).

[3]Q. H. Wang, K. Kalantar-Zadeh, A. Kis, J. N. Coleman, and M. S. Strano, ``Electronics and optoelectronics of two-dimensional transition metal dichalcogenides'', Nature nanotechnology **7**, 699–712 (2012).

[4]H. Hwang, Y. Iwasa, M. Kawasaki, B. Keimer, N. Nagaosa, and Y. Tokura, ``Emergent phenomena at oxide interfaces'', Nature materials **11**, 103–113 (2012).

[5]A. Geim and I. Grigorieva, ``Van der waals heterostructures'', Nature **499**, 419–425 (2013).

[6]C. Dean, A. Young, I. Meric, C. Lee, L. Wang, S. Sorgenfrei, K. Watanabe, T. Taniguchi, P. Kim, K. Shepard, et al., ``Boron nitride substrates for high-quality graphene electronics'', Nature nanotechnology **5**, 722–726 (2010).

[7]K. Bolotin, K. Sikes, Z. Jiang, M. Klima, G. Fudenberg, J. Hone, P. Kim, and H. Stormer, ``Ultrahigh electron mobility in suspended graphene'', Solid State Commum. **146**, 351–355 (2008).

[8]Z. Ezawa, *Quantum Hall Effects: Recent Theoretical and Experimental Developments, 3rd Edition* (World Scientific Publishing Co. Pte. Ltd., Singapore, 2013).

[9]Laughlin, R. B., ``Anomalous Quantum Hall Effect: An Incompressible Quantum Fluid with Fractionally Charged Excitations'', Phys. Rev. Lett. **50**, 1395–1398 (1983).

[10]Halperin, Bertrand I, ``Theory of the quantized Hall conductance'', Helv. Phys. Acta **56**, 75 (1983).

[11]J. K. Jain, ``Composite-fermion approach for the fractional quantum Hall effect'', Phys. Rev. Lett. **63**, 199–202 (1989).

[12]U. Bockelmann, G. Abstreiter, G. Weimann, and W. Schlapp, ``Single-particle and transport scattering times in narrow GaAs/$Al_xGa_{1-x}As$ quantum wells'', Phys. Rev. B **41**, 7864–7867 (1990).

[13]B. Tanatar and D. Ceperley, ``Ground state of the two-dimensional electron gas'', Phys. Rev. B **39**, 5005–5016 (1989).

[14]N. Drummond and R. Needs, ``Phase Diagram of the Low-Density Two-Dimensional Homogeneous Electron Gas'', Phys. Rev. Lett. **102**, 126402 (2009).

[15]J. Huang, L. N. Pfeiffer, and K. W. West, ``Evidence for A Two-dimensional Quantum Wigner Solid in Zero Magnetic Field'', arXiv: **1306.** 4196 (2013).

[16]M. Büttiker, ``Absence of backscattering in the quantum Hall effect in multiprobe conductors'', Phys. Rev. B **38**, 9375–9389 (1988).

[17]J. Weis and K. von Klitzing, ``Metrology and microscopic picture of the integer quantum hall effect'', Philosophical Transactions of the Royal Society of London A: Mathematical, Physical and Engineering Sciences **369**, 3954–3974 (2011).

[18]D. C. Tsui, H. L. Stormer, and A. C. Gossard, ``Two-dimensional magnetotransport in the extreme quantum limit'', Physical Review Letters **48**, 1559 (1982).

[19]J. P. Eisenstein, G. S. Boebinger, L. N. Pfeiffer, K. W. West, and S. He, ``New fractional quantum Hall state in double-layer two-dimensional electron systems'', Phys. Rev. Lett. **68**, 1383–1386 (1992).

[20]J. Shabani, Y. Liu, M. Shayegan, L. N. Pfeiffer, K. W. West, and K. W. Baldwin, ``Phase diagrams for the stability of the $\nu = \frac{1}{2}$ fractional quantum Hall effect in electron systems confined to symmetric, wide GaAs quantum wells'', Phys. Rev. B **88**, 245413 (2013).

[21]Y. Liu, A. L. Graninger, S. Hasdemir, M. Shayegan, L. N. Pfeiffer, K. W. West, K. W. Baldwin, and R. Winkler, ``Fractional Quantum Hall Effect at $\nu = \frac{1}{2}$ in Hole Systems Confined to GaAs Quantum Wells'', Phys. Rev. Lett. **112**, 046804 (2014).

[22]Y. Liu, S. Hasdemir, D. Kamburov, A. L. Graninger, M. Shayegan, L. N. Pfeiffer, K. W. West, K. W. Baldwin, and R. Winkler, ``Even-denominator fractional quantum hall effect at a landau level crossing'', Phys. Rev. B **89**, 165313 (2014).

[23]A. R. Hamilton, M. Y. Simmons, F. M. Bolton, N. K. Patel, I. S. Millard, J. T. Nicholls, D. A. Ritchie, and M. Pepper, ``Fractional quantum Hall effect in bilayer two-dimensional hole-gas systems'', Phys. Rev. B **54**, R5259–R5262 (1996).

[24]W. Pan, H. Stormer, D. Tsui, L. Pfeiffer, K. Baldwin, and K. West, ``Fractional Quantum Hall Effect of Composite Fermions'', Phys. Rev. Lett. **90**, 016801 (2003).

[25]R. L. Willett, R. R. Ruel, K. W. West, and L. N. Pfeiffer, ``Experimental demonstration of a Fermi surface at one-half filling of the lowest Landau level'', Phys. Rev. Lett. **71**, 3846–3849 (1993).

[26]W. Kang, S. He, H. L. Stormer, L. N. Pfeiffer, K. W. Baldwin, and K. W. West, ``Temperature Dependent Scattering of Composite Fermions'', Phys. Rev. Lett. **75**, 4106–4109 (1995).

[27]J. H. Smet, D. Weiss, K. von Klitzing, P. T. Coleridge, Z. W. Wasilewski, R. Bergmann, H. Schweizer, and A. Scherer, ``Composite fermions in periodic and random antidot lattices'', Phys. Rev. B **56**, 3598–3601 (1997).

[28]W. Kang, H. L. Stormer, L. N. Pfeiffer, K. W. Baldwin, and K. W. West, ``How real are composite fermions?'', Phys. Rev. Lett. **71**, 3850–3853 (1993).

[29]D. Kamburov, M. A. Mueed, I. Jo, Y. Liu, M. Shayegan, L. N. Pfeiffer, K. W. West, K. W. Baldwin, J. J. D. Lee, and R. Winkler, ``Determination of Fermi contour and spin polarization of ν=3/2 composite fermions via ballistic commensurability measurements'', Phys. Rev. B **90**, 235108 (2014).

[30]J. H. Smet, D. Weiss, R. H. Blick, G. Lütjering, K. von Klitzing, R. Fleischmann, R. Ketzmerick, T. Geisel, and G. Weimann, ``Magnetic Focusing of Composite Fermions through Arrays of Cavities'', Phys. Rev. Lett. **77**, 2272–2275 (1996).

[31]I. Kukushkin, J. Smet, K. Von Klitzing, and W. Wegscheider, ``Cyclotron resonance of composite fermions'', Nature **415**, 409–412 (2002).

[32]K. Park and J. K. Jain, ``Phase Diagram of the Spin Polarization of Composite Fermions and a New Effective Mass'', Phys. Rev. Lett. **80**, 4237–4240 (1998).

[33]H. C. Manoharan, M. Shayegan, and S. J. Klepper, ``Signatures of a Novel Fermi Liquid in a Two-Dimensional Composite Particle Metal'', Phys. Rev. Lett. **73**, 3270–3273 (1994).

[34]R. R. Du, H. L. Stormer, D. C. Tsui, A. S. Yeh, L. N. Pfeiffer, and K. W. West, ``Drastic Enhancement of Composite Fermion Mass near Landau Level Filling $\nu = \frac{1}{2}$'', Phys. Rev. Lett. **73**, 3274–3277 (1994).

[35]R. R. Du, A. S. Yeh, H. L. Stormer, D. C. Tsui, L. N. Pfeiffer, and K. W. West, ``Fractional Quantum Hall Effect around $\nu = \frac{3}{2}$: Composite Fermions with a Spin'', Phys. Rev. Lett. **75**, 3926–3929 (1995).

[36]P. K. Lam and S. M. Girvin, ``Liquid-solid transition and the fractional quantum-Hall effect'', Phys. Rev. B **30**, 473–475 (1984).

[37]V. J. Goldman, M. Santos, M. Shayegan, and J. E. Cunningham, ``Evidence for two-dimentional quantum wigner crystal'', Phys. Rev. Lett. **65**, 2189–2192 (1990).

[38]R. Morf and N. d'Ambrumenil, ``Stability and Effective Masses of Composite Fermions in the First and Second Landau Level'', Phys. Rev. Lett. **74**, 5116–5119 (1995).

[39]R. Willett, J. P. Eisenstein, H. L. Störmer, D. C. Tsui, A. C. Gossard, and J. H. English, ``Observation of an even-denominator quantum number in the fractional quantum Hall effect'', Phys. Rev. Lett. **59**, 1776–1779 (1987).

[40]W. Pan, J.-S. Xia, V. Shvarts, D. E. Adams, H. L. Stormer, D. C. Tsui, L. N. Pfeiffer, K. W. Baldwin, and K. W. West, ``Exact Quantization of the Even-Denominator Fractional Quantum Hall State at $\nu = 5/2$ Landau Level Filling Factor'', Phys. Rev. Lett. **83**, 3530–3533 (1999).

[41]J. P. Eisenstein, K. B. Cooper, L. N. Pfeiffer, and K. W. West, ``Insulating and Fractional Quantum Hall States in the First Excited Landau Level'', Phys. Rev. Lett. **88**, 076801 (2002).

[42]V. W. Scarola, K. Park, and J. Jain, ``Cooper instability of composite fermions'', Nature **406**, 863–865 (2000).

[43]G. Moore and N. Read, ``Nonabelions in the fractional quantum hall effect'', Nuclear Physics B **360**, 362–396 (1991).

[44]E. Rezayi and S. Simon, ``Breaking of Particle-Hole Symmetry by Landau Level Mixing in the ν=5/2 Quantized Hall State'', Phys. Rev. Lett. **106**, 116801 (2011).

[45]R. H. Morf, ``Transition from Quantum Hall to Compressible States in the Second Landau Level: New Light on the ν=5/2 Enigma'', Phys. Rev. Lett. **80**, 1505–1508 (1998).

[46]C. Nayak, S. H. Simon, A. Stern, M. Freedman, and S. Das Sarma, ``Non-abelian anyons and topological quantum computation'', Rev. Mod. Phys. **80**, 1083–1159 (2008).

[47]L. Tiemann, G. Gamez, N. Kumada, and K. Muraki, ``Unraveling the spin polarization of the ν= 5/2 fractional quantum Hall state'', Science **335**, 828–831 (2012).

[48]M. Stern, B. Piot, Y. Vardi, V. Umansky, P. Plochocka, D. Maude, and I. Bar-Joseph, ``NMR Probing of the Spin Polarization of the ν=5/2 Quantum Hall State'', Phys. Rev. Lett. **108**, 066810 (2012).

[49]M. Dolev, M. Heiblum, V. Umansky, A. Stern, and D. Mahalu, ``Observation of a quarter of an electron charge at the &ngr;= 5/2 quantum Hall state'', Nature **452**, 829–834 (2008).

[50]V. Venkatachalam, A. Yacoby, L. Pfeiffer, and K. West, ``Local charge of the [ngr]= 5/2 fractional quantum Hall state'', Nature **469**, 185–188 (2011).

[51]J. Eisenstein, R. Willett, H. Stormer, D. Tsui, A. Gossard, and J. English, ``Collapse of the Even-Denominator Fractional Quantum Hall Effect in Tilted Fields'', Phys. Rev. Lett. **61**, 997–1000 (1988).

[52]C. R. Dean, B. A. Piot, P. Hayden, S. Das Sarma, G. Gervais, L. N. Pfeiffer, and K. W. West, ``Contrasting Behavior of the $\frac{5}{2}$ and $\frac{7}{3}$ Fractional Quantum Hall Effect in a Tilted Field'', Phys. Rev. Lett. **101**, 186806 (2008).

[53]S. Baer, C. Rössler, T. Ihn, K. Ensslin, C. Reichl, and W. Wegscheider, ``Experimental probe of topological orders and edge excitations in the second Landau level'', Phys. Rev. B **90**, 075403 (2014).

[54]R. Willett, L. Pfeiffer, and K. West, ``Alternation and interchange of e/4 and e/2 period interference oscillations consistent with filling factor 5/2 non-abelian quasiparticles'', Phys. Rev. B **82**, 205301 (2010).

[55]H. C. Choi, W. Kang, S. Das Sarma, L. N. Pfeiffer, and K. W. West, ``Activation gaps of fractional quantum Hall effect in the second Landau level'', Phys. Rev. B **77**, 081301 (2008).

[56]A. Koulakov, M. Fogler, and B. Shklovskii, ``Charge density wave in two-dimensional electron liquid in weak magnetic field'', Physical review letters **76**, 499 (1996).

[57]M. M. Fogler and A. A. Koulakov, ``Laughlin liquid to charge-density-wave transition at high landau levels'', Phys. Rev. B **55**, 9326–9329 (1997).

[58]M. P. Lilly, K. B. Cooper, J. P. Eisenstein, L. N. Pfeiffer, and K. W. West, ``Evidence for an Anisotropic State of Two-Dimensional Electrons in High Landau Levels'', Phys. Rev. Lett. **82**, 394–397 (1999).

[59]R. Du, D. Tsui, H. Stormer, L. Pfeiffer, K. Baldwin, and K. West, ``Strongly anisotropic transport in higher two-dimensional Landau levels'', Solid State Communications **109**, 389–394 (1999).

[60]B. Friess, V. Umansky, L. Tiemann, K. von Klitzing, and J. H. Smet, ``Probing the Microscopic Structure of the Stripe Phase at Filling Factor $5/2$'', Phys. Rev. Lett. **113**, 076803 (2014).

[61]L. Tiemann, T. Rhone, N. Shibata, and K. Muraki, ``NMR profiling of quantum electron solids in high magnetic fields'', Nature Physics (2014).

[62]G. Gamez and K. Muraki, ``ν = 5/2 fractional quantum Hall state in low-mobility electron systems: Different roles of disorder'', Phys. Rev. B **88**, 075308 (2013).

[63]V. Umansky, M. Heiblum, Y. Levinson, J. Smet, J. Nübler, and M. Dolev, ``MBE growth of ultra-low disorder 2DEG with mobility exceeding 35 x 10^6 cm^2/Vs'', Journal of Crystal Growth **311**, 1658–1661 (2009).

[64]D.-K. Ki, V. I. Fal'ko, D. A. Abanin, and A. F. Morpurgo, ``Observation of Even Denominator Fractional Quantum Hall Effect in Suspended Bilayer Graphene'', Nano Letters **14**, PMID: 24611523, 2135–2139 (2014).

[65]Z. Papi ć and D. A. Abanin, ``Topological Phases in the Zeroth Landau Level of Bilayer Graphene'', Phys. Rev. Lett. **112**, 046602 (2014).

[66]Y. Kozuka, A. Tsukazaki, and M. Kawasaki, ``Challenges and opportunities of ZnO-related single crystalline heterostructures'', Applied Physics Reviews **1**, 011303 (2014).

[67]A. Janotti and C. G. V. de Walle, ``Fundamentals of zinc oxide as a semiconductor'', Reports on Progress in Physics **72**, 126501 (2009).

[68]A. Tsukazaki, A. Ohtomo, T. Onuma, M. Ohtani, T. Makino, M. Sumiya, K. Ohtani, S. Chichibu, S. Fuke, Y. Segawa, H. Ohno, H. Koinuma, and M. Kawasaki, ``Repeated temperature modulation epitaxy for p-type doping and light-emitting diode based on ZnO'', Nature Materials **4**, 42 (2005).

[69]K. Nakahara, S. Akasaka, H. Yuji, K. Tamura, T. Fujii, Y. Nishimoto, D. Takamizu, A. Sasaki, T. Tanabe, H. Takasu, H. Amaike, T. Onuma, S. F. Chichibu, A. Tsukazaki, A. Ohtomo, and M. Kawasaki, ``Nitrogen doped Mg_x Zn_{1-x}O/ZnO single heterostructure ultraviolet light-emitting diodes on ZnO substrates'', Applied Physics Letters **97**, 013501, pages (2010).

[70]S. Akasaka, K. Nakahara, A. Tsukazaki, A. Ohtomo, and M. Kawasaki, ``Mg_x Zn_{1-x}O Films with a Low Residual Donor Concentration ($< 10^{15} cm^{-3}$) Grown by Molecular Beam Epitaxy'', Applied Physics Express **3**, 071101 (2010).

[71]S. Akasaka, K. Nakahara, H. Yuji, A. Tsukazaki, A. Ohtomo, and M. Kawasaki, ``Preparation of an epitaxy-ready surface of a zno(0001) substrate'', Applied Physics Express **4**, 035701 (2011).

[72]H. Morkoç and Ü. Özgür, ``General properties of ZnO'', Zinc Oxide: Fundamentals, Materials and Device Technology, 1–76 (2009).

[73]F. Bernardini, V. Fiorentini, and D. Vanderbilt, ``Spontaneous polarization and piezoelectric constants of III-V nitrides'', Phys. Rev. B **56**, R10024–R10027 (1997).

[74]Y. Kozuka, J. Falson, Y. Segawa, T. Makino, A. Tsukazaki, and M. Kawasaki, ``Precise calibration of Mg concentration in Mg_x Zn_{1-x}O thin films grown on ZnO substrates'', Journal of Applied Physics **112**, 043515, pages (2012).

[75]A. Tsukazaki, A. Ohtomo, D. Chiba, Y. Ohno, H. Ohno, and M. Kawasaki, ``Low-temperature field-effect and magnetotransport properties in a ZnO based heterostructure with atomic-layer-deposited gate dielectric'', Applied Physics Letters **93**, 241905, pages (2008).

[76]V. Umansky and M. Heiblum, *in "Molecular Beam Epitaxy: From research to mass production"* (Elsevier, Oxford, 2013).

[77]M. J. Manfra, ``Molecular beam epitaxy of ultra-high-quality algaas/gaas heterostructures: enabling physics in low-dimensional electronic systems'', Annual Review of Condensed Matter Physics **5**, 347–373 (2014).

[78]M. Uchida, J. Falson, Y. Segawa, Y. Kozuka, A. Tsukazaki, and M. Kawasaki, ``Calibration and control of in-plane Mg doping distribution in Mg_x Zn_{1-x}O/ZnO heterostructures grown by molecular beam epitaxy'', Japanese Journal of Applied Physics **54**, 028004 (2015).

[79]E. Hwang and S. Das Sarma, ``Limit to two-dimensional mobility in modulation-doped GaAs quantum structures: How to achieve a mobility of 100 million'', Phys. Rev. B **77**, 235437 (2008).

[80]S. Akasaka, A. Tsukazaki, K. Nakahara, A. Ohtomo, and M. Kawasaki, ``Improvement of Electron Mobility above 100,000 cm^2 V^{-1} s^{-2} in Mg_x Zn_{1-x}O/ZnO Heterostructures'', Japanese Journal of Applied Physics **50**, 080215 (2011).

[81]M. W. Cho, A. Setiawan, H. J. Ko, S. K. Hong, and T. Yao, ``ZnO epitaxial layers grown on c-sapphire substrate with MgO buffer by plasma-assisted molecular beam epitaxy (P-MBE)'', Semiconductor Science and Technology **20**, S13 (2005).

[82]H. Yuji, K. Nakahara, K. Tamura, S. Akasaka, Y. Nishimoto, D. Takamizu, T. Onuma, S. F. Chichibu, A. Tsukazaki, A. Ohtomo, and M. Kawasaki, ``Optimization of the Growth Conditions for Molecular Beam Epitaxy of dilute Mg_x $Zn_{1-x}O$/ZnO ($0 \leq x \leq 0.12$) Films on Zn-Polar ZnO Substrates'', Japanese Journal of Applied Physics **49**, 071104 (2010).

[83]J. Falson, D. Maryenko, Y. Kozuka, A. Tsukazaki, and M. Kawasaki, ``Magnesium Doping Controlled Density and Mobility of Two-Dimensional Electron Gas in Mg_x $Zn_{1-x}O$/ZnO Heterostructures'', Applied Physics Express **4**, 091101 (2011).

[84]A. Tsukazaki, A. Ohtomo, T. Kita, Y. Ohno, H. Ohno, and M. Kawasaki, ``Quantum hall effect in polar oxide heterostructures'', Science **315**, 1388–1391 (2007).

[85]A. Tsukazaki, S. Akasaka, K. Nakahara, Y. Ohno, H. Ohno, D. Maryenko, A. Ohtomo, and M. Kawasaki, ``Observation of the fractional quantum Hall effect in an oxide'', Nature Materials **9**, 889 (2010).

[86]M. Nakano, A. Tsukazaki, A. Ohtomo, K. Ueno, S. Akasaka, H. Yuji, K. Nakahara, T. Fukumura, and M. Kawasaki, ``Electronic-Field Control of Two-Dimensional Electrons in Polymer-Gated–Oxide Semiconductor Heterostructures'', Advanced Materials **22**, 876–879 (2010).

[87]A. Ohtomo, M. Kawasaki, T. Koida, K. Masubuchi, H. Koinuma, Y. Sakurai, Y. Yoshida, T. Yasuda, and Y. Segawa, ``$Mg_xZn_{1-x}O$ as a II–VI widegap semiconductor alloy'', Applied Physics Letters **72**, 2466–2468 (1998).

[88]Y. Nishimoto, K. Nakahara, D. Takamizu, A. Sasaki, K. Tamura, S. Akasaka, H. Yuji, T. Fujii, T. Tanabe, H. Takasu, A. Tsukazaki, A. Ohtomo, T. Onuma, S. F. Chichibu, and M. Kawasaki, ``Plasma-assisted Molecular Beam Epitaxy of High Optical Quality MgZnO Films on Zn-polar ZnO Substrates'', Applied Physics Express **1**, 091202 (2008).

[89]M. D. Neumann, C. Cobet, N. Esser, B. Laumer, T. A. Wassner, M. Eickhoff, M. Feneberg, and R. Goldhahn, ``Optical properties of MgZnO alloys: Excitons and exciton-phonon complexes'', Journal of Applied Physics **110**, 013520, pages (2011).

[90]Q. Li, J. Zhang, J. Chong, and X. Hou, ``Electron Mobility in ZnMgO/ZnO Heterostructures in the Bloch Grüneisen Regime'', Applied Physics Express **6**, 121102 (2013).

[91]W. Walukiewicz, H. E. Ruda, J. Lagowski, and H. C. Gatos, ``Electron mobility in modulation-doped heterostructures'', Phys. Rev. B **30**, 4571–4582 (1984).

[92]H. Tampo, H. Shibata, K. Maejima, A. Yamada, K. Matsubara, P. Fons, S. Kashiwaya, S. Niki, Y. Chiba, T. Wakamatsu, and H. Kanie, ``Polarization-induced two-dimensional electron gases in znmgo/zno heterostructures'', Applied Physics Letters **93**, 202104, pages (2008).

[93]I. Kukushkin and V. Timofeev, ``Magneto-optics of strongly correlated two-dimensional electrons in single heterojunctions'', Advances in Physics **45**, 147–242 (1996).

[94]J. Betancourt, J. J. Saavedra-Arias, J. D. Burton, Y. Ishikawa, E. Y. Tsymbal, and J. P. Velev, ``Polarization discontinuity induced two-dimensional electron gas at ZnO/Zn(Mg)O interfaces: A first-principles study'', Phys. Rev. B **88**, 085418 (2013).

[95]J. D. Watson, S. Mondal, G. Gardner, G. A. Csáthy, and M. J. Manfra, ``Exploration of the limits to mobility in two-dimensional hole systems in GaAs/AlGaAs quantum wells'', Phys. Rev. B **85**, 165301 (2012).

[96]T. Gokmen, M. Padmanabhan, and M. Shayegan, ``Contrast between spin and valley degrees of freedom'', Phys. Rev. B **81**, 235305 (2010).

[97]Y. Xie, C. Bell, M. Kim, H. Inoue, Y. Hikita, and H. Y. Hwang, ``Quantum longitudinal and Hall transport at the LaAlO3/SrTiO3 interface at low electron densities'', Solid State Communications **197**, 25–29 (2014).

[98]A. Shashkin, S. Kravchenko, V. Dolgopolov, and T. Klapwijk, ``Sharp increase of the effective mass near the critical density in a metallic two-dimensional electron system'', Phys. Rev. B **66**, 073303 (2002).

[99]L. Landau, ``On the theory of the Fermi liquid'', Soviet Physics Jetp-Ussr **8**, 70–74 (1959).

[100]A. Tsukazaki, A. Ohtomo, M. Kawasaki, S. Akasaka, H. Yuji, K. Tamura, K. Nakahara, T. Tanabe, A. Kamisawa, T. Gokmen, J. Shabani, and M. Shayegan, ``Spin susceptibility and effective mass of two-dimensional electrons in Mg_x Zn_{1-x}O/ZnO heterostructures'', Phys. Rev. B **78**, 233308 (2008).

[101]Y. Kozuka, A. Tsukazaki, D. Maryenko, J. Falson, C. Bell, M. Kim, Y. Hikita, H. Y. Hwang, and M. Kawasaki, ``Single-valley quantum Hall ferromagnet in a dilute Mg_x Zn_{1-x}O/ZnO strongly correlated two-dimensional electron system'', Phys. Rev. B **85**, 075302 (2012).

[102]D. Maryenko, J. Falson, Y. Kozuka, A. Tsukazaki, and M. Kawasaki, ``Polarization-dependent landau level crossing in a two-dimensional electron system in a mgzno/zno heterostructure'', Phys. Rev. B **90**, 245303 (2014).

[103]A. Kumar, N. Samkharadze, G. Csáthy, M. Manfra, L. Pfeiffer, and K. West, ``Particle-hole asymmetry of fractional quantum hall states in the second landau level of a two-dimensional hole system'', Phys. Rev. B **83**, 201305 (2011).

[104]K. Vakili, Y. Shkolnikov, E. Tutuc, N. Bishop, E. De Poortere, and M. Shayegan, ``Spin-Dependent Resistivity at Transitions between Integer Quantum Hall States'', Phys. Rev. Lett. **94**, 176402 (2005).

[105]E. Abrahams, S. Kravchenko, and M. Sarachik, ``Metallic behavior and related phenomena in two dimensions'', Rev. Mod. Phys. **73**, 251–266 (2001).

[106]I. Herbut, ``The effect of parallel magnetic field on the Boltzmann conductivity and the Hall coefficient of a disordered two-dimensional Fermi liquid'', Phys. Rev. B **63**, 113102 (2001).

[107]V. Dolgopolov and A. Gold, ``Magnetoresistance of a two-dimensional electron gas in a parallel magnetic field'', English, Journal of Experimental and Theoretical Physics Letters **71**, 27–30 (2000).

[108]J. Nuebler, V. Umansky, R. Morf, M. Heiblum, K. von Klitzing, and J. Smet, ``Density dependence of the ν=5/2 energy gap: Experiment and theory'', Phys. Rev. B **81**, 035316 (2010).

[109]Y. Kasahara, Y. Oshima, J. Falson, Y. Kozuka, A. Tsukazaki, M. Kawasaki, and Y. Iwasa, ``Correlation-Enhanced Effective Mass of Two-Dimensional Electrons in $Mg_xZn_{1-x}O/ZnO$ Heterostructures'', Phys. Rev. Lett. **109**, 246401 (2012).

[110]V. Kozlov, A. Van'kov, S. Gubarev, I. Kukushkin, J. Falson, D. Maryenko, Y. Kozuka, A. Tsukazaki, M. Kawasaki, and J. Smet, ``Observation of plasma and magnetoplasma resonances of two-dimensional electrons in a single MgZnO/ZnO heterojunction'', JETP Letters **98**, 223–226 (2013).

[111]V. E. Kozlov, A. B. Van'kov, S. I. Gubarev, I. V. Kukushkin, V. V. Solovyev, J. Falson, D. Maryenko, Y. Kozuka, A. Tsukazaki, M. Kawasaki, and J. H. Smet, ``Microwave magnetoplasma resonances of two-dimensional electrons in MgZnO/ZnO heterojunctions'', Phys. Rev. B **91**, 085304 (2015).

[112]C. Dahl, F. Brinkop, A. Wixforth, J. Kotthaus, J. English, and M. Sundaram, ``Dimensional resonances in elliptic electron disks'', Solid State Communications **80**, 673–676 (1991).

[113]W. Kohn, ``Cyclotron Resonance and de Haas-van Alphen Oscillations of an Interacting Electron Gas'', Phys. Rev. **123**, 1242–1244 (1961).

[114]S. Shokhovets, O. Ambacher, B. K. Meyer, and G. Gobsch, ``Anisotropy of the momentum matrix element, dichroism, and conduction-band dispersion relation of wurtzite semiconductors'', Phys. Rev. B **78**, 035207 (2008).

[115]M. A. Hopkins, R. J. Nicholas, M. A. Brummell, J. J. Harris, and C. T. Foxon, ``Cyclotron-resonance study of nonparabolicity and screening in GaAs-$Ga_{1-x}Al_xAs$ heterojunctions'', Phys. Rev. B **36**, 4789–4795 (1987).

[116]A. H. MacDonald and C. Kallin, ``Cyclotron resonance in two dimensions: Electron-electron interactions and band nonparabolicity'', Phys. Rev. B **40**, 5795–5798 (1989).

[117]F. F. Fang and W. E. Howard, ``Negative Field-Effect Mobility on (100) Si Surfaces'', Phys. Rev. Lett. **16**, 797–799 (1966).

[118]Y. Kozuka, S. Teraoka, J. Falson, A. Oiwa, A. Tsukazaki, S. Tarucha, and M. Kawasaki, ``Rashba spin-orbit interaction in a Mg_x $Zn_{1-x}O$/ZnO two-dimensional electron gas studied by electrically detected electron spin resonance'', Phys. Rev. B **87**, 205411 (2013).

[119]R. Meisels, I. Kulac, F. Kuchar, and M. Kriechbaum, ``Electron spin resonance of the two-dimensional electron system in $Al_xGa_{1-x}As/GaAs$ at subunity filling factors'', Phys. Rev. B **61**, 5637–5643 (2000).

[120]M. Dobers, K. v. Klitzing, and G. Weimann, ``Electron-spin resonance in the two-dimensional electron gas of GaAs-$Al_xGa_{1-x}As$ heterostructures'', Phys. Rev. B **38**, 5453–5456 (1988).

[121]D. Wang, J. Chen, O. Klochan, K. Das Gupta, D. Reuter, A. Wieck, D. Ritchie, and A. Hamilton, ``Influence of surface states on quantum and transport lifetimes in high-quality undoped heterostructures'', Phys. Rev. B **87**, 195313 (2013).

[122]V. Umansky, R. de-Picciotto, and M. Heiblum, ``Extremely high-mobility two dimensional electron gas: Evaluation of scattering mechanisms'', Applied Physics Letters **71**, 683 (1997).

[123]M. Hirmer, *High-mobility two-dimensional hole gases in III-V semiconductor heterostructures: growth and transport properties*, Ph. D thesis, University of Regensburg, March 2013.

[124]J. Lok, M. Lynass, W. Dietsche, K. von Klitzing, and M. Hauser, ``Quantum Hall ferromagnetism of AlAs 2D electrons'', Physica E: Low-dimensional Systems and Nanostructures **22**, 15th International Conference on Electronic Propreties of Two-Dimensional Systems (EP2DS-15), 94–97 (2004).

[125]S. Schmult, M. J. Manfra, A. M. Sergent, A. Punnoose, H. T. Chou, D. Goldhaber-Gordon, and R. J. Molnar, ``Quantum transport in high mobility AlGaN/GaN 2DEGs and nanostructures'', physica status solidi (b) **243**, 1706–1712 (2006).

[126]M. Manfra, S. Simon, K. Baldwin, A. Sergent, K. West, R. Molnar, and J. Caissie, ``Quantum and transport lifetimes in a tunable low-density AlGaN/GaN two-dimensional electron gas'', Applied physics letters **85**, 5278–5280 (2004).

[127]E. Frayssinet, W. Knap, P. Lorenzini, N. Grandjean, J. Massies, C. Skierbiszewski, T. Suski, I. Grzegory, S. Porowski, G. Simin, X. Hu, M. A. Khan, M. S. Shur, R. Gaska, and D. Maude, ``High electron mobility in AlGaN/GaN heterostructures grown on bulk GaN substrates'', Applied Physics Letters **77**, 2551–2553 (2000).

[128]D.-K. Ki and A. F. Morpurgo, ``High-Quality Multiterminal Suspended Graphene Devices'', Nano Letters **13**, PMID: 24080018, 5165–5170 (2013).

[129]C. Dean, A. Young, P. Cadden-Zimansky, L. Wang, H. Ren, K. Watanabe, T. Taniguchi, P. Kim, J. Hone, and K. Shepard, ``Multicomponent fractional quantum Hall effect in graphene'', Nature Physics **7**, 693–696 (2011).

[130]C. Brüne, C. Thienel, M. Stuiber, J. Böttcher, H. Buhmann, E. G. Novik, C.-X. Liu, E. M. Hankiewicz, and L. W. Molenkamp, ``Dirac-screening stabilized surface-state transport in a topological insulator'', arXiv: **1407.** 6537 (2014).

[131]Y. Xu, I. Miotkowski, C. Liu, J. Tian, H. Nam, N. Alidoust, J. Hu, C.-K. Shih, M. Z. Hasan, and Y. P. Chen, ``Observation of topological surface state quantum Hall effect in an intrinsic three-dimensional topological insulator'', Nature Physics (2014).

[132]M. J. Manfra, L. N. Pfeiffer, K. W. West, R. de Picciotto, and K. W. Baldwin, ``High mobility two-dimensional hole system in GaAs/AlGaAs quantum wells grown on (100) GaAs substrates'', Applied Physics Letters **86**, 162106, pages (2005).

[133]G. Ventura and L. Risegari, *The Art of Cryogenics* (Elsevier, Oxford, 2008), pp. 1–364.

[134]E. Kleinbaum, A. Kumar, L. N. Pfeiffer, K. W. West, and G. A. Csáthy, ``Anomalous Gap Reversal of the 3 + 1/3 and 3 + 1/5 Fractional Quantum Hall States'', arXiv: **1410.** 6571 (2014).

[135]Z. Papi ć and D. A. Abanin, ``Topological Phases in the Zeroth Landau Level of Bilayer Graphene'', Phys. Rev. Lett. **112**, 046602 (2014).

[136]R. H. Morf, N. d'Ambrumenil, and S. Das Sarma, ``Excitation gaps in fractional quantum Hall states: An exact diagonalization study'', Phys. Rev. B **66**, 075408 (2002).

[137]A. H. MacDonald and S. M. Girvin, ``Collective excitations of fractional Hall states and Wigner crystallization in higher Landau levels'', Phys. Rev. B **33**, 4009–4013 (1986).

[138]Y. W. Suen, H. C. Manoharan, X. Ying, M. B. Santos, and M. Shayegan, ``Origin of the ν=1/2 fractional quantum Hall state in wide single quantum wells'', Phys. Rev. Lett. **72**, 3405–3408 (1994).

[139]N. Deng, J. D. Watson, L. P. Rokhinson, M. J. Manfra, and G. A. Csáthy, ``Contrasting energy scales of reentrant integer quantum Hall states'', Phys. Rev. B **86**, 201301 (2012).

[140]N. Deng, G. C. Gardner, S. Mondal, E. Kleinbaum, M. J. Manfra, and G. A. Csáthy, ``ν=5/2 Fractional Quantum Hall State in the Presence of Alloy Disorder'', Phys. Rev. Lett. **112**, 116804 (2014).

[141]D. Maryenko, J. Falson, Y. Kozuka, A. Tsukazaki, M. Onoda, H. Aoki, and M. Kawasaki, ``Temperature-Dependent Magnetotransport around $\nu = 1/2$ in ZnO Heterostructures'', Phys. Rev. Lett. **108**, 186803 (2012).

[142]Y. Liu, S. Hasdemir, J. Shabani, M. Shayegan, L. Pfeiffer, K. West, and K. Baldwin, ``Multicomponent fractional quantum Hall states with subband and spin degrees of freedom'', arXiv: **1501.** 06958 (2015).

[143]M. Lilly, K. Cooper, J. Eisenstein, L. Pfeiffer, and K. West, ``Anisotropic states of two-dimensional electron systems in high Landau levels: Effect of an in-plane magnetic field'', Physical review letters **83**, 824 (1999).

[144]W. Pan, R. Du, H. Stormer, D. Tsui, L. Pfeiffer, K. Baldwin, and K. West, ``Strongly anisotropic electronic transport at Landau level filling factor ν = 9/2 and ν= 5/2 under a tilted magnetic field'', Physical review letters **83**, 820 (1999).

[145]G. A. Csáthy, J. S. Xia, C. L. Vicente, E. D. Adams, N. S. Sullivan, H. L. Stormer, D. C. Tsui, L. N. Pfeiffer, and K. W. West, ``Tilt-Induced Localization and Delocalization in the Second Landau Level'', Phys. Rev. Lett. **94**, 146801 (2005).

[146]E. De Poortere, E. Tutuc, S. Papadakis, and M. Shayegan, ``Resistance spikes at transitions between quantum hall ferromagnets'', Science **290**, 1546–1549 (2000).

[147]S. Das Sarma, G. Gervais, and X. Zhou, ``Energy gap and spin polarization in the 5/2 fractional quantum hall effect'', Phys. Rev. B **82**, 115330 (2010).

[148]Y. Kozuka, A. Tsukazaki, D. Maryenko, J. Falson, S. Akasaka, K. Nakahara, S. Nakamura, S. Awaji, K. Ueno, and M. Kawasaki, ``Insulating phase of a two-dimensional electron gas in ZnO heterostructures below $\nu = \frac{1}{3}$'', Phys. Rev. B **84**, 033304 (2011).

[149]E. Menard, V. Podzorov, S.-H. Hur, A. Gaur, M. E. Gershenson, and J. A. Rogers, ``High-performance n- and p-type single crystal organic transistors with free-space gate dielectrics'', Adv. Mater. **16**, 2097–2101 (2004).

[150]B. E. Feldman, B. Krauss, J. H. Smet, and A. Yacoby, ``Unconventional sequence of fractional quantum Hall states in suspended graphene'', Science **337**, 1196–1199 (2012).

[151]T. Tambo, J. Falson, D. Maryenko, Y. Kozuka, A. Tsukazaki, and M. Kawasaki, ``Air-gap gating of MgZnO/ZnO heterostructures'', Journal of Applied Physics **116**, 084310, pages (2014).

[152]B. van Wees, H. van Houten, C. Beenakker, J. Williamson, L. Kouwenhoven, D. van der Marel, and C. Foxon, ``Quantized conductance of point contacts in a two-dimensional electron gas'', Phys. Rev. Lett. **60**, 848–850 (1988).

[153]D. Weiss and K. V Klitzing and K. Ploog and G. Weimann, ``Magnetoresistance oscillations in a two-dimensional electron gas induced by a submicrometer periodic potential'', EPL (Europhysics Letters) **8**, 179 (1989).

[154]D. Weiss, M. Roukes, A. Menschig, P. Grambow, K. von Klitzing, and G. Weimann, ``Electron pinball and commensurate orbits in a periodic array of scatterers'', Phys. Rev. Lett. **66**, 2790–2793 (1991).

List of Publications, Presentations and Awards

Publications

Peer reviewed journal articles

1. Insulating phase of a two-dimensional electron gas in $Mg_xZn_{1-x}O$/ZnO heterostructures below ν=1/3,
   Y. Kozuka, A. Tsukazaki, D. Maryenko, J. Falson, S. Akasaka, K. Nakahara, S. Nakamura, S. Awaji, K. Ueno and M. Kawasaki, *Physical Review B* **84**, 033304 (2011).

2. Magnesium Doping Controlled Density and Mobility of Two-Dimensional Electron Gas in $Mg_xZn_{1-x}O$/ZnO Heterostructures,
   J. Falson, D. Maryenko, Y. Kozuka, A. Tsukazaki and M. Kawasaki, *Applied Physics Express* **4**, 091101 (2011).

3. Single-valley quantum Hall ferromagnet in a dilute $Mg_xZn_{1-x}O$/ZnO strongly correlated two-dimensional electron system,
   Y. Kozuka, A. Tsukazaki, D. Maryenko, J. Falson, C. Bell, M. Kim, Y. Hikita, H. Y. Hwang and M. Kawasaki, *Physical Review B* **85**, 075302 (2012).

4. Temperature-Dependent Magnetotransport around ν =1/2 in ZnO Heterostructures,
   D. Maryenko, J. Falson, Y. Kozuka, A. Tsukazaki, M. Onoda, H. Aoki and M. Kawasaki, *Physical Review Letters* **108**, 186803 (2012).

5. Precise calibration of Mg concentration in $Mg_xZn_{1-x}O$ thin films grown on ZnO substrates,
   Y. Kozuka, J. Falson, Y. Segawa, T. Makino, A. Tsukazaki and M. Kawasaki, *Journal of Applied Physics* **112**, 043515 (2012).

6. Correlation-Enhanced Effective Mass of Two-Dimensional Electrons in $Mg_xZn_{1-x}O$/ZnO Heterostructures,
   Y. Kasahara, Y. Oshima, J. Falson, Y. Kozuka, A. Tsukazaki, M. Kawasaki and Y. Iwasa, *Physical Review Letters* **109**, 246401 (2012).

7. Rashba spin-orbit interaction in a MgZnO/ZnO two-dimensional electron gas studied by electrically-detected electron spin resonance,
   Y. Kozuka, S. Teraoka, J. Falson, A. Oiwa, A. Tsukazaki, S. Tarucha and M. Kawasaki, *Physical Review B* **87**, 205411 (2013).

8. Observation of plasma and magnetoplasma resonances of two-dimensional electrons in a single MgZnO/ZnO heterojunction,
   V. E. Kozlov, A. B. Van'kov, S. I. Gubarev, I. V. Kukushkin, J. Falson, D. Maryenko, Y. Kozuka, A. Tsukazaki, M. Kawasaki and J. H. Smet, *JETP Letters* **98**, 223 (2013).

9. Enhanced quantum oscillatory magnetization and nonequilibrium currents in an interacting two-dimensional electron system in MgZnO/ZnO with repulsive scatterers,
   M. Brasse, S. M. Sauther, J. Falson, Y. Kozuka, A. Tsukazaki, Ch. Heyn, M. A. Wilde, M. Kawasaki and D. Grundler, *Physical Review B* **89**, 075307 (2014).

10. Spontaneous polarization driven Mg concentration profile reconstruction in MgZnO/ZnO heterostructures,
    K. Imasaka, J. Falson, Y. Kozuka, A. Tsukazaki and M. Kawasaki, *Applied Physics Letters* **104**, 242112 (2014).

11. Trajectory of Anomalous Hall Effect toward the Quantized State in a Ferromagnetic Topological Insulator,
    J. Checkelsky, R. Yoshimi, A. Tsukazaki, K. S. Takahashi, Y. Kozuka, J. Falson, M. Kawasaki and Y. Tokura, *Nature Physics* **10**, 731 (2014).

12. Air-gap gating of MgZnO/ZnO heterostructures,
    T. Tambo, J. Falson, D. Maryenko, Y. Kozuka, A. Tsukazaki and M. Kawasaki, *Journal of Applied Physics* **116**, 084310 (2014).

13. Polarization dependent Landau level crossing in a two-dimensional electron system in MgZnO/ZnO-heterostructure,
    D. Maryenko, J. Falson, Y. Kozuka, A. Tsukazaki and M. Kawasaki, *Physical Review B* **90**, 245303 (2014).

14. Calibration and control of in-plane Mg doping distribution in $Mg_xZn_{1-x}O$/ZnO heterostructures grown by molecular beam epitaxy,
    M. Uchida, J. Falson, Y. Kozuka, A. Tsukazaki and M. Kawasaki, *Japanese Journal of Applied Physics* **54**, 028004 (2015).

15. Microwave magnetoplasma resonances of 2D-electrons in MgZnO/ZnO heterojunctions,
    V. E. Kozlov, A. B. Vankov, S. I. Gubarev, I. V. Kukushkin, V. V. Solovyev, J. Falson, D. Maryenko, Y. Kozuka, A. Tsukazaki, J. H. Smet and M. Kawasaki, *Physical Review B* **91**, 085304 (2015).

16. Even-denominator fractional quantum Hall physics in ZnO,
    J. Falson, D. Maryenko, B. Friess, D. Zhang, Y. Kozuka, A. Tsukazaki, J. H. Smet and M. Kawasaki, *Nature Physics, in press*.

17. Quantum Hall Effect on Top and Bottom Surface States of Topological Insulator $(Bi_{1-x}Sb_x)_2Te_3$ Films,
    R. Yoshimi, A. Tsukazaki, Y. Kozuka, J. Falson, K. S. Takahashi, J. G. Checkelsky, N. Nagaosa, M. Kawasaki and Y. Tokura, *Nature Communications, in press*.

18. Optical probing of MgZnO/ZnO heterointerface confinement potential energy levels,
    V. V. Solovyev, A. B. Van'kov, I. V. Kukushkin, J. Falson, D. Zhang, D. Maryenko, Y. Kozuka, A. Tsukazaki, J. H. Smet and M. Kawasaki, *Applied Physics Letters, in press*.

Presentations

International conferences

1. Magnesium doping controlled mobility up to μ = 0.8 x 10^6 cm^2 V^{-1} s^{-1} in ZnO based two-dimensional electron systems, J. Falson, D. Maryenko, Y. Kozuka, A. Tsukazaki and M. Kawasaki, *Workshop for Oxide Electronics 18*, Napa, California, 27th September, 2011. Oral presentation.

2. Even denominator fractional quantum Hall states in ZnO, J. Falson, D. Maryenko, D. Zhang, B. Friess, Y. Kozuka, A. Tsukazaki, J. H. Smet and M. Kawasaki, *Symposium on Quantum Hall Effects and Related Topics*, Stuttgart, Germany, 27th June, 2013. Poster presentation.

3. Even denominator and higher Landau level fractional quantum Hall states in ZnO, J. Falson, D. Maryenko, D. Zhang, B. Friess, Y. Kozuka, A. Tsukazaki, J.H. Smet, M. Kawasaki, *Electronic Properties of Two-Dimensional Systems 20*, Wroclaw, Poland, 3rd July, 2013. Oral presentation.

4. Even denominator fractional quantum Hall states in ZnO, J. Falson, D. Maryenko, D. Zhang, B. Friess, Y. Kozuka, A. Tsukazaki, J.H. Smet, M. Kawasaki, *International Symposium on Nanoscale Transport and Technology*, Atsugi, Japan, 28th November, 2013. Oral presentation.

5. Odd even-denominator fractional quantum Hall physics in ZnO, J. Falson, D. Maryenko, B. Friess, D. Zhang, Y. Kozuka, A. Tsukazaki, J. H. Smet and M. Kawasaki, FIRST-QS^2C Workshop on "Emergent Phenomena of Correlated Materials", Tokyo, Japan, 13th November 2013. Poster presentation.

6. Odd even-denominator fractional quantum Hall physics in ZnO, J. Falson, D. Maryenko, B. Friess, D. Zhang, Y. Kozuka, A. Tsukazaki, J. H. Smet and M. Kawasaki, FIRST International Symposium on “Topological Quantum Technology”, Tokyo, Japan, 29th January 2014. Poster presentation.

7. Odd even-denominator fractional quantum Hall physics in ZnO, J. Falson, *21st International Conference on High Magnetic Fields in Semiconductor Physics*, Panama City Beach, Florida, USA, 8th August, 2014. Invited talk.

Domestic conferences

1. 「Magnesium doping controlled density and mobility of two-dimensional electron gas in $Mg_xZn_{1-x}O$/ZnO heterostructures」 ジョセフ フォルソン, デニス マリエンコ, 小塚裕介, 塚崎敦, 川崎雅司, 日本物理学会2011年年次・秋季大会 2011/9/21-24　富山　口頭発表

2. 「MgZnO/ZnO ヘテロ接合における強相関二次元キャリアーの有効質量解析」ジョセフ フォルソン、デニス　マリエンコ、小塚裕介、塚崎　敦、川崎雅司, 第3回低温センター研究交流会 2012/3/5 東京大学低温センター ポスター発表

3. 「$Mg_xZn_{1-x}O$/ZnOヘテロ界面 における二次元電子ガスの移動度制御」ジョセフ フォルソン, デニス マリエンコ, 小塚裕介, 塚崎　敦, 川崎雅司, 2012年春季第59回応用物理学関係連合講演会 2012/3/15-18 東京　口頭発表　講演奨励賞受賞

4. 「$Mg_xZn_{1-x}O$/ZnOヘテロ界面 における二次元電子ガスの移動度制御」ジョセフ フォルソン, デニス マリエンコ, 小塚裕介, 塚崎　敦, 川崎雅司, 2012年秋季 第73回応用物理学会学術講演会 2012/9/11-14 松山　口頭発表　講演奨励賞受賞記念講演

5. 「ZnO二次元電子系におけるリエントラント整数量子ホール効果の出現」ジョセフ フォルソン, デニス マリエンコ, 小塚裕介, 小野新平, 寺倉千恵子, 塚崎敦, 川崎雅司, 日本物理学会 2012年年次・秋季大会 2012/9/11-14 横浜　口頭発表
6. 「ZnO系二次元電子における偶数分母分数状態の観測」Joseph Falson, Denis Maryenko, Benedikt Friess, Ding Zhang, 小塚裕介, 塚崎敦, Jurgen Smet, JIl崎雅司, 日本物理学会 2013年次・秋季大会 2013/9/25-28 徳島 口頭発表
7. 「ZnO系二次元電子における偶数分母分数状態の観測と制御」Joseph Falson, Denis Maryenko, Benedikt Friess, Ding Zhang, 小塚裕介, 塚崎敦, Jurgen Smet, JIl﨑 雅司, 第3回低温センター研究交流会　 2014/2/27　東京大学低温センター 口頭発表
8. 「占有率＝3/2分数量子ホール状態の安定性と再現性」日本物理学会2014年次・秋季大会 J. Falson, Denis Maryenko, Benedikt Friess, Ding Zhang, 小塚裕介, 塚崎敦, Jurgen Smet, 川﨑 雅司　2014/9/7-11 名古屋　口頭発表

Awards

1. Japanese Government MEXT Funded International Research Student, April 2010 - March 2015.
2. Japanese Society of Applied Physics Young Scientist Presentation Award, September 2012.
3. Marubun Research Promotion Foundation Research Assistance Award (1,000,000 yen), March, 2013.
4. Japanese Proficiency Level Test N1, July, 2014.

Acknowledgements

The entirety of this work has been made possible through the guidance and contributions of the people surrounding me. This has become acutely obvious to me during the process of compiling this thesis. Throughout my time as a student I have had the privilege to work as a grower of samples, which has resulted in many opportunities to participate in collaborations involving experimental techniques that I never would have been able to initiate or pursue by my own means alone. I extend my sincere gratitude to all members of the scientific community I have had the chance to interact with during my time as a student, for each any everyone of you have aided my growth both as a scientist and a human being. In roughly chronological-by-continent order and starting in Japan:

- The door to this work was opened for me by my supervisor, Professor Masashi Kawasaki. From our first meeting I had considered there to be a strong connection on many levels. I thank you for providing the environment for me to grow and work in a free and independent manner while always remaining engaged and supportive.
- I must also thank Professor Takahisa Arima for accepting me as a student during the course of this Ph. D and for giving me the freedom to continue working on this content.
- A large proportion of this work has indeed been instigated and since supported by Professor Atsushi Tsukazaki. I thank you for kindly taking me under your wing, literally from day zero, where you spent many hours going through the train-wreck that was my preparation for the entrance examination presentation. I appreciate the frankness and openness you have shared with me.
- I also extent my sincere gratitude to Dr. Yusuke Kozuka for the never ending efforts to teach and include me in aspects of the project when I was too inept to get involved by my own means alone.
- Also, to my friend Dr. Denis Maryenko for teaching me the basics of the field and for sharing his wealth of ideas, ways of thinking, optimism and ambition with me.
- To all the members of Kawasaki and Arima lab at the University of Tokyo, including my partners-in-crime, soon-to-be-doctor Yuya Matsubara, Masato Ito and Takahiro Fujita, for sharing many laughs and contributing to keeping the lab running smoothly. Also Dr. Masaki Uchida for the discussion on MBE design and for keeping all the students moving in the right direction. I must also thank Tomoki Tambo and Kazunari Tanaka for the experimental efforts and for producing the beautiful data presented in section 6.
- Dr Koji Muraki for the various discussions, critique and suggestions provided since the early days of this project. Also, for supporting my participation in the domestic quantum Hall community.

- Also, to other members of the scientific community in Japan for regular or irregular discussions, including members of RIKEN, Professor Naoto Nagaosa, Professor Yoshihiro Iwasa, Dr. Yoichi Nii, Dr. Kei Takahashi and Dr. Mohammad Saeed Bahramy, as well as those at NTT including Dr. Trevor David Rhone, and all collaborators on published works.

- Finally, to all members of the examination board for evaluating and critiquing this thesis.

Moving to Europe:

- I extend my sincere gratitude to Professor Klaus von Klitzing of the Max Planck Institute in Stuttgart, for initially enabling my visits and for empowering ZnO as a material from the early days of the project.

- Dr Jurgen Smet of the Max Planck Institute in Stuttgart, for the warm hospitality during my numerous stays, for being a tough coach on "vision" and "story" and for engaging ZnO so openly.

- Dr Ding Zhang and Dr Benedikt Friess for accommodating me in Stuttgart and sharing valuable measurement time in the cryostats. I know that you were not excited about cooling down a dirty oxide, but I hope you are happy with the outcomes.

- The students in Stuttgart including Daniel Kärcher, Matthias Kühne, Federico Paolucci and Patrick Herlinger for welcoming me into their circle. I look forward to good times ahead.

- Professor Igor Kukushkin and his team at The Institute of Solid State Physics in Chernogolovka in Russia. The experimental results through our collaboration have contributed extensively to the understanding of the ZnO 2DES. I hope that the collaboration continues in to the future with the same or even more vigorous momentum.

- Professor Werner Wegscheider, Professor Werner Dietsche and Dr. Lars Tiemann of ETH, Zurich, for both accommodating me during my visit and for providing an outlet to discuss the nitty-gritty of MBE design.

Finally moving to America:

- I thank Professor Amir Yacoby and Andrei Levin for the hospitality and scientific aid provided during my brief stay at Harvard. I look forward to advancing these experiments in the near future.

- I am also in indebted to Professor Mansour Shayegan and Dr. Yang Liu for the extensive discussions and critique throughout the development of this thesis and the publications which report its main findings.

- Professor Harold Hwang and his group for collaborative efforts during the early stages of this thesis.

- Finally, Professor Joseph Checkelsky for our many discussions about science and life during his time here in Japan.

I must also extend my gratitude to the Japanese government for sponsoring my stay in Japan for the past five years. The support through the MEXT sponsored research student program provided has enabled me to focus exclusively on science and my studies. I have endeavoured to establish a network

of collaborations which extends beyond university or national boundaries. I believe this thoroughly increases the quality and transparency of science as a discipline, and that this is one of the main goals of such an international scholarship program. To any one reading this, allow me to strongly recommend the option of pursuing further studies or research projects outside of your own community or country. Science is about breaking down boundaries and working for the good of the human race. I do not believe this can be accomplished in a closed environment.

Finally, my family for the continued support and love, despite me packing my bags and putting 6000 km of ocean in between us. The regular visits and parcels have made day-to-day life more enjoyable and have always given me something to look forward to.

Joseph Lindsay Falson
February 16, 2015